

Marcus Diem

Beschreibung der optischen Eigenschaften  
nanostrukturierter Materialien  
mit Methoden der diffraktiven Optik

“Description of the Optical Properties of  
Nanostructured Materials  
using Methods of Diffractive Optics”



Beschreibung der optischen Eigenschaften  
nanostrukturierter Materialien  
mit Methoden der diffraktiven Optik

Zur Erlangung des akademischen Grades eines

DOKTORS DER NATURWISSENSCHAFTEN

von der Fakultät für Physik der Universität  
Karlsruhe (TH)

genehmigte

DISSERTATION

von

Dipl. Phys. Marcus Diem  
aus Calw

Tag der mündlichen Prüfung: 19.01.2007

Referent: Prof. Dr. K. Busch

Korreferent: Prof. Dr. P. Wölffe



# Contents

<b>Preface</b>	<b>ix</b>
<b>1 Introduction to Photonic Crystals</b>	<b>1</b>
1.1 Basic Properties of Photonic Crystals . . . . .	1
1.2 Direct Lattice and Reciprocal Lattice . . . . .	3
1.3 Wave Propagation in Media . . . . .	5
1.3.1 Wave Propagation in Periodic Media . . . . .	6
1.3.2 2D Crystal . . . . .	7
1.3.3 Scaling Properties . . . . .	8
1.4 Band Structures and Finite Samples . . . . .	9
<b>2 Numerical Method</b>	<b>11</b>
2.1 Basic Principles . . . . .	11
2.1.1 Quantities of Interest . . . . .	11
2.2 Fields in Individual Layers . . . . .	14
2.3 Matching Fields in Adjoining Layers . . . . .	24
2.4 Solving for All Layers . . . . .	25
2.4.1 Scattering Matrix Recursion . . . . .	26
2.4.2 Multiplication of Scattering-Matrices . . . . .	27
2.5 Fields Inside the Structure . . . . .	29
2.6 Reflected and Transmitted Modes . . . . .	29
2.7 Dipole Emission . . . . .	30
2.8 Alternative Approaches . . . . .	32
2.8.1 Conceptually Similar Approaches and Improvements . . . . .	32
2.8.2 Conceptually Different Approaches . . . . .	33
2.8.3 Finite Differences and Finite Elements . . . . .	33
2.8.4 Finite-Differences Time-Domain (FDTD) . . . . .	34
<b>3 Implementation and Optimization</b>	<b>35</b>
3.1 Fourier Expansion . . . . .	35
3.1.1 Definition of Diffraction Orders . . . . .	35
3.1.2 Triangular Example . . . . .	36
3.1.3 Correct Choice of Expansion Orders . . . . .	38
3.2 Representation of the Incoming Wave . . . . .	40

3.2.1	Correct Choice of Diffraction Orders . . . . .	41
3.2.2	Polarizations . . . . .	41
3.3	Transmittance and Reflectance Coefficients . . . . .	44
3.4	Optimization . . . . .	46
3.4.1	The Simple Approach . . . . .	46
3.4.2	Avoiding Large Memory Requirements . . . . .	47
3.4.3	Storage of $\hat{\epsilon}/\hat{\eta}$ . . . . .	49
3.4.4	Long Structures Using a Numerical Unit Cell . . . . .	51
3.4.5	Fields . . . . .	53
3.4.6	Implementation of the Fourier Transform . . . . .	55
3.4.7	Homogeneous Eigenvalue Problem . . . . .	56
3.5	Implemented Options . . . . .	57
3.5.1	Frequency and Wavelength . . . . .	57
3.5.2	Parameters . . . . .	57
3.5.3	Parameters Describing the Measurement . . . . .	58
3.5.4	Crystal Parameters . . . . .	59
3.5.5	Dispersive Permittivity . . . . .	59
3.5.6	Smoothing . . . . .	61
3.5.7	Concluding Remarks on Parameters . . . . .	62
3.6	Lattices Classes and Crystal Symmetries . . . . .	64
3.7	Disorder . . . . .	65
3.7.1	Database . . . . .	65
3.7.2	Supercell and Finite-Size Scaling . . . . .	66
3.8	Test Systems . . . . .	67
3.8.1	Analytical Systems . . . . .	67
3.8.2	Physical Expectations . . . . .	69
3.8.3	In-Code Testing . . . . .	69
<b>4</b>	<b>Two-Dimensional Pore System</b> . . . . .	<b>71</b>
4.1	Implementation Differences for Finite Two-Dimensional Structures . . . . .	71
4.2	Numerical Unit Cell . . . . .	72
4.3	Fabrication . . . . .	73
4.4	Previous Studies . . . . .	74
4.5	Length Dependence in Crystals with Absorption . . . . .	76
4.6	Attenuation Length . . . . .	80
4.7	Surface Termination . . . . .	81
4.8	Sampling Problem For Long Crystals . . . . .	85
4.9	Radius Fluctuations . . . . .	87
4.9.1	Statistical Approaches . . . . .	89
4.9.2	Analysis of Distributions . . . . .	91
4.9.3	Manual Selection of Distributions . . . . .	92
4.9.4	Distributions . . . . .	92
4.9.5	Description of Distributions . . . . .	98
4.9.6	Impact of Absorption . . . . .	103

4.9.7	Finite Size Scaling Using Supercells . . . . .	106
4.10	Conclusion and Outlook . . . . .	109
<b>5</b>	<b>2D Distributed Feedback Lasing</b>	<b>113</b>
5.1	Photonic System . . . . .	113
5.1.1	Fabrication . . . . .	114
5.1.2	Description of Corrugation . . . . .	116
5.2	Basic Aspects of Lasing in Corrugated Structures . . . . .	116
5.3	Determination of Lasing Modes . . . . .	120
5.4	Estimates of Coupling Strength . . . . .	122
5.4.1	Determination of Peaks . . . . .	123
5.5	Conclusion and Outlook . . . . .	125
<b>6</b>	<b>Holography</b>	<b>127</b>
6.1	Photonic System . . . . .	127
6.1.1	Fabrication . . . . .	129
6.1.2	Dose formula . . . . .	129
6.2	Testing of the Simulation . . . . .	132
6.3	Impact of Parameters on Transmittance Spectra . . . . .	133
6.3.1	Frequency Resolution (Folding with Apparatus Function) . . .	135
6.3.2	Rotation of the Sample . . . . .	136
6.3.3	Surface Termination . . . . .	136
6.3.4	Absorption of Exposure Beam . . . . .	138
6.3.5	Prefactor/Filling Fraction . . . . .	138
6.3.6	Shrinkage in the Vertical Direction . . . . .	140
6.3.7	Finite Glass and Substrate . . . . .	141
6.4	Characterization of Samples . . . . .	145
<b>7</b>	<b>Conclusions and Outlook</b>	<b>149</b>
<b>A</b>	<b>Distributions for Selected Frequencies</b>	<b>153</b>
<b>B</b>	<b>Transmittance Distributions for Supercells</b>	<b>161</b>
<b>C</b>	<b>Comparison of Experiment and Theory for Holographic Structures</b>	<b>163</b>
	<b>Acronyms</b>	<b>169</b>



# Preface

Over the last years, Photonic Crystals (PC) have generated a lot of interest [1–7] due to both, exciting challenges they pose for basic and materials science and promising optical properties for numerous applications. Most of the fascinating aspects are based on the Photonic Band Gap (PBG) caused by the periodicity of certain PC structures, in which the vanishing density of states in certain frequencies ranges suppresses the propagation of light exponentially<sup>1</sup>.

PCs were first suggested in 1987 by E. Yablonovitch [8] and S. John [9] in different contexts. E. Yablonovitch proposed changes in the spontaneous emission properties of atoms in these structures, whereas S. John discussed the strong localization of (non-interacting) photons. The general public became aware of PCs after the presentation of the “Photonic Micropolis” by J. Joannopoulos [10], which created a vision to the community. The main idea was to create functional elements to replace the electronic systems used in information processing by integrated optical circuits. Today's electronic technologies are based on the band gap for electrons in semiconductors caused by the periodic arrangement of atoms. The possible analogies in the electronic and photonic systems suggested a wide range of applications for this new class of optical materials called PBG materials.

Until now, several optical functional elements have been proposed and created in various experimental groups around the world. This includes standard devices such as waveguides and cavities [5, 7] as well as add/drop filters [11] or de-multiplexer [12, 13]. So far, these elements only exist as single elements or as design proposals (“blueprints”) but they have not yet been combined into an integrated circuit. For the theoretical description of optical circuits, a method has been presented lately [14, 15], combining the simulation of individual elements with a scattering-matrix ( $S$ -matrix) approach to couple them and form a circuit. Besides these optical elements, a few more exotic applications of PCs were presented, such as suppressing higher order modes in electron accelerators [16] and guiding Bose-Einstein condensates in the evanescent fields of a PC waveguide [17].

Except for the structures produced in laboratories, only two representations of PCs are commercially available on larger scales. 1D PCs (Bragg reflectors)<sup>2</sup> [19],

---

<sup>1</sup>For ideal, infinite structures the density of states is equal to zero and the propagation is not only suppressed but impossible.

<sup>2</sup>Fiber-Bragg-gratings are another 1D example with very impressive applications, e. g. as frequency selective mirrors embedded in a 75km long glass fiber allowing a standing wave pattern which can then enhance signals at lower frequencies by subsequent Raman scattering [18].

which were known long before the field of PC research was established. Quasi-2D systems are the foundation of the second commercially successful PC system, Photonic Crystal Fibers [20, 21]. For some applications, e.g. near field enhancement for Surface Enhanced Raman Scattering [22] or polarizers [23], PC are also sold by companies but these products are not very prominent.

Although PCs are always mentioned as a prime example of artificial materials, periodic dielectric arrangements are common in nature as well, mostly as structural colors, e.g. in opals or on the wings of insects [24]. In other cases they are used for heat regulations [25]. The natural counterparts usually do not exhibit a PBG due to the small index contrast of the constituent materials. Still, initial attempts are made to copy nature [26] or to use natural structures as fabrication templates [27] for bulk PCs.

The fabrication of reliable bulk structures on a large scale is still one of the problems which limits the PC to laboratory environments, especially in three dimensions. Therefore, it is not only necessary to study defect modes (e.g. cavity or waveguide modes) but also the bulk material. In addition, bulk material is interesting by itself and can also exhibit functional properties, e.g. polarization beam splitters can be created without defect structures [28] or superrefractive effects making an improvement of the bulk a worthwhile aim.

In this context, it is important to have tools available which allow for an accurate description of experiments to be able to determine the quality of the sample and whether the fabricated crystal corresponds to the desired structure. Consequently, finite, but eventually large crystals have to be simulated. For these structures a large number of parameters is needed to describe the distribution of dielectric material. Recently the term 3 + 1 integrated optics has been introduced, with the frequency as the 4<sup>th</sup> parameter [29] beside the three spatial dimensions. In the spirit of this nomenclature, the problems considered in this work relates to light propagation through 3+ $X$ -dimensional PCs with  $X$  describing e.g. frequency, angle of incidence, surface termination, deviations in structural parameters, etc.

As a consequence, a tool for studying these aspects has to be flexible and fast. In this work such a tool has been implemented based on the Rigorous Coupled Wave Method (RCWA) combined with a scattering-matrix ( $S$ -matrix) approach to calculate the transmittance through finite 2D and 3D periodic structures. The numerical method is presented in Chapter 2 and details of the implementation and optimization of the code with respect to memory and/or computation time requirements are given in Chapter 3.

The possibilities of the program are demonstrated with three selected projects. Firstly, a 2D structure of air pores in silicon is studied on a conceptual level in Chapter 4. The impact of different parameters, such as surface termination and material absorption on the transmittance in different regions of the band structure are studied in this chapter. For this structure, disorder simulations for varying pore sizes are presented using a finite size scaling approach which is possible due to the high efficiency and flexibility of the  $S$ -matrix approach. The analysis of the full transmittance distributions gives insight into the validity of using averaged values

---

for the description of the transmittance in the disordered case. In addition, the robustness of the device performance in different frequency regions can be estimated from these distributions. The main question of this chapter is how to reduce the number of quantities which have to be analyzed to draw conclusions about the structure and how to find the most informative way of looking at large data to extract trends and characteristics.

In the second project (Chapter 5), a finite 3D system is studied. The structure consists of a corrugated substrate onto which an optical active polymer is coated to form a waveguide in which lasing occurs due to distributed feedback. In this case the structure is assumed to be well-known and the coupling strength to the quasi-guided waveguide modes is determined. This parameter is needed to describe the resulting lasing action within an effective theory which will be summarized to motivate the calculations.

The final project (Chapter 6), deals with a 3D PC template which is produced using holographic lithography. The fabrication of a perfect sample is very tedious since many structural changes happen during the development of the photoresist and the final structure cannot be determined using isodose surfaces. In this case, the effects of deviations in different parameters on the transmittance spectra are studied to determine which of them lead to significant changes in the measured spectra from that of the perfect structure. Comparing with experimental data allows to identify the parameters and compensate the distortion to produce samples for which the transmittance corresponds to that of the idealized theoretical simulations.

It should be mentioned that this work can be read in parts. The reader only interested in the basic ideas of the simulation can skip to the results of individual projects (Chapters 4–6) after the overview of the method in Sec. 2.1. People that are familiar with the method and would like to know implementation details can immediately skip to Chapter 3, whereas persons only interested in the results can start reading in Sec. 4. Due to this approach, some content is repeated, e. g. the representation of the incoming mode in Sec. 2.1.1 and Sec. 3.2.



# 1 Introduction to Photonic Crystals

In this chapter, a short introduction to Photonic Crystals (PCs) is given and some important concepts, such as the direct and reciprocal lattice (Sec. 1.2), are presented. Generally speaking, PCs represent a particular class of periodic materials. The implemented simulation tools are suited for all dielectric structures which exhibit a 2D periodicity and other systems than PCs, such as surface relief gratings, are simulated as well. Therefore the discussion of PCs is limited to their main features. For a more detailed discussion of PCs, the reader is referred to [1–7].

In the results section (Chapters 4–6), three different systems are considered. The details of the individual structures and an introduction to the physical relevant quantities for these systems is given in the corresponding chapters.

## 1.1 Basic Properties of Photonic Crystals

Photonic Crystals consist of a periodic arrangement of constitutive materials with different optical properties. Due to the periodicity the photonic states inside a PC can be significantly altered as compared to homogeneous materials. For this to happen, the periodicity has to be on the length scale of the wavelength of the light. The occurring effects are quite similar to the case of electrons in a periodic atomic potential. In our case, the photonic counterpart of the atomic potential is given by the spatially dependent permittivity of the constituent materials<sup>1</sup>. Examples of PCs of different dimensions are shown in Fig. 1.1. The 1D realization is also known as a Bragg stack. In two dimensions, model systems are represented by pores in a substrate as discussed in Chapter 4. The 3D system depicted in Fig. 1.1(c) shows an arrangement of spheres. An artificial opal can be created by arranging them in a close-packed FCC structure [32]. Other 3D structures involve layer-by-layer structures, e. g. the woodpile [33], or ones created by holographic lithography (Chapter 6).

In periodic media, multiple scattering of light may result in the opening of a Photonic Band Gap (PBG). PBGs are resulting in frequency regions, in which propagation of light is prohibited, or, in other words, in which the density of photonic states is equal to zero for a perfect, infinite system. Photonic systems exhibiting this property are called PBG materials. However, not all PCs are PBG materials, since additional constraints are imposed on e. g. the minimum difference in the permittivity of the constituent materials. For instance, the known PBG materials

---

<sup>1</sup>The magnetic permeability is assumed to be unity throughout this work, and meta-materials [30, 31], which exhibit a magnetic response at optical frequencies, are excluded from the discussion.

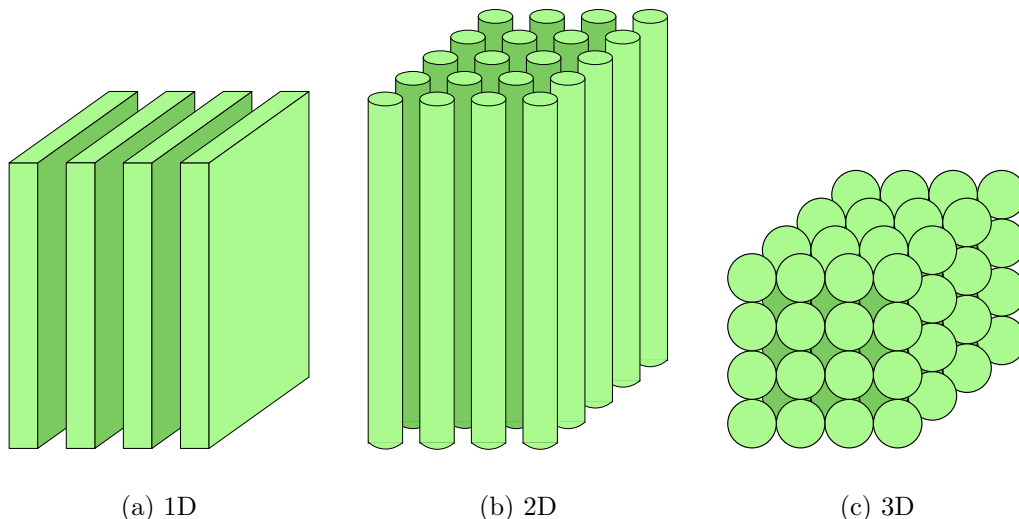


**Figure 1.1:** Schematical representation of PCs in different dimensions. In 2D and 3D a number of other realizations are possible.

in three spatial dimensions require a minimum contrast ( $\frac{n_1}{n_2}$ ) in the refractive index ( $n = \sqrt{\varepsilon}$ ) of more than 2.0 [33, 34]. In a 1D structure, a PBG can open for any index difference greater than zero. But even in this case, some PBG can disappear for specific distributions of the constituent materials in the unit cell. A common property of all periodic systems is a strong modification of the dispersion relation, describing the dependence of the frequency  $\omega$  (energy) on the wave vector  $\vec{k}$  (momentum). The dispersion relation of a specific crystal can be visualized using a band structure diagram in which the frequency is plotted over the wave vector running along high-symmetry directions in the irreducible Brillouin zone (Fig. 1.2).

Due to the vectorial character of the electromagnetic fields, the description is more complicated than for the scalar electronic wave function. The occurrence of two different polarizations in the 2D band structure depicted in Fig. 1.2 is one of the features which is different as compared to the electronic case.

Since the electromagnetic wave propagates through the crystal in a certain direction, different gap types can be distinguished. If the propagation is only prohibited in a certain direction, e. g. only in the  $\Gamma X$  part of the band structure diagram, it is referred to as a stop band. If the propagation is impossible in all directions of  $\vec{k}$ , the frequency range is called PBG. In this case the lines in the diagram exhibit a gap in the frequency region, where they vanish completely. If the band gap occurs for both polarization in 2D, it is referred to as a complete PBG.

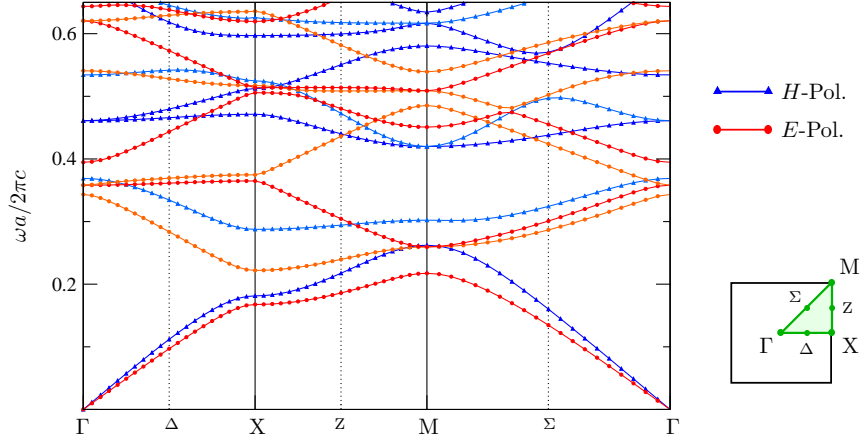


**Figure 1.2:** Band structure for a system of air pores ( $\varepsilon = 1.0$ ) with radius  $r = 0.4a$  in silicon ( $\varepsilon = 11.9$ ) on a square lattice with lattice constant  $a$ . On the right the Brillouin zone is shown. The band structure for the 2 polarizations is plotted for wave vectors along the high symmetry lines (dark-green lines) marking the edges of the irreducible Brillouin zone depicted in light green. [35]

## 1.2 Direct Lattice and Reciprocal Lattice

The fundamental property of all PCs is their periodicity. The crystal is described by a lattice, defining the translational symmetry, and a basis, giving the distribution of the dielectric material in a unit cell.

In  $d$  dimensions, the lattice can be described by  $d$  linearly independent lattice vectors  $\vec{R}_i$ . The permittivity at the positions in space which differ by any combination of the lattice vectors is identical due to the periodicity

$$\varepsilon(\vec{r}) = \varepsilon(\vec{r} + \vec{R}) \quad \text{with} \quad \vec{R} = \sum_{i=1}^d n_i \vec{R}_i, \quad n_i \in \mathbb{Z}. \quad (1.1)$$

It is sufficient to define the dielectric material in the Wigner-Seitz cell (WSC) of the lattice, which is the smallest unit cell containing all the information (spatial distribution, symmetries) about the lattice. By translating the WSC by lattice vectors, the entire  $d$ -dimensional space can be filled. The WSC about a lattice point can be constructed by connecting this point with all surrounding lattice points and bisecting each line. The smallest enclosed part around the center point defines the Wigner-Seitz cell [36].

Each direct lattice is accompanied by a reciprocal lattice, given by reciprocal lattice vectors  $\vec{G}_i$  corresponding to wave vectors of plane waves reproducing the real-space periodicity. The product of a lattice vector  $\vec{R}$  and a reciprocal lattice vector  $\vec{G} = \sum_{i=1}^d m_i \vec{G}_i$ ;  $m_i \in \mathbb{Z}$  is always given as

$$\vec{G} \cdot \vec{R} = 2\pi l \quad l = 0, \pm 1, \pm 2, \dots \quad (1.2)$$

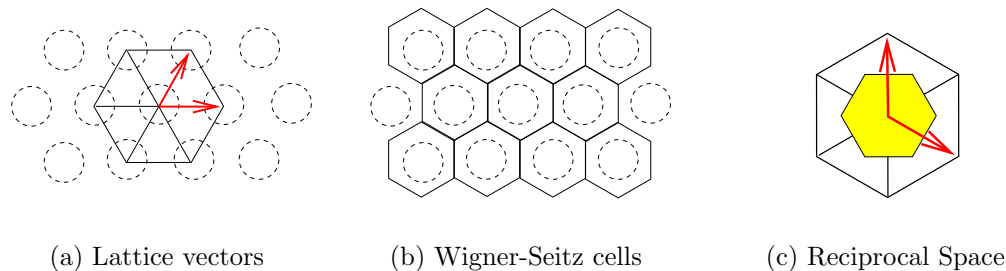


**Figure 1.3:** Triangular lattice in real and reciprocal space. (a) Lattice and lattice vectors. (b) Wigner-Seitz cell: the primitive unit cell retaining all symmetries of the lattice (c) Reciprocal lattice and Brillouin zone (WSC of reciprocal lattice, yellow).

The WSC of the reciprocal lattice is the Brillouin zone (BZ). For a triangular lattice of rods the Brillouin zone is shown on the right in Fig. 1.3. The BZ of a square lattice corresponds to the square shown on the right in Fig. 1.2. As in the case of the direct lattice the wave vectors contained in the BZ are sufficient to describe physical properties for all wave vectors. However, the number of required  $\vec{k}$  can be limited to a smaller range. Using symmetries of the structure, e. g. rotation and inversion symmetries, the area of the BZ used to describe physical properties can be reduced even further to the irreducible BZ. This is the part, which can reproduce the BZ by applying all symmetry operations to it. The symmetry operations are defined by the smallest number of common symmetries of the lattice and the basis. Consequently, the irreducible BZ depends on the lattice and the basis, whereas the BZ only depends on the lattice. For band structure calculations, i. e. calculating  $\omega(\vec{k})$ , the wave vector  $\vec{k}$  is usually restricted to the high symmetry directions forming the edges of the irreducible BZ by assuming that extremes of the band structure are found along these lines.

Anticipating later discussions, it should be mentioned that, although the lattices and unit cells are not unique, the WSZ/BZ or compatible unit cells should always be chosen, since these are the only ones representing the symmetries of the structure correctly<sup>2</sup>.

The reciprocal lattice can be used to understand the existence of a PBG conceptually within a simple picture. Waves with wave vectors at the boundary of the BZ fulfill the Laue condition  $\vec{k}\vec{G} = \frac{1}{2}|\vec{G}|^2$ . The interference of the initial and reflected waves then create a standing wave pattern with a zero group velocity  $v_g = 0$  and, thus, a vanishing slope in the dispersion. This is only possible if the dispersion relation exhibits a gap.

<sup>2</sup>In the numerical method, a finite 3D crystal is simulated. The finite size in one direction does not allow for the definition of a 3D lattice. As a consequence, different types of “unit cells” will be introduced. One corresponds to the 2D in-plane periodicity of the crystal. The second describes the repetition of structural units in the direction of finite size. The latter is required for an efficient implementation of the numerics in the case of long crystals and does not represent physical properties of the system (Sec. 3.4.4).

## 1.3 Wave Propagation in Media

The description of electromagnetic waves is based on the Maxwell equations. In a source-free ( $\rho = 0$ ) and current-free ( $\vec{j} = 0$ ) environment they are given by<sup>3</sup>

$$\nabla \cdot \vec{D}(\vec{r}, t) \stackrel{\rho=0}{=} 0, \quad \nabla \times \vec{E}(\vec{r}, t) = -\frac{\partial \vec{B}(\vec{r}, t)}{\partial t}, \quad (1.3)$$

$$\nabla \cdot \vec{B}(\vec{r}, t) = 0, \quad \nabla \times \vec{H}(\vec{r}, t) \stackrel{\vec{j}=0}{=} +\frac{\partial \vec{D}(\vec{r}, t)}{\partial t}. \quad (1.4)$$

In addition, the constitutive relations are required which relate the electric field  $\vec{E}$  to the displacement  $\vec{D}$  and the magnetic field  $\vec{H}$  to the magnetic induction  $\vec{B}$

$$\vec{D}(\vec{r}, t) = \varepsilon_0 \varepsilon(\vec{r}) \vec{E}(\vec{r}, t), \quad \vec{B}(\vec{r}, t) \stackrel{\mu_r=1}{=} \mu_0 \vec{H}(\vec{r}, t). \quad (1.5)$$

The above representation assumes that only linear polarization ( $\vec{P} = \chi \vec{E}$ ) effects are present and that the constituent materials are isotropic (no tensorial permittivity) and non-magnetic ( $\mu_r = 1$ ).

The time dependent wave equation for the electric field can be obtained by eliminating the magnetic field  $\vec{H}$ . This is done using the curl equation for the electric field, applying a second curl operation and inserting a time derivative of the curl equation of the magnetic field together with the constitutive relations

$$\vec{\nabla} \times \vec{\nabla} \times \vec{E}(\vec{r}, t) = -\varepsilon(\vec{r}) \frac{1}{c_0^2} \frac{\partial}{\partial t^2} \vec{E}(\vec{r}, t). \quad (1.6)$$

For the magnetic field the corresponding transformations yield

$$\vec{\nabla} \times \frac{1}{\varepsilon(\vec{r})} \vec{\nabla} \times \vec{H}(\vec{r}, t) = -\frac{1}{c_0^2} \frac{\partial}{\partial t^2} \vec{H}(\vec{r}, t) \quad (1.7)$$

The vacuum permittivity and permeability give the vacuum speed of light according to  $c_0 = 1/\sqrt{\varepsilon_0 \mu_0}$ . A time independent form of the wave equations can be derived by assuming a harmonic time dependence for the fields  $\vec{E}(\vec{r}, t) = \vec{E}(\vec{r}) e^{i\omega t}$

$$\frac{1}{\varepsilon(\vec{r})} \vec{\nabla} \times \vec{\nabla} \times \vec{E}(\vec{r}) = \frac{\omega^2}{c_0^2} \vec{E}(\vec{r}), \quad (1.8)$$

$$\vec{\nabla} \times \left( \frac{1}{\varepsilon(\vec{r})} \vec{\nabla} \times \vec{H}(\vec{r}) \right) = \frac{\omega^2}{c_0^2} \vec{H}(\vec{r}). \quad (1.9)$$

These equations, together with appropriate boundary conditions, correspond to eigenvalue problems with the eigen-operators defined by the differential operator on the left hand side and the eigenvalues  $\frac{\omega^2}{c_0^2}$ . Since the electric and magnetic fields are related to each other by the Maxwell equations, it is sufficient to solve the equation for either one of the fields. The solutions of the eigenvalue problem give the field distributions in eigenmodes at the corresponding eigenvalue frequencies. The wave vector  $\vec{k}$  is a parameter entering the equations and the eigenvalue problem has to be solved for each  $\vec{k}$ .

<sup>3</sup>In SI units. For different unit systems see appendix of [37].

### 1.3.1 Wave Propagation in Periodic Media

In the wave equations (1.8) and (1.9) the permittivity is space dependent, but the periodicity has not been introduced yet. As a consequence of the periodicity of coefficients in the differential wave equation, the solutions have to obey the Bloch-Floquet theorem. It states that the eigenmodes are described by the product of a lattice periodic function  $u_{n,\vec{k}}$  and a plane wave  $e^{i\vec{k}\vec{r}}$ , where the wave vector  $\vec{k}$  is restricted to the first BZ. A translation of the fields by a lattice vector introduces a phase, keeping the modulus constant [36]

$$\begin{aligned}\vec{H}_{n,\vec{k}}(\vec{r} + \vec{R}, t) &= u_{n,\vec{k}}(\vec{r} + \vec{R}, t) e^{i\vec{k}(\vec{r} + \vec{R})} \\ &= u_{n,\vec{k}}(\vec{r}, t) e^{i\vec{k}(\vec{r})} e^{i\vec{k}\vec{R}} \\ &= \vec{H}_{n,\vec{k}}(\vec{r}, t) e^{i\vec{k}\vec{R}}.\end{aligned}\quad (1.10)$$

The same holds for the electric field. For a complete description, two indices are required:  $\vec{k}$  for the wave vector and  $n$  for the band index. The band index comes about by restricting the wave vector  $\vec{k}$  to the first Brillouin zone. With the use of the Bloch functions in the eigenvalue problem, the eigenvalues inherit the indices and are given by  $\omega_{n,\vec{k}}$  which leads to a band structure such as in Fig. 1.2. Although band structure calculations are not needed in the following, the calculation method known as Plane Wave Method (PWM) is summarized below [38]. The eigenvalue problem can then be compared to the eigenvalue problem used for the transmittance calculations (Chapter 2). An overview of different computational methods for solving the band structure problem can be found in [39].

Because of the periodicity of the problem, an expansion of the fields and the space dependent permittivity in Fourier series is a well suited approach

$$\vec{H}_{\vec{k}}(\vec{r}, t) = \sum_{\vec{G}} C_{\vec{G}}^{\vec{k}} e^{i(\vec{k} + \vec{G})\vec{r}}, \quad (1.11)$$

$$\frac{1}{\varepsilon(\vec{r})} = \sum_{\vec{G}} \eta_{\vec{G}} e^{i\vec{G}\vec{r}}. \quad (1.12)$$

From the divergence equation for the magnetic field it follows that  $\vec{H}_{\vec{k}}$  is perpendicular to  $\vec{k}$  and that two independent polarizations have to be considered. The index  $\vec{k}$  is omitted and the polarizations are labeled using  $\lambda = 1, 2$

$$C_{\vec{G}}^{\vec{k}} = h_{\vec{G}}^1 \hat{e}_{\vec{G}}^1 + h_{\vec{G}}^2 \hat{e}_{\vec{G}}^2 = \sum_{\lambda} h_{\vec{G}}^{\lambda} \hat{e}_{\vec{G}}^{\lambda} \quad (1.13)$$

with the set  $\{\hat{e}_{\vec{G}}^1, \hat{e}_{\vec{G}}^2, \vec{k} + \vec{G}\}$  being orthogonal to each other. By inserting this into the wave equation the following eigenvalue problem can be derived

$$\sum_{\vec{G}'} |\vec{k} + \vec{G}| |\vec{k} + \vec{G}'| \eta_{\vec{G}-\vec{G}'} \begin{pmatrix} +\hat{e}_{\vec{G}}^2 \cdot \hat{e}_{\vec{G}'}^2 & -\hat{e}_{\vec{G}}^2 \cdot \hat{e}_{\vec{G}'}^1 \\ -\hat{e}_{\vec{G}}^1 \cdot \hat{e}_{\vec{G}'}^2 & +\hat{e}_{\vec{G}}^1 \cdot \hat{e}_{\vec{G}'}^1 \end{pmatrix} \begin{pmatrix} h_{\vec{G}'}^1 \\ h_{\vec{G}'}^2 \end{pmatrix} = \left(\frac{\omega_{\vec{k}}}{c_0}\right)^2 \begin{pmatrix} h_{\vec{G}}^1 \\ h_{\vec{G}}^2 \end{pmatrix} \quad (1.14)$$

In this equation the wave vector  $\vec{k}$  with all its components is a parameter which is varied along the high symmetry lines. For each  $\vec{k}$  the eigenfrequencies and eigenmodes can be calculated. The frequency ranges which do not occur as eigenvalue form the PBG. For the actual calculations the Fourier series has to be truncated. A similar procedure (solving for  $k_z$  instead of  $\omega$ ) is discussed in the next chapter in detail. It should be mentioned that the correct calculation of  $\eta_{\vec{G}-\vec{G}'}$  is very important for the convergence behavior [34, 40]. The Ho-Chan-Soukoulis method does not compute the Fourier coefficients of  $\eta$  directly but rather calculates the Fourier transform of  $\varepsilon(\vec{r})$

$$\varepsilon_{\vec{G}} = \frac{1}{V} \int_{WSC} d^2r \varepsilon(\vec{r}) e^{-i\vec{G}\vec{r}}. \quad (1.15)$$

The matrix  $\varepsilon_{\vec{G}\vec{G}'} \equiv \varepsilon_{\vec{G}-\vec{G}'}$  is then inverted and  $\eta_{\vec{G}-\vec{G}'}$  is taken to be the  $(\vec{G}, \vec{G}')$  element of the inverted matrix.

### 1.3.2 2D Crystal

A system which is uniform in the  $z$ -direction, e.g. infinite rods or pores, can be treated in a 2D formalism. In this case, the electric and magnetic fields decouple and two different scalar eigenvalue problems for the  $z$ -component of the fields ( $H_z$ ,  $E_z$ ) can be derived. E- and H-polarization are defined as having the electric and magnetic, respectively, field oriented parallel to the rods (Fig. 1.4).

Physically the decoupling is caused by the different behavior of the magnetic and electric field upon inversion at the  $x$ - $y$ -plane. In the calculation, decoupling is caused by the vanishing derivatives with respect to the homogeneous  $z$ -direction. Without giving a derivation the equations read as

$$\sum_{\vec{G}'} |\vec{k} + \vec{G}| |\vec{k} + \vec{G}'| \eta_{\vec{G}-\vec{G}'} |\vec{k} + \vec{G}'| E_{\vec{G}'}^{\vec{k}} = \frac{\omega_{\vec{k}}^2}{c_0^2} |\vec{k} + \vec{G}| E_{\vec{G}}^{\vec{k}}, \quad (1.16)$$

$$\sum_{\vec{G}'} (\vec{k} + \vec{G}) \cdot (\vec{k} + \vec{G}') \eta_{\vec{G}-\vec{G}'} H_{\vec{G}'}^{\vec{k}} = \frac{\omega_{\vec{k}}^2}{c_0^2} H_{\vec{G}}^{\vec{k}}. \quad (1.17)$$

In this case  $E$  and  $H$  correspond to the  $z$ -component and all vectors  $(\vec{G}, \vec{G}', \vec{k})$  only have  $x$ - and  $y$ -components. Since the standard eigenvalue problem for the electric field is not symmetric, it has been turned into a symmetric generalized eigenvalue problem by introducing the factor  $|\vec{k} + \vec{G}|$  on both sides of the equation.

An example for a 2D band structure is shown in Fig. 1.2 for a 2D system of air pores ( $\varepsilon = 1.0$ ) with radius  $r = 0.4a$  in silicon ( $\varepsilon = 11.9$ ) on a square lattice with lattice constant  $a$ .

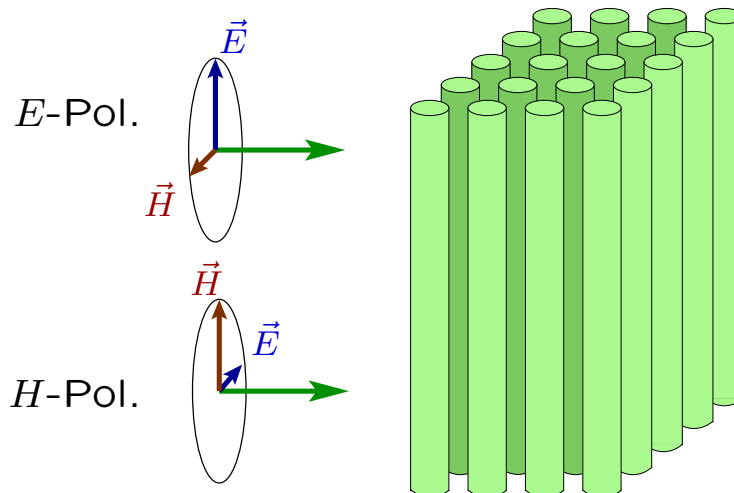


**Figure 1.4:** E-Polarization and H-Polarization for a 2D crystal with rods on a square lattice, which is homogeneous in the vertical ( $z$ -) direction. For E-(H-) polarization the electric (magnetic) field has only a component parallel to the rods. For each polarization a scalar eigenvalue problem can be derived.

### 1.3.3 Scaling Properties

A very useful property of the Maxwell equations is the absence of a length scale. By rescaling all physical quantities with the lattice constant  $a$ , they can be made dimensionless. All PCs with the same lattice and size ratios can be described by the same band structure. This was especially useful in the early days of the field, when nanostructuring was hardly available. The early experiments were all done using microwaves with a wavelength of several cm but the results are all valid for optical wavelengths as well, provided the sample can be scaled accordingly.

The dimensionless quantities are given by

$$\omega' = \frac{\omega a}{2\pi c_0} = \frac{a}{\lambda}, \quad \vec{k}' = \vec{k}a, \quad \lambda' = \frac{\lambda}{a}, \quad \vec{r}' = \frac{\vec{r}}{a}. \quad (1.18)$$

It should be mentioned here, that this property is usually lost in real samples with dispersive permittivities<sup>4</sup>. A dispersion relation for the permittivity relates the dielectric constant to a frequency, e.g. through a Drude model. In this case a frequency scale is introduced into the system. Rescaling the structure by changing the lattice constant  $a$  would not change the dimensionless frequency, but the regular frequency would scale with the inverse of the lattice constant  $\omega = \frac{2\pi c_0 \omega'}{a}$  and, hence, the permittivity of the dispersive material would have to be changed. This can only

<sup>4</sup>Modeling dispersion in band structure calculations is not straightforward since the frequency is calculated as a solution of the eigenvalue problem. Iterative solutions are, however, possible [35, 41].

be avoided if the permittivity depends only on the dimensionless frequency, e. g. in the two-level model discussed in Sec. 3.5.5 where the resonance frequency can be defined in terms of the dimensionless frequency. However, this is a purely theoretical model and in a real experiment, a material must be found for which the resonance frequency can be tuned so that the system exhibits the properties assumed in the model. For realistic modeling, simulation tools capable of dispersive material are required to manage both systems, dimensionless and regular units.

## 1.4 Band Structures and Finite Samples

The properties discussed above are related to infinite and perfectly periodic crystals. In the following chapters, the transmittance through finite structures is calculated and discussed in detail.

The calculation of transmittance is a frequency domain problem, since in transmittance experiments, the frequency is defined by the incoming probe beam. The magnitude of the wave vector is fixed and only its orientation can change. Although the wave vectors and frequencies are related by the same dispersion relation, solving for the wave vector instead of the frequency leads to major differences. Whereas the physical interpretation of a complex frequency is difficult, a complex wave vector can be easily related to the experiment. In a finite structure propagation will occur even in the PBG, however, this propagation is exponentially damped. The PBGs then appear as strong dips in the transmittance and show a distinct (exponential) length dependence.

Beside the fact that small transmittance can occur in the PBG, a finite structure can also show a very low transmittance, even if photonic bands are available for this frequency range. In Fig. 4.3 this can be seen in the regions of the dashed bands. Although a band exists, the transmittance is very low. The reason for this is a symmetry mismatch of the incoming wave and the Bloch mode inside the crystal. The parity of the incoming mode is always even across the slab surface. If the Bloch mode for the considered band exhibits an odd parity, the incompatible symmetries prevent coupling of the incoming wave to the crystal modes.

Another “finite” structure that is of great importance are the Photonic Crystal Fibers (PCF) [20]. The cross section of these fibers consists of a 2D system with a defect in the center. This pattern is constant along the fiber and propagation takes place in the direction normal to the 2D system. If the defect is ignored and the 2D periodic structure is extended infinitely, the 2D band structure can be calculated. In first approximation this gives the frequency ranges in which the fiber can guide light due to the PBG.

The PCF is not a 2D system, for which the wave vector parallel to the pores would be zero, since, for a 2D system, the derivatives with respect to the  $z$ -coordinate have to vanish. In the case of PCFs, the modeling has to include the wave vector component  $k_z$  in the propagation direction as additional parameter, making a full 3D treatment necessary. In the presented calculations a similar situation occurs.

In all cases the periodic system is parallel to the propagation direction, as in the case of PCFs. Whereas in calculations of the PCF, the propagation constant and the in-plane wave vector are considered as parameters and the possible frequencies are determined, the transmittance calculations presented in the following, use the frequency and in-plane wave vector as parameters and solve for the propagation constant perpendicular to the periodic system.

# 2 Numerical Method

In this chapter, the numerical method which is used to model the photonic systems based on an approach by Whittaker et al. [42] is described without any implementation details. These details, together with the concepts used for code optimization, is the topic of the following chapter.

At the beginning (Sec. 2.1) an overview about the ideas and concepts of the simulation will be given as an introduction to the following calculations. Readers only interested in the results may skip ahead to Chapter 4 after this section without missing any parts necessary for a general understanding.

Starting in Sec. 2.2 until the end of the chapter the calculations will be discussed in detail, including the calculation of basis functions for the fields (Sec. 2.2), the propagation of the fields through the crystal (Secs. 2.3–2.6), the determination of fields inside the crystal (Sec. 2.5) and the introduction of dipole sources (Sec. 2.7). At the end improvements and alternative approaches are mentioned Sec. 2.8.

## 2.1 Basic Principles

In this section, the method is outlined to allow for an understanding of the individual steps presented later in the context of a broader picture.

The aim in the simulation is to connect the incoming wave to all outgoing (transmitted or reflected) waves. For this the wave has to be propagated through the structure and correct expressions for the fields have to be found in all regions. This is done by dividing the structure into several layers, expressing the fields in each layer using eigenmodes and matching (propagating) them across layer boundaries. Methods of this type are known as Multilayer Modal Method (MMM) [43]. The modes are calculated using a Fourier expansion in the reciprocal lattice vectors introduced as the Rigorous Coupled Wave Analysis method (RCWA) by Moharam et al. [44].

### 2.1.1 Quantities of Interest

Before describing the simulation, its goal should be defined. In this work, the focus is on calculating the complex amplitudes of reflected and transmitted waves for a plane wave impinging with oblique incidence on a periodic photonic structures<sup>1</sup>. From these amplitudes, further quantities can be calculated, e.g. total transmittance

---

<sup>1</sup>The term photonic structure is chosen, since not only PCs can be studied with this method, but also periodic surface relief gratings used in distributed feedback lasing, etc.

and reflectance or scattering phases. In addition, the fields inside a structure should be accessible.

### Periodic Structures and Bragg-orders

As a first step, a coordinate system has to be introduced. For each system, the surface<sup>2</sup> of the structure defines the  $x$ - $y$ -directions, also called in-plane later on, whereas the perpendicular  $z$ -direction is called propagation direction<sup>3</sup>. The structure is finite in the  $z$ -direction and has to be periodic in the  $x$ - $y$ -direction to allow for the definition of a unit cell and an in-plane lattice. This periodicity has to be constant with  $z$ , however the distribution of materials inside the unit cell (basis) can change arbitrarily with  $z$ .

As a consequence of the periodicity, the structure can be considered as a 2D diffraction grating. An incoming plane wave will be reflected, respectively transmitted, into several diffraction orders. The incoming wave is defined by the frequency  $\omega$ , the angle to the surface normal  $\theta$ , and the angle  $\phi$  between the  $x$ -axis and the projection of the wave vector onto the surface. The propagation direction follows as

$$\begin{pmatrix} \vec{k}_{\parallel,\text{in}} \\ k_{z,\text{in}} \end{pmatrix} = k_{0,\text{in}} \begin{pmatrix} \sin \theta \cos \phi \\ \sin \theta \sin \phi \\ \cos \theta \end{pmatrix}. \quad (2.1)$$

A schematic representation using a 1D grating for simplicity is shown in Fig. 2.1. The dark blue arrows indicate the incoming and the 0<sup>th</sup>-order reflected/transmitted wave. The other arrows represent diffraction-/Bragg-orders. The wave vector components parallel to the surface  $\vec{k}_{\parallel} := \vec{k}$  obey crystal momentum conservation, i. e. for different Bragg-orders a combination of the two reciprocal lattice vectors is added to them

$$\vec{k}_{nm} = \vec{k}_{\text{in}} + n\vec{G}_1 + m\vec{G}_2. \quad (2.2)$$

In Fig. 2.1 this is illustrated for a 1D system, where the parallel component is given by  $k_x$  and only one reciprocal lattice “vector”  $G_x = \frac{2\pi}{a}$  exists. In homogeneous materials the component in the (vertical) propagation direction can immediately be calculated by the dispersion relation

$$k_{z,nm}^2 = \left(\frac{\omega}{c}\right)^2 - k_{x,nm}^2 - k_{y,nm}^2, \quad (2.3)$$

with the speed of light in the surrounding media given by the the vacuum speed of light divided by the index of refraction  $c = \frac{c_0}{n_{\text{in}}}$ . Depending on the Bragg-order,  $k_z$  can be imaginary and non-propagating order occur, which are depicted by the dashed arrows in the illustration. The representation of the field as sum of Bragg

---

<sup>2</sup>This surface is assumed to be flat in the description given here, but it can be structured, e. g. a surface relief grating. The only constraint is the periodicity, making e. g. a tilted surface impossible.

<sup>3</sup>Strictly spoken this is only the propagation direction of a wave with perpendicular incidence.

orders<sup>4</sup> is commonly known as Rayleigh expansion. In the homogeneous regions, different orders decouple and hence the energy transport for each mode is given by the corresponding Poynting vector, allowing to calculate the transmittance/reflectance for each mode individually. In the periodic areas, the above description has to be modified and the plane waves have to be replaced by other modes as is shown later.

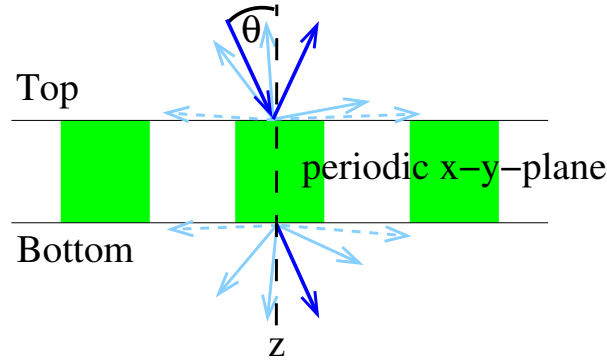


**Figure 2.1:** Example for a grating system. The incoming and  $0^{\text{th}}$ -orders are depicted in dark blue. Solid light blue arrows represent propagating Bragg orders, dashed arrows non-propagating orders. In the 1D system only the azimuthal angle  $\theta$  to the surface normal and the frequency are needed to describe the incoming wave. The side of the incoming/reflected(outgoing/transmitted) wave will be referred to as top/bottom.

Changes in the  $z$ -direction are modeled using a staircase approximation [45] as illustrated in Fig. 2.2. Again, for simplicity the layers are 1D in this illustration, creating a finite 2D crystal. In this approach, the crystal is sliced into layers parallel to the surface and each layer is considered as an individual grating which is homogeneous in the  $z$ -direction. For a finite 3D structure, the layers are 2D periodic systems.

In structured layers, the Rayleigh expansion turns into a Fourier expansion in the reciprocal lattice vectors for the fields and the permittivity. After inserting into Maxwell equations, this leads to an eigenvalue problem for the eigenmodes and the propagation constant in  $z$ -direction, instead of a differential equation.

### Relating fields in different parts of the crystal

Once the fields in each layer are expressed in the corresponding eigenmodes, the question arises how to relate them in different layers. For this, the boundary conditions of the tangential fields between adjacent layers are used. More than two layers can then be related by an appropriate matrix formalism. The simplest possible approach is the transfer-matrix ( $T$ -matrix) formalism, which directly relates fields in

<sup>4</sup>For a full description the forward(incoming) and backward(reflected) waves have to be included in the Rayleigh expansion.

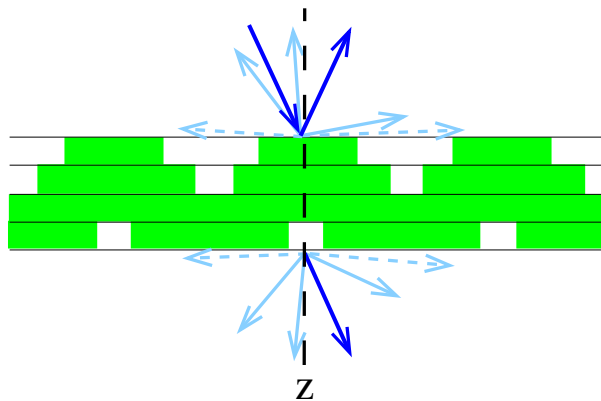


**Figure 2.2:** Example for a grating system with a  $z$ -dependence modeled by a staircase approximation by replacing the structure layers which, individually, are constant in the  $z$ -direction. The periodicity has to be the same in all layers for this approach to be applicable.

different layers. However, this is known to be numerically unstable [46, 47]. Another possibility is the more complex scattering-matrix ( $S$ -matrix), which is used in this work and is discussed in more detail later. Further possibilities include the (only conditionally stable)  $R$ -matrix method<sup>5</sup> [48, 49] or the enhanced  $T$ -matrix method [50]. It has been shown by L. Li that the  $S$ -matrix is the most efficient method for most cases [49].

## 2.2 Fields in Individual Layers

In each layer of the staircase approximation a suitable description of the electromagnetic fields is required. By using a Fourier expansion in reciprocal lattice vectors the electromagnetic fields in the Maxwell equations can be expressed in terms of eigenmodes. Before starting with the actual calculations a few notations and quantities have to be defined:

- The vector symbol  $\vec{v}$  is used for two types of quantities:
  - 2D vectors within the layers ( $\vec{r}$ ,  $\vec{G}$ ,  $\vec{k}$ ) with in-plane-components ( $x$ ,  $y$ )
  - field vectors ( $\vec{H}$ ,  $\vec{E}$ ) and differential operators ( $\vec{\nabla}$ ) with  $x$ -,  $y$ - and  $z$ -components.
- A tilde  $\tilde{t}$  is used for Fourier transformed quantities.
- A hat  $\hat{h}$  is used for matrices  $(\hat{k}_x, \hat{k}_y)$  containing  $N \times N$  elements for Fourier series truncated at order  $N$ . If these matrices contain Fourier transformed quantities, the tilde is omitted.

---

<sup>5</sup>The layer thickness has to be chosen so that the growing exponential is smaller than a threshold defined by the precision of the computer.

- The widehat  $\widehat{wh}$  is used for matrices containing  $2N \times 2N$  elements which involve combinations of the above.
- Capital letters are used for matrices containing  $4N \times 4N$  elements for all fields ( $S$ -matrices,  $T$ -matrices,...)

### Determination of Eigenmodes

The governing equations of motion in electrodynamics are the Maxwell equations. Although they are already presented in Chapter 1, they are repeated here to start the calculations at a basic point. In contrast to the previous discussion, the dependencies are split into in-plane ( $\vec{r}$ ) and vertical ( $z$ ) components:

$$\vec{\nabla} \cdot \vec{D}(\vec{r}, z, t) = \rho_0, \quad (2.4)$$

$$\vec{\nabla} \cdot \vec{H}(\vec{r}, z, t) = 0, \quad (2.5)$$

$$\vec{\nabla} \times \vec{E}(\vec{r}, z, t) = -\partial_t \vec{B}(\vec{r}, z, t), \quad (2.6)$$

$$\vec{\nabla} \times \vec{H}(\vec{r}, z, t) = \vec{j}_0 + \partial_t \vec{D}(\vec{r}, z, t). \quad (2.7)$$

For spatially varying but isotropic and non-magnetic material with a linear polarization, the constitutive relations are given by

$$\vec{D}(\vec{r}, z, t) = \varepsilon_0 \varepsilon(\vec{r}) \vec{E}(\vec{r}, z, t), \quad \vec{B}(\vec{r}, z, t) = \mu_0 \vec{H}(\vec{r}, z, t). \quad (2.8)$$

The staircase approximation requires that, within each layer, the electric permittivity  $\varepsilon(\vec{r})$  only depends on the in-plane spatial vector  $\vec{r}$ . In addition, the dielectric function in different layers is restricted to the same periodicity<sup>6</sup>. To distinguish different layers, the dielectric function is labeled with the layer number  $l$ . However, in this section the calculations are restricted to one layer and the index is dropped. For the fields a time-harmonic dependence is used

$$\vec{E}(\vec{r}, z, t) = \vec{E}(\vec{r}, z) e^{-i\omega t}, \quad \vec{H}(\vec{r}, z, t) = \vec{H}(\vec{r}, z) e^{-i\omega t}. \quad (2.9)$$

In the following situations without free charges ( $\rho_0 = 0$ ) and currents ( $\vec{j}_0 = 0$ ) are assumed. The variables are replaced by the dimensionless ones from Sec. 1.3.3.

$$\omega' = \frac{\omega a}{2\pi c_0} = \frac{a}{\lambda}, \quad \vec{k}' = \vec{k} a, \quad \lambda' = \frac{\lambda}{a}, \quad \vec{r}' = \frac{\vec{r}}{a}. \quad (2.10)$$

<sup>6</sup>This requirement can be relaxed slightly if one uses supercells. In this case their periodicities only have to be integer multiples of each other.

In subsequent calculations the prime is omitted and, consequently, Maxwell equations<sup>7</sup> read as

$$\vec{\nabla}_{\varepsilon_0 \varepsilon(\vec{r})} \vec{E}(\vec{r}, z) = 0, \quad (2.11)$$

$$\vec{\nabla} \vec{H}(\vec{r}, z) = 0, \quad (2.12)$$

$$\vec{\nabla} \times \vec{E}(\vec{r}, z) = 2\pi c_0 i \omega \mu_0 \vec{H}(\vec{r}, z), \quad (2.13)$$

$$\vec{\nabla} \times \vec{H}(\vec{r}, z) = -2\pi c_0 i \omega \varepsilon_0 \varepsilon(\vec{r}) \vec{E}(\vec{r}, z). \quad (2.14)$$

The periodicity in  $x$ - and  $y$ -direction is ideally suited for a plane wave expansion (Fourier expansion) using the reciprocal lattice vectors as a basis. Since oblique incidence is of special interest, the expansion has to be centered around an arbitrary in-plane wave vector  $\vec{k}_0$

$$\vec{H}(x, y, z) = \sum_m \vec{H}_m(z) e^{i(\vec{k}_0 + \vec{G}_m) \vec{r}}, \quad (2.15)$$

$$\vec{E}(x, y, z) = \sum_n \vec{E}_n(z) e^{i(\vec{k}_0 + \vec{G}_n) \vec{r}}. \quad (2.16)$$

The composite index  $m(n)$  is an abbreviation for a pair of integers  $(m_1, m_2)$  defining the vector  $\vec{G} = m_1 \vec{G}_1 + m_2 \vec{G}_2$  as a linear combination of reciprocal lattice vectors  $\vec{G}_1$  and  $\vec{G}_2$ , which depend on the 2D in-plane lattice of the crystal. In the incoming (outgoing) region above (below) the crystal, the individual orders correspond to the Bragg-orders of the crystal defined by the 2D periodicity in the layers, reproducing the Rayleigh expansion automatically. The dielectric function can be expressed using the same expansion

$$\epsilon(x, y) = \sum_n \tilde{\epsilon}_{n'} e^{i\vec{G}_{n'} \vec{r}}, \quad \tilde{\epsilon}_{n'} = \frac{1}{V} \int d^2 r \epsilon(\vec{r}) e^{-i\vec{G}_{n'} \vec{r}}. \quad (2.17)$$

In the following, the ensuing manipulation of eq. (2.14) is considered as an example. For simplicity the dependencies are dropped

$$\frac{\partial}{\partial y} H_z - \frac{\partial}{\partial z} H_y = -2\pi c_0 i \omega \varepsilon_0 \varepsilon E_x, \quad (2.18)$$

$$\frac{\partial}{\partial z} H_x - \frac{\partial}{\partial x} H_z = -2\pi c_0 i \omega \varepsilon_0 \varepsilon E_y, \quad (2.19)$$

$$\frac{\partial}{\partial x} H_y - \frac{\partial}{\partial y} H_x = -2\pi c_0 i \omega \varepsilon_0 \varepsilon E_z. \quad (2.20)$$

---

<sup>7</sup>With  $a = 1$  in dimensionless units. Using  $\vec{k}' = \frac{\vec{k}a}{2\pi}$  would avoid dealing with the factor  $2\pi$ , however then one would have to use  $\vec{G}' = \frac{\vec{G}}{2\pi}$  and rescale the Fourier transform or the real space unit cell, which would contradict solid state textbooks and possibly lead to confusions.

Since the calculations are straightforward, the individual steps will only be presented for the first of the 3 above equations. Inserting the expansions leads to

$$\begin{aligned} & \frac{\partial}{\partial y} \sum_m \tilde{H}_{z,m}(z) e^{i(\vec{k}_0 + \vec{G}_m)\vec{r}} - \frac{\partial}{\partial z} \sum_m \tilde{H}_{y,m}(z) e^{i(\vec{k}_0 + \vec{G}_m)\vec{r}} \\ & = -2\pi c_0 i \omega \varepsilon_0 \sum_{n'} \tilde{\varepsilon}_{n'} e^{i\vec{G}_{n'}\vec{r}} \sum_n \tilde{E}_{x,n}(z) e^{i(\vec{k}_0 + \vec{G}_n)\vec{r}}. \end{aligned} \quad (2.21)$$

Keeping in mind that  $\vec{k}_0$  is fixed throughout the system, the index “0” is dropped now. Differentiating and collecting terms then gives

$$\begin{aligned} & \sum_m \left[ i(k_y + G_{y,m}) \tilde{H}_{z,m}(z) - \frac{\partial}{\partial z} \tilde{H}_{y,m}(z) \right] e^{i(\vec{k} + \vec{G}_m)\vec{r}} \\ & = -2\pi c_0 i \omega \varepsilon_0 \sum_{n,n'} \tilde{\varepsilon}_{n'} \tilde{E}_{x,n}(z) e^{i(\vec{k} + \vec{G}_{n+n'})\vec{r}}. \end{aligned} \quad (2.22)$$

The double summation on the right side couples different orders due to the periodicity of the system<sup>8</sup>. A comparison of the exponential factors leads to the requirement  $m = n+n'$  for the orders of the expansion of the dielectric function  $n'$  respectively the electric field  $n$  whose products show the same spatial behavior as the magnetic field with order  $m$ . Therefore, the summation of all combinations of  $n$  and  $n'$  fulfilling this requirement contribute to the corresponding magnetic field order.

Due to the linearity of the Maxwell equations, each order of the magnetic field can be treated separately leading to a set of equations (one for each order  $m$ ) instead of the summation over all orders

$$i(k_y + G_{y,m}) \tilde{H}_{z,m}(z) - \frac{\partial}{\partial z} \tilde{H}_{y,m}(z) = -2\pi c_0 i \omega \varepsilon_0 \sum_{\substack{n,n' \\ n+n'=m}} \tilde{\varepsilon}_{n'} \tilde{E}_{x,n}(z). \quad (2.23)$$

All Fourier coefficients of one of the field components are now combined into a Fourier vector, which has to be truncated for actual computation. This truncation could be implemented differently (see Sec.2.8.1) in case that convergence is not good enough, e. g. for metallic structures, but for the systems studied in this work convergence was always achieved using the presented way

$$h_i(z) = (\tilde{H}_{i,m=-\infty}(z), \dots, \tilde{H}_{i,m=\infty}(z))^T, \quad i = x, y, z. \quad (2.24)$$

In addition, diagonal matrices containing the in-plane wave vector components related to corresponding modes are required  $(\hat{k}_i)_{mm'} = (k_{0,i} + G_{i,m})\delta_{mm'}$ ,  $i = x, y$ . To be consistent, the Fourier coefficients of the permittivity function have to be written in a form which guarantees that the sum on the right side is correctly reproduced

<sup>8</sup>In a homogeneous system all coefficients of the expansion of the dielectric function would be zero except the 0<sup>th</sup>-order one and the summation over  $n'$  collapses into one term and the coupling vanishes.

when multiplying with the Fourier vector of the electric field. This is facilitated by a Toeplitz-matrix with matrix elements  $(\hat{\varepsilon})_{nn'} = \tilde{\varepsilon}_{n-n'}$ . Products of Toeplitz-matrices preserve the order in all elements, whereas products of Toeplitz-matrices with Fourier vectors preserve the order in the Fourier vectors.

Using these expressions, a more compact representation of the curl equations (2.13) and (2.14) can be obtained:

$$i\hat{k}_y e_z(z) - \frac{\partial}{\partial z} e_y(z) = 2\pi i \omega \mu_0 c_0 h_x(z), \quad (2.25)$$

$$\frac{\partial}{\partial z} e_x(z) - i\hat{k}_x e_z(z) = 2\pi i \omega \mu_0 c_0 h_y(z), \quad (2.26)$$

$$i\hat{k}_x e_y(z) - i\hat{k}_y e_x(z) = 2\pi i \omega \mu_0 c_0 h_z(z), \quad (2.27)$$

$$i\hat{k}_y h_z(z) - \frac{\partial}{\partial z} h_y(z) = -2\pi i \omega c_0 \varepsilon_0 \hat{\varepsilon} e_x(z), \quad (2.28)$$

$$\frac{\partial}{\partial z} h_x(z) - i\hat{k}_x h_z(z) = -2\pi i \omega c_0 \varepsilon_0 \hat{\varepsilon} e_y(z), \quad (2.29)$$

$$i\hat{k}_x h_y(z) - i\hat{k}_y h_x(z) = -2\pi i \omega c_0 \varepsilon_0 \hat{\varepsilon} e_z(z). \quad (2.30)$$

Due to the homogeneity in the  $z$ -direction, each mode will propagate as a plane wave  $e^{iqz}$  with a propagation constant<sup>9</sup>  $q$  and a separation of the  $z$ -dependence from the lateral dependence is possible. If these dependencies are combined and used in the divergence equation for  $\vec{H}$  eq. (2.5), an expression for  $\vec{H}$  in eq. (2.15) can be found

$$\vec{H}(\vec{r}, z) = \sum_{\vec{G}} \begin{pmatrix} \Phi_{x,\vec{G}} \\ \Phi_{y,\vec{G}} \\ -\frac{1}{q}(k_x + G_x)\Phi_x - \frac{1}{q}(k_y + G_y)\Phi_y \end{pmatrix} e^{i(\vec{k}+\vec{G})\cdot\vec{r}} e^{iqz}. \quad (2.31)$$

The only unknown variables are the propagation constants  $q$  and the space-independent Fourier coefficients<sup>10</sup>  $\Phi_x$  and  $\Phi_y$ . The reciprocal lattice vectors  $\vec{G}$  are determined by the lattice and the in-plane wave vector  $\vec{k}$  is given by the incoming wave. In the incoming region the Fourier coefficients  $\Phi_i$  are also completely defined by the incoming wave and only the 0<sup>th</sup>-order is present<sup>11</sup>. Re-writing the magnetic field Ansatz using the concept of Fourier vectors eq. (2.24) for  $\Phi$  leads to

$$h(\vec{r}, z) = \begin{pmatrix} \phi_x \\ \phi_y \\ -\frac{1}{q}(\hat{k}_x\phi_x + \hat{k}_y\phi_y) \end{pmatrix} e^{iqz}. \quad (2.32)$$

---

<sup>9</sup>This is not labeled  $k_z$  to avoid confusion with the in-plane wave vector  $\vec{k}$

<sup>10</sup>They however still differ from layer to layer.

<sup>11</sup>In some cases a different order than the 0<sup>th</sup>-order is used to describe the incoming wave for convergence reasons (Sec. 3.2.1).

This matches the notations in eq. (2.25) to eq. (2.30) and allows for a formulation of the curl-equations for the electric field with an Ansatz fulfilling  $\vec{\nabla} \cdot \vec{H} = 0$ :

$$i\hat{k}_y \left( -\frac{1}{q}\hat{k}_x\phi_x - \frac{1}{q}\hat{k}_y\phi_y \right) - iq\phi_y = -2\pi i \omega c_0 \varepsilon_0 \hat{e}_x e_x e^{-iqz}, \quad (2.33)$$

$$iq\phi_x - i\hat{k}_x \left( -\frac{1}{q}\hat{k}_x\phi_x - \frac{1}{q}\hat{k}_y\phi_y \right) = -2\pi i \omega c_0 \varepsilon_0 \hat{e}_y e_y e^{-iqz}, \quad (2.34)$$

$$i\hat{k}_x\phi_y - i\hat{k}_y\phi_x = -2\pi i \omega c_0 \varepsilon_0 \hat{e}_z e_z e^{-iqz}. \quad (2.35)$$

This equation relates the Fourier coefficients of the electric field to the ones used in the expansion of the magnetic field. During this transformation, it is necessary to invert the Toeplitz-matrix of the dielectric function  $\hat{\varepsilon}$ . The inverted matrix is labeled  $\hat{\eta} = \hat{\varepsilon}^{-1}$ . The validity of this transformation requires that the elements of  $\hat{\eta}$  are not calculated by a Fourier transform of  $1/\varepsilon(x, y)$ . The inversion must be done numerically, so that  $\hat{\varepsilon}\hat{\eta} = 1$  is always true. The inverse Fourier transform of  $\hat{\eta}$  does not reproduce the inverse of the permittivity in real space  $1/\varepsilon(x, y)$ , except for an infinity number of modes. As a consequence, the product of the permittivity and its inverse in real space is not unity ( $\varepsilon(x, y)\eta(x, y) \neq 1$ ) if both quantities are calculated by an inverse Fourier transform of  $\hat{\varepsilon}$  and  $\hat{\eta}$ . The final expression for the electric field in terms of the coefficients of the magnetic field is

$$e(\vec{r}, z) = \frac{1}{2\pi \omega c_0 \varepsilon_0 q} \begin{pmatrix} \hat{\eta}\hat{k}_y\hat{k}_x\phi_x + (\hat{\eta}q^2 + \hat{\eta}\hat{k}_y\hat{k}_y)\phi_y \\ -(\hat{\eta}q^2 + \hat{\eta}\hat{k}_x\hat{k}_x)\phi_x - \hat{\eta}\hat{k}_x\hat{k}_y\phi_y \\ \hat{\eta}q(\hat{k}_y\phi_x - \hat{k}_x\phi_y) \end{pmatrix} e^{iqz}. \quad (2.36)$$

This expression can be inserted into eqs. (2.25)–(2.27). In this step most of the coefficients cancel out

$$\hat{k}_y\hat{\eta}(\hat{k}_y\phi_x - \hat{k}_x\phi_y) + \hat{\eta}[(q^2 + \hat{k}_x\hat{k}_x)\phi_x + \hat{k}_x\hat{k}_y\phi_y] = (2\pi\omega)^2\phi_x, \quad (2.37)$$

$$\hat{\eta}\hat{k}_y\hat{k}_x\phi_x + (\eta q^2 + \hat{\eta}\hat{k}_y\hat{k}_y)\phi_y - \hat{k}_x\hat{\eta}(\hat{k}_y\phi_x - \hat{k}_x\phi_y) = (2\pi\omega)^2\phi_y. \quad (2.38)$$

The third of the resulting equations is linearly dependent on the others and can be neglected

$$\begin{aligned} -\hat{k}_x \left[ (\hat{\eta}q^2 + \hat{\eta}\hat{k}_x\hat{k}_x)\phi_x + \hat{\eta}\hat{k}_x\hat{k}_y\phi_y \right] - \hat{k}_y \left[ \hat{\eta}\hat{k}_y\hat{k}_x\phi_x + (\hat{\eta}q^2 + \hat{\eta}\hat{k}_y\hat{k}_y)\phi_y \right] \\ = (2\pi\omega)^2 (\hat{k}_x\phi_x + \hat{k}_y\phi_y). \end{aligned} \quad (2.39)$$

Simplifying the equations leads to an eigenvalue problem for  $\omega^2$ . This however is not a band structure eigenvalue problem since it depends not only on the in the plane-components of the wave vector  $\vec{k}$  and the reciprocal lattice vectors  $\vec{G}$  (which would be the case for a 2D band structure calculation) but also on the out-of

plane component  $q$  of the wave vector. The 2D band structure would be calculated with scalar fields for both polarizations (E-Pol, H-Pol) by taking advantage of the symmetry [4, 38](Sec. 1.3.2)

$$\left[ \hat{k}_y \hat{\eta} \hat{k}_y + \hat{\eta} \left( q^2 + \hat{k}_x \hat{k}_x \right) \right] \phi_x + \left[ \hat{\eta} \hat{k}_x \hat{k}_y - \hat{k}_y \hat{\eta} \hat{k}_x \right] \phi_y = (2\pi\omega)^2 \phi_x, \quad (2.40)$$

$$\left[ \hat{\eta} \hat{k}_y \hat{k}_x - \hat{k}_x \hat{\eta} \hat{k}_y \right] \phi_x + \left[ \hat{k}_x \hat{\eta} \hat{k}_x + \hat{\eta} \left( q^2 + \hat{k}_y \hat{k}_y \right) \right] \phi_y = (2\pi\omega)^2 \phi_y. \quad (2.41)$$

Combining  $\phi_x$  and  $\phi_y$  into a vector  $\vec{\phi}$ <sup>12</sup> leads to the final eigenvalue problem for  $\omega^2$  and  $\vec{\phi}$

$$\left[ \begin{pmatrix} \hat{\eta} & 0 \\ 0 & \hat{\eta} \end{pmatrix} \left[ q^2 + \begin{pmatrix} \hat{k}_x \hat{k}_x & \hat{k}_x \hat{k}_y \\ \hat{k}_y \hat{k}_x & \hat{k}_y \hat{k}_y \end{pmatrix} \right] + \begin{pmatrix} \hat{k}_y \hat{\eta} \hat{k}_y & -\hat{k}_y \hat{\eta} \hat{k}_x \\ -\hat{k}_x \hat{\eta} \hat{k}_y & \hat{k}_x \hat{\eta} \hat{k}_x \end{pmatrix} \right] \vec{\phi} = (2\pi\omega)^2 \vec{\phi}. \quad (2.42)$$

For simplicity in notation the following  $2N \times 2N$  matrices are introduced

$$\widehat{k\hat{k}} = \begin{pmatrix} \hat{k}_x \hat{k}_x & \hat{k}_x \hat{k}_y \\ \hat{k}_y \hat{k}_x & \hat{k}_y \hat{k}_y \end{pmatrix}, \quad \widehat{k\hat{n}\hat{k}} = \begin{pmatrix} \hat{k}_y \hat{\eta} \hat{k}_y & -\hat{k}_y \hat{\eta} \hat{k}_x \\ -\hat{k}_x \hat{\eta} \hat{k}_y & \hat{k}_x \hat{\eta} \hat{k}_x \end{pmatrix}, \quad \widehat{\eta} = \begin{pmatrix} \hat{\eta} & 0 \\ 0 & \hat{\eta} \end{pmatrix}. \quad (2.43)$$

The product of the two matrices containing the wave vector ( $\widehat{k\hat{k}}$ ,  $\widehat{k\hat{n}\hat{k}}$ ) vanishes. Remembering that the  $\hat{k}_i$ -matrices are diagonal and can be commuted in front of the  $\hat{\eta}$  matrix, it is easy to prove

$$\begin{aligned} \widehat{k\hat{k}} \widehat{k\hat{n}\hat{k}} &= \begin{pmatrix} \hat{k}_x \hat{k}_x & \hat{k}_x \hat{k}_y \\ \hat{k}_y \hat{k}_x & \hat{k}_y \hat{k}_y \end{pmatrix} \begin{pmatrix} \hat{k}_y \hat{\eta} \hat{k}_y & -\hat{k}_y \hat{\eta} \hat{k}_x \\ -\hat{k}_x \hat{\eta} \hat{k}_y & \hat{k}_x \hat{\eta} \hat{k}_x \end{pmatrix} \\ &= \begin{pmatrix} \hat{k}_x \hat{k}_x \hat{k}_y \hat{\eta} \hat{k}_y - \hat{k}_x \hat{k}_y \hat{k}_x \hat{\eta} \hat{k}_y & -\hat{k}_x \hat{k}_x \hat{k}_y \hat{\eta} \hat{k}_x + \hat{k}_x \hat{k}_y \hat{k}_x \hat{\eta} \hat{k}_x \\ \hat{k}_y \hat{k}_x \hat{k}_y \hat{\eta} \hat{k}_y - \hat{k}_y \hat{k}_y \hat{k}_x \hat{\eta} \hat{k}_y & -\hat{k}_y \hat{k}_x \hat{k}_y \hat{\eta} \hat{k}_x + \hat{k}_y \hat{k}_y \hat{k}_x \hat{\eta} \hat{k}_x \end{pmatrix} \\ &= \begin{pmatrix} 0 & 0 \\ 0 & 0 \end{pmatrix}. \end{aligned} \quad (2.44)$$

In this notation, the equation reduces to

$$\left[ \widehat{\eta} \left[ q^2 + \widehat{k\hat{k}} \right] + \widehat{k\hat{n}\hat{k}} \right] \vec{\phi} = (2\pi\omega)^2 \vec{\phi}. \quad (2.45)$$

Solving for the eigenvalue of interest  $q^2$  leads to the final eigenvalue problem for the expression of the fields in an individual layer

$$\left[ \widehat{\varepsilon} \left( (2\pi\omega)^2 - \widehat{k\hat{n}\hat{k}} \right) - \widehat{k\hat{k}} \right] \vec{\phi} = q^2 \vec{\phi}. \quad (2.46)$$

---

<sup>12</sup>The vector symbol is used to describe the in-plane character. It contains  $2N$  components (Fourier coefficients for the  $x$ - and  $y$ -components.)

The total number of  $2N$  (double the number of orders kept in the Fourier expansion) eigenvectors  $\vec{\phi}_n$  form the new basis for expanding the fields. Each eigenvector contains  $N$  Fourier coefficients of each of the the Fourier vectors  $h_x$  and  $h_y$  in this order.  $e_x$  and  $e_y$  can be determined using eq. (2.36).

The eigenvalue  $q_n^2$  is the square of the propagation constant in  $z$ -direction of the corresponding  $n^{\text{th}}$  eigenmode. The propagation is described by a simple exponential plane-wave propagation due to the homogeneity in the  $z$ -direction within this layer.

Since the product of a diagonal and a full matrix does not commute the matrix  $\widehat{knk}$  is non-symmetric due to the product of  $\hat{k}_i \hat{\eta} \hat{k}_j$  and the eigenvalue problem is non-symmetric as well. In addition, the dielectric function can be complex if there is absorption in the system. It can still be solved but the eigenvectors in general do not exhibit special properties.

The problem can be made symmetric by multiplying with  $(\omega^2 - \widehat{knk})$  and then using the relation between  $\widehat{k\hat{k}}$  and  $\widehat{knk}$  (eq. (2.44))

$$\left[ \left( (2\pi\omega)^2 - \widehat{knk} \right) \eta^{-1} \left( (2\pi\omega)^2 - \widehat{knk} \right) - (2\pi\omega)^2 \widehat{k\hat{k}} \right] \vec{\phi} = q^2 \left( (2\pi\omega)^2 - \widehat{knk} \right) \vec{\phi}. \quad (2.47)$$

The eigenvectors of such a generalized eigenvalue problem fulfill a generalized orthogonality relation with the matrix  $((2\pi\omega)^2 - \widehat{knk})$  sandwiched between the eigenvector

$$\vec{\phi}_n^T \left( (2\pi\omega)^2 - \widehat{knk} \right) \vec{\phi}_{n'} = \delta_{nn'}. \quad (2.48)$$

Using this orthogonality relation later on, a matrix inversion of a  $4N \times 4N$  matrix can be done analytically but it is not needed otherwise. The computational advantage is lower than expected, since the general eigenvalue problem takes longer than a regular one and, in addition, one has to make sure that eigenvectors for degenerate eigenvalues are orthogonalized as well.

### Expressing the fields in eigenmodes

Knowing the eigenmodes in an individual layer, they can be used as a basis to express the fields. As mentioned before, the entries in eigenvectors determine the Fourier components of the field pattern, which moves in  $z$ -direction as a plane wave with propagation constant  $q (= k_z)$ .

This makes it possible to express the field as a superposition of all  $N$  eigenmodes, each occurring twice, once propagating forward and once propagating backward. The unknowns are the amplitudes  $a_n$  and  $b_n$  associated with each mode

$$\begin{pmatrix} h_x(z) \\ h_y(z) \end{pmatrix} = \sum_n \begin{pmatrix} \phi_{x,n} \\ \phi_{y,n} \end{pmatrix} (e^{iq_n z} a_n + e^{-iq_n(z-d)} b_n). \quad (2.49)$$

The two different exponentials for the forward ( $e^{iq_n z}$ ) and backward ( $e^{-iq_n(z-d)}$ ) propagating wave are needed for better numerical stability.

The result of the eigenvalue problem is not the propagation constant  $q$  but the square of it. When taking the root, there are two different possibilities. If one takes the root with the positive imaginary part of  $q$  the forward propagating wave will decay so that it has its biggest amplitude at  $z = 0$  (top of the layer). By introducing the additional phase  $e^{iqnd}$ , the biggest amplitude of the backward propagating wave at the bottom of the layer ( $z = d$ ) is on the order of 1 and not exponentially larger than the one of the forward propagating wave. Therefore, the coefficients  $a_n$  and  $b_n$  are of the same order too, which is numerically preferable. As a consequence, the coefficient  $a_n$  describes the forward propagating wave at the top of the layer, whereas  $b_n$  describes the backward propagating wave at the bottom. These phases will be present in the  $S$ -matrix later on, but their introduction avoids a layer  $T$ -matrix which propagates the fields through the layer [49].

Simplifying the expression using the  $2N \times 2N$  matrix  $\hat{\phi}$  containing all eigenvectors in the columns, the  $2N \times 2N$  diagonal matrix  $\hat{f}(z)$  containing the phases  $(\hat{f}(z))_{nn} = e^{-iqnz}$  and the  $2N$ -dimensional vectors  $a$  and  $b$  containing the coefficients leads to

$$\vec{h}_{||} = \hat{\phi} \left( \hat{f}(z)a + \hat{f}(z-d)b \right). \quad (2.50)$$

Doing the same for the electric field starting from eq. (2.36) yields

$$\begin{aligned} \begin{pmatrix} -e_y \\ e_x \end{pmatrix} &= \sum_n \begin{pmatrix} \hat{\eta} & 0 \\ 0 & \hat{\eta} \end{pmatrix} \left[ q_n^2 + \begin{pmatrix} \hat{k}_x \hat{k}_x & \hat{k}_x \hat{k}_y \\ \hat{k}_y \hat{k}_x & \hat{k}_y \hat{k}_y \end{pmatrix} \right] \begin{pmatrix} \phi_{x,n} \\ \phi_{y,n} \end{pmatrix} \times \\ &\times \frac{1}{q_n} (e^{iqnz} a_n - e^{-iqn(z-d)} b_n) \end{aligned} \quad (2.51)$$

which can be brought into the more compact form

$$\vec{e}_{||} = \sum_n \hat{\eta} \left( \widehat{k\hat{k}} + q_n^2 \right) \phi_n (e^{iqnz} a_n - e^{-iqn(z-d)} b_n). \quad (2.52)$$

This can be cast into a similar form as eq. (2.50) by using the matrix  $\hat{\phi}$  for the eigenvectors as well as a diagonal matrix  $\hat{q}^{-1}$  with the inverse of the eigenvalues  $(\hat{q}^{-1})_{nn'} = \frac{1}{q_n} \delta_{nn'}$ . In addition, one has to use eq. (2.45) to replace<sup>13</sup>  $\hat{\eta} \left( \widehat{k\hat{k}} + q_n^2 \right)$  by  $\left( \omega^2 - \widehat{k\hat{n}\hat{k}} \right)$

$$\vec{e}_{||} = \left( (2\pi\omega)^2 - \widehat{k\hat{n}\hat{k}} \right) \hat{\phi} \hat{q}^{-1} \left( \hat{f}(z)a - \hat{f}(z-d)b \right). \quad (2.53)$$

Combining eq. (2.50) and eq. (2.53) into one equation, gives the final expression for

---

<sup>13</sup>This requires again that  $\hat{\varepsilon}\hat{\eta} = 1$  because, in the other case, the eigenvalue problem in eq. (2.45) would not provide the required relation, even if it was valid.

the tangential fields in a layer

$$\begin{aligned} \begin{pmatrix} \vec{e}_{||} \\ \vec{h}_{||} \end{pmatrix} &= \begin{pmatrix} \left( (2\pi\omega)^2 - \widehat{knk} \right) \widehat{\phi q}^{-1} & - \left( (2\pi\omega)^2 - \widehat{knk} \right) \widehat{\phi q}^{-1} \\ \widehat{\phi} & \widehat{\phi} \end{pmatrix} \begin{pmatrix} \widehat{f}(z)a \\ \widehat{f}(d-z)b \end{pmatrix} \\ &= M \begin{pmatrix} \widehat{f}(z)a \\ \widehat{f}(d-z)b \end{pmatrix}. \end{aligned} \quad (2.54)$$

The signs in the  $M$ -matrix are a general property of these matrices [51]. In order to match the fields in adjacent layers one has to determine the relation between the coefficients  $a$  and  $b$  in both layers (Sec. 2.3). Using the inverse of the  $M$ -matrix, which can be calculated easily using the orthogonality relation eq. (2.48), this gives

$$M^{-1} = \frac{1}{2} \begin{pmatrix} \phi^T & \phi^T \left( (2\pi\omega)^2 - \widehat{knk} \right) \\ -\phi^T & \phi^T \left( (2\pi\omega)^2 - \widehat{knk} \right) \end{pmatrix}. \quad (2.55)$$

As mentioned before, this is not necessary and can also be done numerically. Otherwise the orthogonality for equal eigenvalues has to be checked and eventually corrected. Inverting numerically avoids any problems related to similar but not exactly the same eigenvalues and their treatment.

### Homogeneous Layer

The homogeneous problem in case with 2D layers cannot be written in a straightforward and simple way for several modes but already taking into account only the  $0^{th}$ -order is instructive to understand the nature of the eigenvalue problem.

For the  $0^{th}$ -order, the matrices in the eigenvalue problem eq. (2.46) reduce to 2x2 matrices and the Toeplitz-matrix reduces to the value of the dielectric constant

$$\begin{aligned} \left[ \begin{pmatrix} \epsilon & 0 \\ 0 & \epsilon \end{pmatrix} \begin{pmatrix} (2\pi\omega)^2 - k_y \frac{1}{\epsilon} k_y & k_y \frac{1}{\epsilon} k_x \\ k_x \frac{1}{\epsilon} k_y & (2\pi\omega)^2 - k_x \frac{1}{\epsilon} k_x \end{pmatrix} - \begin{pmatrix} k_x k_x & k_x k_y \\ k_y k_x & k_y k_y \end{pmatrix} \right] \begin{pmatrix} \phi_x \\ \phi_y \end{pmatrix} \\ = q^2 \begin{pmatrix} \phi_x \\ \phi_y \end{pmatrix}. \end{aligned} \quad (2.56)$$

Solving this equations leads to a diagonal eigenvalue problem with two orthogonal eigenvectors, each having only one component ( $\phi_x \neq 0$ , respectively  $\phi_y \neq 0$ ), corresponding to a different orientation of the magnetic and, hence, the electric field. The two equations for those eigenvalues and eigenvectors then are

$$\begin{aligned} (\epsilon (2\pi\omega)^2 - k_y k_y - k_x k_x) \phi_x &= q_1^2 \phi_x, \\ (\epsilon (2\pi\omega)^2 - k_y k_y - k_x k_x) \phi_y &= q_2^2 \phi_y. \end{aligned} \quad (2.57)$$

If  $q$  is identified as  $k_z$  this corresponds to the regular dispersion relation of a plane wave. The two eigenvalues are identical, since the dispersion is independent of the orientation of the electric field in a homogeneous medium

$$q = k_z = \pm \sqrt{\left(\frac{wn}{c}\right)^2 - (k_x^2 + k_y^2)}. \quad (2.58)$$

The generalization to more modes is straightforward. The orders differ in the reciprocal lattice vector added to the in-plane wave vector. The eigenvalue for the  $l^{\text{th}}$ -mode then reads as

$$q_l = \pm \sqrt{\left(\frac{wn}{c}\right)^2 - (\vec{k} + \vec{G}_l)^2}. \quad (2.59)$$

## 2.3 Matching Fields in Adjoining Layers

The in-plane field components described by eq. (2.53) are tangential with respect to boundaries and hence continuous across them

$$\begin{pmatrix} \vec{e}_{||} \\ \vec{h}_{||} \end{pmatrix}_l = \begin{pmatrix} \vec{e}_{||} \\ \vec{h}_{||} \end{pmatrix}_{l+1}. \quad (2.60)$$

If the coefficients  $a$  and  $b$  in the  $l^{\text{th}}$  layer are known, they can easily be related to the ones in the  $l+1^{\text{st}}$  layer. The coordinate system in which each layer is solved starts with  $z = 0$  at the top of an individual layer and ranges to  $z = d$  at the bottom, with  $d$  being the thickness. Therefore, the  $l^{\text{th}}$  layer must be considered at the end  $z = d$  and the  $l+1^{\text{st}}$  layer at  $z = 0$ . The phase prefactor matrices  $\hat{f}_i(z)$  can be ignored if their argument is 0 since the exponential of 0 is always 1. As a consequence, these matrices only occur with the layer thickness as their argument and the argument can be suppressed in what follows

$$\begin{pmatrix} a_{l+1} \\ \hat{f}_{l+1}(d_{l+1})b_{l+1} \end{pmatrix} = M_{l+1}^{-1}M_l \begin{pmatrix} \hat{f}_l(d_l)a_l \\ b_l \end{pmatrix} = I_{l,l+1} \begin{pmatrix} \hat{f}_l(d_l)a_l \\ b_l \end{pmatrix}. \quad (2.61)$$

The interface matrix  $I_{l,l+1} = M_{l+1}^{-1}M_l$  is a regular  $T$ -matrix. For simple systems the  $T$ -matrix can be used but for more complex systems which involves evanescent modes, the  $T$ -matrix is numerically unstable.

The primary reason for this is the coexistence of very large values from the growing waves together with very small values for the decaying waves. This leads to numerical errors as was shown in several articles for electronic and photonic systems [46, 47, 52]. The problem is caused by the repetitive multiplication of the exponentially growing wave. In the calculations, modes with large amplitudes have to be subtracted from each other and in this case the number of significant digits is insufficient [43, 49].

## 2.4 Solving for All Layers

Since the  $T$ -matrix is unstable, another approach is needed which avoids the simultaneous occurrence of exponentially growing and decaying waves.

Relating the incoming to the outgoing waves by using  $S$ -matrices circumvents the above problem. For decaying modes, the outgoing waves will always have a smaller amplitude than the incoming ones. The matrix relating the incoming modes onto of the structure to the outgoing waves behind the structure is defined as<sup>14</sup> (compare Fig. 2.3)

$$\begin{pmatrix} \mathbf{a}_{\text{out}} \\ \mathbf{b}_{\text{in}} \end{pmatrix} = S(\text{in, out}) \begin{pmatrix} \mathbf{a}_{\text{in}} \\ \mathbf{b}_{\text{out}} \end{pmatrix} = \begin{pmatrix} S_{11} & S_{12} \\ S_{21} & S_{22} \end{pmatrix} \begin{pmatrix} \mathbf{a}_{\text{in}} \\ \mathbf{b}_{\text{out}} \end{pmatrix}. \quad (2.62)$$

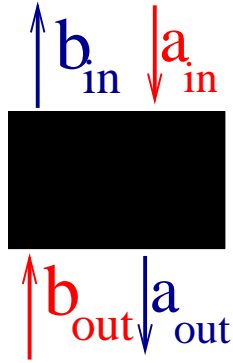


**Figure 2.3:** Schematic representation of a  $S$ -matrix. The black box contains an arbitrary structure.

The corresponding  $T$ -matrix is defined as

$$\begin{pmatrix} \mathbf{a}_{\text{out}} \\ \mathbf{b}_{\text{out}} \end{pmatrix} = T(\text{in, out}) \begin{pmatrix} \mathbf{a}_{\text{in}} \\ \mathbf{b}_{\text{in}} \end{pmatrix} = \begin{pmatrix} T_{11} & T_{12} \\ T_{21} & T_{22} \end{pmatrix} \begin{pmatrix} \mathbf{a}_{\text{in}} \\ \mathbf{b}_{\text{in}} \end{pmatrix}. \quad (2.63)$$

In general, due to the phase factor introduced in eq. (2.49) we have to take into account that the forward propagating wave is taken at the top of a layer and the backward propagating wave is taken at the bottom, so that the correct situation in this case is represented in Fig. 2.4. The box denotes the structure divided into  $N$  layers and the  $S$ -matrix relates the fields in the top ( $0^{\text{th}}$ -) layer to those in the bottom ( $N^{\text{th}}$ -) layer (compare Fig. 2.4). The  $0^{\text{th}}$ - and  $N^{\text{th}}$ -layer could correspond to the incoming and outgoing region or to the first and last layer in the structure at the moment. At the moment it is only important to discuss the occurrence of the

<sup>14</sup>To derive this we set the thickness of the air layer above and below the crystal to be zero, leading to  $\hat{f}(0) = 1$ . How to handle non propagating orders in this case will be discussed in Sec. 3.3. Changing the thickness will only introduce a phase in the propagating orders.

phase factor  $\hat{f}$  in the amplitudes for a given layer width

$$\begin{pmatrix} \mathbf{a}_N \\ \mathbf{b}_0 \end{pmatrix} = S(0, N) \begin{pmatrix} \mathbf{a}_0 \\ \mathbf{b}_N \end{pmatrix} = \begin{pmatrix} S_{11} & S_{12} \\ S_{21} & S_{22} \end{pmatrix} \begin{pmatrix} \mathbf{a}_0 \\ \mathbf{b}_N \end{pmatrix}. \quad (2.64)$$

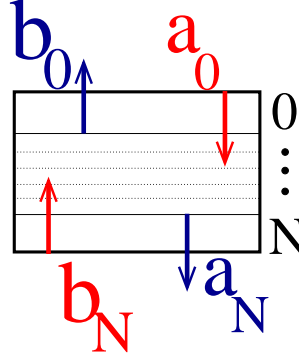


**Figure 2.4:** Schematical representation of a  $S$ -matrix. The box represents the structure in the  $z$ - (propagation) direction. 0 and  $N$  refer to the first respective last layer in the structure. The beginning of the arrows indicates at which position the fields are taken.

### 2.4.1 Scattering Matrix Recursion

Now that the  $S$ -matrix is defined, it has to be solved for a given structure composed of  $N$  layers, each with thickness  $d_l$ .

The beginning is rather simple - the first  $S$ -matrix relates the  $0^{th}$  layer with itself and is given by the unit matrix

$$S(0, 0) = \begin{pmatrix} 1 & 0 \\ 0 & 1 \end{pmatrix}. \quad (2.65)$$

Relating the  $m^{th}$  layer with the next ( $m+1^{st}$ ) needs evaluation of the boundary conditions at the interface, which define the interface matrix eq. (2.3). The phase matrix  $\hat{f}(d_m)$  also has to be taken into account. Starting with eq. (2.62) for layers 0 and  $m$  and eq. (2.63) for layers  $m$  and  $m+1$  yields

$$\begin{aligned} \begin{pmatrix} a_m \\ b_0 \end{pmatrix} &= S(0, m) \begin{pmatrix} a_0 \\ b_m \end{pmatrix} \\ &= \begin{pmatrix} S_{11} & S_{12} \\ S_{21} & S_{22} \end{pmatrix} \begin{pmatrix} a_0 \\ b_m \end{pmatrix}, \end{aligned} \quad (2.66)$$

$$\begin{aligned} \begin{pmatrix} \hat{f}(d_m)a_m \\ b_m \end{pmatrix} &= I(m, m+1) \begin{pmatrix} a_{m+1} \\ \hat{f}(d_{m+1})b_{m+1} \end{pmatrix} \\ &= \begin{pmatrix} I_{11} & I_{12} \\ I_{21} & I_{22} \end{pmatrix} \begin{pmatrix} a_{m+1} \\ \hat{f}(d_{m+1})b_{m+1} \end{pmatrix}. \end{aligned} \quad (2.67)$$

This can be rewritten as

$$a_m = S_{11}a_0 + S_{12}b_m, \quad (2.68)$$

$$b_0 = S_{21}a_0 + S_{22}b_m, \quad (2.69)$$

$$a_m = \hat{f}(d_m)^{-1} \left[ I_{11}a_{m+1} + I_{12}\hat{f}(d_{m+1})b_{m+1} \right], \quad (2.70)$$

$$b_m = I_{21}a_{m+1} + I_{22}\hat{f}(d_{m+1})b_{m+1}, \quad (2.71)$$

Equating eq. (2.68) and eq. (2.70), and inserting eq. (2.71) for  $b_m$  leads to:

$$\hat{f}(d_m)^{-1} \left[ I_{11}a_{m+1} + I_{12}\hat{f}(d_{m+1})b_{m+1} \right] = S_{11}a_0 + S_{12} \left[ I_{21}a_{m+1} + I_{22}\hat{f}(d_{m+1})b_{m+1} \right], \quad (2.72)$$

$$b_0 = S_{21}a_0 + S_{22} \left[ I_{21}a_{m+1} + I_{22}\hat{f}(d_{m+1})b_{m+1} \right]. \quad (2.73)$$

Then,  $a_{m+1}$  can be calculated using eq. (2.72)

$$a_{m+1} = \left( I_{11} - \hat{f}(d_m)S_{12}I_{21} \right)^{-1} \left[ \hat{f}(d_m)S_{11}a_0 + \left( \hat{f}(d_m)S_{12}I_{22} - I_{12} \right) \hat{f}(d_{m+1})b_{m+1} \right]. \quad (2.74)$$

Comparing with the definition of the  $S$ -matrix allows for determination of  $S_{11}(0, m+1)$  and  $S_{12}(0, m+1)$ . Inserting this into eq. (2.73), with  $\bar{S}_{ij}$  labeling components for the new matrix  $S(0, m+1)$  yields

$$b_0 = [S_{21} + S_{22}I_{21}\bar{S}_{11}] a_0 + [S_{22}I_{22}\hat{f}(d_{m+1}) + S_{22}I_{21}\bar{S}_{12}] b_{m+1}. \quad (2.75)$$

The prefactors for  $a_0$  respectively  $b_{m+1}$  correspond to  $S_{21}(0, m+1)$  respectively  $S_{22}(0, m+1)$ , so that the final form of the matrix  $\bar{S}(0, m+1)$  can be determined

$$S_{11}(0, m+1) = \left[ I_{11} - \hat{f}(d_m)S_{12}(0, m)I_{21} \right]^{-1} \hat{f}(d_m)S_{11}(0, m), \quad (2.76)$$

$$S_{12}(0, m+1) = \left[ I_{11} - \hat{f}(d_m)S_{12}(0, m)I_{21} \right]^{-1} \left[ \hat{f}(d_m)S_{12}(0, m)I_{22} - I_{12} \right] \hat{f}(d_{m+1}), \quad (2.77)$$

$$S_{21}(0, m+1) = S_{21}(0, m) + S_{22}(0, m)I_{21}S_{11}(0, m+1), \quad (2.78)$$

$$S_{22}(0, m+1) = S_{22}(0, m)I_{22}\hat{f}(d_{m+1}) + S_{22}(0, m)I_{21}S_{12}(0, m+1). \quad (2.79)$$

By repeating this step the matrix for a complete crystal consisting of  $N$  layers  $S(0, N)$  can be calculated recursively.

## 2.4.2 Multiplication of Scattering-Matrices

As in the case of the  $T$ -matrix, long crystals can be calculated by “multiplying” several  $S$ -matrices together. This “multiplication” is not a regular matrix multipli-

cation but it can be derived by starting with two  $S$ -matrices  $S(0, l)$  and  $S(l, N)$ .

$$\begin{aligned} \begin{pmatrix} a_l \\ b_0 \end{pmatrix} &= S(0, l) \begin{pmatrix} a_0 \\ b_l \end{pmatrix} \\ &= \begin{pmatrix} S_{11} & S_{12} \\ S_{21} & S_{22} \end{pmatrix} \begin{pmatrix} a_0 \\ b_l \end{pmatrix}, \end{aligned} \quad (2.80)$$

$$\begin{aligned} \begin{pmatrix} a_N \\ b_l \end{pmatrix} &= S(l, N) \begin{pmatrix} a_l \\ b_N \end{pmatrix} \\ &= \begin{pmatrix} \tilde{S}_{11} & \tilde{S}_{12} \\ \tilde{S}_{21} & \tilde{S}_{22} \end{pmatrix} \begin{pmatrix} a_l \\ b_N \end{pmatrix} \end{aligned} \quad (2.81)$$

or in form of the corresponding linear equations

$$a_l = S_{11}a_0 + S_{12}b_l, \quad (2.82)$$

$$b_0 = S_{21}a_0 + S_{22}b_l \quad (2.83)$$

$$a_N = \tilde{S}_{11}a_l + \tilde{S}_{12}b_N, \quad (2.84)$$

$$b_l = \tilde{S}_{21}a_l + \tilde{S}_{22}b_N. \quad (2.85)$$

Inserting eq. (2.85) into eq. (2.82), and solving for  $a_l$  yields

$$a_l = \left(1 - S_{12}\tilde{S}_{21}\right)^{-1} \left(S_{11}a_0 + S_{12}\tilde{S}_{22}b_N\right). \quad (2.86)$$

This can be used to solve eq. (2.84) for  $a_N$

$$a_N = \left[\tilde{S}_{11} \left(1 - S_{12}\tilde{S}_{21}\right)^{-1} S_{11}\right] a_0 + \left[\tilde{S}_{11} \left(1 - S_{12}\tilde{S}_{21}\right)^{-1} S_{12}\tilde{S}_{22} + \tilde{S}_{12}\right] b_N. \quad (2.87)$$

The prefactors for  $a_0$  and  $b_N$  now correspond to  $S(0, N)_{11}$  and  $S(0, N)_{12}$ . The two missing matrix elements can be derived using eq. (2.85) and eq. (2.83)

$$b_0 = S_{21}a_0 + S_{22} \left(\tilde{S}_{21}a_l + \tilde{S}_{22}b_N\right) \quad (2.88)$$

in conjunction with eq. (2.86) the final formula for  $b_0$  follows as

$$b_0 = \left[S_{21} + S_{22}\tilde{S}_{21} \left(1 - S_{12}\tilde{S}_{21}\right)^{-1} S_{11}\right] a_0 + \left[S_{22}\tilde{S}_{21} \left(1 - S_{12}\tilde{S}_{21}\right)^{-1} S_{12}\tilde{S}_{22} + S_{22}\tilde{S}_{22}\right] b_N. \quad (2.89)$$

Again the prefactors to  $a_0$  and  $b_N$  correspond to the matrix elements of  $S(0, N)$ . Summarizing all information defines the multiplication rules for  $S$ -matrices

$$\begin{aligned} S_{11}(0, N) &= S_{11}(l, N) [1 - S_{12}(0, l)S_{21}(l, N)]^{-1} S_{11}(0, l), \\ S_{12}(0, N) &= S_{12}(l, N) + S_{11}(l, N) [1 - S_{12}(0, l)S_{21}(l, N)]^{-1} S_{12}(0, l)S_{22}(l, N), \\ S_{21}(0, N) &= S_{21}(0, l) + S_{22}(0, l)S_{21}(l, N) (1 - S_{12}(0, l)S_{21}(l, N))^{-1} S_{11}(0, l), \\ S_{22}(0, N) &= S_{22}(0, l)S_{22}(l, N) + S_{22}(0, l)S_{21}(l, N) (1 - S_{12}(0, l)S_{21}(l, N))^{-1} S_{12}(0, l)S_{22}(l, N). \end{aligned} \quad (2.90)$$

Despite the complicated form, the  $S$ -matrix-multiplication is associative [49], a property which can be helpful during the implementation.

## 2.5 Fields Inside the Structure

In order to calculate the fields in the  $l^{\text{th}}$  layer, the  $S$ -matrix which relates these fields with the first layer  $S(0, l)$  and the last layer  $S(l, N)$  the structure is required

$$\begin{pmatrix} a_l \\ b_0 \end{pmatrix} = S(0, l) \begin{pmatrix} a_0 \\ b_l \end{pmatrix} = \begin{pmatrix} S_{11} & S_{12} \\ S_{21} & S_{22} \end{pmatrix} \begin{pmatrix} a_0 \\ b_l \end{pmatrix}, \quad (2.91)$$

$$\begin{pmatrix} a_N \\ b_l \end{pmatrix} = S(l, N) \begin{pmatrix} a_l \\ b_N \end{pmatrix} = \begin{pmatrix} \hat{S}_{11} & \hat{S}_{12} \\ \hat{S}_{21} & \hat{S}_{22} \end{pmatrix} \begin{pmatrix} a_l \\ b_N \end{pmatrix}. \quad (2.92)$$

Without matrices this can be cast into the following set of linear equations

$$a_l = S_{11}a_0 + S_{12}b_l, \quad (2.93)$$

$$b_0 = S_{21}a_0 + S_{22}b_l, \quad (2.94)$$

$$a_N = \hat{S}_{11}a_l + \hat{S}_{12}b_N, \quad (2.95)$$

$$b_l = \hat{S}_{21}a_l + \hat{S}_{22}b_N. \quad (2.96)$$

Using eq. (2.96), and eq. (2.93) and inserting them into each other yields the equation for the coefficients  $a_l$  and  $b_l$  which are necessary to describe the fields inside the structure

$$\begin{aligned} a_l &= \left(1 - S_{12}\hat{S}_{21}\right)^{-1} \left[S_{11}a_0 + S_{12}\hat{S}_{22}b_N\right], \\ b_l &= \left(1 - \hat{S}_{21}S_{12}\right)^{-1} \left[\hat{S}_{21}S_{11}a_0 + \hat{S}_{22}b_N\right]. \end{aligned} \quad (2.97)$$

In experiments, one usually has only a single wave impinging from the top so that the coefficient for the backward propagating wave below the system can be set to zero ( $b_N = 0$ ). The fields can then be calculated using the  $M$ -matrix (eq. (2.54)).

## 2.6 Reflected and Transmitted Modes

Once the  $S$ -matrix is known, the calculation of the reflectance, respectively, transmittance is done by setting the amplitude of the correct expansion order  $m$  of the incoming wave to the required value  $a_{m,\text{in}}$  in the homogeneous incoming region<sup>15</sup>. The amplitudes of the backward propagating mode at the bottom is set to zero,

<sup>15</sup>The Rayleigh expansion is only valid in a homogeneous region. In periodic regions, the eigenmodes would have to be calculated and only those could be excited. Any other field configuration, e. g. a Bloch-mode, would have to be expanded in the eigenmodes and the amplitudes of the individual modes would have to be set accordingly.

assuming no wave impinging on the system from below. The amplitudes of the outgoing modes are then given by

$$b_{\text{in}} = S_{21}(\text{in, out})a_{\text{in}}, \quad (2.98)$$

$$a_{\text{out}} = S_{11}(\text{in, out})a_{\text{in}}. \quad (2.99)$$

In this case “in” and “out” label the region in which the amplitude is considered and  $S(\text{in, out})$  relates the incoming region via the structure to the outgoing region. A more detailed definition is given in Sec. 3.4.4. Given these amplitudes, the fields in these regions can be calculated using the  $M$ -matrix in eq. (2.54). The value for  $z$  in these layers can be chosen arbitrary since it is only adding a phase to the amplitudes, but when accessing the phase from the amplitudes it should be the same for  $a_{\text{in}}$  and  $b_{\text{in}}$ . If only the far field pattern is required, the non-propagating modes have to be excluded in the calculation of the fields (see Sec. 3.3).

## 2.7 Dipole Emission

The emission of a dipole inside the structure requires a reformulation of the problem. So far, an incoming wave from the top <sup>16</sup> without any additional sources inside the crystal, was considered.

Introducing a dipole can be done by changing the boundary conditions for adjoining layers. Since it will not be used it in the following only a brief description will be given here. A more detailed description can be found in [42].

In what follows a harmonic time dependence  $e^{-i\omega t}$  is assumed for the dipole which is located at position  $(\vec{r}_0, z_0)$ . The coupling of the dipole to the fields is supposed to be weak, so that its amplitude is independent of the electric and magnetic at the position of the dipole. The dipole can then be described by a current density

$$\vec{J}(\vec{r}, z) = J_0 \delta(\vec{r} - \vec{r}_0) \delta(z - z_0) \quad (2.100)$$

$$= \sum_{\vec{k}, \vec{G}} J_{\vec{k}, \vec{G}} e^{i(\vec{k} + \vec{G})(\vec{r} - \vec{r}_0)} \delta(z - z_0) \quad (2.101)$$

$$= \sum_{\vec{k}, \vec{G}} J'_{\vec{k}, \vec{G}} e^{i(\vec{k} + \vec{G})\vec{r}} \delta(z - z_0). \quad (2.102)$$

In order to represent a point-like dipole all values of  $\vec{k}$  inside the Brillouin zone in the summation are needed. Using only one value for  $\vec{k}$  leads to a current throughout the unit cell. A single  $\vec{k}$  describes the emission into all diffraction orders with an in-plane wave vector given by  $\vec{k} + \vec{G}_n$ . Intuitively, a periodically arranged dipole leads to an emitted plane wave, and only the superposition of several dipoles with different  $\vec{k}$  can create a more structured emission pattern. In the simulations all

---

<sup>16</sup>In the formulas presented an incoming wave from the bottom was also considered. In realistic simulation this wave described by  $b_N$  is set to zero.

values of  $\vec{k}$  for the dipoles have to be calculated in separate runs, and, in the end, the complex fields have to be added up of to study the emission of a localized dipole.

Implementing the current into Maxwell equations eqs. (2.28)–(2.30) is done by defining the Fourier vector for the current density in the same way as before

$$i\hat{k}_y h_z(z) - \frac{\partial}{\partial z} h_y(z) = j_x \delta(z - z_0) - 2\pi i \omega c \hat{e} e_x(z), \quad (2.103)$$

$$\frac{\partial}{\partial z} h_x(z) - i\hat{k}_x h_z(z) = j_y \delta(z - z_0) - 2\pi i \omega c \hat{e} e_y(z), \quad (2.104)$$

$$i\hat{k}_x h_y(z) - i\hat{k}_y h_x(z) = j_z \delta(z - z_0) - 2\pi i \omega c \hat{e} e_z(z). \quad (2.105)$$

The current density can be related to a charge density by  $\vec{\nabla} \cdot \vec{J} = i\omega\rho$ . This guarantees that Maxwell equations are always fulfilled. These additional terms give rise to discontinuities of the parallel fields at  $z_0$

$$e_{\parallel}(z_0^+) - e_{\parallel}(z_0^-) = p_z, \quad h_{\parallel}(z_0^+) - h_{\parallel}(z_0^-) = p_{\parallel}. \quad (2.106)$$

The component  $p_z$  respectively  $p_{\parallel}$  is due to a dipole oriented in the  $z$ -direction respectively a dipole oriented parallel to the layers. Their values are given by<sup>17</sup>:

$$p_{\parallel} = \begin{pmatrix} -j_y \\ -j_z \end{pmatrix}, \quad p_z = \begin{pmatrix} -\hat{k}_y \hat{\eta} \frac{j_z}{\varepsilon_0 \omega} \\ \hat{k}_x \hat{\eta} \frac{j_z}{\varepsilon_0 \omega} \end{pmatrix}. \quad (2.107)$$

In the  $S$ -matrix approach the dipole will be included in between two layers, so that one of the fields corresponds to the field at the end of the  $l^{\text{th}}$  layer,  $e_{\parallel}(z_0^-) = e_{\parallel,l}(z = d_l)$ , and the other to the field at the beginning of the  $l + 1^{\text{st}}$  layer  $e_{\parallel}(z_0^+) = e_{\parallel,l+1}(z = 0)$ . Using the previous definitions for the  $M$  and  $\hat{f}$  matrices the discontinuity condition can be written as:

$$M_{l+1} \begin{pmatrix} a_{l+1} \\ f_{l+1} b_{l+1} \end{pmatrix} - M_l \begin{pmatrix} f_l a_l \\ b_l \end{pmatrix} = \begin{pmatrix} p_z \\ p_{\parallel} \end{pmatrix}. \quad (2.108)$$

Since there are no incoming waves in this example ( $a_0 = 0$  and  $b_N = 0$ ) the fields in the  $l^{\text{th}}$  and  $l + 1^{\text{st}}$  layer are related to the fields in the first and last layer<sup>18</sup>

$$a_l = S_{12}(0, l) b_l, \quad (2.109)$$

$$b_0 = S_{22}(0, l) b_l, \quad (2.110)$$

$$a_N = S_{11}(l + 1, N) a_{l+1}, \quad (2.111)$$

$$b_{l+1} = S_{21}(l + 1, N) a_{l+1}. \quad (2.112)$$

<sup>17</sup>Since  $\hat{\eta}$  usually is different in adjacent layers of the structure, it should be calculated by an interpolation or averaging process to describe the situation between the layers.

<sup>18</sup>The coupling to the regions above and below would still have to done by appropriate matrices (Sec. 3.4.5).

Inserting eq. (2.109) and eq. (2.112) into eq. (2.108) leads to a set of linear equations which can be solved for  $a_{l+1}$  and  $b_l$ .

$$M_{l+1} \begin{pmatrix} a_{l+1} \\ f_{l+1} S_{21}(l+1, N) a_{l+1} \end{pmatrix} - M_l \begin{pmatrix} f_l S_{12}(0, l) b_l \\ b_l \end{pmatrix} = \begin{pmatrix} p_z \\ p_{\parallel} \end{pmatrix}. \quad (2.113)$$

Inserting  $a_{l+1}$  and  $b_l$  into eq. (2.111), respectively eq. (2.110) then solves the full emission problem for a fixed direction  $\vec{k}$  and frequency  $\omega$  for all diffraction orders.

## 2.8 Alternative Approaches

Beside the method presented here, conceptually similar implementations of the RCWA are known, which might even lead to better convergence in some of the cases. For these implementations, most of the optimization and implementation details in the following chapter hold as well. In addition to conceptually similar approaches, conceptually completely different methods can also be used to model transmittance and reflectance.

### 2.8.1 Conceptually Similar Approaches and Improvements

Tikhodeev et al. presented a method, which is based on the expansion of the electric field [53]. Their Ansatz does not fulfill the divergence equations and one has to use

$$-\Delta \vec{E} + \vec{\nabla}(\vec{\nabla} \cdot \vec{E}) = \frac{\omega^2}{c^2} \varepsilon \vec{E} \quad (2.114)$$

as the basic equation, consequently leading to a more complicated eigenvalue problem. In their formulation, the Toeplitz-matrix has never to be inverted directly, making the requirement  $\hat{\varepsilon} \hat{\eta} = 1$  obsolete. For dielectric structures, as discussed in this work, they found convergence using the regular Fourier transform of  $\varepsilon(x, y)$  used in this work as well. For other materials, e. g. metals, the convergence of both implementations, the one by Tikhodeev and the one presented here, is very slow. This is based on the use of truncated Fourier expansions and the folding of  $\tilde{\varepsilon}$  with  $\vec{E}$ .

L. Li pointed out that the folding of the Fourier transform of two functions, which have concurrent jumps, has to be adjusted [54, 55]. This is the case for the permittivity and *only* the normal component of the electric field. Therefore one should use the inverse rule to ensure convergence

$$\sum_{n', n} \tilde{\varepsilon}_{n'} E_{\perp, n} \rightarrow \sum_{n', n} \tilde{\eta}_{n'}^{-1} E_{\perp, n}, \quad \tilde{\eta} = \begin{bmatrix} \tilde{1} \\ \tilde{\varepsilon} \end{bmatrix}. \quad (2.115)$$

These two representation are only equivalent in the case of an infinite number of orders. The implementation for a lattice other than a square lattice is complicated

[56] and requires several Fourier transforms of the dielectric function, depending on whether the component of  $\vec{E}$  is tangential or perpendicular. Therefore, the structure has to be approximated by lines parallel to the two grating vectors. David et al.[57] showed for band structure calculations that this only works well for square holes (parallel to the lattice vectors of the square lattice used) and that for other pore shapes the “simple” version suggested by Ho et al. [34] works better. For this work, the straightforward approach would correspond to the method of calculating  $\tilde{\epsilon}$  and inverting to achieve  $\tilde{\eta}$ . They also provide a solution for arbitrary hole shape, for which the contour of the hole needs to be known. For the structures discussed in Chapter 5 and Chapter 6, these contours are unknown and obtaining them would require difficult calculations. Li also showed that even the improved method fails for 1D metallic gratings in TM polarization [58] although he claimed before that it works even for 2D metallic crossed-gratings [56]. From the large amount of papers, also by others groups, it is evident, that the perfect method does not exist and that convergence has to be checked in each case.

## 2.8.2 Conceptually Different Approaches

In this section, only a brief summary of different methods will be given as an overview. Some of them might be used to reformulate parts of the method (e.g. Finite Elements or Finite Differences to determine the modes).

## 2.8.3 Finite Differences and Finite Elements

Finite Differences (FD) use a grid of points to discretize the derivatives resulting in a sparse matrix relating points to their neighboring points. Depending on the order (number of neighboring points used in the discretization) the sparsity changes. Each entry in the eigenvector corresponds to the field at a point in space, which allows for a simple matching procedure between layers. A poor convergence is observed if any of the material parameters, e.g. dielectric constant, has discontinuities although a number of improvements have been suggested in the literature. FD could be used to calculate the eigenmodes in the individual layers and then apply the  $S$ -matrix formalism or it could be used to model the entire 3D crystal. However, Silberstein et al. found that the expansion in Fourier series offers a better convergence performance than the FD approach for diffraction problem that involve dielectric or metallic gratings [59].

The approach using Finite Elements (FE) [60] offers the same possibilities. For 2D FE, the crystal is divided into smaller areas of special shapes, e.g. triangles. For this purpose mesh generators exist which approximate any geometry by smaller polygons. Within the smaller sections the material properties are constant, so that discontinuities only occur on boundaries of these segments. The fields are then represented by several vector elements in each of the polygons chosen to ease the matching (e.g. Whitney Elements only have parallel or perpendicular components along the edges). Matching of the fields at boundaries leads to an eigenvalue problem

whose eigenvectors are the coefficients of all functions in the smaller areas. Since the discontinuities never occur inside the smaller segments, they can be incorporated easily by the boundary conditions.

It could also be used in 3D with volume elements representing the complete 3D photonic structure. The disadvantage is the resulting very large eigenvalue problem.

However using the method in conjunction with the  $S$ -matrix is more difficult since changes in the geometry from layer to layer lead to different meshes. Consequently the coefficients of the vector functions can not be matched from layer to layer. A possible (however costly) solution to that introduces a fixed grid, interpolates the values for the field at the grid points and then solves for the coefficients in the adjoining layer using these standardized grid points.

The disadvantage of these two methods, if one wants to model transmittance and reflectance experiments is that it is not straightforward to extract transmittance coefficients. The result of these methods are field distributions above and below the crystal expressed in spatial modes. Extracting diffraction orders from these fields can only be done by an additional Fourier transformation.

#### 2.8.4 Finite-Differences Time-Domain (FDTD)

FDTD [61] models the complete 3D unit cell or crystal. Since the solutions depend numerically on space and time, an extraction of modes is difficult in contrast to FD and FE, which could also be used to model the complete crystal without using layers and a  $S$ -matrix. All geometries can be simulated, although discontinuities also represent a challenge. On the plus side, all frequencies can be calculated at once using a pulsed excitation. The results for individual frequencies are then obtained by a Fourier transformation in time. However, the frequency range is limited by the validity of analytical models used for the material dispersion. This advantage is partly destroyed by the large computational domain leading to memory- and time-consuming calculations. The large computational domain is caused by the constraint that the entire structure has to be represented in contrast to slicing in layers. Large structures in the propagating direction hence require a large number of grid points. In addition, long simulations have to be done since contributions close to stop bands move slowly through the PC and require a long time for stabilization.

# 3 Implementation and Optimization

This chapter contains information about the details of the implementation. It can be divided into three sections: The first describes approaches necessary for the correct computation and convergence of the results (Secs. 3.1–3.3). In the second (Sec. 3.4) remarks are given on structuring the program so that it can be optimized for memory and/or CPU-time consumption. The last bigger part describes different implemented options for modeling a variety of systems (Sec. 3.5) together with the implementation of disorder calculations (Sec. 3.7). At the end a small section concerned with testing the simulation tool is included (Sec. 3.8).

Most parts of this chapter might be too technical and only be interesting to readers who wish to implement the method themselves. The parts of more general interests are probably the implementation of long crystals (Sec. 3.4.4), due to the definition of the numerical unit cell, a term which is often used in the following and the discussion of the implementation of disorder (Sec. 3.7).

## 3.1 Fourier Expansion

In the previous chapter, it was mentioned that the Fourier Expansion correspond to the diffraction orders in the homogeneous area. This statement adds physical meaning to the mathematical method of Fourier expansion. However, this is only true if one does the Fourier expansion correctly.

### 3.1.1 Definition of Diffraction Orders

The basic Bragg-diffraction from a periodic structure can be found in any standard textbook of solid state physics, such as Ashcroft/Mermin [36]. The difference in the incoming and diffracted wave vector corresponds to a vector of the reciprocal lattice. In the problem of finite PCs the lattice is defined in the  $x$ - $y$ -plane and this argument holds for the in-plane components of the wave vector. The  $k_z$ -component of the diffracted orders outside the crystal is then given by the dispersion of a plane wave

$$k_z = \sqrt{k_0^2 - (k_{x,0} + G_x)^2 - (k_{y,0} + G_y)^2}. \quad (3.1)$$

As a consequence the Fourier expansion can only be interpreted physically if the chosen expansion orders contain the correct reciprocal lattice vectors  $\vec{G}$ . The choice of a unit cell is however not unique in 2D. For the Fourier transformation, unit cells could

be chosen for which the corresponding vectors in reciprocal space do not correspond to the physically relevant reciprocal lattice vectors  $\vec{G}$ . In this case the formulation is still mathematically correct, in the sense that the inverse transformation reproduces the correct fields and lattices but not the diffraction pattern. In this case the efficiency of the individual orders cannot be extracted from the expansion coefficients. If for a high enough frequency, respectively short enough wavelength, several propagating modes exist, even the  $0^{th}$ -order is wrong since the energy transmitted into higher order modes is not described correctly. As an example, a triangular lattice is discussed in the following.

### 3.1.2 Triangular Example

The lattice vectors and the Wigner-Seitz cell as well as the reciprocal lattice for a 2D triangular lattice are shown in the chapter about basic properties of PCs (Fig. 1.3).

The Wigner-Seitz cell is the smallest possible unit cell that retains the symmetry of the lattice[36]. However, other unit cells can reproduce the 2D periodic pattern as well (Fig. 3.1). The corresponding lattice vectors and reciprocal lattice vectors<sup>1</sup> here are listed in Tab. 3.1. The unit cell can be shifted arbitrarily without changing the lattice vectors as shown in Fig. 3.1(a) and Fig. 3.1(b) leading to different distributions of dielectric material inside.

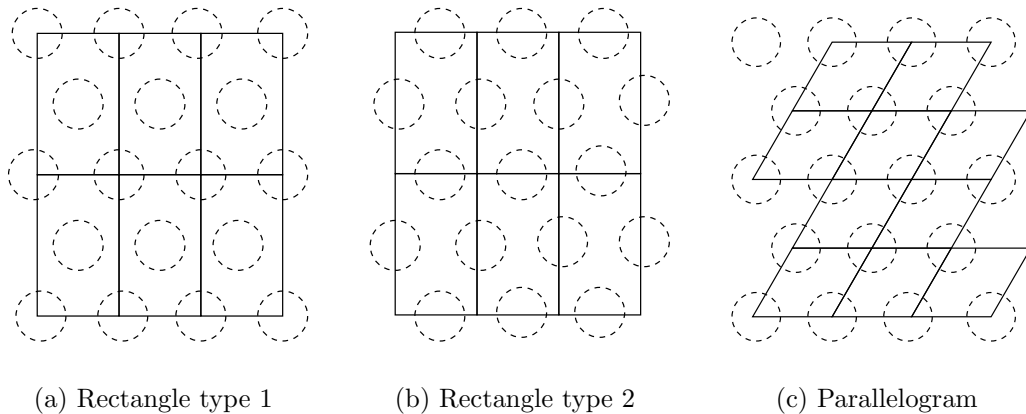


**Figure 3.1:** Different unit cells for a triangular lattice. (a) and (b) contain more than 1 cylinder and are no primitive unit cells.

An expansion in both reciprocal lattice vectors is possible, however it is obvious that only the (reciprocal) lattice vectors associated with the parallelogram corre-

<sup>1</sup>The term (reciprocal) lattice vector is basically used incorrectly here. The lattice is defined by the arrangement of pores and hence the lattice vectors are unique. In the Fourier expansion all periodic unit cells could be used and in this section the (reciprocal) lattice vectors are generalized to the periodic cell used in this expansion to show the differences. This corresponds to assuming that the (translational) lattice is defined by the unit cell.

Type	Real Space	Modulus	Reciprocal Space	Modulus
Rectangular	$\begin{pmatrix} a \\ 0 \end{pmatrix}, \begin{pmatrix} 0 \\ \sqrt{3}a \end{pmatrix}$	$a, \sqrt{3}a$	$\begin{pmatrix} \frac{2\pi}{a} \\ 0 \end{pmatrix}, \begin{pmatrix} 0 \\ \frac{2\pi}{\sqrt{3}a} \end{pmatrix}$	$\frac{2\pi}{a}, \frac{2\pi}{\sqrt{3}a}$
Parallelogram	$\begin{pmatrix} a \\ 0 \end{pmatrix}, \begin{pmatrix} \frac{a}{2} \\ \frac{\sqrt{3}}{2}a \end{pmatrix}$	$a, a$	$\begin{pmatrix} \frac{2\pi}{a} \\ -\frac{2\pi}{\sqrt{3}a} \end{pmatrix}, \begin{pmatrix} 0 \\ \frac{4\pi}{\sqrt{3}a} \end{pmatrix}$	$\frac{4\pi}{\sqrt{3}a}, \frac{4\pi}{\sqrt{3}a}$

**Table 3.1:** Lattice vectors and reciprocal lattice vectors for different unit cells discussed in Fig. 3.1. The lattice vectors for the parallelogram correspond to the ones in Fig. 1.3.

sponds to the physical diffraction orders. In addition only those fulfill the sixfold rotation symmetry of the triangular lattice.

Consequently the rectangular unit cell exhibits problems. Since the rectangular real space unit cell is bigger than the parallelogram, the reciprocal lattice vectors are shorter and are more propagating orders occur. In other words, the propagation constant for expansions orders

$$k_{z,i}^{\text{rect}} = \sqrt{k_0^2 - (k_{x,0} + G_{x,i}^{\text{rect}})^2 - (k_{y,0} + G_{y,i}^{\text{rect}})^2} \quad \vec{G}_i^{\text{rect}} = m_i \vec{G}_1^{\text{rect}} + n_i \vec{G}_2^{\text{rect}} \quad (3.2)$$

can be real for more orders than in the description of the parallelogram. Propagating orders also appear at different frequencies, whether one adds  $\vec{G}_1^{\text{rect}}$  or  $\vec{G}_2^{\text{rect}}$  due to their different modulus. Therefore, the transmittance or reflectance can only be calculated from the superposition of all expansion orders (fields for all  $G_i^{\text{rect}}$ ) and not be determined from the coefficients of each individual mode  $i$ . This is already true for the 0<sup>th</sup>-order and extracting transmittance and reflectance fails. In general one always has to take the smallest possible unit cell for a correct representation [56].

The physical meaning of the parallelogram is immediately visible if one compares it with the Wigner-Seitz cell. The two correspond to each other if the non-overlapping parts are translated by a lattice vector as illustrated in Fig. 3.2.

In any Fourier expansion, they correspond exactly to each other due to the relation of real space lattice vectors  $\vec{R}$  and reciprocal space lattice vectors  $\vec{G}$

$$e^{i(\vec{k}+\vec{R})\vec{G}} = e^{i\vec{k}\vec{G}} e^{i\vec{R}\vec{G}} = e^{i\vec{k}\vec{G}}. \quad (3.3)$$

Now that the link between the parallelogram and the WSC is established, the question arises how to implement the Fourier transformation. Fortunately this can be done very easily. For a square Fourier transformation equally spaced points in space are used. They can be written in terms of lattice vectors

$$\vec{r}(i, j) = \frac{i}{N} \begin{pmatrix} a \\ 0 \end{pmatrix} + \frac{j}{N} \begin{pmatrix} 0 \\ a \end{pmatrix} = \frac{i}{N} \vec{R}_1 + \frac{j}{N} \vec{R}_2 \quad i, j = 0, 1, \dots, N-1. \quad (3.4)$$

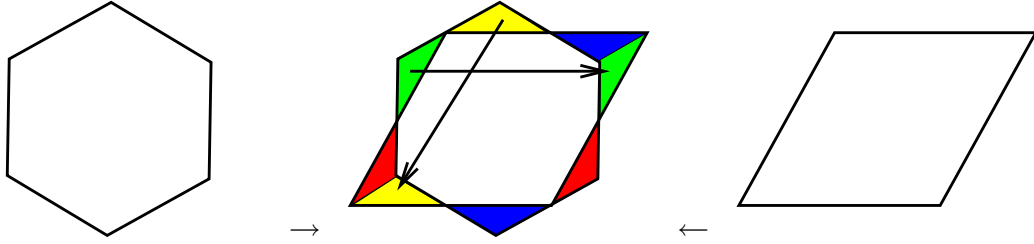


**Figure 3.2:** Translating parts of the Wigner-Seitz cell using lattice vectors leads to a parallelogram of the same area and same physical properties.

For the Fourier transformation of the parallelogram the lattice vectors have to be replaced by the ones in table 3.1 [62, 63]. Then any standard Fast Fourier Transform package can be used. In the present work FFTW [64, 65] was used which was programmed as a tool for the MIT band structure package [66], which heavily depends on Fast Fourier Transforms.

### 3.1.3 Correct Choice of Expansion Orders

Knowing the correct expansion vectors, it is important to know how many and which ones are needed. The answer to “How many ?” can only be found by increasing them until the result converges. Convergence can be checked by either looking at the differences when increasing the number of orders used or by plotting the results over the inverse number of modes  $1/N$  and extrapolating the value for  $N \rightarrow \infty$ . Increasing the modes by adding a few modes more is usually not sufficient and the comparison should be done with a significantly larger number of modes.

The truncation scheme for the expansion orders (or expansion vectors)  $\vec{G} = m\vec{G}_1 + n\vec{G}_2$  with  $\vec{G}_i$  taken from the third column for the parallelogram in table 3.1 can be selected in two different ways. In this discussion perpendicular incidence is assumed and, therefore, the in-plane wave vector  $\vec{k}$  used in the previous chapter (for a definition see eq. (2.15) or eq. (2.16)) is set to zero. However, all statements are still valid for  $\vec{k} \neq 0$ .

In the first case the expansion vectors are chosen in the range  $m = -N, \dots, N$  and  $n = -N, \dots, N$ . The resulting vectors are all located within a parallelogram. In Fig. 3.3, the expansion vectors, coefficients  $m$  and  $n$  as well as the modulus of the resulting vectors is shown. All vectors with the same magnitude are located on a circle. For a given frequency all orders inside the circle correspond to modes propagating in the  $z$ -direction, whereas all modes outside have an imaginary  $k_z$ . Assuming that modes which are further away from the center contribute less, since they strongly decay, the parallelogram is not a perfect choice. It includes many modes far from the center in the upper left and lower right corner in Fig. 3.3(b) but none of the closer modes in the upper left and lower right corner. As a consequence, each horizontal line in Fig. 3.3(c) (depicting vectors with equal modulus) may gain additional points if more orders are added.

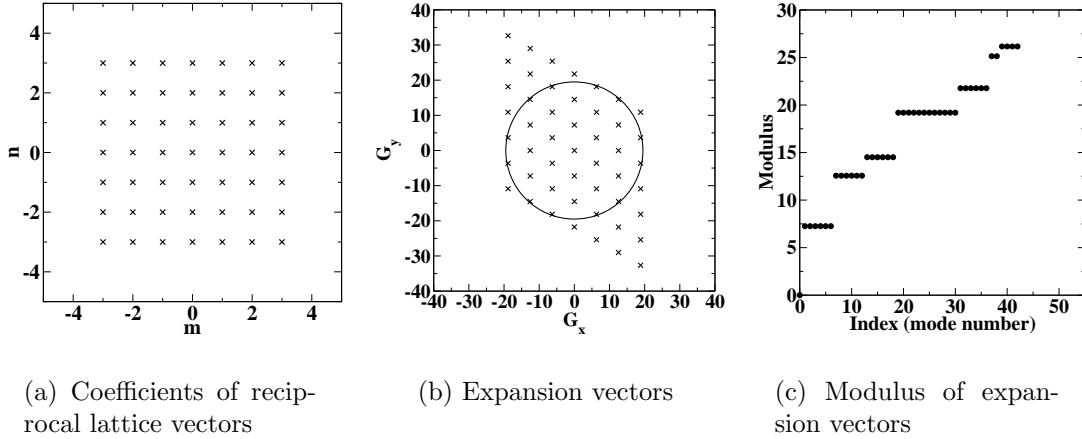


**Figure 3.3:** Selection of 49 modes in a parallelogram. Increasing  $m, n$  adds orders with different modulus of the expansion vector since they are not symmetric with respect to the origin, hence the horizontal lines in (c) can exhibit many different number of points.

This can be avoided by choosing the expansion vectors based on their modulus. The result for a similar number of expansion orders (55 instead of 49) as in the previous case is shown in Fig. 3.4. Each circle corresponds to a closed shell. In each shell, an integer multiples of 6 expansion vectors are added. This also ensures the correct implementation of the six-fold symmetry of a hexagonal lattice.

Determining the coefficients needed is not straightforward in this case. In addition the number of expansion orders can only be guessed as long as the numbers for each shell are not known. In the program the expansion vectors are determined iteratively by setting up a large array of vectors, then defining the radius of a circle and counting the number of modes therein. If this number is more than 10% off of the guessed (requested) number of expansion orders, the circle is resized and the calculation is redone.

For most calculations, this is the best method for choosing the expansion orders. However, if the symmetry of the lattice is broken, because the unit cell itself has a lower symmetry, then the parallelogramic truncation is better in the one case when the lower symmetry corresponds to the parallelogram (no circular holes but holes in the shape and alignment of the parallelogram) [56]. This is caused by the fact that all orders along the edges of the parallelogram are needed to reproduce the unit cell in real space. The convergence in terms of propagating modes would still be better in the circular truncation scheme but this would not reproduce the symmetry of the structure and, therefore, violate more important principles. In all other cases, the circular truncation is preferable.

Although it is not discussed here in detail, the same holds for the square lattice. The truncation scheme based on the circular arrangement is also preferable as long as the unit cell does not have the symmetry of a square.

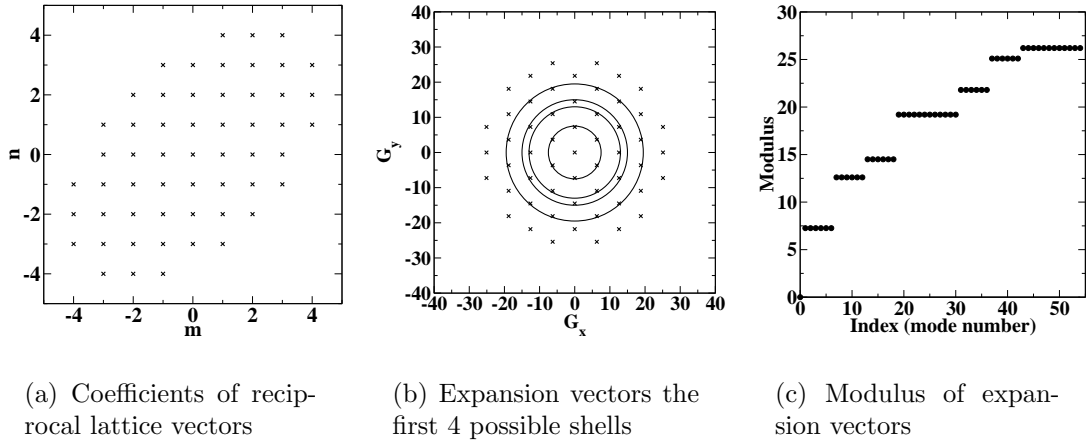


**Figure 3.4:** Selection of 55 modes in a circular array. The biggest shell corresponds to the circle in Fig. 3.3. New orders can only be added in multiples of 6. Compare the difference to Fig. 3.3(c) in the number of points for a modulus of  $\approx 25$ .

## 3.2 Representation of the Incoming Wave

The representation of the incoming wave is another important topic. In the simplest case, it can be represented by a plane wave having a frequency/wavelength, a direction defined by two angles and a polarization of the electric field. This is usually a good enough approximation for simulating the experiment<sup>2</sup>. All required parameters are easily adjustable in the experiment making the comparison of theoretical and experimental spectra straightforward.

The angles correspond to a spherical coordinate system with the zenith angle  $\theta$  and  $\phi$  being the azimuthal angle. In other words,  $\theta$  is the angle with respect to the surface normal and describes the tilting from perpendicular incidence, whereas  $\phi$  describes alignment with respect to the  $x$ -axis of the in-plane unit cell. Knowing these angles and the frequency, all components of the incoming wave vector are

<sup>2</sup>A finite beam width can be simulated by creating a superposition of waves with different  $\vec{k}$ . Using Gaussian quadratures [67] for choosing the wave vectors and corresponding amplitudes allows a correct representation of a finite (Gaussian) beam width with a small number of plane waves. This is, however, not a Gaussian beam since it's width is constant but it is suited to model e.g. a finite spot size. The transmittance/reflectance has to be calculated for each  $\vec{k}$  and summed up with the amplitudes as weight factors. The resulting fields can be plotted as a superposition of all complex fields. This approach has been implemented but is not discussed further in this work.

defined<sup>3</sup>

$$\begin{pmatrix} \vec{k}_{\parallel,\text{in}} \\ k_{z,\text{in}} \end{pmatrix} = k_{0,\text{in}} \begin{pmatrix} \sin \theta \cos \phi \\ \sin \theta \sin \phi \\ \cos \theta \end{pmatrix}, \quad k_{\text{in}} = 2\pi \omega \sqrt{\varepsilon_{\text{in}}}. \quad (3.5)$$

Once the wave vector is known, the spatial dependence is completely described by a plane wave expression

$$\vec{E}(x, y, z) = \vec{E} e^{i\vec{k}_{\text{in}} \vec{r}} e^{ik_{z,\text{in}} z}, \quad \vec{H}(x, y, z) = \vec{H} e^{i\vec{k}_{\text{in}} \vec{r}} e^{ik_{z,\text{in}} z}. \quad (3.6)$$

Please keep in mind that the  $\vec{x}$  sign describes a 2D object in case of the fields but only an in-plane( $x$ - $y$ ) object in the case of the spatial and the wave vector.

### 3.2.1 Correct Choice of Diffraction Orders

These fields can now easily be introduced into the calculation by inspecting equations (2.16) and (2.15) and replacing the wave vector around which the expansion is centered  $\vec{k}$  with  $\vec{k}_{\text{in}}$ . If the incoming layer is homogeneous, e.g. air surrounding the sample, the modes of the eigenvalue problem are plane waves and  $k_{z,0}$  corresponds to  $q_0$  in eq. (2.59).

As a consequence, it is not necessary to solve the full expansion for the electric and magnetic field defined in eqs. (2.49) and (2.52) for the coefficients. All the coefficients will be zero, except the the  $0^{\text{th}}$ -mode with  $\vec{k} = \vec{k}_{\text{in}}$  ( $\vec{G}_0 = 0$ ).

However, is not always the best choice to center the expansion around the wave vector of the incoming wave. If the parallel component of the incoming plane-wave  $\vec{k}_{\parallel}$  is outside the Brillouin zone it is then better to chose the wave vector  $\vec{k}$  for the center of the expansion inside the Brillouin zone and use the  $m^{\text{th}}$  mode with  $\vec{k} + \vec{G}_m = \vec{k}_{\text{in}}$  ( $\vec{G}_m \neq 0$ ) to describe the incoming plane-wave. Therefore, all coefficients except the one of the  $m^{\text{th}}$  mode will be zero. The expansion is then centered around the origin, since the  $0^{\text{th}}$ -mode is inside the Brillouin-zone. Together with the circular truncation discussed in the previous section, this makes sure that the considered modes are the ones closest to the origin and, therefore, the propagating ones in  $z$ -direction or at least the ones with the smallest imaginary  $k_z$ . This makes them the most important ones for energy transport through the structure. Fig. 3.5 illustrates this with a small number of modes. In the presented case even a propagating mode is lost by choosing the wrong center for the expansion.

### 3.2.2 Polarizations

Beside the wave vector, the amplitudes  $\vec{E}_{\text{in}}$  of the incoming modes have to be described. For the orientation of the incoming electric and magnetic fields, two po-

---

<sup>3</sup> $\varepsilon_{\text{in}}$  usually describes the air in the incoming are and is set to 1.0. Incorporating it allows to simulate experiments in a different environment, e.g. a solution. The difference in prefactors compared to eq. (2.3) is due to the use of rescaled variables.

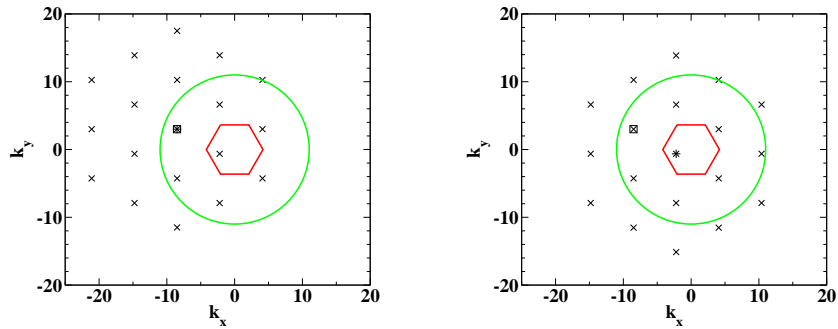


**Figure 3.5:** Expansion orders  $e^{i(\vec{k}+\vec{G})\vec{r}}$  used with the two possibilities to choose the order  $m$  and  $\vec{k}$  of the incoming wave. The square represents the  $\vec{k}_{\text{in}}$ , the star shows the center of the expansion ( $0^{\text{th}}$ -mode) and the “X”s correspond to expansion orders. The hexagon is the Brillouin-zone and the circle defines the propagating modes. On the left side the expansion is centered around the wave vector of the incoming wave  $\vec{k}_{\text{in}} = \vec{k}$ , on the right the center of the expansion  $\vec{k}$  is located in the Brillouin-zone and the  $m^{\text{th}}$ -mode with  $\vec{k}_{\text{in}} = \vec{k} + \vec{G}_m$  corresponds to the incoming wave. Only in the second case does the expansion include all propagating modes.

larizations are possible. In the homogeneous part, they remain decoupled and each wave can be described as either one or the other. The difference between the two possibilities is the alignment of the fields relative to the plane of incidence. The plane of incidence is perpendicular to the surface and includes the wave vector of the incoming wave. The angle  $\phi$  defines the orientation with respect to the  $x$ -axis. The other important reference plane is the surface, respectively the layers obtained by the slicing process. Depending on which of these reference planes is chosen, the nomenclature for the polarization is chosen differently, although the result is the same.

If one uses the plane of incidence as reference (as usually done in spectroscopy experiments) s- or p-polarization is chosen. In the numerics one prefers the layers as a natural reference system and speaks of transverse-electric (TE) or transverse-magnetic (TM) modes. The latter description is also used in the terminology of slab waveguides.

For s-type(TE) the electric field is in the plane parallel to the surface, respectively the layers used in the simulation, and perpendicular to the plane of incidence. For p-type(TM) the electric field is in the plane of incidence and the magnetic field is parallel to the surface, respectively layers. In the following, the surface/layers will be used as the reference system and TE respective TM will be employed<sup>4</sup>. The

---

<sup>4</sup>Inside the crystal a classification into TE and TM is not always possible, since the required inversion symmetry discussed in Sec.1.3.2 is missing. In most cases it is, however, possible to characterize a mode as TE-like or TM-like, depending on the ratio of the in-plane field components to the out-of-plane components.

incoming field components for TE polarization are given by:

$$E_x = 2\pi\omega\frac{\sqrt{Z}}{\mu_0 c_0}\sin\phi \quad H_x = \frac{1}{\sqrt{Z}}\cos\phi\cos\theta \quad (3.7)$$

$$E_y = -2\pi\omega\frac{\sqrt{Z}}{\mu_0 c_0}\cos\phi \quad H_y = \frac{1}{\sqrt{Z}}\sin\phi\cos\theta \quad (3.8)$$

$$E_z = 0 \quad H_z = -\frac{1}{\sqrt{Z}}\sin\theta \quad (3.9)$$

and the same for TM polarization:

$$E_x = 2\pi\omega\frac{\sqrt{Z}}{\mu_0 c_0}\cos\phi\cos\theta \quad H_x = -\frac{1}{\sqrt{Z}}\sin\phi \quad (3.10)$$

$$E_y = 2\pi\omega\frac{\sqrt{Z}}{\mu_0 c_0}\sin\phi\cos\theta \quad H_y = \frac{1}{\sqrt{Z}}\cos\phi \quad (3.11)$$

$$E_z = -\sin\theta \quad H_z = 0 \quad (3.12)$$

The impedance  $Z$  also depends on the material above the structure and is defined as  $Z = \sqrt{\frac{\mu_0}{\varepsilon_0\varepsilon_{\text{in}}}}$ .

For determining the reflectance and transmittance coefficients, the absolute value of the incoming amplitude is not of importance but the relative amplitudes between the electric and magnetic field, given by the Maxwell equations in rescaled units (eqs. (2.11)–(2.14)), must be correct.

Since the expansion of both fields is done with the same expansion coefficients  $a_n$  (compare eq. (2.49) and eq. (2.52)) setting the coefficient to 1.0 for the correct order/expansion mode insures the correct ratio.

However, the sorting of eigenmodes is not unique in the numerics and, therefore, it is not obvious, which eigenvector corresponds to the correct eigenmode<sup>5</sup>. As a consequence, one can not set the coefficient of a specific mode but has to solve either problem eq. (2.50) or eq. (2.52) for the coefficient vector  $a$  at the top ( $z = 0$ ) of the structure or determine the mode in a different way.

So far, only linearly polarized light has been considered. Using superposition, other polarization can be used as well, e.g. circular polarized light can be achieved by adding a TM-polarized wave with amplitude  $A$  and a TE-polarized wave with the same amplitude and a phase factor  $Ae^{i\frac{\pi}{2}}$ . Inserting the superposition in the complex input amplitudes returns the corresponding transmittance and reflectance coefficients.

---

<sup>5</sup>For the 0<sup>th</sup>-order the mode can still be extracted but any other mode depends on the sorting of the eigenmodes. For perpendicular it is obvious since all eigenvalues of the 6 first order modes are the same and no sorting criterion exists.

### 3.3 Transmittance and Reflectance Coefficients

For the calculation of the reflectance and transmittance coefficients, the energy flux perpendicular to the surface is required. This quantity is given by the  $z$ -component of the Poynting vector in the far field without the contributions of the evanescent diffraction orders

$$\vec{S} = \frac{1}{2} \vec{E} \times \vec{H}^* \quad \Rightarrow \quad S_z = \frac{1}{2} E_x \cdot H_y^* - E_y \cdot H_x^*. \quad (3.13)$$

From the Poynting-vector in eq. (3.13) it is evident that the  $z$ -component depends only on the in-plane components of the fields, which are readily available in the calculations, so that no additional calculations are necessary.

Using the scattering matrix, the amplitudes of the backward propagating modes in the input region (reflected) and the forward propagating in the output region (transmitted) can be calculated using eq. (2.99). Inserting these amplitudes into the field representation eq. (2.54) leads to the final vector containing the amplitudes for each Fourier expansion order for arbitrary values of the  $z$ -coordinate. However, several aspects have to be considered in this step.

A nice feature of the homogeneity in these areas is the decoupling of all modes and the resulting simple eigenvectors, which each only contain a single entry, corresponding to a plane wave as discussed in Sec. 2.2. This allows for an easy interpretation and makes it possible to compare the transmittance/reflectance for each order individually. The cross-product can, therefore, be evaluated by multiplying the electric and magnetic field using the corresponding entries in the Fourier-vectors. As a consequence one obtains a vector in which the entries correspond to the  $z$ -components of the Poynting vector for individual diffraction orders.

It is not even necessary to solve for all the fields in eq. (2.99). Since the incoming wave consists of only one mode in general, the Poynting vector is known. Assuming no incoming wave from the back, the backwards propagating mode in the output region is known to be zero as well. The only required components are the reflected wave, with the electric field components given by the product of  $\hat{f}_{\text{in}}(d_{\text{in}} - z)b_{\text{in}}$  with the upper right submatrix of the  $M$ -matrix using the quantities in the incoming region. The magnetic field is given by using the lower right submatrix. Analogously the transmitted modes are given by the product of  $\hat{f}_{\text{out}}(z)a_{\text{out}}$  with the upper, respectively lower, left submatrix of the  $M$ -matrix in the outgoing region.

So far the value for  $z$  is not specified. For the far field,  $z$  should be as small as possible in the incoming region and as big as possible in the outgoing region. Although these layer have a finite width in the calculation, which limits the range of  $z$  in principle, any value for  $z$  can be used, since this thickness is only needed to fix a coordinate system for the layers in the calculations. The far field can be represented better by suppressing all evanescent modes in the construction of the  $M$ -matrix from the beginning. This can be done by setting all eigenvectors with an imaginary part in the eigenvalue (propagation constant in  $z$ -direction) to zero. The resulting  $M$ -matrix is sparse and the multiplication with the amplitudes results only

in non-zero values in the Fourier-vector of the fields if the corresponding order in the Rayleigh expansion is propagating. The value for  $z$  can then be chosen arbitrarily and leads only to a phase in the field amplitudes but does not change transmittance or reflectance.

At this stage, the vector containing the  $z$ -component of the Poynting-vector for the different orders is known for the incoming, reflected and transmitted wave. All components still have to be normalized to the incoming energy flux. The resulting vector of transmittance and reflectance coefficients does by itself not provide enough information for interpreting the results since the ordering of the reciprocal lattice vectors and thus the corresponding modes are not known. It is not even known which lattice vectors were chosen in the selection process described in Sec. 3.1.3. In addition, the incoming mode might have been folded back as described in Sec. 3.2.1.

During the calculation of the incoming wave representation, the position of it in the Fourier-vector is saved and the transmittance and reflectance of it can be identified immediately. All other modes need to be characterized now.

There are two possible approaches. Either the results for a specific mode is required. In this case, the reciprocal lattice vector for this mode is known and the transmittance and reflectance can be found by comparing the lattice vector with the list of the vectors used in the expansion giving the position in the Fourier-vector of the resulting fields.

Alternatively, the diffraction pattern in real space should be calculated. In this case, it is possible to calculate the  $\vec{k}$  for all propagating modes using the list of reciprocal lattice vectors and use the eigenvalues  $q = k_z$  for each mode to calculate the diffraction angles  $\phi$  and  $\theta$  for each mode to add them to the output. This is also necessary if a detector with a solid-angle for detection should be modeled. In this case, only modes entering the cone defined by the detector are measured. Comparing the direction of the diffracted wave with the detector position allows for ruling out the wrong ones.

Additional information about the transmittance properties can be gained by looking at the fields instead of the Poynting-vector. Since the Poynting-vector is the product of the transposed magnetic field and the electric field and both fields experience the same scattering, their phases cancel each other in the propagating case.<sup>6</sup> Therefore, all phase information is lost and can only be obtained using the fields. If the incoming modes are chosen with real amplitudes the phase shift is given by

$$\Phi = \arctan \left( \frac{\text{Im}E_i}{\text{Re}E_i} \right) = \arctan \left( \frac{\text{Im}H_i}{\text{Re}H_i} \right), \quad i = x, y. \quad (3.14)$$

---

<sup>6</sup>The imaginary part of the propagation constant of the evanescent modes would enter twice into the Poynting-vector.

## 3.4 Optimization

In the previous sections of this chapter, the correct representation of the physical system was discussed without taking into account efficiency. Of course using the correct expansion reduces the number of modes needed for convergence and, therefore, enhances efficiency.

Beside choosing the correct expansion, several strategies can be used to optimize the method for speed or minimal memory consumption. Solving standard numerical problems, e.g. the eigenvalue problems, is not discussed here, since for all matrix operations efficient standard libraries are used. Matrix multiplications and other linear algebraic operations are done using LAPACK [68] and fast Fourier transforms using FFTW [64, 65].

Beside the optimization of the numerical methods, the structure of the program can be adjusted to save memory for calculations that require many modes or layers, or to avoid doing the same calculations twice. The different options will be discussed for one numerical unit cell of the crystal in the  $z$ -direction. Calculation of crystals with a length of several of these unit cells will be discussed later. In addition, the parameters for the incoming wave (angles, frequency) are fixed to one set of parameters, although remarks will highlight (dis-)advantages if, for example, the frequency is changed. For changing any other property, such as angles, the remarks hold as well.

### 3.4.1 The Simple Approach

The conceptually easiest approach is based on doing the calculations of all intermediate steps for each layers. This is very easy to do, since all steps can be placed into one function and arbitrary layers can be treated very easily. All subtleties could be hidden in a class for the layers.

```
for all layers
{
  calculate  $\hat{\epsilon}$ 
  set up eigenproblem
  solve eigenproblem
  create  $M$ -matrix
  create inverse  $M$ -matrix
}

calculate  $S$ -matrix          using stored  $M_l$ ,  $M_{inv,l}$  and eigenvalues
                           of all layers  $l$ 
```

In a second step the  $S$ -matrix can be calculated easily using the stored  $M$ -matrices, their inverse and the eigenvalues of all layers. However this needs tremendous memory, since the two matrices and the eigenvalues and eigenvectors need to be stored. In addition  $\hat{\epsilon}$  would be recalculated each time, although it is independent of the

frequency of the incoming wave, as long as the material is not dispersive. Clearly this method is simple but requires a lot of memory.

The same is true for a setup in which each operation is done for all layers:

calculate $\hat{\varepsilon}$	for all layers
set up eigenproblem	for all layers
solve eigenproblem	for all layers
create $M$ -matrix	for all layers
create inverse $M$ -matrix	for all layers
calculate $S$ -matrix	using stored $M_l$ , $M_{\text{inv},l}$ and eigenvalues of all layers $l$

Again this would lead to a very easy implementation that requires a lot of memory. However, the frequency independent  $\hat{\varepsilon}$  could be calculated once and only the following steps would have to be redone, if the frequency is changed.

### 3.4.2 Avoiding Large Memory Requirements

The large amount of memory can be reduced by executing the operations in a specific order. In each step of the loop over the layers only one  $\hat{\varepsilon}$ , one  $\hat{\eta}$ , one  $M$ -matrix and one inverse  $M$ -matrix is needed at a time. Only the eigenvalues are needed for two layers. For reasons discussed in the next chapter, it is still preferable to store the  $\hat{\varepsilon}$ - and  $\hat{\eta}$ -matrices for all layers.

Assuming that layer  $l$  has been solved and the inverse  $M$ -matrix and the eigenvalues, as well as  $S(0,l)$  are available, the  $S$ -matrix can be advanced to  $S(0,l+1)$  by the following steps<sup>7</sup>:

set up eigenproblem	for layer $l+1$
solve eigenproblem	for layer $l+1$
create $M$ -matrix	for layer $l+1$
calculate $I$ -matrix	using $M_{\text{inv},l}$ and $M_{l+1}$
advance to $S(0,l+1)$	using $I$ -matrix, $S(0,l)$ , eigenvalue $_l$ and eigenvalue $_{l+1}$
create inverse $M$ -matrix	for layer $l+1$

Now the step can be repeated for layer  $l+2$  and the memory usage is minimized. Only one minor problem is still existing.

The routine for the calculation of the  $S$ -matrix requires the following arguments which in the function call have to be listed exactly in this sequence

- old  $S$ -matrix  $S(0,l)$  (on output: new  $S$ -matrix  $S(0,l+1)$ )

<sup>7</sup>The calculation of  $\hat{\varepsilon}$  is ignored in this section. At the moment it is assumed that it is either known (stored) or calculated during the setup of the eigenvalue problem

- $I$ -matrix
- eigenvalues of layer  $l$
- eigenvalues of layer  $l + 1$

and this is placed inside a loop over all layers, the eigenvalues have to be treated with care. In each step of the loop, the 4<sup>th</sup> argument has to be the eigenvalues of the current layer and the 5<sup>th</sup> argument has to be the eigenvalues of the next layer. In addition, the other variables also have to correspond to the correct layers in each step of the loop.

For the  $M$ -matrix this poses no problem, since the inversion of  $M_{l+1}$  is done after advancing the  $S$ -matrix, when the previous  $M_{inv,l}$  is not required anymore. Also  $M_{l+1}$  is not needed in the next step and can be overwritten by  $M_{l+2}$  upon solving the next eigenvalue problem. For the eigenvalues this is not the case since they need to swap positions in subsequent steps of the layer loop. The eigenvalues, which were the 4<sup>th</sup> argument in the current step have to be the 5<sup>th</sup> argument in the next step. Inside a loop the variables can, however, not be renamed, since the function call always uses the same variables. A simple approach to this problem would be to copy the eigenvalues at the end of each recurrence step. The copying process can be avoided by using pointers and decoupling the physical position of the eigenvalues in the memory from the name of the variable pointing to it as illustrates in the following boxes. The terms “memA” and “memB” correspond to the positions in memory and “point1” and “point2”, respectively, are pointers to these positions in memory. The main aspect in the following is that the positions to which the pointers are pointing can be changed without changing the content in the physical memory. The brackets combine pairs of associated position in memory with the pointer for the depicted eigenvalue.

In the  $l^{th}$ -layer, the following quantities are known:  $S(0, l)$ ,  $M_{inv,l}$  and the known eigenvalue is given by:  $eigenvalues_l$  (memA, point1) The pair (memB, point2) contains no required information and can be used in the next eigenvalue problem.

set up eigenproblem	for layer l+1
solve eigenproblem	for layer l+1
	→ $eigenvalues_{l+1}$ (memB, point2)
create $M_{l+1}$	
calculate $I(l, l+1)$	using $M_{inv,l}$ and $M_{l+1}$
advance to $S(0, l+1)$	using $I$ -matrix, $S(0, l)$ , point1, point2
create $M_{inv, l+1}$	
swap pointers	→ $eigenvalues_{l+1}$ (memB, point1)

Now the following quantities known:  $S(0, l+1)$ ,  $M_{inv, l+1}$  and the known eigenvalues is given by:  $eigenvalues_{l+1}$  (memB, point1). The pair (memA, point2) contains no required information and can be used in the next eigenvalue problem.

set up eigenproblem	for layer l+1
solve	for layer l+1 → eigenvalues <sub>l+2</sub> (memA, point2)
create $M_{l+2}$	
calculate $I(l+1,l+2)$	using $M_{inv,l+1}$ and $M_{l+2}$
advance to $S(0,l+2)$	using $I$ -matrix, $S(0,l+1)$ , point1, point2
create $M_{inv,l+2}$	
swap pointers	→ eigenvalues <sub>l+2</sub> (memA, point1)

Giving:  $S(0,l+2)$ ,  $M_{inv,l+2}$ , eigenvalues<sub>l+2</sub> (memB, point1) and the position of the eigenvalues is given by: memA (point1) eigenvalues<sub>l+2</sub> and memB (point2) free.

The ongoing use of this recursion always keeps the pointers used in advancing the  $S$ -matrix fixed, so that the function call can be implemented in a simple loop over all layers. In each step the eigenvalues of the current layer ( $l+1$  in the  $2^{nd}$  box) are kept and eigenvalues of the previous layer ( $l$  in the  $2^{nd}$  box) are overwritten by the eigenvalue of the next layer ( $l+2$  in the  $2^{nd}$  box), reducing the required memory to a minimum and avoiding copying large matrices.

For the  $M$ -matrices the same situation occurs. At all points in time, only the two required matrices ( $M_{l+2}$  and  $M_{inv,l+1}$  in the  $2^{nd}$  box) are stored, and the inversion after calculating the next  $S$ -matrix avoids copying again, since  $M_{inv,l+1}$  can be discarded as well as  $M_{l+2}$ .

### 3.4.3 Storage of $\hat{\varepsilon}/\hat{\eta}$

In the previous, section the dielectric Toeplitz-matrices  $\hat{\varepsilon}$  and  $\hat{\eta}$  did not appear because they need some special thought as well. If one does calculations for several frequencies (or angles) these matrices are the only quantities that don't change. Therefore, it would make sense to calculate them once and then re-use for each frequency. This, however, requires more memory since they have to be stored for all layers.

To be flexible, these matrices have been implemented into the layer class but are usually not initialized and are only a pointer to NULL space. In the routine for calculating the  $S$ -matrix the Toeplitz-matrices are required. They can now be calculated for each layer during the recursion or be copied from the layer class if they have been set before. Hence, it is possible to chose between faster calculation for systems using only a few layers, or for memory saving for computers with limited memory and/or large systems.

### Adaption to Dispersive Constituent Material

Even for dispersive materials, the usage of  $\hat{\varepsilon}$  and  $\hat{\eta}$  can be optimized. On first sight, the Fourier expansion has to be done for each frequency, since the transform of a composite system, e.g. holes in a substrate, can not be manipulated to reflect

changes in the dielectric material, except if the dielectric material change by the same factor  $\alpha$  in all regions of a layer

$$\alpha \cdot \tilde{\epsilon}(n') = \int d\vec{r} \alpha \cdot \epsilon(x, y) e^{-i\vec{G}_{n'}\vec{r}}. \quad (3.15)$$

Fourier transforms can, however, be added, since they are linear

$$\tilde{\epsilon}_1(n') + \tilde{\epsilon}_2(n') = \int d\vec{r} (\epsilon_1(x, y) + \epsilon_2(x, y)) e^{-i\vec{G}_{n'}\vec{r}}. \quad (3.16)$$

This property can be used to avoid the re-calculation of the Toeplitz-matrices in the case of dispersive material.

Fig 3.6 illustrates the idea for a hole ( $\epsilon = \epsilon_b$ ) in a dispersive substrate with  $\epsilon_a(\omega)$ . First the unit cell is separated in a homogeneous unit cell with the dielectric constant

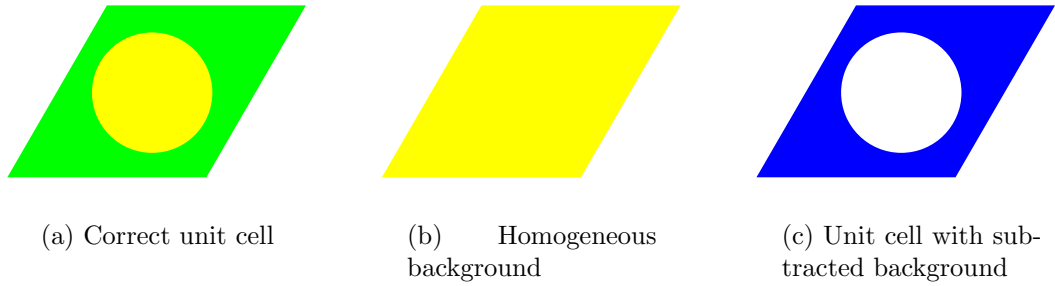


**Figure 3.6:** Representation of a unit cell with 2 materials  $\epsilon_a$ (blue) and  $\epsilon_b$ (yellow) (a). This unit cell can be represented by the sum of a homogeneous background (b) and the unit cell with subtracted background (c). In (c) the values for the dielectric constants are  $\epsilon_c = 0.0$ (white) and  $\epsilon_d = \epsilon_a - \epsilon_b$ (green). If the Fourier transform of (c) is calculated with  $\epsilon_d = 1.0$  it can be scaled to arbitrary values for the dielectric constant of the substrate. The Toeplitz-matrix of (b) is a diagonal matrix containing only  $\epsilon_b$ .

of the hole (background). Using eq. (3.16), a unit cell representing the difference to the original one has to be added. This is a very suitable unit cell for scaling. Since the dielectric constant in the area of the hole is 0.0 now, the scaling in eq. (3.15) can be applied to the entire unit cell and the Fourier expansion of Fig. 3.6(c) for arbitrary values of  $\epsilon_d$  can be calculated once it is done for an example, e.g.  $\epsilon_d = 1.0$ . The Toeplitz-matrix of the homogeneous unit cell can be written down immediately since it is a diagonal matrix only containing  $\epsilon_b$ . Therefore, this approach does not add any significant calculation time for dispersive materials. In this form, the approach can be used for arbitrary shaped unit cells, which contain two materials with one being frequency independent (e.g. air holes). For more complicated layers, the original unit cell has to be broken down into individual unit cells, which only contain one material or regions with  $\epsilon = 0.0$  for the scaling to work.

### 3.4.4 Long Structures Using a Numerical Unit Cell

In the previous sections, the structures have been described by a number of layers, which provided a discretization in the  $z$ -direction. Using this staircase approximation, any structure can be represented. However, in most cases it is not necessary to slice the complete crystal. Often recurrent parts in the  $z$ -direction exist, which define a 3D numerical unit cell, given by the in-plane unit cell of the lattice and the repeating section in the vertical direction. This unit cell usually does not correspond to a crystallographic unit cell. Correspondence can only be achieved if the ends of the crystallographic unit cell correspond to numerical layers. Whether this is possible depends not only of the unit cell itself but also on the alignment of it with respect to the  $z$ -direction. For example, even for a simple cubic unit cell, alignment of the  $z$ -axis along the diagonals of the cube leads to a crystallographic unit cell which does not end parallel to the layers. However, the numerical unit cell can still be used.

In order to simulate a long crystal with many repeating identical unit cells in the vertical direction, only the  $S$ -matrix of a numerical unit cell is needed, which from now on will be called  $S_{\text{Unit}}$ . This  $S$ -matrix connects the fields in the first layer of the numerical unit cell (labeled 1) with the last layer ( $N$ ).

The crystal can then be simulated by “multiplying” several of these matrices together. As always with  $S$ -matrices, this multiplication is only meant conceptually. Comparing with eq. (2.90) shows that in order to multiply two  $S$ -matrices, they have to be in the same layer ( $l$  in the discussed case in Sec. 2.4.2). This is not the case for  $S_{\text{Unit}}$ , so another matrix is needed to connect the  $N^{\text{th}}$ -layer with the  $1^{\text{st}}$ . This matrix is called  $S_{\text{Loop}}$ . Using a combination of these two makes it possible to build long crystals by using the  $S$ -matrix multiplication. Further improvement can be achieved by exponentiating the matrix. Since by exponentiating only powers of two can be achieved ( $S \cdot S = S^2 \rightarrow S^2 \cdot S^2 = S^4 \rightarrow \dots$ ) a better scheme is needed.

In the implementation 3 variables are used to create arbitrary length with only a few multiplications. The total length and  $S$ -matrix multiplications are given by

$$L = a \cdot 2^b + c, \quad (3.17)$$

$$S_L = \underbrace{(S \cdot \tilde{S} \dots \tilde{S})^b}_a \cdot \underbrace{(\tilde{S} \cdot \tilde{S} \dots \tilde{S})}_c \quad (3.18)$$

with  $\tilde{S}$  representing the combination of  $S_{\text{Loop}}$  and  $S_{\text{Unit}}$  ( $\tilde{S} = S_{\text{Unit}} \cdot S_{\text{Loop}}$ ).

The number of total operations is then given by  $a + b + c$ . In most simulations  $L$  is known and  $a, b$  and  $c$  can be optimized and placed in a list to choose from automatically. For the general case  $a, b$  and  $c$  need to be determined. This has been done by choosing  $c$  so that  $L - c$  can be divided by 4, then determining  $b$  and, finally,  $a$ . Depending on the length ranges the 4 should be increased for better results.

In comparison with straightforward slicing, the method of multiplying unit cell has one big disadvantage. The beginning(top) of the crystal and the end(bottom) are fixed by the unit cell boundaries. In addition, the unit cell does not incorporate

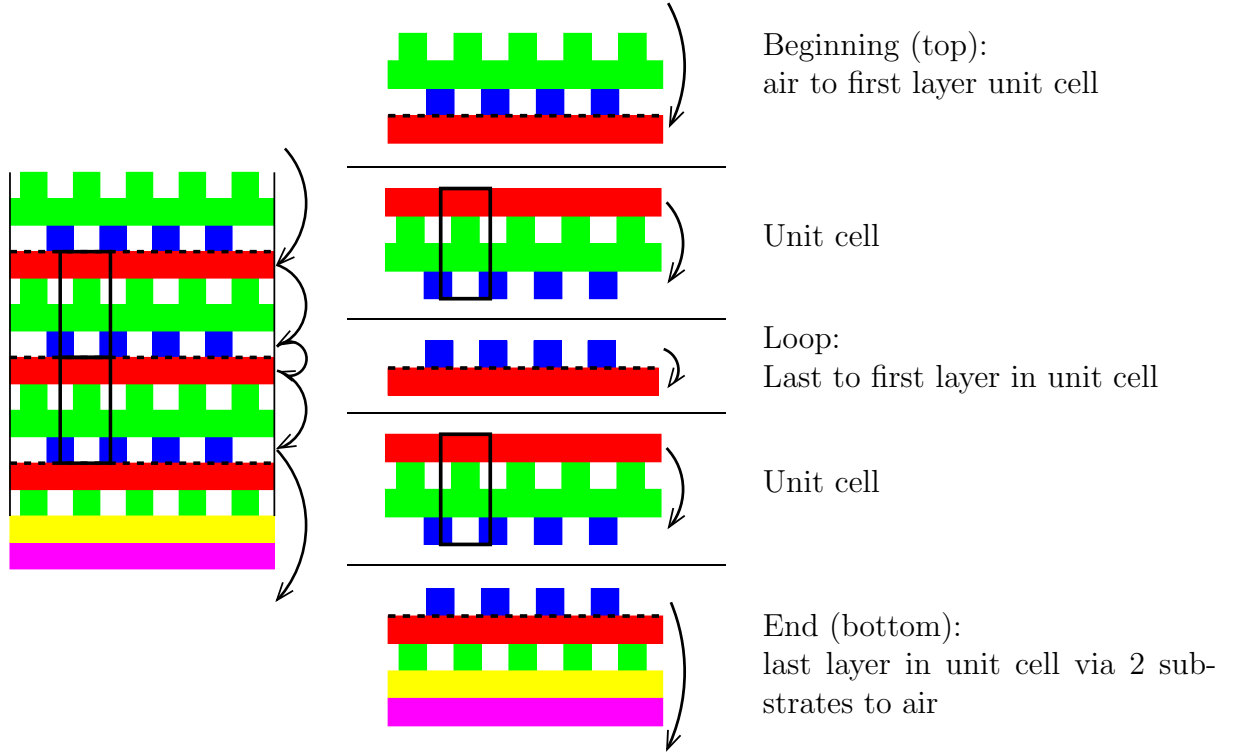


**Figure 3.7:** Representation of a crystal with finite length using  $S_{\text{Begin}}$ ,  $S_{\text{Unit}}$ ,  $S_{\text{Loop}}$  and  $S_{\text{End}}$ . On the left the crystal is shown and the right shows the corresponding partition into different units. Since the multiplication of  $S$ -matrices requires them to be in the same layer, all end layers occur in two  $S$ -matrices. The black boxes represent a unit cell made out of 4 layers, e.g. a woodpile structure. The dashed lines indicate unit cell boundaries. The different colors illustrate the ordering of the layers in the unit cell. The two last layers can represent an adhesion layer and a glass substrate. The length of the crystal can be increased by inserting pairs of  $S_{\text{Loop}}$  and  $S_{\text{Unit}}$ . For optimization  $S_{\text{Loop}}$  and  $S_{\text{Unit}}$  should be combined into one matrix.

the air above and below the crystal as well as possible adhesion layers or glass substrates.

Therefore, beside  $S_{\text{Unit}}$  and  $S_{\text{Loop}}$  two more building blocks for arbitrary crystals are needed:  $S_{\text{Begin}}$  and  $S_{\text{End}}$ . These matrices relate the modes in the incoming, respectively outgoing, area with the unit cell.

In both cases, additional layers can be included to model e.g. parts of a unit cell on top or additional layers on top of the bottom. If the crystal only contains complete unit cells,  $S_{\text{Begin}}$  and  $S_{\text{End}}$  are still needed to couple from the air region above to the crystal or from the crystal to the region below. Fig. 3.7 shows an example for an entire crystal containing all four  $S$ -matrices.

If the top, respectively bottom part is the same as the unit cell and only contains parts of it  $S_{\text{Begin}}$  ( $S_{\text{End}}$ ) can be calculated parallel to  $S_{\text{Unit}}$  by using only parts of the layer loop. In general it is necessary to decide individually for each problem what

approach is the best depending on the number of unit cells, length of the crystal and surface termination.

### 3.4.5 Fields

In order to calculate the fields inside the crystal, eq. (2.97) has to be solved for the amplitudes  $a_l$  and  $b_l$  of the modes in the  $l^{\text{th}}$ -layer. Before solving the amplitudes, the scattering matrices  $S(\text{in}, l)$  and  $S(l, \text{out})$  have to be calculated. If the crystal is composed of several unit cells, one has to do a similar calculation as discussed in the section about long crystals (Sec. 3.4.4), but this time the incoming area has to be related to the  $l^{\text{th}}$ -layer in the unit cell, in which the fields are calculated.

For the fields in the  $m^{\text{th}}$ -unit cell of a crystal with a total Length of  $L$  unit cells, the following  $S$ -matrix-multiplications are needed

$$S(\text{in}, l) = S_{\text{Begin}} (S_{\text{Unit}} S_{\text{Loop}})^{m-1} S(0, l), \quad (3.19)$$

$$S(l, \text{out}) = S(l, N) (S_{\text{Loop}} S_{\text{Unit}})^{L-m} S_{\text{End}}. \quad (3.20)$$

The scheme is illustrated for  $L = 2$ ,  $m = 2$  in Fig. 3.8 and Fig. 3.9.

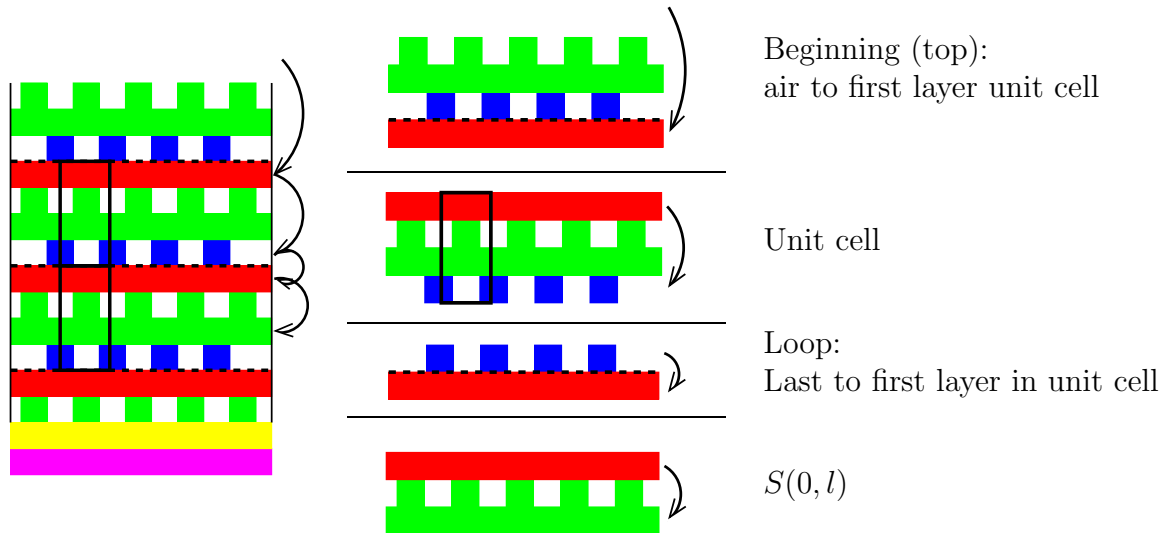


**Figure 3.8:** Using  $S_{\text{Begin}}$ ,  $S_{\text{Unit}}$ ,  $S_{\text{Loop}}$  and the matrix  $S(0, l)$ , relating the  $l^{\text{th}}$  layer with the beginning of the unit cell to calculate the scattering matrix relating the incoming area with the layer  $l$  in which the fields are determined. For longer crystals additional combinations of  $S_{\text{Unit}}$  and  $S_{\text{Loop}}$  must be inserted to propagate the fields to the correct unit cell.

Using the  $S$ -matrices and eq. (2.97) one can obtain the Fourier components of the in-plane components of the electric and magnetic field by inserting the coefficients in the equations for the fields (2.54). The corresponding fields at each point in space can then be calculated by summing up the Fourier expansion with the correct

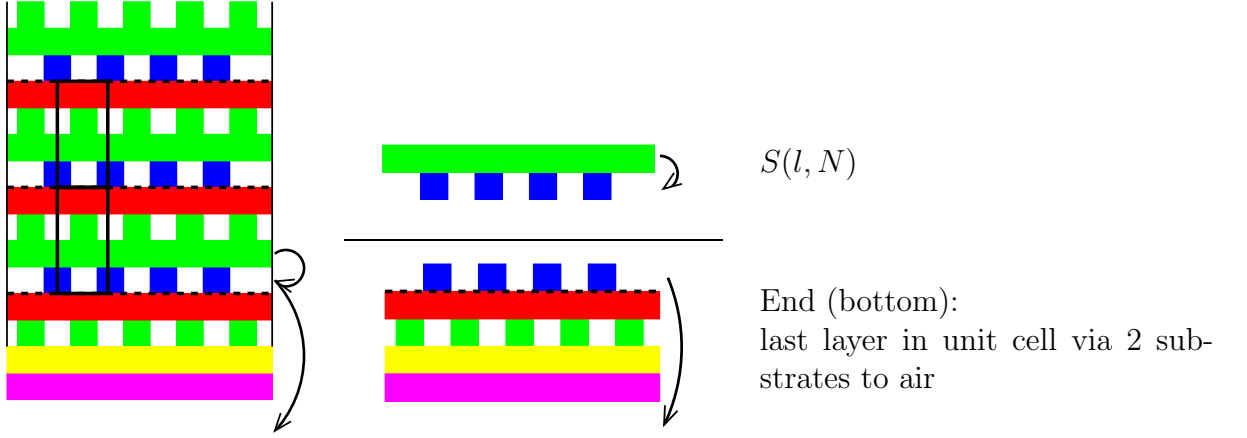


**Figure 3.9:** Using  $S_{\text{End}}$  and the matrix  $S(l, N)$ , relating the  $l^{\text{th}}$ -layer with the last layer of the unit cell, to calculate the scattering matrix relating the  $l^{\text{th}}$ -layer in which the fields are determined with the region below the structure. If the fields are not calculated in the last unit cell of the crystal, additional combinations of  $S_{\text{Unit}}$  and  $S_{\text{Loop}}$  must be inserted.

exponential factors

$$H_{\parallel(l,m)}(\vec{r}, z) = \sum_{\vec{G}} h_{\parallel(l,m)}(z, \vec{G}) e^{i(\vec{k} + \vec{G})\vec{r}}. \quad (3.21)$$

The  $z$ -component of the magnetic field can then be calculated by using eq. (2.31) with the eigenmodes, coefficients and eigenvalues of the corresponding layer. The indices for the layer  $(l, m)$  are dropped for simplification.

$$H_z(\vec{r}, z) = \sum_{\vec{G}} \left[ (K_x + G_x) h_{z,x}(z, \vec{G}) + (K_y + G_y) h_{z,y}(z, \vec{G}) \right] e^{i(\vec{k} + \vec{G})\vec{r}} \quad (3.22)$$

with

$$h_{z,x}(z) = - \sum_n \frac{1}{q_n} \Phi_x (e^{iq_n z} a_n + e^{-iq_n(z-d)} b_n), \quad (3.23)$$

$$h_{z,y}(z) = - \sum_n \frac{1}{q_n} \Phi_y (e^{iq_n z} a_n + e^{-iq_n(z-d)} b_n). \quad (3.24)$$

Alternatively, the Fourier components can be calculated using equation (2.27)

$$h_{z,\vec{G}} = - \frac{1}{2\pi \omega \mu_0 c} \left( \hat{k}_x e_y(z, \vec{G}) - \hat{k}_y e_x(z, \vec{G}) \right) \quad (3.25)$$

with  $e_x, e_y$  being the components of  $e_{\parallel}$  and  $\hat{k}_x, \hat{k}_y$  the diagonal matrices defined in Chapter 2. The field is then given by eq. (3.21) with  $h_{\parallel}$  replaced by  $h_z$ . Using eq. (2.30) or eq. (2.36) the same can be done for the electric field.

### 3.4.6 Implementation of the Fourier Transform

Beside the physical aspect of the Fourier transform discussed before, its implementation is another important part.

FFTW is very efficient, because it adapts the Fourier-transform to the available hardware. This adaption requires some time and needs to be done every time a program is started if the underlying hardware is not consistent. The simulations presented later are done on two different Clusters at the Universität Karlsruhe (Germany) and University of Central Florida in Orlando, FL (USA) containing several different types of computational nodes and on several desktops, so that the underlying hardware is very diverse.

One of the requirements of FFTW is a constant position in the physical memory for the array containing the points in real space and for the array with the values of the Fourier-transform. As a consequence, this array has to be created in the beginning and cannot be changed throughout the execution of the program or the optimization has to be done again. Using a class, this can be implemented easily. However there are some other things to look at using FFTW. Although the claim of the authors is that there are no restrictions on the number of points in real space<sup>8</sup>, some differences are found. In addition, the real space points have to be selected on a suitable grid. As a test, a symmetric unit cell containing only real dielectric functions can be implemented. For this setup, the Fourier-coefficients can be completely real and for specific geometries they can be calculated analytically. In case of holes on a hexagonal lattice ( $\varepsilon_h$  with radius  $\rho$ ) in a substrate ( $\varepsilon_s$ ) they are given by

$$\begin{aligned}\varepsilon(\vec{G}) &= 2(\varepsilon_h - \varepsilon_s) f \frac{J_1(G\rho)}{G\rho} & \vec{G} \neq 0, \\ \varepsilon(\vec{G} = 0) &= \varepsilon_h f + \varepsilon_s(1 - f)\end{aligned}\quad (3.26)$$

with the filling fraction  $f = \frac{2}{3}\sqrt{3}\pi\frac{\rho^2}{a^2}$ .

Especially the canceling of the imaginary part is a suitable measure for the correctness of the Fourier transform. With a Monkhorst-Pack mesh [69] or a mesh which includes points at all boundaries of the unit cell, a purely real Fourier-coefficient can not be obtained, except if a very large number of real space points is used. For a grid, for which the points start at the lower left corner of the 2D lattice unit cell and end one point before the end the unit cell, so that the points on the edge of the unit cell don't enter twice through periodicity, the imaginary parts of Fourier coefficients are zero with numerical accuracy ( $10^{-15}$ ).

In all three cases, the inverse Fast Fourier transform, using *all* reciprocal points in FFTW, leads to an exact reproduction of the previously used real space points. Also the reconstruction using only a limited number, e.g. the number of orders kept in the expansion of the fields, does not show significant differences. But only in the

---

<sup>8</sup>The results is supposed to be unaffected but the required computation time strongly depends on the number of used points.

third case above, the Fourier coefficients fulfill the expectations for a symmetric unit cell.

The difference can be explained by looking at the Monkhorst-Pack mesh compared to the grid starting at the edge. They are shifted by half the distance of the points in real space. A shift by  $\vec{r}_0$  leads to a phase  $e^{-i2\pi \vec{G}\vec{r}_0}$  which would explain why the coefficients are not purely real and why the difference decreases with the number of real space points used in the transform.

Also the total number of real space points used should be carefully checked and in principle as many points as possible should be taken. The most efficient number of real space points for FFT would be an exponential of 2 but to achieve purely real values, an odd number of points had to be taken. An oversampling of 2 (twice as many points in real space as expansion orders needed) as required as a minimum by the sampling theorem (see e.g. [67]) is not good enough for convergence. Good results were achieved with five times more points in real space than total modes in each direction, corresponding to a total of roughly 25 times more points in real space than total modes in the field expansion. In the Toeplitz-matrix, twice the number of modes of the fields occurs  $(-2N, \dots, +2N)$ , so that the oversampling is only about 10 times.

It should also be noted that the FFTW transformation is not normalized, so that a forward- followed by a backward-transformation yields a factor of  $x$ -dimension  $\cdot$   $y$ -dimension, so that this normalization has to be included in the implementation of the transform.

### 3.4.7 Homogeneous Eigenvalue Problem

For faster calculations, the parts of the problem which can be solved analytically, should be implemented using the analytical solution.

This is the case for all homogeneous layers, which were solved in Sec. 2.2. Incoming and outgoing layers as well as e.g. glass substrate layers can be implemented using the analytical solution and the solution of the eigenvalue problem can be avoided. All the matrices are diagonal in this case, and, even without knowing the ordering, can be solved row by row, yielding the eigenvalues and eigenvectors with only one entry in the corresponding row.

Layers in the numerical unit cell have to be treated with more care. Since the number of layers might change it is not straightforward to say that the  $n^{th}$ -layer is homogeneous. During the setup of the layers, the program package has to mark layers as being homogeneous or not by a flag in the layer class, so that eigenvalue problem solver can use the regular version or the optimized one for homogeneous layers. For many structures for which the distribution of the constituent material is given implicitly by e.g. a threshold formula as in Chapter 6, this cannot be done<sup>9</sup> and the full routine has to be used.

---

<sup>9</sup>It could, of course, be done by analyzing the Fourier coefficients but since most layers will not be homogeneous, this has been omitted and only known homogeneous layers are treated as such.

## 3.5 Implemented Options

The second part of this chapter illustrates the possibilities of the program package by listing most of the implemented options. Since the only limit on the structure is its periodicity in the  $x$ - $y$ -plane, many structures are possible, each requiring parameter to describe the size, distribution of material, etc. They depend on the individual structure and are not discussed here. The discussion is limited to general parameters and their handling.

### 3.5.1 Frequency and Wavelength

In theoretical studies, one always uses dimensionless units as introduced in Sec. 1.3.3 and all quantities are scaled, so that the lattice parameter represents the unit of length. In the experiment this is not the case and often the lattice parameter is one of the parameters which are studied. The measurements are also not done at dimensionless (rescaled) frequencies  $\omega[1]$  but at 'real' frequencies  $\nu$  [Hz], wavelengths  $\lambda$  [nm], energies [eV] or wave numbers [1/cm].

One can still conduct all calculations in dimensionless units and post-process the data to reflect the properties of the system under study. It is, however, more convenient to provide output that directly matches the experimental data. In some parts of the code, e.g. the definition of the crystal, it is also more convenient to use units instead of rescaled quantities to ease communication<sup>10</sup>.

Another aspect to consider in this context, is the scanning of frequencies/wavelengths. In principle, this is done in a simple loop over the dimensionless frequency starting at  $\omega_{start}$  ending at  $\omega_{end}$  and using a step size of  $\omega_{step}$ . This creates equally spaced points in frequency which are not consistent with equally spaced steps in wavelengths due to the reciprocal relation between them. For the determination of other quantities, e.g. the dielectric constant from a Drude model, the frequency is needed in Hz again.

To avoid confusion during the use of the program all these conversions are done automatically and it only has to be specified whether the in/output is in wavelengths or other quantities. The program then uses the information available about the crystal to adjust all parameters, e.g. step size, in/output units, ..., internally. The calculations are always done using dimensionless units.

### 3.5.2 Parameters

In this section a list of general parameters will be given, mostly without many details, since they have been introduced before. For most of these parameters, e.g. frequency, a range has to be calculated. This is usually done by using a for-loop, which can be controlled by a scheme using 6 parameters:

<sup>10</sup>Anything that can ease the communication should always be implemented. Different, for each group "obvious" definitions can be a rather tricky source of misunderstandings.

- starting value of e. g.  $\omega$ , angles, surface, etc.
- ending value of e. g.  $\omega$ , angles, surface, etc.
- number of steps used in the loop to go from the starting to the ending value
- starting index of the loop
- ending index of loop
- step size used in the loop

The first two correspond to actual parameters values, the following three are integers which govern the execution of the loop and the last one calculated by

$$\frac{\text{ending value} - \text{starting value}}{\text{number of steps} - 1}. \quad (3.27)$$

On first sight this looks very complicated and some parameters seem to be redundant, e.g. starting value and starting index of the loop. The reason for this complicated structure is to define the step size independent of the range used in the loop. The starting and ending frequencies can for example be set to describe the experiment. Together with the number of steps the resolution is fixed and the  $j^{\text{th}}$ -frequency steps always corresponds to exactly the same value. By choosing the starting and ending value of the loop, the calculation can be split up into several tasks in a very convenient way using integer command line arguments. They can then easily be implemented in a shell script which is very convenient for using the program on different clusters without having to worry about specific implementation of parallelization. Especially for large computation, it is very helpful, if the details are set and one only has to worry about integer ranges when starting the job.

Beside these variables a number of variables are set but they are fixed for each project and do not fit the approach above. They might have to be determined for convergence, e.g. number of layer, number of modes. For the field plots, the resolutions and the size of the plots has to be controlled.

### 3.5.3 Parameters Describing the Measurement

In total there are 3 parameters that fit the scheme presented above and one parameter which can only take two values if one uses plane waves as incoming mode. The three parameters consist of the two angles  $\theta$  and  $\phi$  and the frequency. The frequency has the added complexity that for this parameter two sets of starting and ending value exist, one for the dimensionless frequency and one set for the wavelength, which can be set independently. In the loop only the rescaled frequency occurs but the starting and ending values as well as the step size are chosen automatically so that the requested quantity ( $\omega$  or  $\lambda$ ) is spaced equidistantly. Which of the two is chosen is determined by a flag.

The parameter which does not obey the outlined scheme is the polarization. Either TE or TM is used and set by a flag.

### 3.5.4 Crystal Parameters

The second class of parameters using the loop-scheme are determining the crystal.

The first is describing the surface by shifting the numerical unit cell in the  $z$ -direction. Shifting the unit cell up and down corresponds to shifting layers in the staircase approximation (Fig. 3.10). By default the beginning value here is 0.0 and



**Figure 3.10:** Changing the surface/bottom termination by shifting the layers in the numerical unit cell. On the right, the unit cell is shifted. The surface is now defined by the green layer and the red layer re-enters at the bottom, due to the periodicity of the unit cell in the  $z$ -direction. For the entire setup of the structure compare Fig. 3.7.

the ending value is the end of the unit cell in the  $z$ -direction. Shifting the unit cell corresponds to changing the top and the bottom simultaneously if only connect the top (bottom) layer of the crystal with the input(output) area. For changing both terminations independently,  $S_{\text{Begin}}$  ( $S_{\text{End}}$ ) (Sec. 3.4.4) have to be changed to include several layers. In this case the shift of the unit cell becomes obsolete.

Another parameter built in using this scheme is setting the length of the crystal in number of numerical unit cells for length dependent calculations.

### 3.5.5 Dispersive Permittivity

As already discussed in the optimization section (Sec. 3.4.3), dispersive material can be simulated as well. Since all calculations are done separately for each frequency, any dispersion can be used as long as  $\varepsilon(\omega)$ ,  $\varepsilon(\lambda)$  or  $\varepsilon(\nu)$  are known. The following models are already implemented.

#### Spline Interpolation

The most general method uses tabulated values for the complex index of refraction for given wavelengths. For wavelengths in between the listed ones a cubic spline interpolation following Chapter 3.3 in Numerical Recipes [67] is used.

This allows for simulation of all possible behavior of the dielectric function. The values can also be taken from experimental measurements. Using frequency/wavelength conversion tools also listings containing dielectric constant/frequency pairs can be used.

#### Drude Modell

Beside the use of data for the dielectric constant, the Drude model can be used (see e.g. [70]). The two required parameters are the plasma frequency  $\omega_p$  and

the relaxation time  $\tau$ . Given these two the real respective imaginary parts of the dielectric function are given by

$$\operatorname{Re} \varepsilon = 1 - \frac{\omega_p^2 \tau^2}{1 + \nu^2 \tau^2}, \quad \operatorname{Im} \varepsilon = \frac{\omega_p^2 \tau}{\omega(1 + \nu^2 \tau^2)}. \quad (3.28)$$

Alternatively the complex value can be calculated directly

$$\varepsilon = 1 - \frac{\omega_p^2}{\omega(\omega + i\frac{1}{\tau})}. \quad (3.29)$$

The Drude formula can be used for noble metals in the far infrared, e.g. good values are obtained for gold in the range from  $2\mu\text{m}$  up to  $30\mu\text{m}$ . For higher energies in the visible or near-ultraviolet, the free electron approximation is not possible any more and, for example, inter band transitions have to be taken into account [71, 72]. An example for gold is given in Fig. 3.11(a). In the long wavelength limit the correspondence with experimental data is very good but in the range below  $1\mu\text{m}$  deviations occur. In the literature the values for the index of refraction as well as the plasma frequency and the relaxation rate vary over large scales, depending on the measurement setup, quality of the sample and method. A listing of different values can for example be found in volume 15 of Landolt-Börnstein [73]. It should be mentioned however that in several small projects which were using the Drude formula for the dielectric constant of gold in the (far)infrared region no convergence of the results was achieved. Since the focus was on the main project using dielectric materials the implementation has never been adapted to the ideas discussed in Sec. 2.8.1, which could eventually solve this problem.

### Maxwell-Garnett for Embedded Two-Level Systems

A mixture of two-level systems embedded in host material with  $\varepsilon_m$  can be described using the Maxwell-Garnett formula [74, 75]. The two-level systems are described by a concentration  $\rho$ , a resonance frequency  $\omega_0$ , an oscillator strength  $\omega_p$  and a damping (line width)  $\gamma$ . For the dielectric constant of the composite structure it follows:

$$\varepsilon(\omega) = \varepsilon_m \left[ 1 + \frac{3\rho\alpha(\omega)}{1 - \rho\alpha(\omega)} \right] \quad (3.30)$$

with the polarizability

$$\alpha(\omega) = \frac{\varepsilon_{tl}(\omega) - \varepsilon_m}{\varepsilon_{tl}(\omega) + 2\varepsilon_m} \quad (3.31)$$

and the dielectric constant of the two-level system

$$\varepsilon_{tl}(\omega) = 1 + \frac{\omega_p^2}{\omega_o^2 - \omega^2 - i\gamma\omega}. \quad (3.32)$$

An example is shown in Fig. 3.11(b).

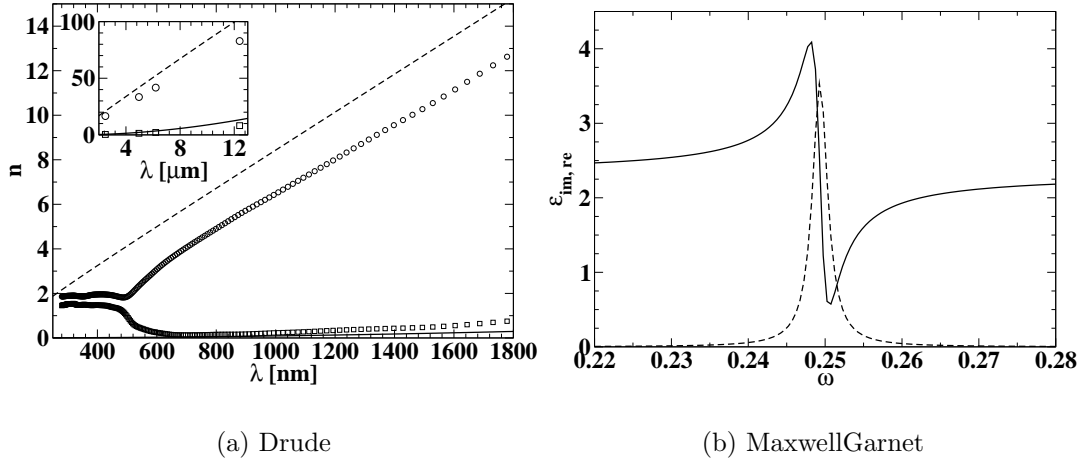


**Figure 3.11:** (a) Index of refraction  $n$  calculated using the Drude model with  $\omega_p = 1.6 \cdot 10^{16}$  and  $\tau = 2.5 \cdot 10^{-14}$ . The solid(dashed) line shows the real(imaginary) part. The circles in the large graph are experimental data taken from [72]. The Drude model reproduces the general behavior, although the exact values differ slightly. The inset shows good agreement for long wavelengths in the far infrared. (b) Dielectric constant  $\varepsilon$  for a two-level system embedded in a host material. The parameters in dimensionless units are:  $\varepsilon_m = 2.4$ ,  $\rho = 0.05$ ,  $\omega_0 = 0.24$ ,  $\omega_p = 0.7\omega_0$  and  $\gamma = 0.01\omega_0$ .

### 3.5.6 Smoothing

In most approaches, the dielectric function is assumed to be a step function which jumps at the boundaries of different regions from the pore value (e.g. air  $\varepsilon = 1.0$ ) to the surrounding substrate (e.g. silica  $\varepsilon = 11.9$ ). In simple cases, such as round pores the Fourier transformation can be carried out analytically.

Numerically, however jumps are always hard to simulate and cause problems. To avoid (smoothen) these problems, the value of the dielectric function at boundaries can be smeared out.

The main idea of smoothing is to use a function of a scalar  $f(d)$  which turns from 0 to 1 as  $d$  passed through zero. The dielectric constant can then be described by

$$\varepsilon(d) = \varepsilon_s + (\varepsilon_p - \varepsilon_s) f(d). \quad (3.33)$$

If  $d$  is the distance from the boundary, e.g. the radius of a pore,  $r - r_0$ , then  $\varepsilon_p$  is dielectric constant of the pore (inside,  $d < 0$ ) and  $\varepsilon_s$  belongs to the substrate (outside,  $d > 0$ ). To adjust the smoothing  $d$  should be scaled using a width  $\Delta r$ .

Using a hyperbolic tangent this can be done by rescaling it according to:

$$f(r, r_0, \Delta r) = 0.5 + 0.5 \tanh \left( 4.95 \frac{r - r_0}{\Delta r} \right). \quad (3.34)$$

The hyperbolic tangent ranges from  $-1$  at  $-\infty$  to  $+1$  at  $\infty$  and reaches values of  $-0.9999$  at  $-4.95$  and  $0.9999$  at  $4.95$ . The factor of  $4.95$  together with the prefactors

leads to a function which returns  $10^{-4}$  at  $r = r_0 - \Delta r$  and  $1 - 10^{-4}$  at  $r = r_0 + \Delta r$ . Fig. 3.12 shows only the behavior of the rescaled tangent.

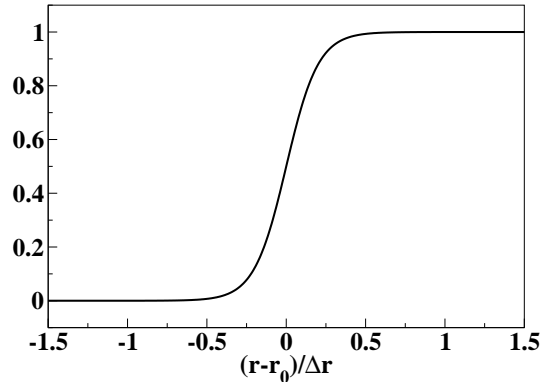


**Figure 3.12:** Rescaled hyperbolic tangent according to eq. (3.34).

In most cases a 1D smoothing can be used for one parameter. In addition, smoothing based on the distance from a point in 2D is implemented using a circle around that point with  $r_0$  as radius as well as using an ellipse with two axis  $a$  and  $b$  and an angle defining its orientation of it.

There are several possible alternatives to the hyperbolic tangent, e.g. supergaussians, which have not been implemented. For a quadratic smoothing within a certain range, analytical coefficients can be calculated [76], which take rather complicated forms and are not needed if fast Fourier transform is used. For a lot of crystals, e.g. all holographic structures discussed in Chapter 6, these boundaries can not be determined directly, so that smoothing using one parameter, e.g. a smoothed threshold for the cross-linking, is the more suitable approach.

It should be mentioned that smoothing can help to improve the representation of the spatial dependence of the permittivity. In the Fourier transform of step functions usually the Gibbs phenomenon lead to oscillations in the inverse transform which increase the jump in real space by 18%. Introducing smoothing can avoid this and reproduce a smooth function. The inverse transformation of the inverse dielectric function using  $\hat{\eta}$  is not improved significantly by this and still shows strong oscillations and even negative values. For the convergence also no general improvement has been found using smoothing.

### 3.5.7 Concluding Remarks on Parameters

From the above listing of different options and systems under study, it is obvious that the parameter space is basically unbound. Therefore, the control and setting of parameters is a complicated issue and often several aspects have to be considered. For example the change of some specific parameter, e.g. lattice constant, will change other parameters, e.g. the layer thickness, as well. Each new photonic system will add more parameters needed to describe the specifics of the unit cell and/or

crystal. Therefore, all-purpose routines, especially for the crystal parameters, are very difficult to implement due to the possible dependencies on each other.

For the main parameters, which occur in all problems (angles, frequency range,...) routines have been developed to store the parameters to a file and read them back in. For project specific parameters, interfaces have been created to pass their listing of parameters to the routines which control the storage and retrieval of them via class objects using specified methods.

Some routines, however, can not be generalized for all systems. A general all-purpose command line tool is basically impossible to implement and no attempt was done to do so. Of course, all possible parameters could be added to a command line interpreter but that would make the system very complex and hard to work with. Also with each added system the inter-dependencies would become more incomprehensible. This problem has been circumvented by using classes for the program parameters and crystal parameters which can be passed to a general routine to handle command line arguments. The detailed implementation of these routines must then be carried out individually for each project.

The other part of the code which has to be generated for each project is the setup of the layers. In principle, it would be possible to take the number of layers as a parameter and then specify a function for the dielectric constant depending on all coordinates  $\varepsilon(x, y, z)$ . Slicing the unit cell then in equidistant layers would work but would be highly inefficient. For example homogeneous parts should not be sliced but represented by one layer independent of their thickness. In addition, the definition of  $S_{\text{Unit}}$ ,  $S_{\text{Loop}}$ ,  $S_{\text{Begin}}$  and  $S_{\text{End}}$  in Sec. 3.4.4 is only symbolic and has to be used more flexible. Consider for example a structure made of bars in one direction followed by a spacer and again followed by bars rotated by  $90^\circ$ . In general such a structure would be terminated by bars on top and on the bottom. However, to add several unit cell an additional spacer layer has to be placed between the bar layer at the bottom of a unit cell and the one on top. This layer can be implemented in  $S_{\text{Loop}}$  which then connects the last layer in the unit cell to the first via the spacer. Also  $S_{\text{Begin}}$  and  $S_{\text{End}}$  cannot be set up in general. In some cases, additional layers should be added there, e.g. to model half a unit cell with broken pores on top or several substrates below. During the implementation this flexibility has always been one of the key points. As a consequence, in some cases preference was given to routines which allow easy setting up of arbitrary systems over saving memory. Creating only one program version capable of all adjustments needed to model the options mentioned above would be possible, e.g. by defining three unit cells, one for  $S_{\text{Begin}}$ ,  $S_{\text{Unit}}$  and  $S_{\text{End}}$  respectively. In some cases all of them would be needed, in some cases the top and bottom unit cell would only contain an air layer and in some cases the top and bottom unit cell would in principle be the same as the regular unit cell, except that only a part of it is included. In all cases, however, the additional overhead would require additional memory and the handling would be very complicated and even small changes would be very difficult to implement.

For the 2D code a version exists in which the program decides when to use 1,2 or 3 unit cells depending on the input but setting up the parameters for each systems

takes as long as creating a new program with the tools provided in the 3D program.

## 3.6 Lattices Classes and Crystal Symmetries

Since the list of possible 2D lattices is limited they should be listed here. Firstly, it is important to remember that the lattice is always connected to the layers. The diffraction orders are a direct result of the 2D in-plane periodicity introduced by this lattice and the lattice describes the arrangements of the unit cells. Although symmetry considerations are usually connected to a lattice this is not correct. The primitive cells might have less internal symmetries than the lattice and in this case the symmetry of the structure is only given by the symmetry common to both of them. This is also the reason why in Sec. 3.1.3 the circular choice is usually better most of the times but not always. In most practical cases the symmetry is based on the lattice, (e.g. pores or other object with continuous rotation symmetry) and then the circular choice reproduces the lattice symmetries. If the unit cell shows different symmetries and other choices are better suited to model these symmetries they might converge better.

Beside the lattice and the basis of the 2D layers, the third dimension has to be included in symmetry considerations as well. If the symmetry of the unit cell changes in different layers, then the symmetry of the entire structure corresponds to the smallest common symmetry.

Since symmetries are a very important phenomena, they are a very important property to check. A simulation which fails to reproduce the symmetries of the crystal is violating a strong physical requirement.

In two dimensions, there exist three major arrangements of lattice points of experimental relevance. They can be described by the square lattice (as a specific case of a rectangular lattice), the triangular lattice (as a specific case of an oblique) and the honeycomb lattice. All three are depicted in Fig. 3.13. In all lattices, a rectangular unit cell could be chosen as well (compare Sec. 3.1) but this cell would have a larger area and not exhibit the correct symmetries. Only the first two of them are Bravais lattices, meaning that the crystal looks the same from each point. The honeycomb can be described as a triangular lattice with a two point basis, as can be seen in Fig. 3.13(c). Beside the square and triangular lattice, three other Bravais lattices exist in 2D<sup>11</sup>, which are not implemented at the moment. Following the implementation presented in Sec. 3.1.2, they can be simulated by using the appropriate lattice vectors in the Fourier transform. Fig. 3.13(c)

In the code for 2D structures, the layers are one-dimensional and the lattice defining the diffraction orders is fixed. The crystal structure is then defined by  $z$ -dependence of the layers. This is discussed in detail in previous work [77] and will be omitted here. The parameters of the lattice used Chapter 4 are given there.

---

<sup>11</sup>I. Generalized cases of the square lattice with different lengths of the lattice vector; II. same as I. but with an additional lattice point in the center; III. generalized case of the triangular with an arbitrary angle and side lengths of the parallelogram.

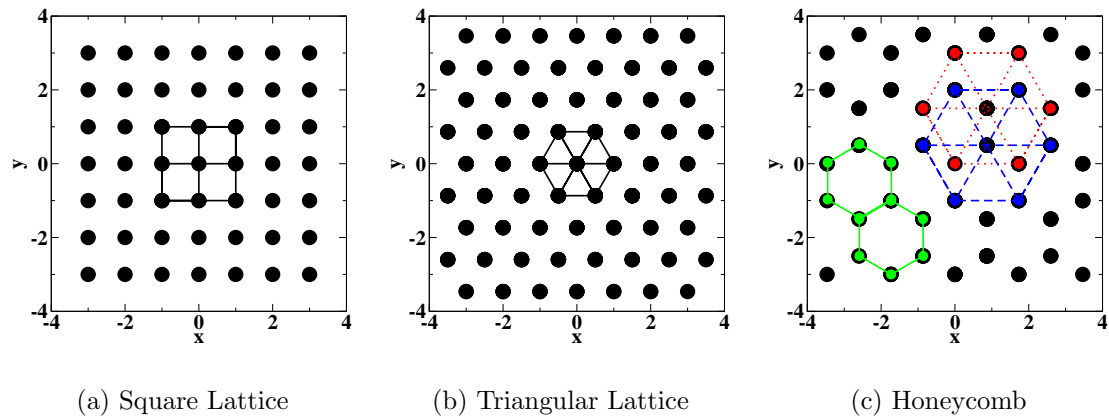


**Figure 3.13:** The three main experimental realization of lattices in two dimensions. (a) and (b) are also Bravais lattices. The Bravais lattice for (c) is a hexagonal lattice with a two point basis. This can be seen from the red(dotted) and blue(dashed) lines.

## 3.7 Disorder

Another interesting problem is the impact of fluctuations in the parameters introduced during the fabrication process. This requires a statistical description of the transmittance and reflectance coefficients and the calculation of many realizations with different values for the parameters, e.g. the pore radius.

The disorder calculations are not based on the code for 3D structures but on an improved version of an older code for 2D structures. The underlying principle is the same instead that a 2D crystal is sliced into 1D layers. The main difference is that due to the decoupling of the TE and TM modes in 2D, two different eigenvalue problems arise, depending whether the electric field is perpendicular to the 1D layers or not. Details of the calculations can be found in previous works [77, 78].

The calculation of transmittance or reflectance has not been changed for the most parts but the code was extended to allow for automated disorder calculations. The system under consideration is a 2D system of pores in silicon and will be discussed in greater detail in Chapter 4.

### 3.7.1 Database

For a crystal with a given length defined by the number of cylinders in propagation direction, fluctuations e.g. in the radius could be introduced by slicing the entire crystal. For the radii, values drawn from a distribution, would have to be used and statistics had to be done. Each crystal would consist of a large number of layers that have to be solved for each realization. Since in this approach, the calculation of each representation would take very long, an alternative is needed. A suitable way is not to calculate the  $S$ -matrix for the entire crystal but to use a database of

$S$ -matrices corresponding to different radii and multiply them to build the crystal as in the case for long crystals Sec. 3.4.4 but in this case, each  $S_{\text{Unit}}$  would correspond to a different radius.

The different  $S$ -matrices, each describing a unit cell with a specific value for the radius, are pre-calculated once and stored. A disordered crystal is then generated by drawing the radius from a distribution. In the next step, the  $S$ -matrix for the closest radius is taken from the database and used to build the crystal. In the database only a finite number of matrices can be stored. Consequently, the possible choices for the radii are limited to the values in the database. To avoid that the individual representations are just permutations of each other, the database requires a substantial size, at least several times bigger than the crystal length studied.

Using this approach, a lot of realizations can be calculated quickly by simple  $S$ -matrices multiplications, once the database is set up. In addition the length can be varied easily by adjusting the number of multiplications.

Another advantage of the database is the re-usability if the  $S$ -matrices are stored in a file. During the calculations the database should be stored in the physical memory to avoid the costly opening of thousands of files. On most clusters these files would be accessed from several nodes and, consequently, an enormous amount of network traffic would be created. A local storage would lower the traffic but new calculations would require the same node. Copying the database prior to calculations to a local node should be done if the database is too big to be kept in memory. In the calculations the database was always stored, which limited the number of available nodes for the supercell calculations mentioned below.

#### 3.7.2 Supercell and Finite-Size Scaling

The approach mentioned in the previous section is only a quasi-disordered system. Since the method relies on a Fourier expansion in each layer and any changes in radii are periodic in the in-plane direction and all pores in one row perpendicular to the propagation direction are equal.

For a correct disorder calculation, one would have to model all pores individually, so that the in-plane periodicity vanishes. This can, however, only be done in a Finite-Difference-Time-Domain simulation or using Multiple-Multipole method. In both simulations the total computation time would be too long for simulating thousands of realizations for several frequencies and lengths. To make use of the advantage of the RCWA method and overcome the limitations of the periodic in-plane arrangement, a supercell method and finite-size scaling was used. Finite-size scaling is used in various methods, where calculation based on a unit cell need to be extended to bigger systems, e.g. DFT [79] or study of localization in electronic systems [80, 81].

In the supercell calculations, the numerical unit cell extends several lattice constants in the in-plane direction. The number of layers and length in the  $z$ -direction is kept constant. Since an increase of the in-plane lattice constant leads to a smaller unit cell in the reciprocal space and, therefore, to smaller reciprocal lattice vectors, more expansion orders are needed. In the 2D code with 1D layers, the number of re-



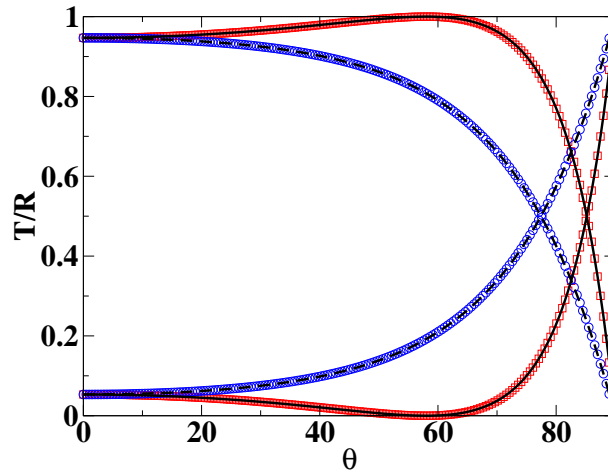


**Figure 3.15:** Calculation of the transmittance and reflectance at an interface of two homogeneous materials with  $n_1 = 1.0$  and  $n_2 = 1.6$ . The solid(dashed) black curves show the analytical results for TM(TE) polarization. The symbols are results of calculations with the dielectric function of the pores equal to the substrate. The calculations show now  $\phi$  dependence (not shown).

two different materials, also the normalization of the Poynting vector is being tested. Fig. 3.15 shows the result for reflectance and transmittance at an interface between two materials with  $n_1 = 1.0$  and  $n_2 = 1.6$ . The Brewster angle for TM polarization is given by  $\arctan \frac{n_2}{n_1} \rightarrow \theta \approx 57.9^\circ$  independent of the in-plane angle  $\phi$ .

Another easy to handle test systems are homogeneous slabs. They should demonstrate Fabry-Perot resonances and allow for testing of geometries, e.g. unit cell length, scaling, as well as for testing the multiplication of  $S$ -matrices. Fig. 3.16 shows a comparison of the calculation (circles) with the analytic formula (solid line) for a system with a thickness of  $180\mu\text{m}$  and  $n = \sqrt{2}$ . The plot in the middle shows only the calculated Fabry-Perot resonances. Although the plots seems strange they are correct. The unusual behavior around  $500\text{nm}$  is a sampling artifact, which also does not disappear if the transmittance is plotted over frequency. Comparing the results with the analytical Fabry-Perot formula in the left plot shows the exact correspondence. The strange behavior is due to the very thick layer as compared to the wavelength. Although the example seems to be an extreme case, glass plates of roughly this thickness are used in the experiments. In Chapter 6 it will be shown that these Fabry-Perot resonances can be measured. It is, therefore, important to be aware of such effects, which seem to be strange at first sight.

In crystals with several substrates, several configurations have to be checked to make sure all layers are incorporated correctly in the corresponding  $S$ -matrices ( $S_{\text{Begin}}, S_{\text{Unit}}, S_{\text{Loop}}, S_{\text{End}}$ ).

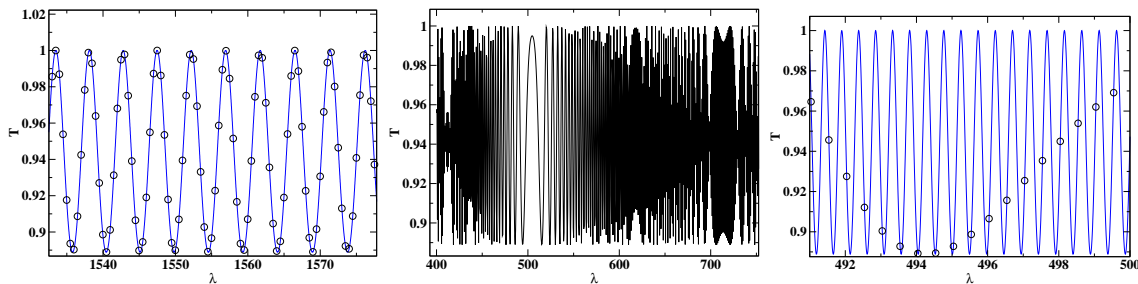


**Figure 3.16:** Fabry-Perot resonances of a  $180\mu\text{m}$  thick plate with  $n = \sqrt{2}$ . On the left the analytical formula (solid line) is compared with the simulation. The middle shows only the simulation. The unusual behavior around  $500\text{nm}$  is a sampling artifact, which becomes clear if parts are blown-up and compared with the formula (solid line) as is shown on the right side.

### 3.8.2 Physical Expectations

Other methods to check the code are not based on comparing with formulas or previous calculation but to check, whether the results fulfill physical expectations, e.g. symmetry.

For a unit cell with a triangular symmetry (six-fold rotation symmetry, inversion symmetry for the axis through the  $M$  and  $K$  points) the transmittance and reflectance have to reflect this symmetry, e.g. same values for changing  $\phi$  by multiples of  $\frac{\pi}{3}$  or changing  $\theta \rightarrow -\theta$  for  $\phi$  perpendicular any of the inversion axis. As discussed above, not only the lattice has to be considered in this case but also the symmetry of the unit cell. In Chapter 6 an example will be shown, where this property is important.

Other methods to test the code using physical expectation is introducing a modulation of the dielectric function which only contains one Fourier order. Consequently, only this order should occur in the reflectance and transmittance even if several propagating orders could exist. In the case of PCs with a stop band, the position of the stop band can be used to test the correct implementation.

Depending on the structure, additional tests might be possible, e.g. length dependence if absorption is present and should be introduced based on the system.

### 3.8.3 In-Code Testing

Beside using the results as testing criteria, the numerical implementation and accuracy can be tested by inserting the results for the eigenvalue problem in  $q^2 = k_z^2$  (eq. (2.46)) into the eigenvalue problem for  $\omega$  (eq. (2.45)) or the generalized eigenvalue problem (eq. (2.47)).

Errors in the multiplication of  $S$ -matrices during setting up the crystal leads to a violation of energy conservation, so that this is another possibility to check the outcome as long as absorption-free materials are used.

Only if all of the above criteria are met, can the program be used for simulation of realistic experiments. Failing any of the expectations mentioned above makes the

program unusable. However, failing is not uniquely defined but most of the test should be passed with numerical precision (e.g.  $10^{-12}$ ,  $\dots$ ,  $10^{-15}$  for double precision). In the case of eigenvalue problems the error might also be larger, especially if a lot of modes are used, and the eigenvalues  $q$  have a large imaginary part. Using the obtained eigenvalues  $q$  and eigenvectors for a fixed frequency  $\omega$  and inserting them into the eigenvalue problem for  $\omega$  as discussed at the beginning of this section can lead to errors on the order of  $10^{-8}$  for individual eigenvectors.

# 4 Two-Dimensional Pore System

In this chapter, results are presented for a PC consisting of air pore arrays in a silicon substrate. Since this is a 2D system, the implementation of the code is slightly different (simpler) than presented in the previous chapter. It has been discussed in detail before [77] and the differences to the implementation for finite three-dimensional structures are pointed out in Sec. 4.1. After defining the crystal parameters (Sec. 4.2), the fabrication (Sec. 4.3) as well as previous results (Sec. 4.4) are summarized. In the following, certain aspects which cannot be accessed directly in the experiments, are discussed, such as length-dependence (Sec. 4.5) and the impact of surface termination (Sec. 4.7). After discussing spectra of very long crystals (Sec. 4.8), the main part of this chapter deals with radius fluctuations and the resulting transmittance distributions (Sec. 4.9).

## 4.1 Implementation Differences for Finite Two-Dimensional Structures

The simulation of a finite 2D system is based on simpler equations than the ones presented in Chapter 2. Nevertheless, the simulation principles are the same. The individual layers are one-dimensional, corresponding to the schematical figures shown previously. The structure is supposed to be periodic in  $x$  and homogeneous in the  $y$ -direction<sup>1</sup>. Propagation takes place in the  $z$ -direction perpendicular to the cylinders (Fig. 4.2) with an angle  $\theta$  to the surface normal.

As a consequence of this setup,  $k_y = 0$  is always true and the expansion in  $y$ -direction vanishes due to this homogeneity. All terms containing either  $k_y$  or  $G_y$  are dropped in the equations and the angle  $\phi$  can be omitted leading to a simplified version of the problem. For such a strictly 2D problem two polarizations exist:

- E-polarization: electric field parallel to the pores  $\vec{E} = (0, E_y, 0)$ , magnetic field in propagation plane  $\vec{H} = (H_x, 0, H_z)$
- H-polarization: magnetic field parallel to the pores  $\vec{H} = (0, H_y, 0)$ , electric field in propagation plane  $\vec{E} = (E_x, 0, E_z)$

These two polarizations decouple in the simulation and two different independent eigenvalue problems for the scalar in-plane component of the field, one for each polarization, can be derived [77]. For a conical mounting, allowing for a rotation

---

<sup>1</sup>This is assuming that the pores are infinite in the  $y$ -direction

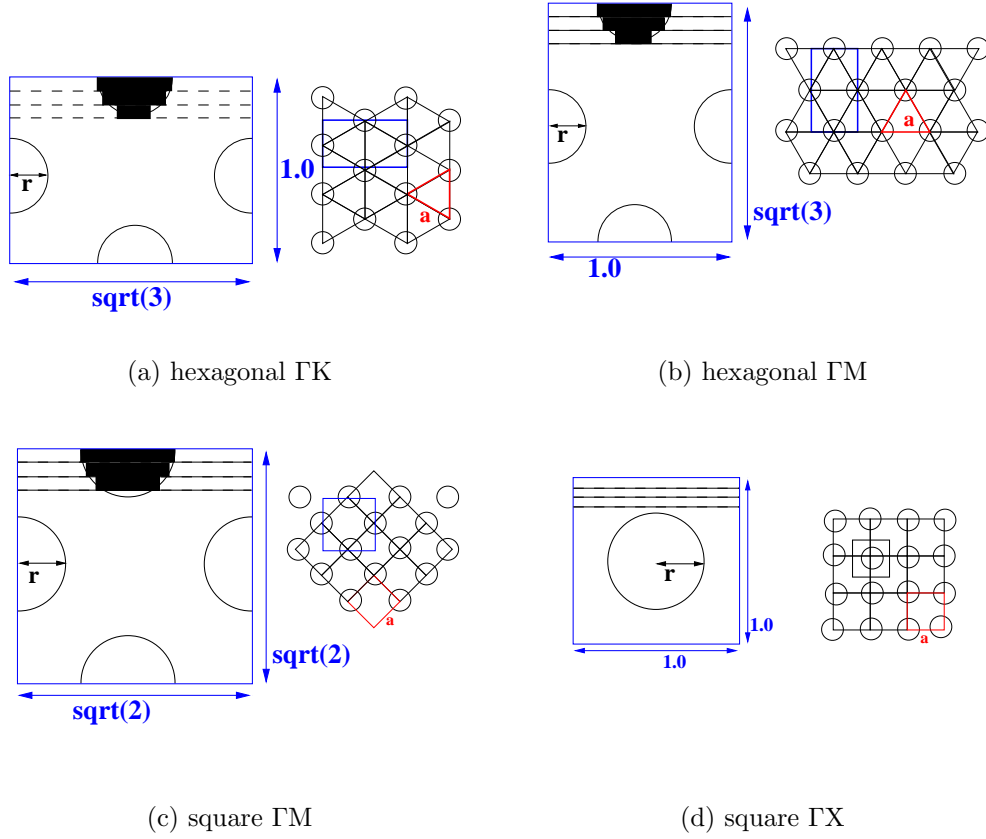


**Figure 4.1:** (Numerical) Unit cells of different 2D systems with a hexagonal/square lattice. The label describes the high symmetry direction in the reciprocal lattice along which a wave with perpendicular incidence is traveling given by the orientation of the sample. The lines indicate layers used in the simulation with the black boxes representing the staircase approximation. About 100 layers are needed to discretize one unit cell.

of the incoming wave with respect to the cylinder orientation, the full equations in Chapter 2 can be used to model the occurring  $k_y \neq 0$ , limiting  $G_y$  to the  $0^{th}$ -order and, hence,  $\vec{G}_m = (m\frac{2\pi}{a}, 0)^T$ .

## 4.2 Numerical Unit Cell

For a periodic 2D arrangement of cylinders, two types of lattices (hexagonal and square) are considered in the following. Their numerical unit cells are depicted in Fig. 4.1.

For each lattice type, two main orientations of the crystal exist, for which an incoming wave with perpendicular incidence is traveling along one of the high sym-

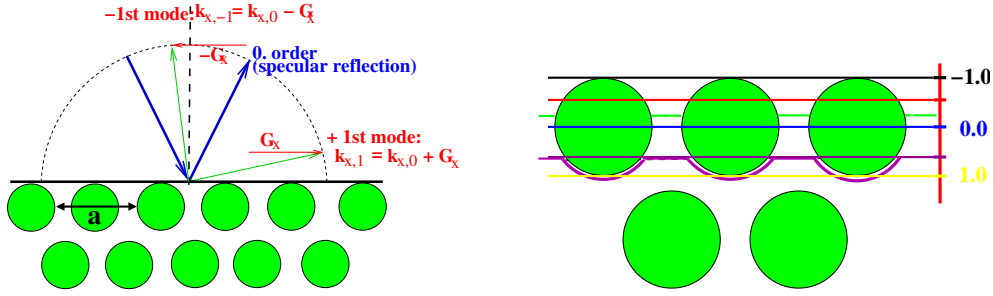


**Figure 4.2:** Left: Relation between different diffraction orders. The parallel component of the wave vector  $k_x$  differs by multiples of the 1D reciprocal lattice vector. For propagating modes the magnitude is constant. For non-propagating modes the magnitude of the in-plane component is higher than the total modulus of the wave vector and  $k_z$  has to be imaginary. Right: Different surface cuts (in units of the radius) lead to different pore openings at the top of the structure. This can be achieved by moving the blue numerical unit cell in Fig. 4.1 vertically (see text).

metry lines through the  $\Gamma$ -point<sup>2</sup>. Both setups are shown for each lattice.

In total, 4 experimentally relevant crystal setups with differing 1D grating periodicity and, therefore, different diffraction orders exist for the pore arrays. In addition, the surface termination can be altered by shifting the unit cell vertically leading to different pore openings at the top (Fig. 4.2). In the numerics this is done by shifting the cylinders inside the numerical unit cell presented in Fig. 4.1. The presented unit cell for the hexagonal lattice in  $\Gamma K$  orientation has a pore which is broken in the middle at the top and bottom. Shifting the numerical unit cell up in the lattice on the right of Fig. 4.1(a) or the cylinders down in the unit cell, leads to a pore with a smaller opening at the top and the bottom. This would correspond to samples with different surface terminations. Other surface termination could also be achieved by rotating the lattice and cutting along arbitrary crystallographic planes but these termination are not present in samples and omitted.

The presented studies, except the disorder for reasons discussed there, are restricted to the hexagonal lattice as an example system.

## 4.3 Fabrication

The PC studied in this chapter is based on Silicon which is a very promising material heavily used in electronics. Sophisticated processing technology is available for this material making nanostructuring possible. It also exhibits good optical properties and even active optical components, e.g. an electrically pumped laser [82], were presented recently. This allowed for the integration of both, electronic and photonic systems, using one material. It is one of the most used materials for nano-

<sup>2</sup>Using oblique incidence corresponds to propagation along arbitrary directions in the Brillouin zone with a fixed surface.

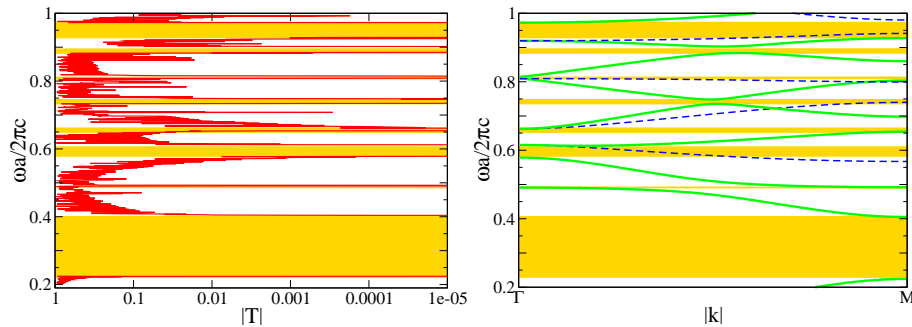


**Figure 4.3:** Transmittance (left) and band structure (right) for a hexagonal lattice of air pores ( $\varepsilon = 1.0$ ) with radius  $r = 0.4a$  in silicon ( $\varepsilon_{\text{Si}} = 11.9$ ) for a wave in H-polarization propagating in  $\Gamma\text{M}$  direction [77]. The dashed lines correspond to non-coupling bands (Sec.1.4) for which transmittance is impossible since the incoming wave exhibits different symmetries than the Bloch mode in the crystal. The yellow parts mark the stop bands for comparison of the two plots. Strong dips in the transmittance occur in these regions.

structuring. The macropores in silicon which are discussed in this chapter actually represented the first model system for PCs [83, 84].

The pores are defined by photolithographic prepatterning with a very high precision and then electrochemically etched [85]. In these structures high aspect ratios [86] as well as three-dimensional structures by changing the pore diameter [87] with depth are possible.

## 4.4 Previous Studies

In previous works a hexagonal lattice of air pores ( $\varepsilon = 1.0$ ) with radius  $r = 0.4a$  in silicon ( $\varepsilon = 11.9$ ) has been studied to characterize samples by comparing experimental and theoretical data for angle resolved transmittance spectra [77, 78]. A band structure comparison for propagation in  $\Gamma\text{M}$  direction with H-polarization can be found in Fig. 4.3.

In the experiments and simulations the anti-parallel reflection into the direction of the incoming wave was measured<sup>3</sup> using a detector with an opening angle of  $1.5^\circ$ . A reflected Bragg-order only contributed if the angle to the surface was within the opening cone of the detector. By comparing spectra as the one in Fig. 4.4, e. g. the radius in rescaled units  $r/a$  with  $a$  being the lattice constant could be determined with an accuracy of 0.025, showing the quality of the samples and the simulation.

Having tested the program successfully in simulating the experiment it can be used to study transmittance for situations which can not easily be accessed experimentally, e. g. very long samples or different surface terminations. In addition, the

<sup>3</sup>In the case of the first order being anti-parallel to the incoming wave this setup is called Littrow mount.

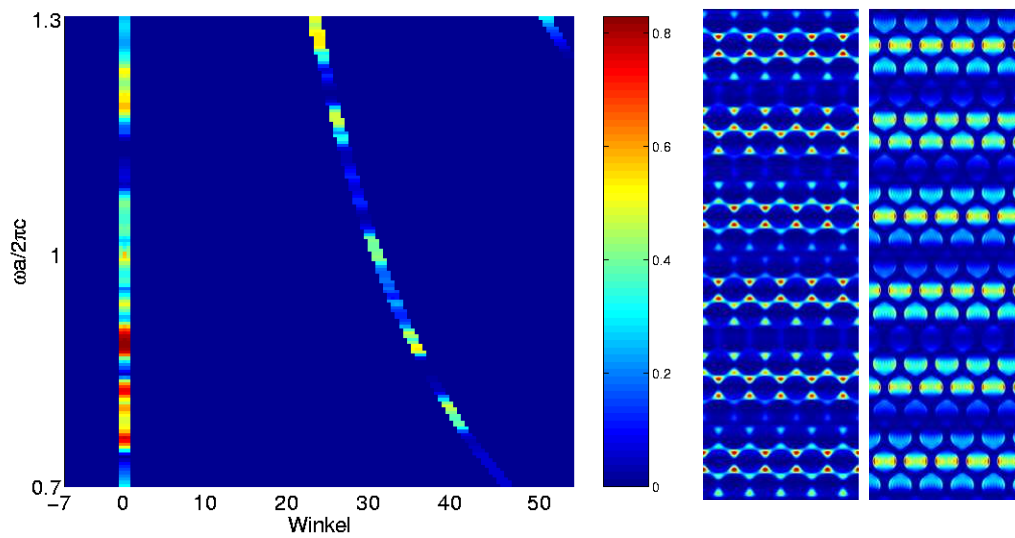


**Figure 4.4:** Left: Angle resolved reflectance spectra showing reflection anti-parallel to the incoming wave into a cone with an opening angle of  $1.5^\circ$ . Comparison with experimental data revealed a radius of 0.375. The spectra is reduced to lines for which the reflected Bragg-order enters the detector. Right: Absolute value of the in-plane components of the magnetic/electric field for  $\omega = 0.435$  for a crystal consisting of 20 pores in propagation direction. The interplay of (quasi) Bloch modes with a standing wave pattern due to the finite size can be seen [77].

tools can be used to study a large amount of “numerical samples” for the statistical analysis of fluctuations, e. g. in the pore diameter, and the determination of fabrication tolerances. These results of these calculations are presented in the following. By using some extreme examples, specific points which are important in interpreting the data are discussed. As compared to the version of the code used in [77], significant adjustments following the presented implementation schemes in Chapter 3 had to be implemented to increase the efficiency of the program and to simulate and analyze disorder in these structures.

## 4.5 Length Dependence in Crystals with Absorption

In this section, the transmittance or reflectance for a crystal with small material absorption is divided into a surface and length dependent part. The structure is the same as introduced before (hexagonal lattice of air pores  $\frac{r}{a} = 0.4$  in silicon  $\epsilon_{\text{Si}} = 11.9$ , orientation in  $\Gamma\text{M}$ , H-Polarization).

To allow for an efficient computation,  $S$ -matrix multiplication is used and only complete numerical unit cells such as those depicted in Fig. 4.1(b) can be taken into account. The resulting discrete length changes lead to a non-trivial length dependence of the transmittance. The aim of this section is to compress the information of a large number of transmittance values into fewer quantities, allowing to separate the impact of different parameters.

From a simple picture, a finite structure leads to Fabry-Perot resonances due to the resonances caused by the reflection at the two ends [19]. Since the length varies discontinuously, not all resonance conditions can be fulfilled and the transmittance shows a rather complex behavior as shown in Figs. 4.5–4.9, where transmittance is plotted over length for different frequencies. The black curves show the transmittance without absorption, whereas the red curves show the transmittance using a small imaginary part <sup>4</sup> in the index of refraction of silicon ( $\text{Im } n = 0.001$ ). For short crystals, the two curves are close to identical although the transmittance with absorption is slightly smaller than expected. Narrow features such as the resonance peaks in Fig. 4.8 are not reproduced with absorption. For longer crystals, the absorption leads to a reduction of the oscillations and an overall exponential decay of the transmittance. The frequencies are chosen in the lowest band (Fig. 4.5), at the upper (Fig. 4.6) and lower band edge (Fig. 4.8), in the stop band (Fig. 4.7) and in the second band (Fig. 4.9). As is shown later, the effect of absorption is enhanced with increasing frequency. At the stop band edges the group velocities are very low and the effect of absorption is also enhanced. In the stop band the attenuation due to the stop band is typically magnitudes stronger than the effect of absorption.

It is possible to approximate the transmittance in the case with absorption by  $T(N) = A e^{-B \cdot N}$  which allows to study the behavior of a length independent coefficient  $A$  independent of the length dependence given by  $B$ . In the beginning, this

---

<sup>4</sup>This absorption describes out-of plane losses due to the finite height of the pores caused by scattering at imperfections such as pore roughness as well as material absorption[88].

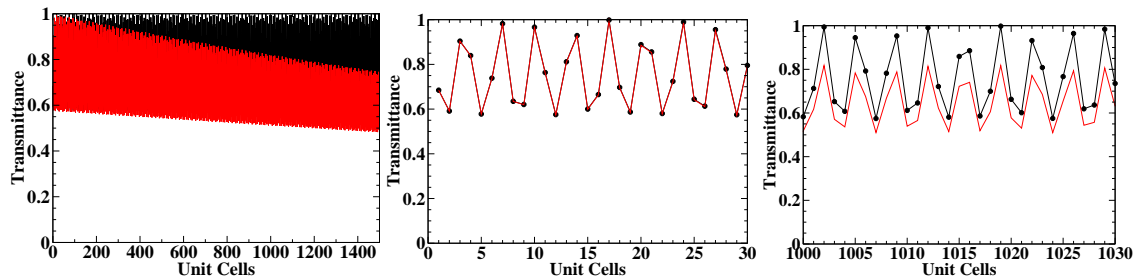


**Figure 4.5:** Transmittance over length in unit cells for  $\omega = 0.1$  (lowest band - compare Fig. 4.3). The black curve shows the transmittance without absorption, the red curve corresponds to small imaginary part in the index of refraction for silicon ( $\text{Im } n = 0.001$ ). The left plots enlarge the results for a short/long crystal.

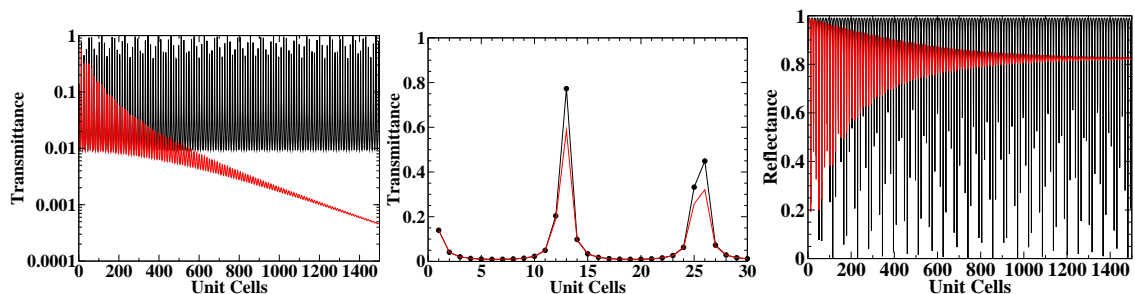


**Figure 4.6:** Left/Middle: Same as Fig. 4.5 with  $\omega = 0.224$  (lower band edge - compare Fig. 4.3) using a logarithmic scale on the left. Right: Plot of the reflectance.

seems to be a very crude approximation but since all crystals show a small absorption [88], e.g. by pore roughness, all the oscillations are damped out in real systems. This approach is a compromise which allows to reduce the otherwise too big data set of length dependent transmittance spectra to a smaller number of parameters which can then be analyzed. The alternative would be to plot the transmittance  $T(N)$  for each frequency and scanned parameter, e.g. surface, and compare all curves which is not very promising.

This Ansatz does however not allow to study the Fabry-Perot type length behavior. The transmittance is mainly determined by the absorption, except for cases in the stop band, but it can give insight into the dependence on the surface termination as well as into the impact of absorption strength in different regions of the crystal, e.g. pores or substrate, and different frequency regions. Due to the absorption, the coupling from the back side is strongly suppressed and the reflectance stabilizes at a constant value as can be seen in the right figure of Fig. 4.6. Although it is not discussed here, this approach has been used to estimate the attenuation length for a crystal containing dispersive material based on two-level systems embedded in a dielectric material and compared to results calculated with the Wannier function approach [89]. A description of the Fabry-Perot resonances using discrete length steps can be found in [90] for 1D PCs.

In the stop band this method can be applied to study the length dependence and

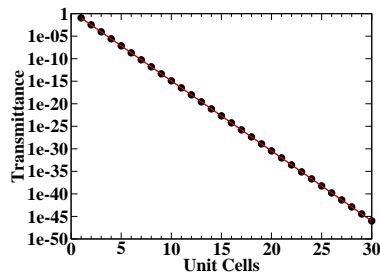


**Figure 4.7:** Same as Fig. 4.5 with  $\omega = 0.35$  (stop band - compare Fig. 4.3). No enlargement is necessary in this case.

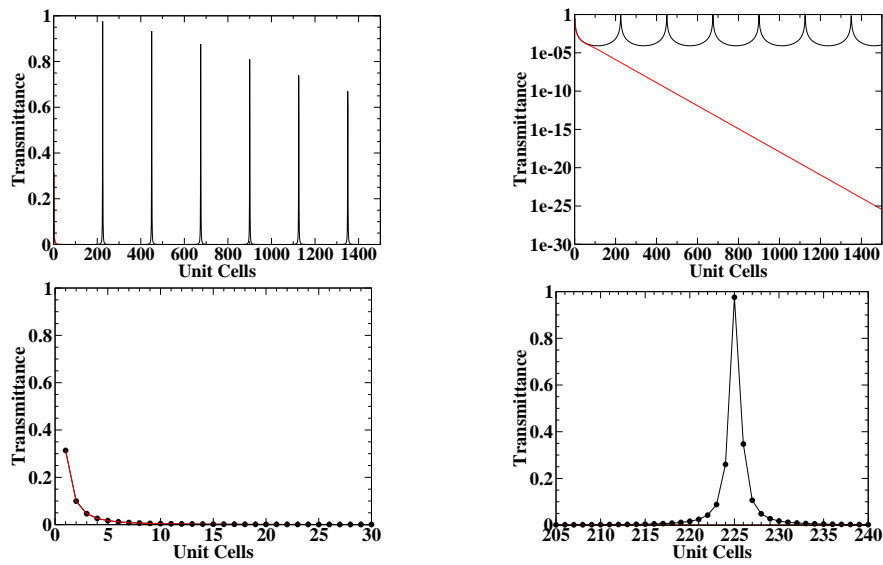


**Figure 4.8:** Same as Fig. 4.5 with  $\omega = 0.405$  (stop band edge - compare Fig. 4.3).

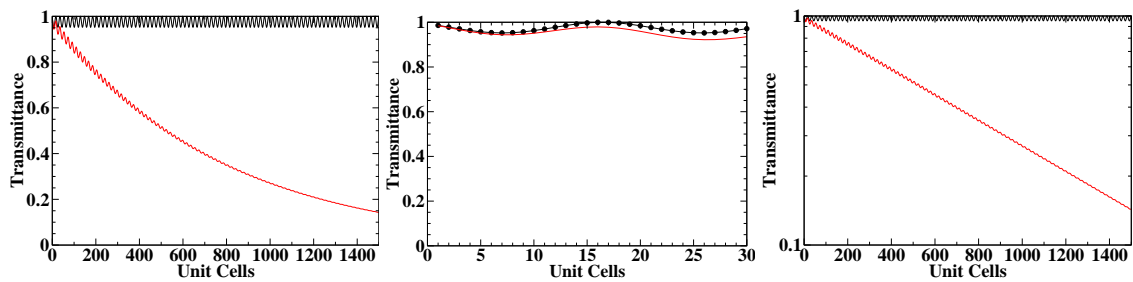


**Figure 4.9:** Same as Fig. 4.5 with  $\omega = 0.466$  (second band).

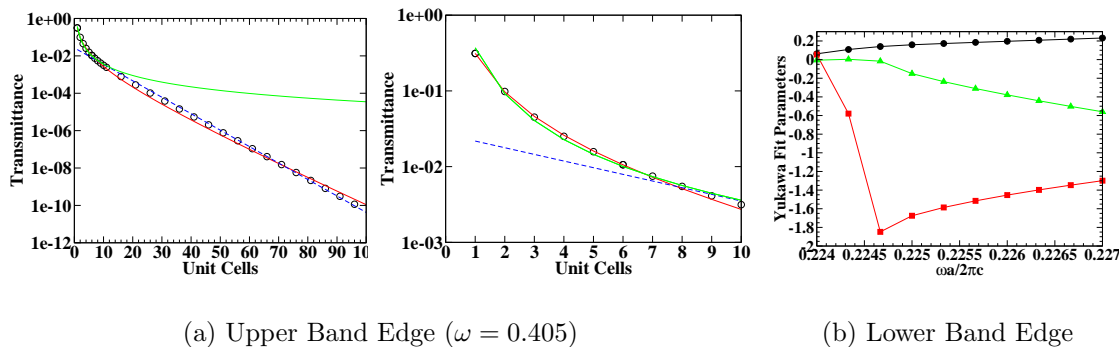


**Figure 4.10:** (a) Transmittance at the upper band edge ( $\omega = 0.405$ ). The colored lines show different fits. blue line: exponential fit  $T = 0.03 e^{-0.20N}$ , green line: power law fit  $T = 0.37N^{-2.01}$  and red: combination of both  $T = 0.36N^{-1.47} e^{-0.15N}$ . (b) Parameter for fitting at different frequencies at the lower band edge with the combined Ansatz using a prefactor (black circles), power law exponent (red squares), attenuations factor in exponent (green triangles). For a power law exponent of 1.0, this Ansatz would turn into a Yukawa potential. The parameters of the structure correspond to the ones given in Fig. 4.3

determine the attenuation length once the stop band is formed. This approximation is, however, not valid for short crystals at frequencies close to the band edge. Fig. 4.10(a) shows the transmittance over the number of unit cells at the upper band edge and different fits. The blue line shows an exponential fit ( $T = Ae^{BN}$ ), the green line a fit using powers of  $N$ s ( $T = AN^B$ ) and the red line shows a fit using a combination of both ( $T = AN^C e^{BN}$ ). The last Ansatz would turn into the well-known Yukawa potential for a power law exponent of  $C = -1.0$  (see caption for fit parameters). The power law fit is only applied to the first 10 unit cells. It strongly deviates for larger crystals. None of these fits can be used to describe all parts of the curve. For most other frequencies the agreement becomes even worse. A study for a series of frequencies at the lower band edge shows that the fit parameters vary strongly with frequency. Fig. 4.10(b) shows the results for the fitting to the Yukawa-like Ansatz at different frequencies. The two lowest frequencies are too close to the band to show a clear decrease of transmittance and the power law as well as the attenuation factor are close to zero. For the other frequencies, it can be seen that the prefactor (black curve, circles) stays approximately constant. The power law exponent becomes smaller, whereas the attenuation factor in the exponential becomes larger. In the stop band (Fig. 4.7) the simulation shows a purely exponential decay as expected. In all cases the curves for long crystals are better represented by the exponentials. A power law fitting has also been tried and in general represents the decay for short crystals better, but fails for more than 10 unit cells. The exponent starts at roughly -1 and decreases to -3.5 expressing the stronger decay for frequencies deeper in the stop band.

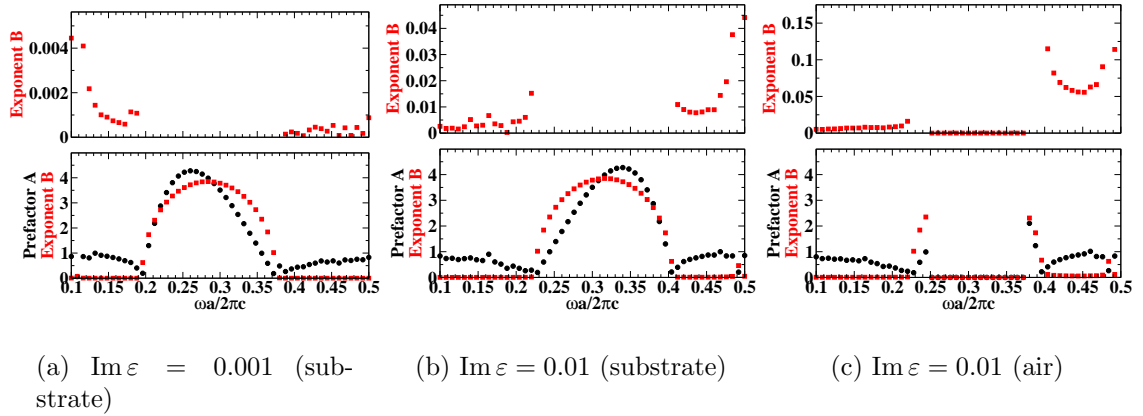


**Figure 4.11:** Results for the prefactor  $A$  and the attenuation factor  $B$  in the exponent describing the length dependence  $T(N) = A e^{-BN}$  obtained by fitting for different frequencies. The length was varied from 1 to 300 in steps of 10 unit cells, which is good enough to determine the exponential decay but no finer structure of the length dependence. In the left plot the imaginary part of the substrate is  $\text{Im } \varepsilon = 0.001$ , in the middle  $\text{Im } \varepsilon = 0.01$  and on the right  $\text{Im } \varepsilon = 0.01$  but inside the air pores instead of the substrate. The upper plots enlarge  $B$  for the area in the bands.

## 4.6 Attenuation Length

The attenuation length describes the decay of the transmittance with length. In the stop bands this decay is due to the multiple scattering in a PC. Outside the stop bands the attenuation length would be non applicable for a finite crystal without absorption and the length dependence would have to be described using a Fabry-Perot Ansatz. As discussed before, losses allow for the introduction of an imaginary part to the permittivity.

In this section, the effect of absorption introduced either in the air pores in or the dielectric substrate for a range of frequencies is studied. For the absorption two different imaginary parts ( $\text{Im } \varepsilon = 0.001/0.01$ ), are introduced in the permittivity of either the pores or the substrate in the previously presented structure.

Fig. 4.11 shows the results up to the (very narrow) second stop band<sup>5</sup> obtained by fitting the length dependent transmittance for each frequency using lengths from 1 to 301 numerical unit cells as depicted in Fig. 4.1(b) with a step size of 10. The prefactor  $A$  is only listed for completeness and the attenuation factor  $B$  is studied in the following. For a small absorption, especially in the short wavelength regions, the oscillations in the transmittance with length are still visible over the complete

<sup>5</sup>It is not resolved in the plots due to the limited number of frequency points. The peak in the attenuation factor  $B$  in the lower plots with absorption close to a frequency of 0.5 shows the position. The slight shift caused by the higher absorption moved one frequency point close enough to the stop band to resolve it.

length and the decay depends on the sampling points in the length  $N$ . The first two data points use sampling points at the bottom of the oscillations, which explains the large absorption in this area. Therefore, the results with higher absorption are better suited for analysis since the absorption effect becomes more pronounced. In Fig. 4.11(b) the absorption has been increased by a factor of 10 compared to Fig. 4.11(a). In the middle of the stop band the attenuation is unchanged and only small changes occur at the edges, showing that the structural contribution due to multiple scattering is dominating. In the bands the impact, of the oscillations is diminished and especially in the first band the absorption is nearly constant, due to the linear dispersion and the resulting constant group velocity, except for a strong increase at the stop band edge. In the second band, the increase is much stronger. This can be explained with the low group velocity of the flat second band, compared to the first band. The increased matter-light interaction time increases the attenuation. Introducing the imaginary part in the air pores leads to another large increase of a factor of about 3 in the first and about 5 in the second band. This effect cannot be explained with the air filling factor, which is only about  $f = \frac{\pi r^2}{0.5 \cdot \sqrt{3}} \approx 58.04\%$ . It could be nicely explained if the second band was concentrated in air, which unfortunately is not the case in this system. Very often a generalization of 1D results [7] is used and the first (second) band is described as dielectric (air) band. However generally this is only true in the 1D case. For 2D systems e.g. square lattice of air pores in silicon with  $\frac{r}{a} = 0.4$  in E- and H-polarization [35] or hexagonal lattice of air pores in silicon with  $\frac{r}{a} = 0.475$  in H-polarization [91], the first air band occurs at much higher frequencies than the ones considered in this work <sup>6</sup>.

## 4.7 Surface Termination

Another interesting parameter for finite structures is the termination at the top and the bottom of the crystal. The unit cell in Fig. 4.1(b) shows the situation in which the sample cleavage corresponds to the position with the smallest substrate thickness at the surface. Changing the top and the bottom simultaneously corresponds to breaking at different points and is simulated by shifting the numerical unit cell as illustrated in Fig. 4.12. If both terminations should be changed independently, the matrices  $S_{\text{Begin}}$  and  $S_{\text{End}}$  have to be adjusted (compare Fig. 3.7). In order to study the surface termination, only the upper half of the numerical unit cell has to be considered. This can be seen from Fig. 4.12. Shifting the unit cell about half its length in the  $z$ -direction corresponds to a shift in  $x$  about  $\frac{ax}{2}$ . For 1D layers, this shift results in a phase in the 1D Fourier transform of the permittivity of  $e^{-iG_x ax/2} = -1$  in all orders. Due to the periodicity in  $x$ , the position of the numerical unit cell in  $x$  is not uniquely defined. If the inversion symmetry about the center is required, the cylinders have to be either in the middle or on the sides which is still the case after shifting by  $\frac{ax}{2}$ . Therefore, this shift does not change the transmittance and

---

<sup>6</sup>The inverse system (silicon cylinders in air) can however have an air band in this frequency range.

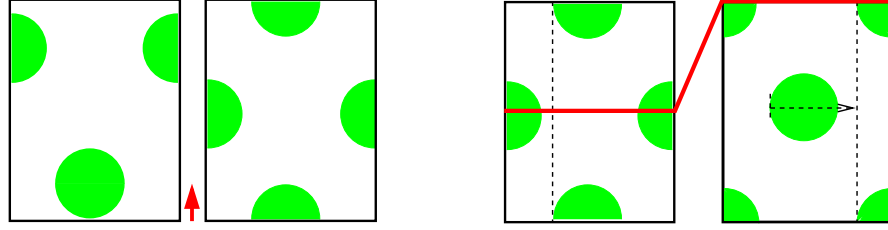


**Figure 4.12:** Left: Changing both terminations by shifting the numerical unit cell vertically. Right: A vertical shift of half a unit cell corresponds to a horizontal shift of half a unit cell and leads to the same transmittance as the phase shift introduced into the Fourier expansion of the permittivity is given by  $e^{-iG_x a_x/2} = -1$ .

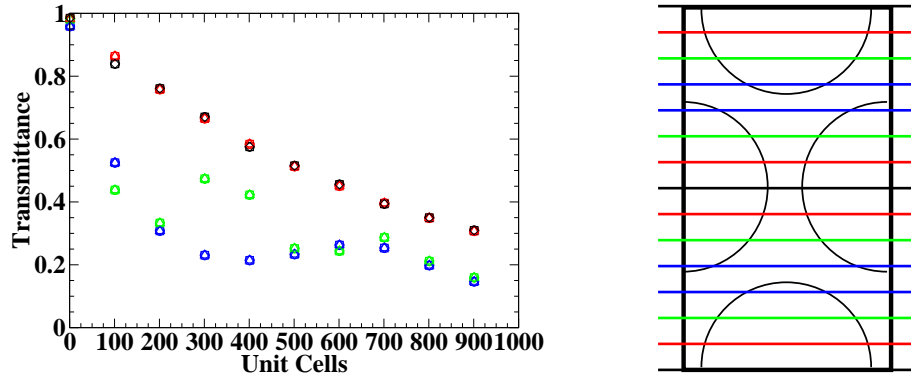


**Figure 4.13:** Left: Transmittance over length for  $\omega = 0.466$  for different surface terminations. Each data point consists of all terminations marked with the same color on the right. They are listed in Tab. 4.1. Right: Definitions of surface termination using correct scaling of the unit cell. The color coding on the left corresponds to the surface cuts along the lines with same color on the right. For longer crystals the four curves become parallel but shifted with respect to each other. The same transmittance (color) occurs for terminations symmetric around the termination at maximum pore size (black line).

termination in the second half of the numerical unit cell corresponds to the first.

The impact of surface termination is illustrated in Fig. 4.13. Each set of data points on the left represents different surface terminations corresponding to a surface cut marked by a line with the corresponding color in the right plot. The surface cut influences the oscillation strength and the mean value around which the transmittance oscillates with length. For long crystals, the curves become parallel, but shifted with respect to each other, in a logarithmic plot. From this plot one could conclude that the surface dependence is only based on the interface between air and the structure, since, for instance the 2<sup>nd</sup> and 7<sup>th</sup> cut yield the same result although in one case the pore becomes smaller and in the other larger with depth. Tab. 4.1 lists the surface cuts and values for the shift of the unit cell in  $z$ -direction for which the transmittances are equal.

For the determination of  $A$  and  $B$ , crystals with 1 to 2501 numerical unit cells

Cut number	$z$ shift of unit cell
0, 7, 14	0.0, 0.866025, 1.73205
1, 6, 8, 13	0.123718, 0.742307, 0.989743, 1.60833
2, 5, 9, 12	0.247436, 0.61859, 1.11346, 1.48461
3, 4, 10, 11	0.371154, 0.494872, 1.23718, 1.3609

**Table 4.1:** List of surface cuts and the required shift of the unit cell. All values in the same row lead to the same transmittance behavior. Colors correspond to the ones used in Fig. 4.13.

were calculated with a step size of 10 unit cells. As imaginary part of the silicon  $\text{Im } \varepsilon = 0.001$  was chosen. Fig. 4.14 shows the result for several frequencies. The upper plots in Figs. 4.14(a)–4.14(e) show the attenuation factor  $B$ , which does not change if the surface termination is changed, since it is related to absorption.

In the middle graphs of Figs. 4.14(a)–4.14(e), the prefactor  $A$  is plotted using black dots. As a comparison, the transmittance through one unit cell is plotted in red on the same scale, except for the frequency in the stop band. The two curves show a similar behavior for most cases. In the stop band (Fig. 4.14(b)), the prefactor is significantly higher reflecting the non-exponential drop of the transmittance in the first numerical unit cells as discussed in Sec. 4.5. Therefore, the prefactor has to push up the transmittance for short crystals to compensate the exponential decay which is stronger for longer crystals. The similarities are not always so strong, a weaker similarity can i. e. be found in Fig. 4.14(d) and Fig. 4.14(e). However, the trends are still visible. The lowest plot in Figs. 4.14(a)–4.14(e) shows the transmittance coefficient  $T_{\text{eff}}$  across a boundary of two homogeneous materials using the Fresnel formula for perpendicular incidence, with  $n_{\text{air}}$  and  $n_{\text{eff}}$  in the crystal, which is based on filling factor of the first layer in the staircase approximation. This clearly is not a feasible way to discuss the surface termination, even in the long wavelength limit (In Fig. 4.14(a)  $\lambda = 5.55a$ ) although the previous plot Fig. 4.13 might suggest such a simple dependence. The observation that the transmittance is equivalent for all crystals with the same surface termination in the first layer is not caused by the termination but by the reciprocity of the crystal. The symmetry of the transmittance around a vertical shift of 0.0 (black line) corresponds to propagation through the crystal from the two different sides, since the symmetric cases, e. g. up/down shift of the red lines with respect to the black, correspond to an inversion of the crystal. If the numerical unit cell is shifted up by  $\Delta z$  with a wave impinging from the top, it corresponds to a (down) shift of  $-\Delta z$  and a wave impinging from the bottom or back since the two surfaces are shifted simultaneously by the choice of the unit cell. This behavior is a consequence of the reciprocity of the device. This symmetry could be broken by adapting  $S_{\text{Begin}}$  and/or  $S_{\text{End}}$  so that only one of the crystal terminations is changed.

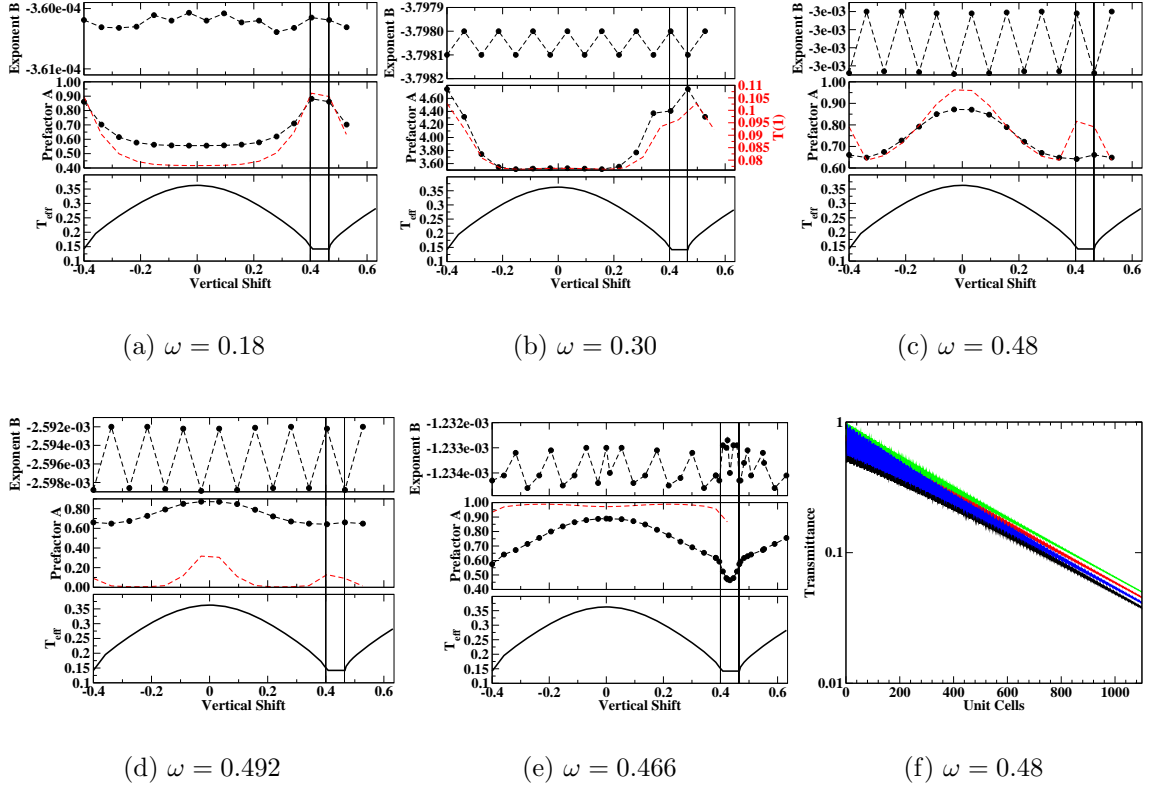


**Figure 4.14:** (a-e) Results of the exponential fit for the length dependent transmittance using 1–2501 numerical unit cells in steps of 10 unit cells. The upper plot shows the attenuation factor  $B$ , the middle plot shows the prefactor  $A$  (black) as well as the transmittance through 1 numerical unit cell for a comparison. The lowest plot shows transmittance across a boundary of two homogeneous materials using  $n_{\text{eff}}$  in the crystal based on the filling factor of first layer used in slicing the crystal. The vertical lines indicate the region in which the surface is not broken by air pores. A vertical shift of 0.0 corresponds to a surface with a maximum opening of the pore (black line in Fig. 4.13). (f) Transmittance for  $\omega = 0.48$  over length for different termination, showing the parallel behavior of the transmittance for long crystals.

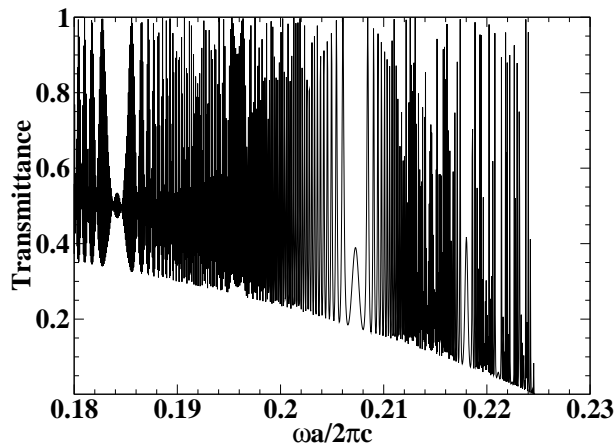


**Figure 4.15:** Spectra for a long crystal (4096 numerical unit cells), showing two interesting spectral features around  $\omega = 0.184$  and  $\omega = 0.208$  due to a low frequency resolution.

## 4.8 Sampling Problem For Long Crystals

Previously (e.g. Fig. 4.8), it was mentioned that the length dependent transmittance can show some interesting features which one would not expect initially due to the discrete step size.

Similarly, on first sight surprising, transmittance features can be found in frequency dependent spectra for long crystals. Fig. 4.15 shows the spectra for an extremely long crystal<sup>7</sup> ( $N=4096$ ) where this problem can be studied very well although it already appears in shorter crystals as well. There seem to be two interesting spectral features around  $\omega = 0.184$  and  $\omega = 0.208$ . In Fig. 4.16 close-ups of these regions are plotted together with an improved frequency resolution in green from which it follows that these are sampling artifacts, which disappear if the resolution is increased. Although the structure is very long for illustration purposes, similar effect can occur at higher frequencies for shorter crystals. Typical crystals in experiments are only a few tens of unit cells long and these features cannot be found. In addition occurring oscillations usually are damped by to imperfections or are not resolved in the measurement process. Similar signatures can be found, if the crystal is fabricated on top of thick glass substrate. In this case, very narrow Fabry-Perot resonances occur. In Fig. 6.6 calculations of an example are shown for a glass plate ( $170\mu\text{m}$ ) with an adhesion layer ( $10\mu\text{m}$ ) as used in the experiment in Chapter 6. With the measurement setup used during regular characterization, these oscillation are not resolved, but by changing the experimental setup they were also found experimentally.

Fig. 4.16(f) shows a close up of the area at the stop band. Here, even the increased frequency resolution is not capable of resolving the resonances due to the very flat

<sup>7</sup>This number has been chosen since any multiple of two can be calculated very fast by exponentiating  $S$ -matrices.

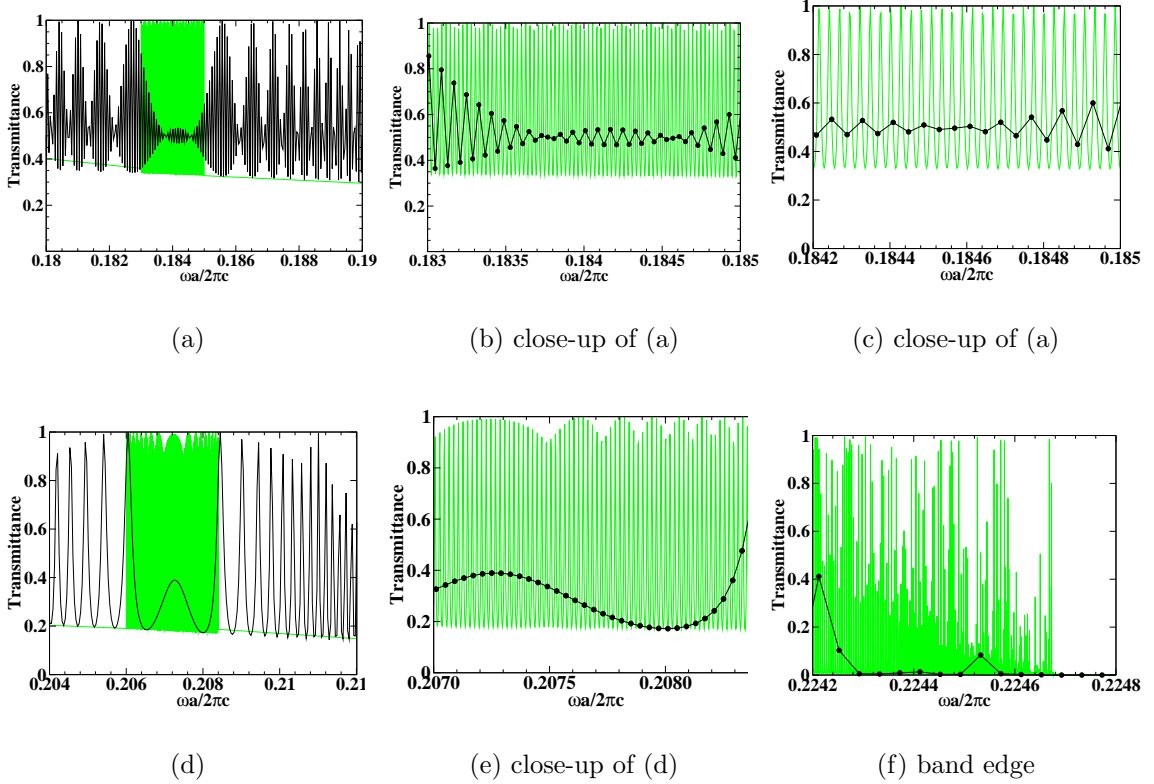


**Figure 4.16:** Transmittance spectra and close-ups for selected regions for a very long crystal (4096 numerical unit cells). Increasing the frequency resolution exposes the transmittance features as sampling problems and not as a physical effect. The refinement was only done for certain regions and the flat green lines connect these regions but do not show actual data.

bands. From this plot it is also visible that increasing the length of a crystal is a possible way to determine the stop band edge more precisely. In some of the following spectra we will see that for short crystals the first significant increase of the transmittance can be away from the stop band edge (compare e.g. Fig. 4.19(b) and Fig. 4.19(c)).

In general one analyzes these Fabry-Perot resonances by plotting the transmittance over the frequency and obtains equidistant resonances. This is only true for structures without dispersion, since it depends on a constant optical path length. The effects of a PC are based on changing the dispersion relation, so that this can't be expected and the behavior for finite structures will exhibit many features, which can not be described by simple analytical methods. In comparing theory with experiment one should always be aware that this sampling problem exist and might change the spectra significantly if not enough care is taken during the interpretation.

## 4.9 Radius Fluctuations

In previous chapters, the influence of structural parameters on the transmittance and reflectance properties of 2D Photonic Crystal were studied. The main idea was to reduce the large information available in spectra to easier accessible and analyzable quantities to find general properties of PCs.

In all the cases the parameters varied in a determined way and changes of the optical properties were analyzed. In this chapter, the influence of unwanted but unavoidable parameter fluctuations are studied for pore size fluctuations. The idea is to analyze the entire spectra for several lengths by reducing the large amount of data from a lot of disorder spectra to a few descriptive parameters.

The radius has been chosen as fluctuating parameter, because, in most PC systems the periodicity is defined much better than the actual structure of the unit cell, e.g the radius in a pore array. In the macroporous silicon system, for example the pore locations are defined by lithography, which is very precise. A constant pore thickness and shape is harder to achieve during electrochemical etching, since this depends on the distance to neighboring pores, the uniformity of the electric voltage, etc. For a rod system it is shown by Asatryan et al. that disorder in the refractive index or radius have the most influence on the averaged logarithmic transmittance [92].

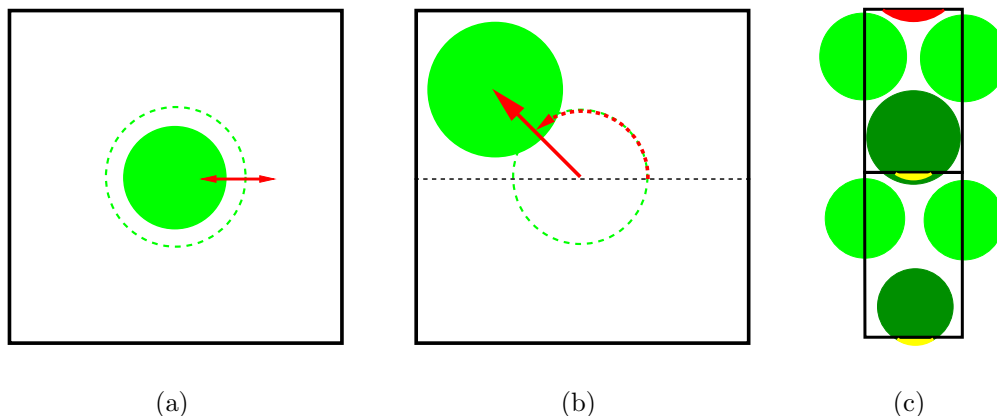
In holographic structures a similar situation occurs. The periodicity is given by the wavelength of the incident exposure beams and the angles in between them. During the development, several processes such as shrinking, diffusion, etc. lead to a distortion of the pattern and might change the global lattice constant of the sample but it does not fluctuate locally. The structural details of individual unit cells are one order smaller and, therefore, effected stronger by distortions [93].

Fig. 4.17(a) shows the radius disorder in the chosen model system (square lattice in  $\Gamma X$  orientation as depicted in Fig. 4.1(d)). In this case, only the radius is allowed to fluctuate with a Gaussian distribution around a mean value  $r_0$  with a given standard deviation of  $\sigma_r$ . Displacement disorder (Fig. 4.17(b)) requires two parameters. The coordinates of the position vector  $(x, y)^T$  can fluctuate around a mean value  $x_0$ , respective  $y_0$ . Alternatively, the displacement can exhibit Gaussian fluctuations around 0.0 (center) together with the direction of it given by an uniformly distributed angle in the range  $[0, \pi]^8$ .

The reason for a square model system becomes clear from Fig. 4.17(c). As discussed in Sec. 3.7 an efficient method to calculate many realizations depends on the calculation of a database containing  $S$ -matrices for different radii and building up crystals by multiplying them picking the radius from a distribution. In the hexagonal structure the cylinders are not always confined to one numerical unit cell for which the  $S$ -matrix can be calculated. For larger radii the situation depicted in Fig. 4.17(c) occurs. The cylinder rows overlap and the red part in the upper unit cell differs from the yellow in the lower, leading to a radius mismatch in adjoining

---

<sup>8</sup>This covers the complete 2D unit cell, since the displacement can take positive and negative values



**Figure 4.17:** Definition of radius fluctuation, using one parameter, (a) and displacement disorder requiring two parameters (b). In (c) two adjoining unit cells for a hexagonal system in  $\Gamma M$  orientation are shown. The cylinders spread over two numerical unit cells and the corresponding  $S$ -matrices can not be multiplied due to the radius mismatch indicated by the differences in the red and yellow areas in adjoining layers.

unit cells. This makes the  $S$ -matrix multiplication impossible. Hence, the efficient implementation using the  $S$ -matrix methods with the database approach cannot be used. This poses no problem for perfect structures since the radius is equal in all unit cells.

In the following discussion a Gaussian distribution is used for the radius. The standard deviation of it is given by  $\sigma = \frac{r_0 p}{W}$  with the radius of the perfect structure  $r_0$ , the percentage deviation  $p$  and the scaling factor  $W$  allowing to set the minimum and maximum values independent of the width of the distributions. The maximum and minimum radii are given by  $r_{\max, \min} = r_0 \pm p r_0$ . The minimal and maximal radii correspond to a distance of  $W\sigma$  from the the center. Typically  $W$  is chosen as 3.

In Fig. 4.18, the band structure for the model system of air pores in silicon is shown on the left for a structure with a radius of  $r = 0.4$ . The propagation is along  $\Gamma X$ -direction and H-polarization is used. On the right it is repeated and the band structures for a radius of  $+5\%$  ( $r_{\max} = 0.42$ ) and  $-5\%$  ( $r_{\min} = 0.38$ ) are included as well. Below the first stop band only small differences in the three band structures are visible. For higher frequencies the differences become larger and starting at roughly  $\omega = 0.5$ , different bands start to overlap (5<sup>th</sup> band for  $r = 0.38$  with the 3<sup>rd</sup> and 4<sup>th</sup> for  $r = 0.42$ ). One would therefore expect a higher sensitivity to fluctuations in the upper region.

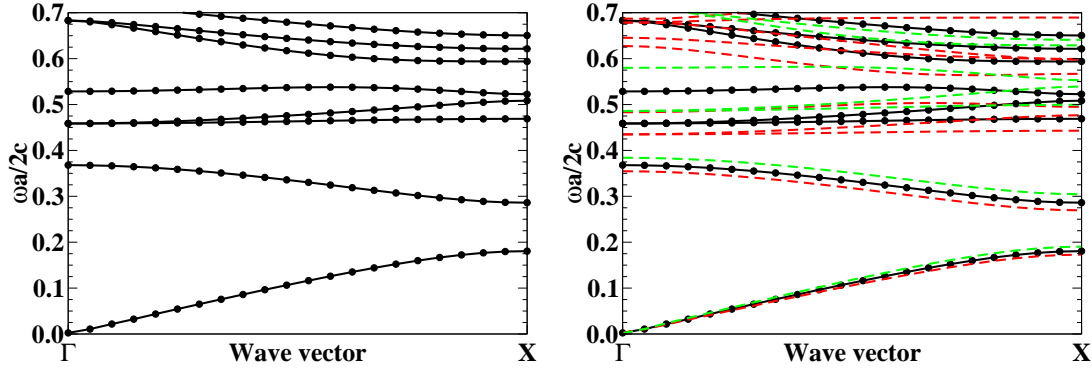


**Figure 4.18:** Left: Band Structure for a square lattice of air pores with radius  $r = 0.4$  in silicon in  $\Gamma X$  direction for H-polarization. Right: Same but including band structure for  $r = 0.38$  (dashed, red) and  $r = 0.42$  (dashed, green), corresponding to values of  $r = r_0 \pm 5\%$ . At  $\omega = 0.5$  different band start to overlap ( $5^{th}$  for  $r = 0.38$  with the  $3^{rd}$  and  $4^{th}$  for  $r = 0.42$ ).

### 4.9.1 Statistical Approaches

Since the idea is to analyze the impact of fluctuations in the pore radius on transmittance, one has to look at entire distributions of transmittance data calculated with fluctuating parameters.

In previous works, this was mostly done for frequencies close to the first stop band and only the (logarithm of the) transmittance has been studied [92, 94–96]. The main goal of these papers was to determine the localization length  $l$  given as

$$l = - \lim_{N \rightarrow \infty} \frac{2N}{\langle \ln T \rangle}. \quad (4.1)$$

By an analogy to the insulating regime in electron transport theory, a log-normal distribution is expected in this region. In the stop band no propagation is possible, so the transmittance is expected to decay exponentially. Therefore, transmittance through each unit cell can be described by an exponential. Transmittance through several unit cells can be described by multiplying the exponential factors, leading to an addition of the factor in the exponentials<sup>9</sup>. As a consequence the transmittance shows a log-normal distribution. This log-normal distribution is always expected as long as there is only one channel, even if this channel is propagating. In the stop band all channels are exponentially damped, so one can conclude that all other channels are exponentially weaker than the least damped one and one effectively has the situation of only one propagating channel ( $e^{-\alpha z} = e^{-\delta \alpha z} e^{-\alpha_{min} z}$ ). However, as soon as several channels interact, more complicated descriptions are required.

<sup>9</sup>This picture is not entirely correct, since the occurrence of a stop band in a PC is an effect of the periodic arrangement of the unit cell. A single unit cell can, therefore, not lead to an exponential decay. In a longer crystal, each unit cell will, however, decrease the transmittance exponentially

In the region with many propagating channels (metallic regime), electronic systems exhibit a Gaussian distribution, due to the contribution of all channels in a continuum approximation. Recently, deviations from the log-normal were found in the crossover regime between the metallic and deeply insulating limit, leading to “one-sided” log normal distributions with a cut-off [97, 98]. These distributions occur, if one channel is treated independently, as in the insulating regime, and all the others are treated as a continuum.

For photonic systems in the band, the description is more complicated and the interplay of the ordered Bragg-scattering at the periodic structures and the scattering from disorder is difficult to describe. In a PC, disorder disturbs an otherwise periodic system, which is not the case for an electronic system, where usually impurities are regarded as perturbing the free propagation in a otherwise homogeneous medium. Markos et al. [99] mapped transport through a system of dielectric cylinders onto an electronic system, however, the cylinders are not ordered periodically and their number stays rather small (filling factor of 0.1–0.2).

For photonic systems, most publications so far are focused on the stability of the band gap [94, 100, 101]. Other papers limit their calculation to a few cylinders, e. g. using a supercell [102] or a Multiple Multipole expansion [103]. A lot of work has been done in opals, where a lot of stacking faults and size fluctuations occur [104–106]. All these papers have in common that not too many realizations (ranging from a few to a few hundred) were used and no statistical analysis of the data has been carried out. It is, therefore, not certain, whether the discussed quantities, usually the averaged logarithm of the transmittance, describe the transmittance properly. Also the correspondence to electronic systems, except in the stop band, is not as straightforward. Beside the simulation of propagation in bulk PCs, disorder in functional elements, e. g. waveguides, and losses due to fabrication tolerances is studied often using only a few realizations in FDTD simulations.

In this work, transmittance distributions and their correct description in several regions of the spectra will be studied. This makes it possible to determine possible parameter ranges, for which a PC can be used in applications. The calculation of a database of  $S$ -matrices and the assembling of a crystal by the efficient  $S$ -matrix multiplication allows for the calculations of many realizations. The length can in principle be chosen arbitrarily without adding a lot of computational time by multiplying a longer sequence of  $S$ -matrices.

From the above discussion, one problematic aspect becomes clear already. Physically, a description using log-normal distributions might be favorable but on the other hand, in the consideration of the robustness of device performance narrow distributions in the transmittance (which are limited to values between 0.0 and 1.0) on a normal scale are required. One, therefore, always has to check both distributions to be able to comment on the properties of the PC and the possibilities to use it in a device.

## 4.9.2 Analysis of Distributions

One of the problems is how to study the distributions for several parameters in an efficient way and how to characterize them. This means determining the type (normal distribution, log-normal distribution or distributions following e.g. Levy-statistics, for which large changes in the quantity are more likely than in the other distributions and the tails become more important).

The most straightforward way is to calculate the distributions and then compare them with sample distributions having the same properties, e. g. mean and standard deviation. For this purpose two main tests are used: Kolmogorov-Smirnov and Anderson-Darling<sup>10</sup> [67, 107]. Strictly speaking these tests do not show whether two distributions are the same but they rather tell, whether they are different. Both these test rely on comparing the cumulated probability distribution using different methods, with the Anderson-Darling test giving more power to the tails. The well-known Chi-Square test should not be used for un-grouped data sets such as the continuous transmittance.

Since the mean and standard deviation of the distribution are determined from the data itself, the Kolmogorov-Smirnov test cannot be used and Anderson-Darling becomes the method of choice [67, 107]. For the implementation, Chapter 4.8 of [107](Empirical Distribution Function tests for the normal distribution with unknown parameter) in the case in which mean and standard deviation are determined from the sample has been employed. For comparison, the Kolmogorov-Smirnov test has been implemented as well following Chapter 14.3 in [67] although it is not recommended. The principal aim was to use the results of these tests to create a map describing what reference distribution is best suited to describe the transmittance fluctuations in the 2D parameter space given by frequency and length. Together with the mean and standard deviation this data can be used to determine ranges in which the crystal can be used in applications. Adaption had to be made since the transmittance and, therefore, the distributions are limited to the range from 0.0 to 1.0. Consequently, the cumulated distribution was adapted to reflect these limitations.

Unfortunately, this approach failed due to the uncertainty in the results of the statistical test. Testing the tools with distributions generated using routines in [67] by creating “meta-distributions” failed. In this context, meta-distributions mean that a number of  $M$  distributions each containing  $N$  random numbers has been produced. For each of these  $M$  distributions, the Kolmogorov-Smirnov and Anderson-Darling test has been performed, giving a significance of  $p_M$ . These  $M$  numbers have then been analyzed to yield an average result and a standard deviation for the two methods comparing numbers created with the same random number generator. Even for  $N = 10^7$  points in the distribution, these tests return all possible results for the significance  $p$  if more than  $M = 100$  presumably equal distributions are compared with a reference. Therefore, an automated analysis in the frequency-length plane is

---

<sup>10</sup>Other statistical tests, which only allow to compare selected properties, such as the Student’s t-test (mean) or F-test (variance), are not considered.

not possible. For completeness the Chi-Squared test has been tested as well with equally bad results.

### 4.9.3 Manual Selection of Distributions

Since an automatic distribution analysis is impossible, a manual procedure has to be used. For practicability, the number of analyzed distributions has to be limited and some representative points have to be chosen. For this the perfect transmittance was calculated for a number of lengths and specific points selected from corresponding spectra. Fig. 4.19 shows these points for 3 different lengths ( $N = 1, 5, 10$ ) which will be discussed later. Other values ( $N = 3, 20$ ) show similar results and are not included discussed here. The frequencies were selected to represent minima and maxima of the transmittance as well as points on the edge and the middle of the stop band. In addition, 300 equidistant points in the range of 0.1 and 0.7 are used to give an impression of the behavior in all parts of the spectra.

### 4.9.4 Distributions

In the following, the transmittance distributions are discussed using a crystal with a length of  $N = 5$  and radius fluctuations of  $\pm 5\%$  as an example. In later sections the result for different lengths and fluctuations strengths is presented. A length of 5 unit cells corresponds to the length scale which is mostly used in applications, e. g. as separation between elements. This length is chosen because it corresponds to the length after which the transmittance is assumed to be inhibited in a stop band. For each setup (frequency, length, disorder strength) 1000 realizations are computed. Testing some of the distributions with larger numbers showed that changes occur until about 500 realizations and that the key quantities, including tails, vary little for a larger number of realizations. The calculation of realizations using the database is a lot faster than setting up the database, so that 1000 realization can easily be calculated to be sure that the distributions converged although a smaller number would have been sufficient.

Since an automated analysis is not possible and not all distributions can be analyzed in detail, other parameters allowing to access the distributions qualitatively are introduced and only sample transmittance histograms will be shown. The histograms are produced by binning the data<sup>11</sup> in 100 bins ranging from  $-3\sigma$  to  $+3\sigma$ . Data points outside of this range are counted in the bins corresponding the lowest-/highest values. In all histograms, the actual data is shown in red, whereas the black curve corresponds to the theoretical distribution with the average and standard deviation of the actual data to allow for a comparison.

---

<sup>11</sup>All other parameters and the statistical test are calculated using un-binned data.

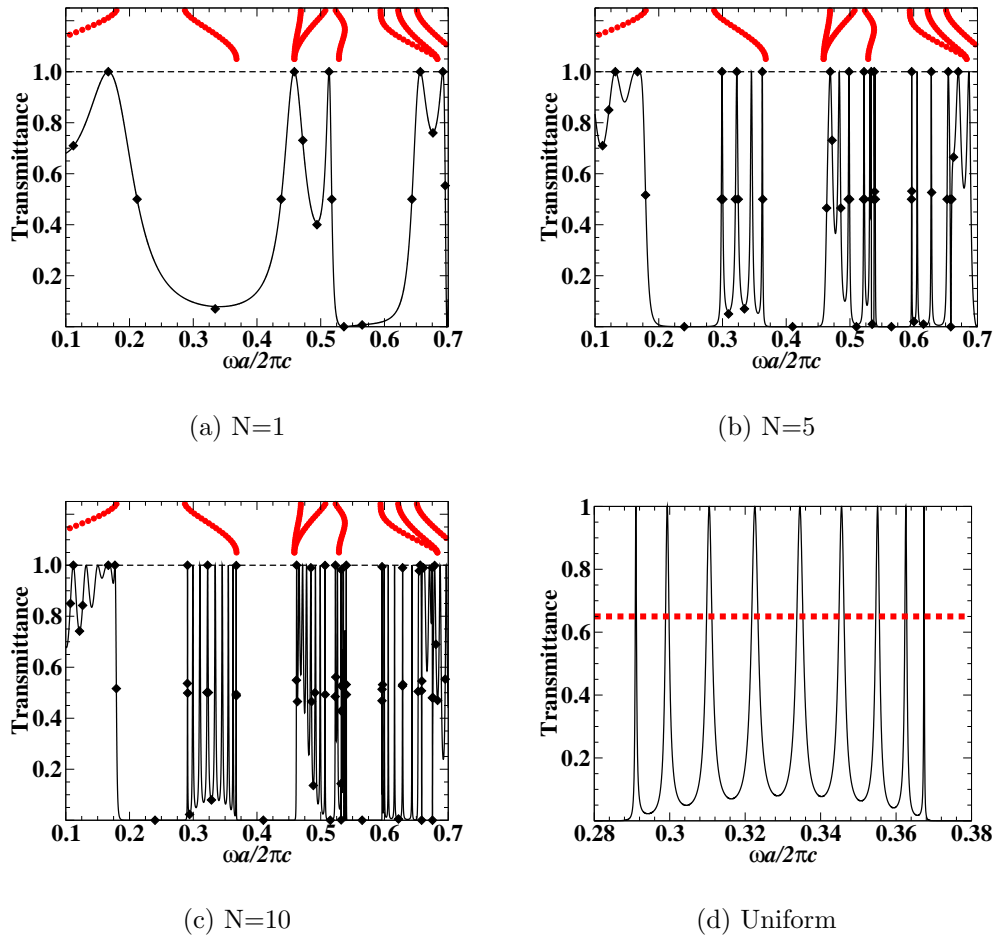


**Figure 4.19:** (a)-(c) Selected frequencies at special points (minima, maxima or mid-points of Fabry-Perot resonances or at the edge/middle of the stop bands) shown as dots.  $N$  describes the number of the unit cells used. The black line belongs to the transmittance through a perfect structure and the red dots indicate the band structure. The increase of the transmittance does not always start at the upper band edge ( $\omega \approx 0.26$ ) which is due to the finite length. With increasing length, the transmittance starts at the band edge. (d) Parts of the uniformly distributed frequencies shown as red dots for the second band. The transmittance curve belongs to  $N = 10$ .

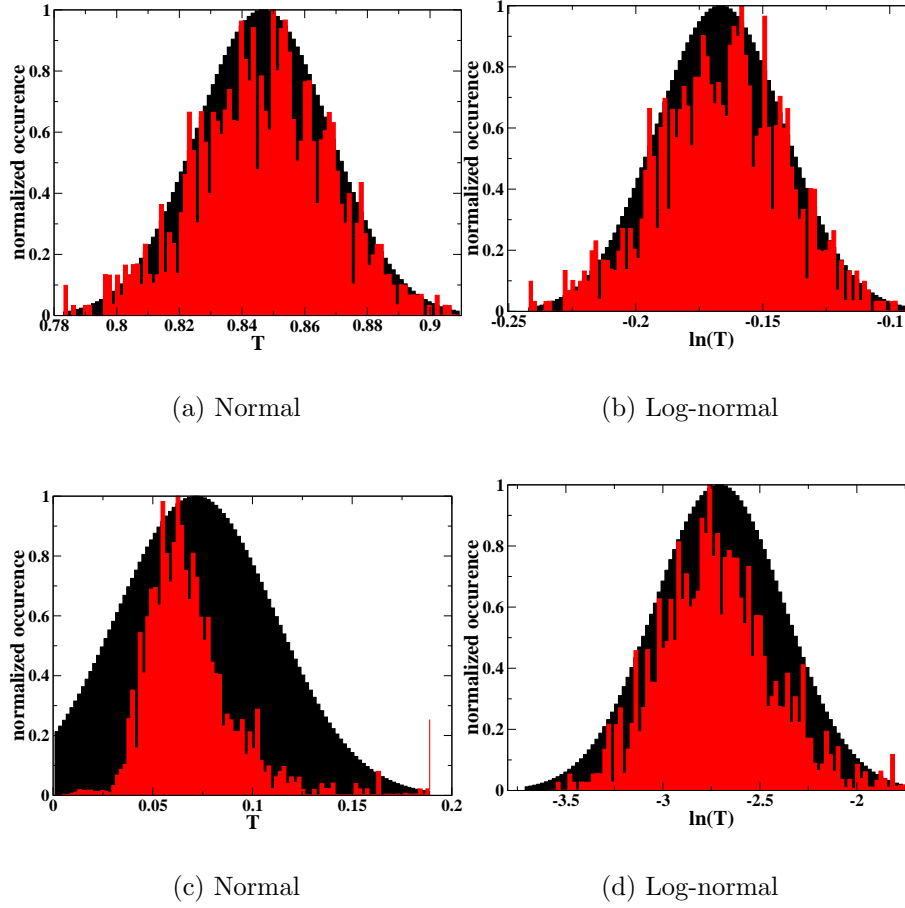


**Figure 4.20:** Distribution of the transmittance and the logarithm of it for a 5 unit cell long crystal at  $\omega = 0.12163$  (a)+(b) and  $\omega = 0.30949$  (c)+(d). The red curve shows actual data, the black curve the theoretical distribution with the average and standard deviation calculated from the actual data.

### Normal and Log-normal Distributions

Fig. 4.20 and Fig. 4.21 show normal and log-normal distributions for four frequencies. The lowest frequency (Fig. 4.20 a,b ) is below the first stop band and both distributions seem to be equally good. However, in the second band (Fig. 4.20 c,d) the normal distribution is not fitting as was motivated in the beginning of this section. In the narrow 3<sup>rd</sup> stop band (Fig. 4.21 a,b), which closes in the band structure with several radii (Fig. 4.9) the same situation occurs. For even higher frequencies, the normal distribution consists of a narrow peak close to a zero transmittance with a very wide tail spanning the entire region 0.0 – 1.0 (Fig. 4.21 c,d).

This will be shown again in the plots that analyze the distributions. These pictures already show the best correspondence for the normal case in each part of the band structure. It is obvious that one cannot use the terms average and standard

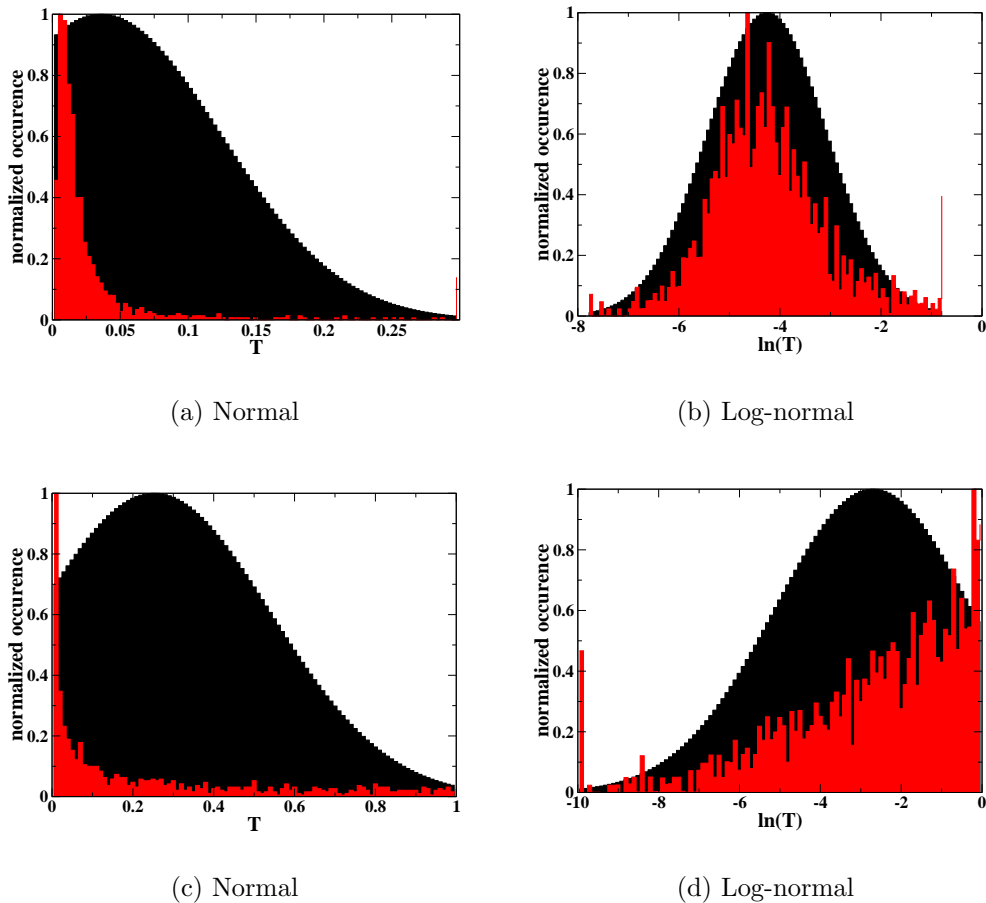


**Figure 4.21:** Same as Fig. 4.20 at  $\omega = 0.51004$  (a)+(b) and  $\omega = 0.65825$  (c)+(d).

deviation to describe the normal distribution of transmittance in a PC with fluctuating parameters. Using the average and standard deviation for the log-normal distribution seems so far to be valid in these examples.

### Typical Log-normal Distributions

For a more detailed study, representations of log-normal distributions are shown in Fig. 4.22. The frequency ranges for which these distributions are typical are listed in Tab. 4.2.

From the distributions it is immediately clear that also a log-normal distribution fails to describe the actual data for many frequency ranges.

It can, however, be used for most parts of the first band, excluding the maxima of the Fabry-Perot resonances. At the maxima the distribution is peaked at  $\ln(T) = 0$  corresponding to  $T = 1.0$  with a long tail as in Fig. 4.22(a). Comparing the black distribution with the average and standard deviation determined from the data and the actual data, a correspondence can only be found for stop bands 1–3, although the

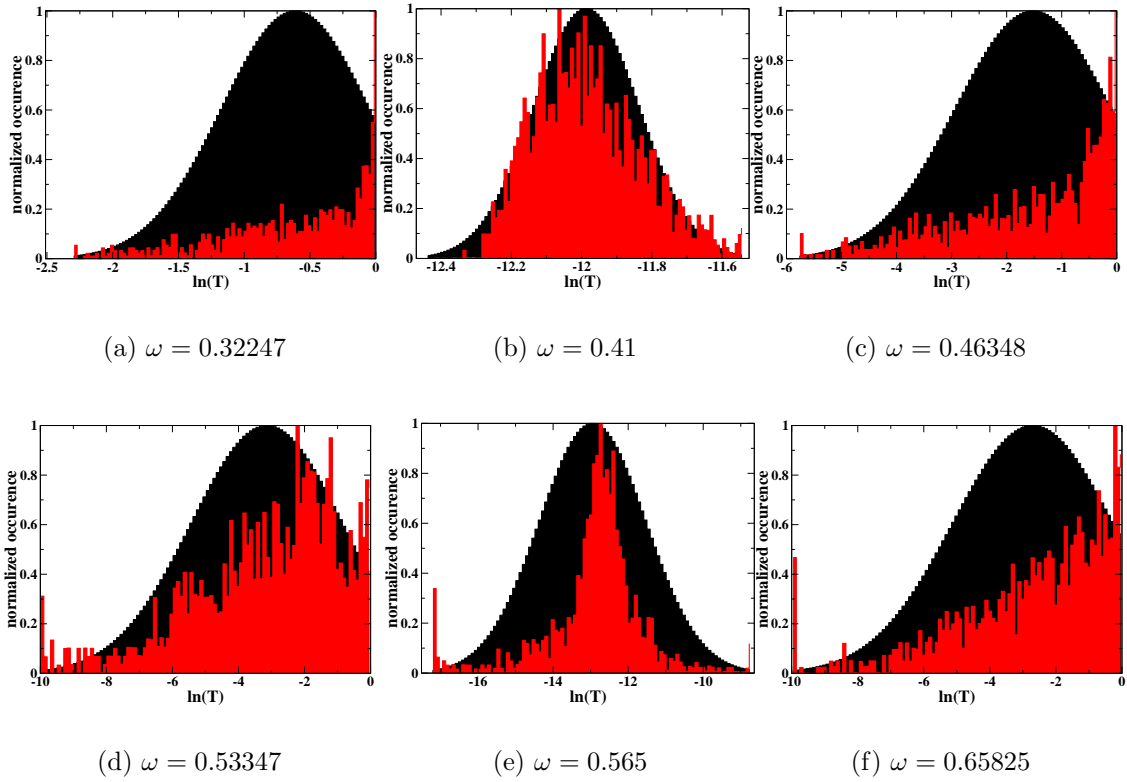


**Figure 4.22:** Representations of log-normal distribution at different frequencies above the first stop band. Tab. 4.2 lists the frequency ranges for which these types of distributions are typical.

Figure	Frequency $\omega$	Description of typical situation Min/Mid/Max := Minimum/Middle/Maximum of Resonances
Fig. 4.20(b)	0.12163	Min & Mid of 1 <sup>st</sup> band incl. Mid of band edge, 1 <sup>st</sup> stop band
Fig. 4.20(d)	0.30949	Min 2 <sup>nd</sup> band
Fig. 4.21(b)	0.51004	3 <sup>rd</sup> stop band
Fig. 4.21(d)	0.65825	All frequencies in the 5 <sup>th</sup> band
Fig. 4.22(a)	0.32247	Mid & Max 2 <sup>nd</sup> band, Max 1 <sup>st</sup> band with a narrower distribution
Fig. 4.22(b)	0.41	2 <sup>nd</sup> stop band
Fig. 4.22(c)	0.46348	All frequencies in the 4 <sup>th</sup> band,
Fig. 4.22(d)	0.53347	All frequencies 3 <sup>th</sup> band with a narrower width but same shape
Fig. 4.22(e)	0.56515	4 <sup>th</sup> stop band
Fig. 4.22(f)	0.65825	All frequencies in the 5 <sup>th</sup> band (same as row 4)

**Table 4.2:** Description of the log-normal distributions shown in different figures with the typical frequencies for which distribution with the same shape and width appear. This table is not valid for the normal distributions in Fig. 4.20 and Fig. 4.21. See text for more detail.

distributions are not perfectly symmetric and higher transmittance is more likely than described by the black distributions with the opposite being true for lower transmittance. For the 3<sup>rd</sup> stop band (Fig. 4.21(b)) this is surprising, since the band structures for the different radii occurring in the distribution overlap.

The 3<sup>rd</sup> differs from 1<sup>st</sup> and 2<sup>nd</sup> stop band in the average transmittance. Whereas the average values for stop bands 1–2 correspond to the values of the perfect structure, in the 3<sup>rd</sup> stop band this value is magnitudes larger and it is shown later that the stop band disappears on a non-logarithmic scale. In contrast, the 4<sup>th</sup> stop band (Fig. 4.22(e)), which is much wider, has an average around the value of the perfect structure but the distribution exhibits wide tails on both sides. The different behavior of the 3<sup>rd</sup> and 4<sup>th</sup> stop band can be explained by their different width.

The 3<sup>rd</sup> stop band is very narrow and can be closed already by small deviations, leading to an increased transmittance compared to the perfect structure. The wide log-normal is then caused by those parts in the crystal, where the deviation is very small and the stop band is still present. In the 4<sup>th</sup>, much wider stop band, most configuration will have exponential decaying modes, leading to a narrow peak at low transmittance. Only the rare configuration with significant radii fluctuation throughout the crystal will, however, show a strong deviation of this value, giving rise to tails. Comparing Fig. 4.21(b) and Fig. 4.22(e) shows that the plotted range has the same width but the peak width is different and it is centered at different values of  $\ln(T)$  in accordance with the above interpretation.

Taking into consideration the rest of the plots, frequencies for which the log-normal distribution is not suited can be identified. This includes the maxima of the Fabry-Perot resonances in any band as well as mid-points of these starting from the 2<sup>nd</sup> and any distribution for any frequency in and above the 3<sup>rd</sup> band. Looking more carefully at the total width of the distribution shows that they become wider with higher bands. In the 2<sup>nd</sup>, the logarithm for the maximum and middle values ranges from approximately -3.0 – 0.0. At the edges of the 2<sup>nd</sup> stop band as well as in the entire 3<sup>rd</sup> band they span a range from -6.0 – 0.0. For higher bands the minimal transmittance value decreases from -6.0 to -12.0 in the 4<sup>th</sup> band and higher up in frequency all the distributions look alike as the one in Fig.4.22(f). Some of these distributions show a slightly better comparison to the log-normal, but their width stays constant. Since the range -3.0 – 0.0 in the logarithm already corresponds to 0.05 – 1.0 for the normal transmittance, these structures cannot be turned into devices at these frequencies since the distribution spans the whole range of available transmittance values. All analyzed distributions are shown in the appendix (Chapter A) to ease the understanding of the presented summary of their behavior.

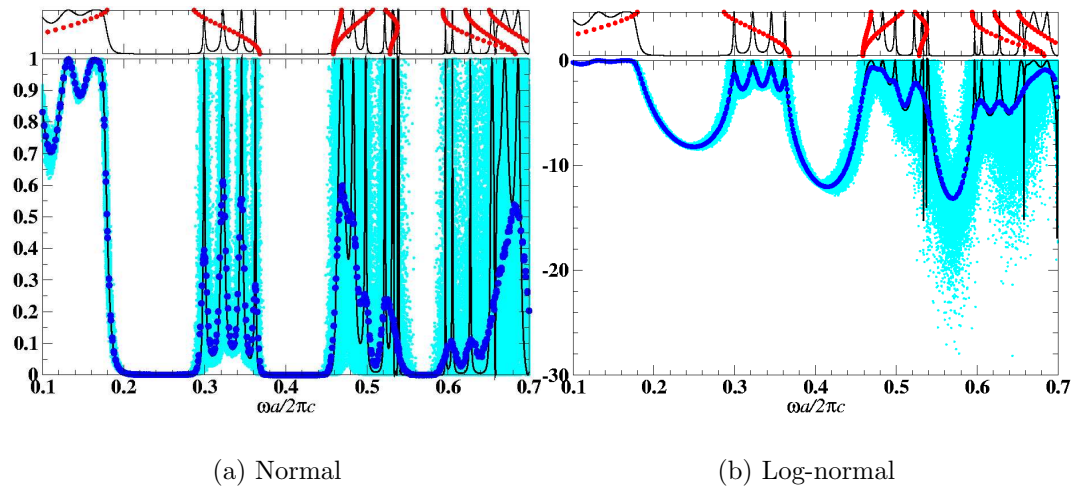
Authors of previous works were mostly looking only at the averaged logarithm of the transmittance and in very few cases the standard deviation was included as well. Since in addition, a small number of realizations (a few up to a few hundreds) were used which will not allow for the formation of significant tails, these results need to be interpreted taking into account that the description of the distribution only by the 1<sup>st</sup> moment (average) is inaccurate. Even adding the standard deviation, or equivalently the 2<sup>nd</sup> moment, is not improving the results if the distribution can not be described (reproduced) using these parameters. Therefore, in the following, other figures of merit will be used to discuss the distributions.

### 4.9.5 Description of Distributions

In order to access the characteristics of the distributions several quantities, are introduced and studied in this section. The aim is to formulate conclusions about the properties without inspecting each distribution in detail.

As a model system a crystal with a length of 5 unit cells and 5% radius fluctuations is used in the beginning and 1000 realizations are studied for selected frequencies at special points in the transmittance (minima, maxima,...) as shown in Fig.4.19. In addition, 300 equidistant frequency points in the range  $\omega = 0.1, \dots, 0.7$  are used and the impact of length variation and percentage variation is discussed at the end.

The following plots always look similar to the one presented in Fig.4.23. At the top the band structure and the transmittance through the perfect structure is shown for comparison. In the main part of the plot, the quantity of interest is plotted. They are discussed using a normal distribution, which is important for devices, and the log-normal, which is better suited to describe the distributions and corresponds to the physical more meaningful quantity.



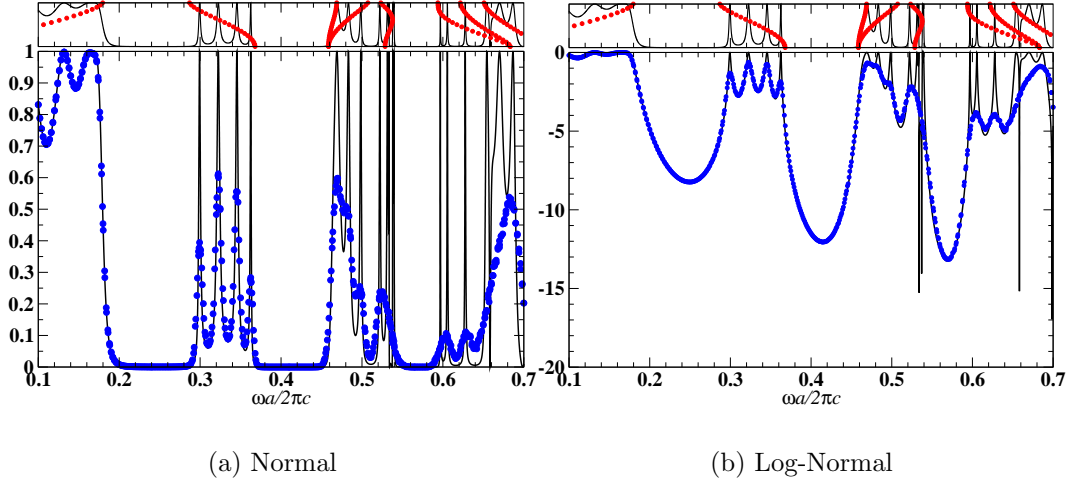
**Figure 4.23:** Top: Band structure (red dots) and transmittance for a perfect structure with a length of 5 unit cells used as a marker in all plots in this section. Bottom: Transmittance through a perfect structure (solid black curve), average of transmittance of the individual distributions (blue dots), all 1000 transmittance values per frequency (cyan dots) as an overview over the occurring transmittance values.

Fig. 4.23 shows all occurring transmittance values on a log and on a linear scale and several things are noticeable. The average is plotted as well but is discussed later.

The first observation is that the width of the distribution is in general increasing with increasing frequencies, since the system becomes more and more sensitive to deviations as the wavelength decreases.

In the log-plot of the first two stop bands, the short wavelength side is more sensitive. The least sensitive frequency can be found in the middle of the stop band, not at position of the smallest transmittance. On the right side of each stop band, significant broadening can be seen as compared to the left. Asastryan et al. [92] reported the opposite in systems of rods in air in which they studied fluctuations in the refractive index. They found a higher sensitivity at the low frequency band edge. However, their interpretation can not be used here and does not contradict the findings. They stated that the field is concentrated in the cylinders at the lower band edge and in the low index (air) area at the upper band edge and attributed the stronger effect to the concentration of the field in the disordered cylinders at the more sensitive side. This statement is, however, not true in the case discussed here, because all considered bands are dielectric bands. An explanation for the higher sensitivity to disorder at higher frequencies could be the higher resolution associated with a shorter wavelength. Small deviations can be resolved better at the upper band edge and cause stronger deviations.

Outside the stop band, the distributions follow the perfect structure closely in



**Figure 4.24:** Bottom: Transmittance through a perfect structure (solid black curve), average of transmittance of the individual distributions (blue dots).

the 1<sup>st</sup> band as well as the 1<sup>st</sup> and 2<sup>nd</sup> stop band. The features of the 2<sup>nd</sup> band can still be estimated from the distributions but any structure in the transmittance for frequencies higher than the 2<sup>nd</sup> stop band is completely washed out, except for the 4<sup>th</sup> stop band, which can be identified at the center frequency. Especially the 3<sup>rd</sup> stop band and the isolated band above do not exhibit distinct features in the transmittance distributions. Although the distributions at the maxima of the Fabry-Perot resonances can not be described by the normal or log-normal distribution they are at least as narrow as the well described ones in their vicinity. Their deviation from a well-behaved distribution can be explained by the very high transmittance of approximately 1.0, which does not allow for higher transmittance values to occur and, consequently, leads to an asymmetric distribution.

Omitting the realizations, one can look at the average of the two distributions in more detail (Fig. 4.24). It qualitatively follows most of the main features as can be seen from the log-plot. In general, the minima are reproduced quite well, although the transmittance is slightly higher. The resonances are strongly reduced. From the high frequency resolution it is also clear, that smaller features are not reproduced.

In previous results, it was concluded that the PC is surprisingly stable with disorder based on the averaged logarithm of the transmittance. A detailed analysis of the Fabry-Perot peaks has never been done. Even for Fabry-Perot resonances, the conclusion based on the average transmittance would be, that the maxima are only slightly reduced. Comparing with the actual transmittance values in Fig. 4.23 leads to a different conclusion. The structural features of the transmittance spectra, including the 3<sup>rd</sup> stop band are washed out completely due to the wide distributions. Despite the fact that the average stays surprisingly stable, the PC generates a very wide distribution of transmittance values. Each individual representation of the PC is therefore very sensitive to disorder.

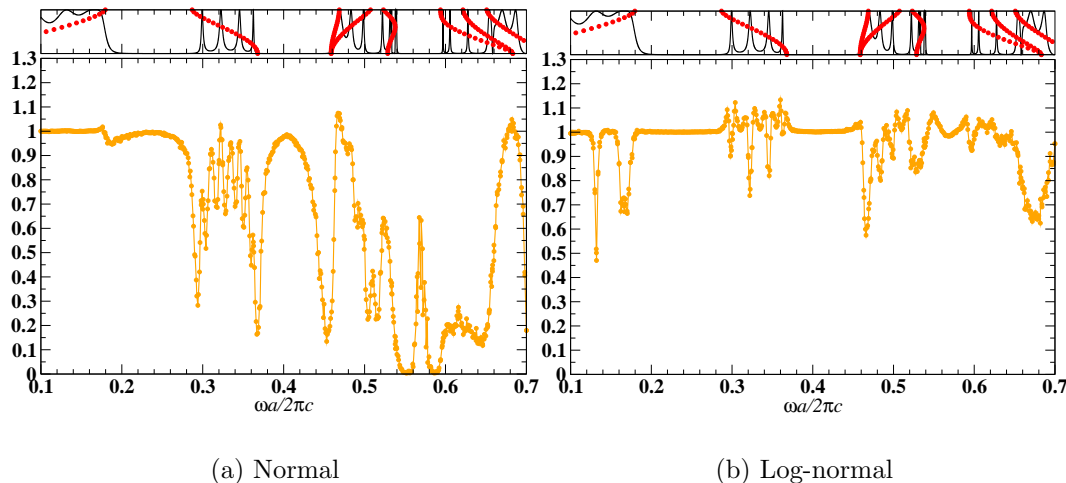


**Figure 4.25:** Median of the distribution divided by the average. For a symmetric distribution the two values are equal. In non-symmetric cases the median gives more weight to the area in the tails (number of realizations), whereas the mean gives more weight to the length of the tails (distance).

To characterize the symmetry of a distribution the mean and the median can be compared. For a symmetric distribution the two values are equal. In other cases the median gives more weight to the area in the tails (number of realizations), whereas the mean gives more weight to the length of the tails (distance). A median higher than the mean is caused by having only a few points in the lower tail which are spread out far. Looking at Fig. 4.25 one can immediately see that for the normal distribution these values differ substantially with the median usually being smaller than the mean value. For the log-normal distribution all maxima can be identified by dips in the curve. This means that many points are below the average but still close to it, in accordance with the above statement that the distribution is not log-normal but narrow. It is also visible in the log-plot that at the band edges the mean is smaller than the median, showing that many points are above the average but some points are far below.

The 3<sup>rd</sup> stop band, which vanishes completely, shows this effect very strongly and in the 4<sup>th</sup> the ratio of mean divided by average reaches 1.0 only in the middle. For values in the 3<sup>rd</sup> and 4<sup>th</sup> band the two values differ for all frequencies.

From the standard deviation and the standard deviation divided by the average plotted in Fig. 4.26 in green and magenta, respectively, one can estimate the width of the distribution<sup>12</sup>. If the standard deviation becomes larger than the average the description with the given distribution fails. In these cases the one-sigma-range around the mean would already contain negative (positive) values for the (logarithm)

<sup>12</sup>The term “estimate” is used on purpose here, since the standard deviation is only defined for (log-)normal distributions. In this case this quantity can, consequently only be used as an indicator for comparison.

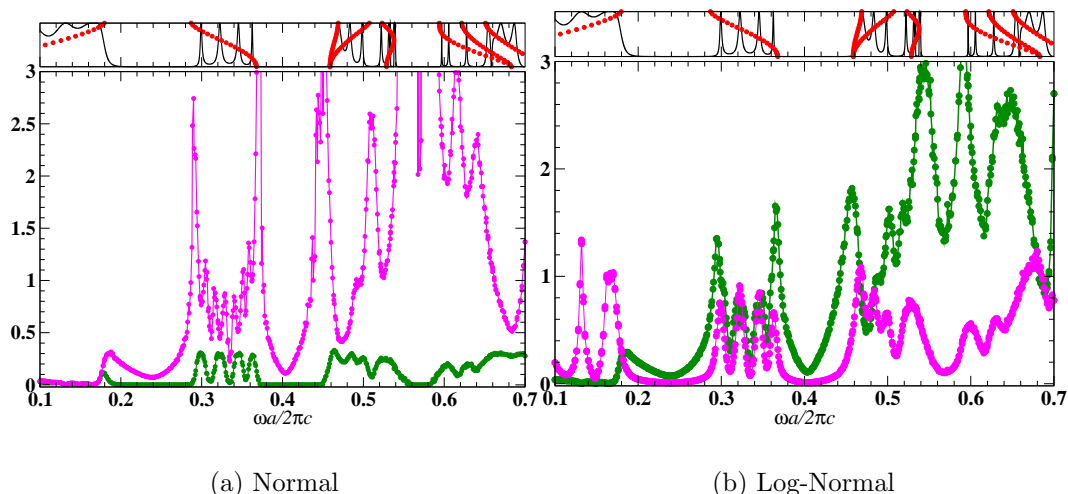


**Figure 4.26:** Standard deviation (green) and standard deviation divided by the average (magenta).

of the transmittance, which cannot occur. For the normal distribution this is the case at the upper band edge of the 1<sup>st</sup> stop band and for higher frequencies. For the log-normal distributions this happens already at the maxima in the first band, but this is caused by the very high transmittance which has a very low logarithmic value close to 0.0<sup>13</sup>. Together with the asymmetric distribution, the peak occurs although the standard deviation is very small. It is a consequence of the description of a non log-normal distribution by an average of the logarithm and a standard deviation. For the log-normal the ratio is smaller than 1.0 in most areas, however a value of 0.5 already states that  $\pm\sigma$  covers a very large transmittance range.

The standard deviation and the normalized standard deviation show the same peaks as the transmittance and they are especially strong at the edges of the stop bands. Again the high-frequency side has a higher standard deviation due to the wider distribution.

Using the 4 quantities (realizations, average, median, and standard deviation) above together with the distribution histograms presented before, a clearer picture can be developed for disorder in PCs. None of these parameters by itself can describe the distributions, since they are not normal or log-normal in most of the cases, but together they can be used as an indicator for the distribution even if the exact type is unknown. Further quantities that could be studied are the difference between the minimum and the maximum of the distributions giving the total width. This width can also be identified from the plots of all the realizations (Fig. 4.23). An additional remark on a possible improvement regarding the distribution will be made in the outlook section, since studies for other distributions than normal and log-normal are

<sup>13</sup>Dividing by it always leads to high values for the normalized transmittance. Compare also the discussion of these points in the previous paragraphs.

not included here.

### 4.9.6 Impact of Absorption

Now that 4 quantities for describing the distributions without examining all histograms are identified, parameters and their impact on the transmittance distributions can be studied. In the first case, absorption is added to the substrate by introducing an imaginary part into the permittivity of silicon  $\varepsilon = 11.9 + i0.01$ .

From Fig. 4.27 one can see that the transmittance reduction due to absorption is very small. This is owed to the short crystal length. For longer crystals, absorption might become more important and the transmittance distributions might be dominated by the exponential decay<sup>14</sup>.

The small reduction in the overall transmittance “improves” the transmittance distribution at the maxima in the log-normal description, since the modulus of logarithmic average becomes larger and values of  $\ln(T) \approx 0.0$  are avoided. This is visible in the plots of the median divided by the average (Fig. 4.27(d)). Especially in the lowest band this is also visible in the standard deviation divided by the average (Fig. 4.27(c)).

It can be concluded that small material absorption improves the quality of the distribution in terms of getting them closer to a log-normal distribution by lowering the impact of the Fabry-Perot resonances.

### Length Dependence

For the use of PCs the length dependence of the transmittance is an important quantity. In Fig. 4.28 several of the indicators are plotted for 4 different lengths (3,5,10 and 20 unit cells). There are no major changes in the behavior but some aspects need to be looked at in more detail. For longer crystals the Fabry-Perot resonances become closer and their maximum values drop with the length for frequencies higher than the 2<sup>nd</sup> band. Also the transmittance in the stop bands drops and the band edge becomes sharper. The average still follows the values of the perfect structure for the first band. In the second band for longer crystals the average values at the minima are increased more compared to the perfect structure than for shorter crystals so that the resonances show smaller oscillations. At the stop band edge the Fabry-Perot peaks disappear and the curve is smeared out, starting to decrease into the stop band earlier than in the perfect case. For higher bands (3<sup>rd</sup> and up) the average approximately follows the minima of the resonances and no other structural features of the transmittance are reproduced. The realizations are scattered as in the case discussed before.

The standard deviation increases with length, especially at the stop band edges. In addition, more and more peaks are visible. The middle of the stop bands is only weakly affected, but the region of small standard deviation becomes narrower. In

---

<sup>14</sup>This situation has not been studied since it would be uninteresting for experiments or applications because of the high losses.

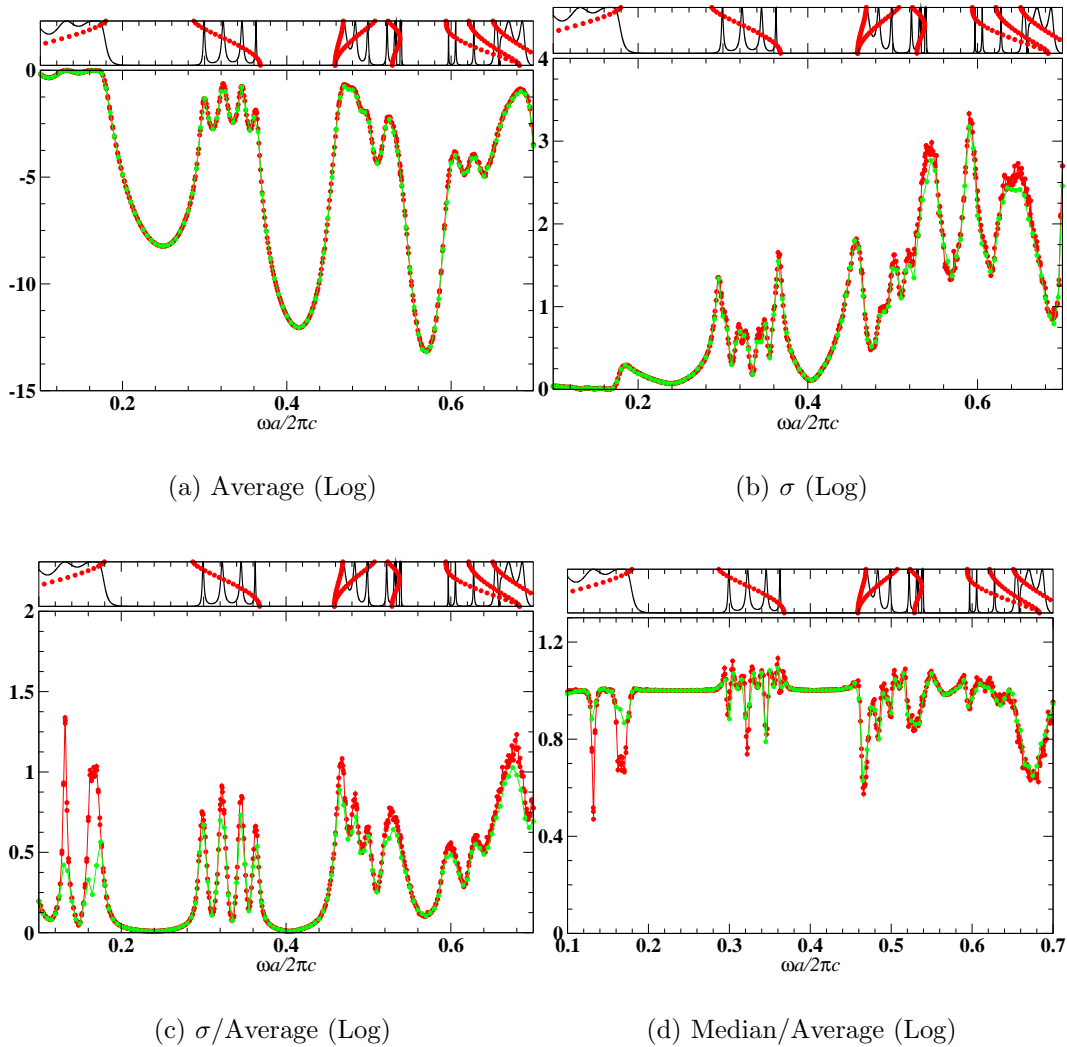


**Figure 4.27:** Impact of absorption in the substrate ( $\varepsilon = 11.9 + i0.01$ ) on the log-normal distribution. The red curve is without absorption, the green has absorption included. For the absorption only distributions at the selected frequency points Fig. 4.19 are used.

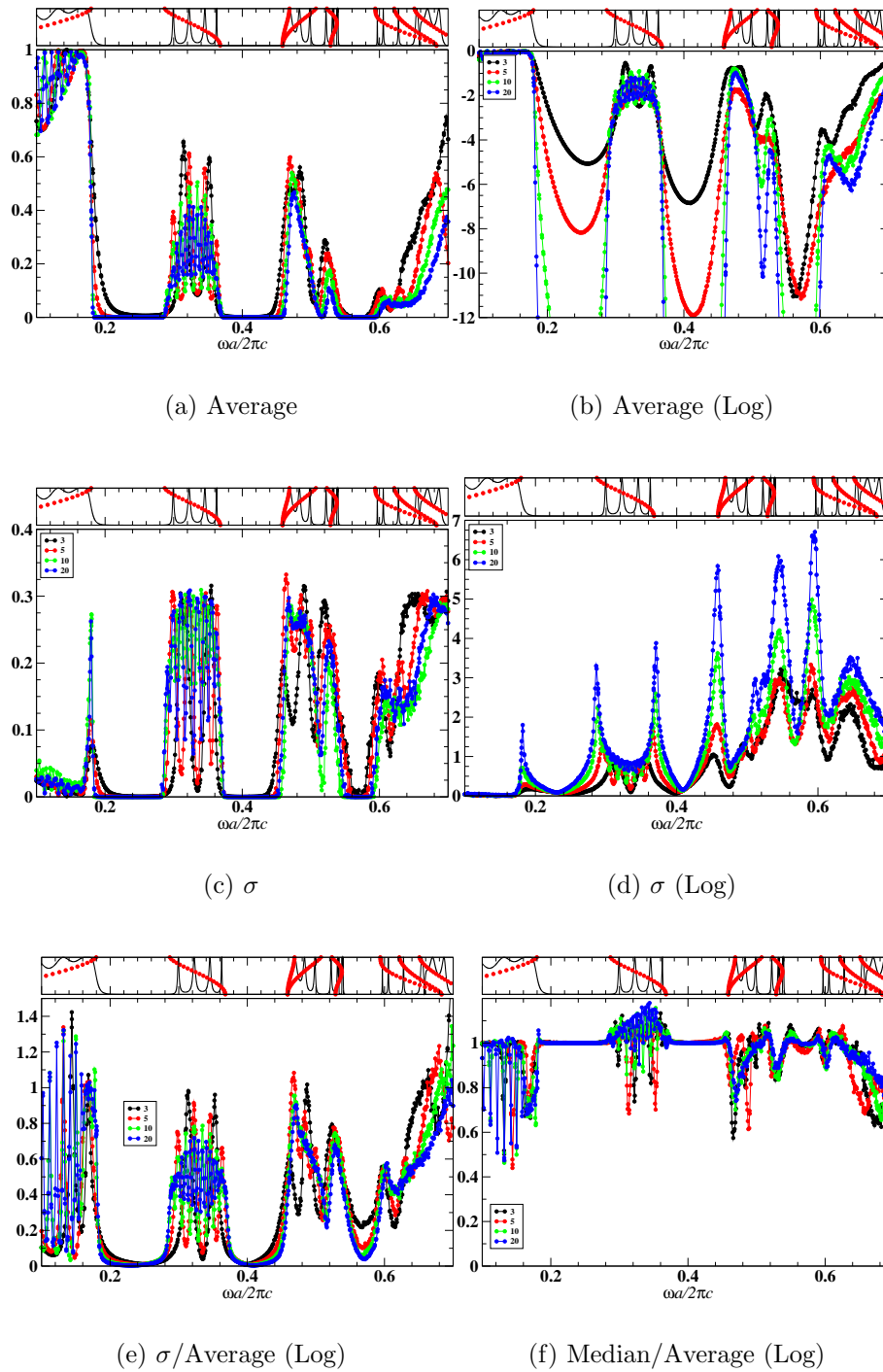


**Figure 4.28:** Length dependence for several lengths (black=3 unit cells, red=5 (as before), green=10, blue=20). The corresponding transmittance spectra for the perfect crystals can be found in Fig. 4.19.

other words, although the stop band edges becomes sharper in the perfect structure, the opposite is the case for the distribution of the disordered structure. This is especially visible in the plot of the normalized standard deviation ( $\sigma/\text{average}$  in Fig. 4.28(e)). The appearance of the slightly disturbed Fabry-Perot peaks in the first band leads to many peaks in the normalized standard deviation and median. Although the height of the peaks of these indicators does not increase, they become closer (Distance between two peaks is expected to scale with  $\frac{1}{N}$ ,  $N$  being the length), leading to large fluctuation of the indicators outside the stop bands.

As a summary, one can conclude that building longer structures makes the transmittance in the bands more complicated due to closely spaced resonances. The stop band edges and the distributions in these areas become much wider, whereas the transmittance in the middle of the stop band drops significantly with the distributions staying centered and having a small width. In the parameter range studied, no significant drop in the transmittance with length, which could be attributed to localization, can be identified. Around  $\omega \approx 0.65$  is the only region, where a monotonic drop of transmittance with length is visible. For a detailed analysis the simulation of length dependent systems (Sec. 4.5) would have to be combined with the database approach to determine a localization length, if such a description is possible. Increasing the fluctuation in this approach should reveal different regions of transmittance from weakly disordered to strongly localized.

### Different Disorder Strengths

The last parameter in this work is the disorder strength, or the distribution of the radius. The results for 3 different percentage values ( $p = 2\%, 5\%, 10\%$ ) are plotted in Fig. 4.29.

For low frequencies in the first band no significant changes are visible. The standard deviation is increased slightly with a higher percentage but the peaks in the normalized standard deviation and the mean stay approximately identical. For higher bands the transmittance peaks decrease with increasing disorder strength and the structure of the transmittance spectra disappears. The clearest signal of the increase can be found in the plots of the standard deviation. It is obvious from Fig. 4.29(d) that the band edges and higher bands are very sensitive to the increase of disorder. The same is true for the 4<sup>th</sup> stop band, in which the transmittance increases significantly at higher disorder. In general, however, higher disorder reduces transmittance.

### 4.9.7 Finite Size Scaling Using Supercells

The limitation of the above method is the assumption that all cylinders in one row are the same. In a disordered system this of course will not be the case. The validity of the approach can be tested using a supercell calculation and compare the results for different supercell sizes. Each supercell includes several of the unit cells for the

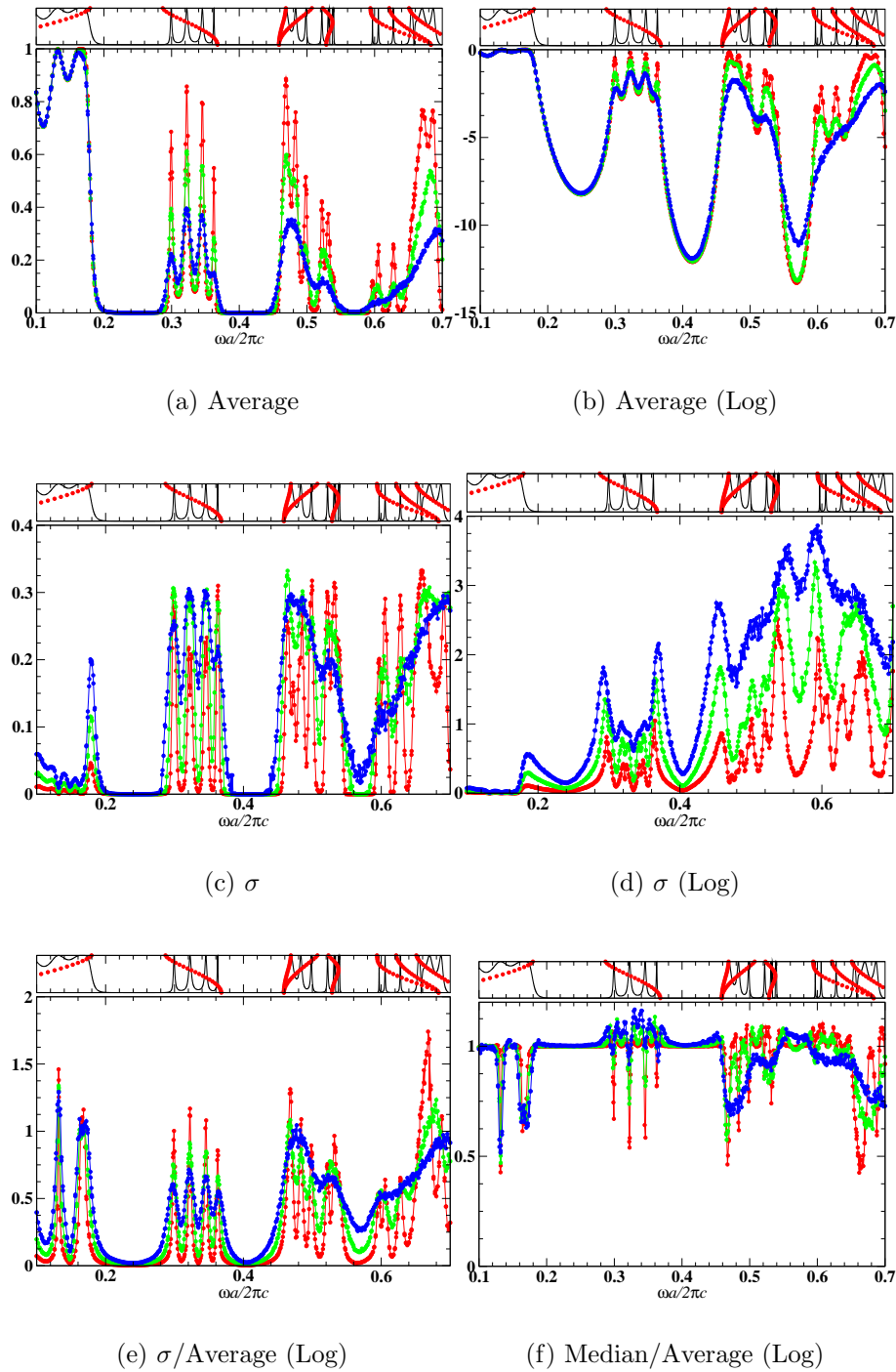


**Figure 4.29:** Dependence of the transmittance distribution of different disorder strength. (rot=2%, green=5%(as before), blue=10%).

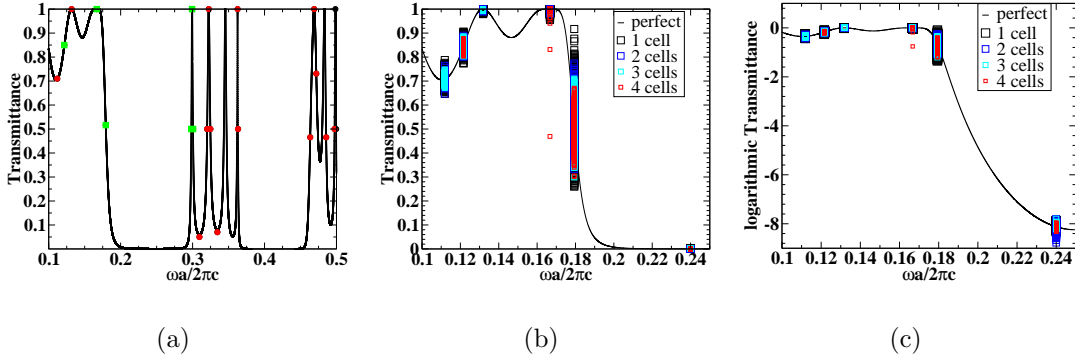


**Figure 4.30:** Used frequencies for the supercell calculation. Green squares - up to 4 cylinders, Red Dots - up to 3 cylinders used in supercell. Due to the required computational time only a few frequency points could be selected. (b) shows the transmittance values of all realizations for the supercells calculations. The narrowing of the transmittance distribution with increasing size of the supercell can be seen from the spread of the transmittance values. (c) Same as (b) but on logarithmic scale.

lattice (1D layers in this case) in the horizontal direction, as shown in Fig. 3.14. In contrast to the waveguide shown there, no cylinder is missing in this approach.

Since the number of required modes  $M$  scales linearly with the supercell size  $C$  and the computational time of the most expensive calculations scales as  $M^3$ , the frequencies for which the supercells can be tested is limited. The calculation for a supercell of size 2(3,4) required about 14(38,112) hours. In addition memory scales with  $M^2$  as well, so that only a limited number of machines was available for these calculations. For the larger supercell, the focus has been on the area of the spectra, where the transmittance can be described by a log-normal distribution, to test the results in these regions. For supercells with 2 cylinders the simulation was done for all frequencies. The distributions are included together with the available ones for supercells with 3 cylinders in the list of distributions shown in the appendix A. All supercell distributions can be found in the appendix B.

Fig. 4.30 shows the frequencies for which up to 4 (green squares) respectively 3 (red dots) cylinders were used in the supercell calculation. On the right side of the plot the transmittance values of all realizations are plotted. It is already visible that the distributions become narrower. In this frequency range, the wavelength is longer than 5 lattice constants, so that it samples several cylinders. If all of these cylinders are fluctuating around the nominal value, an averaging occurs, explaining why the supercell results tend to give better results in terms of narrow distributions. In Fig. 4.30(b) two distinct points for  $\omega = 0.16671$  are visible, which do not fit into this pattern. Unfortunately, no further study could be done to explain their occurrence. Their large deviation from the rest of the distribution is also visible, if one looks at some quantities of the distributions vs. the size of the supercell.

Fig. 4.31 shows the scaling behavior of the average, minima and maxima of the distributions together with the standard deviation and the normalized standard deviation as a function of the inverse of the supercell size  $C$ .

For convergence, the values should stabilize for  $\frac{1}{C} \rightarrow 0$  ( $C \rightarrow \infty$ ). As before the average remains very constant but the minimum and maximum still exhibit some changes. The general behavior is a narrowing of the distribution together with a decrease of the standard deviation. The shape of the distribution is approximately constant and the descriptive parameters also exhibit only minor changes, if the number of cylinders in the supercell is increased. Therefore, the description of disorder in the PC using the  $S$ -matrix approach is feasible for the studied frequencies. The distributions for higher frequencies shown in the appendix A also show a close correspondence between the simulations using a regular and a supercell with 2 and 3, respectively, cylinders, although a detailed study has not been conducted. Since the distributions are very wide for higher frequencies, only substantial changes would be detectable.

## 4.10 Conclusion and Outlook

The main conclusion of this chapter is, that a PC, even without any included functional element, is already a very complex structure, whose behavior is determined by many different factors. The lower stop bands are the only characteristic features which are stable to some extent to possible parameter changes. This includes deterministic parameters such as surface termination as well as pore size fluctuations. Higher bands are very sensitive to fluctuations and individual samples might show all allowed transmittance values in the range  $[0, 1]$  on a normal scale. For applications these areas, including higher stop bands, are, therefore, uninteresting. In the process of characterizing PCs by comparing experimental data with theoretical simulations, one has to focus on the low frequency areas and consider all parameters including, but not being limited to, the ones studied in this chapter in detail (length, surface termination, etc.).

The same considerations have to be included, if one wants to draw conclusions from calculated data. Calculations of a localization length by using the fit to an exponential as discussed in Sec. 4.5 in combination with disorder calculations need to be aware of the large amount of parameters which determine the distribution. If the length is changed for a fixed frequency, the transmittance might change from a minimum of a Fabry-Perot resonance to a maximum. This would result in a different sensitivity to radius fluctuations especially for very long localization length, when the Fabry-Perot oscillations are dominating the transmittance behavior. For the calculation of the localization length it is, therefore, not enough to insert results for a few length steps into eq. (4.1). This will very likely produce strongly fluctuating values, except for cases where the localization length is very short and no other effects, such as the Fabry-Perot resonances, are present in the length dependent transmittance. Reliable results can only be obtained by using a fitting technique

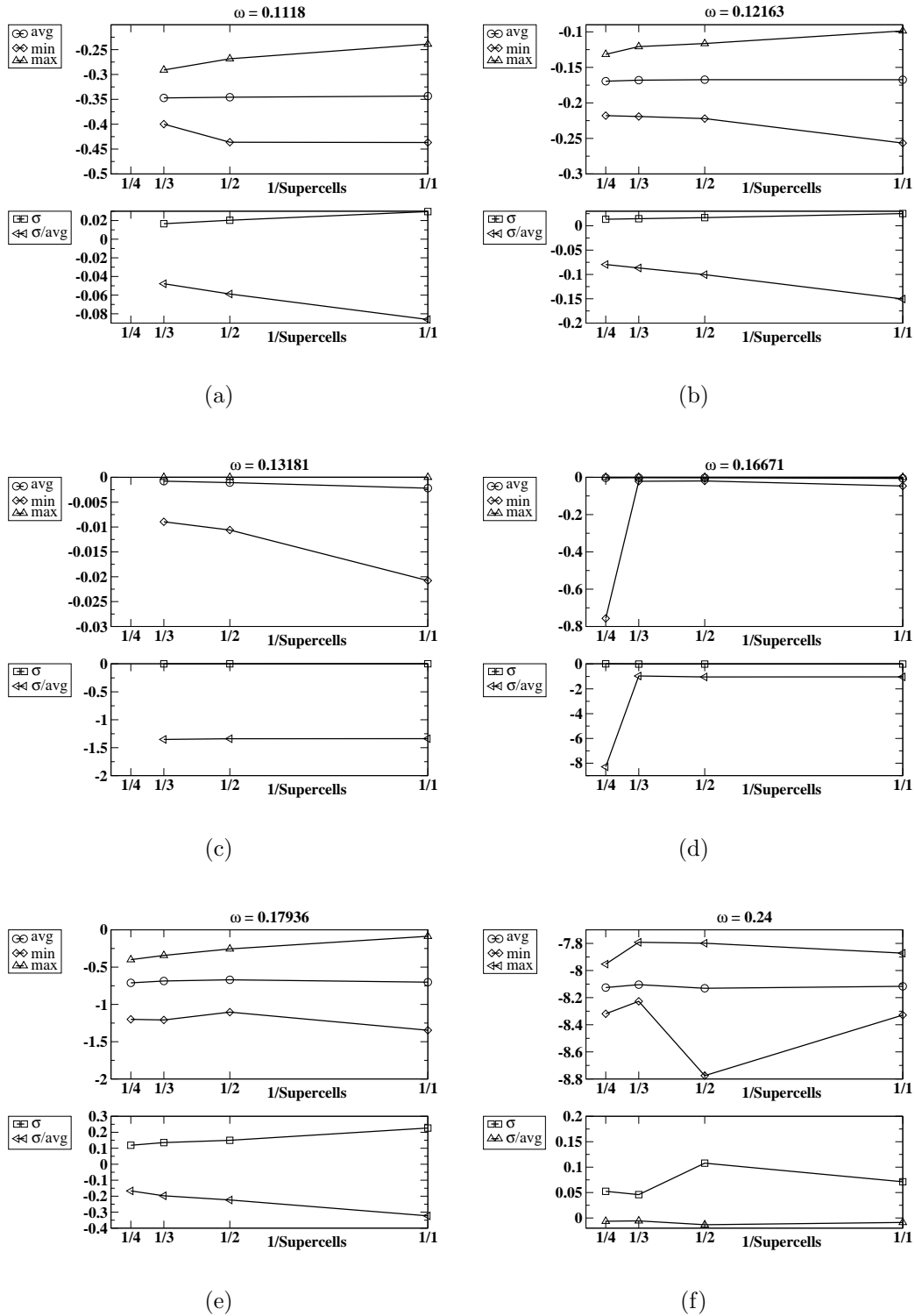


**Figure 4.31:** Scaling behavior of characteristic quantities. The median is skipped here, since it is always very close to 1.0 in this frequency range, except for  $\omega = 0.16671$ , where two strongly deviating points complicate the analysis.

(regression) and analyzing more indicators than the average to test assumptions on the distributions. In addition, all parameters discussed in this chapter (surface, absorption, etc.) change the observed spectra, and e.g. the localization length, in different ways depending on the frequency range. Any analysis has, therefore, to be done with great care, taking into consideration all points mentioned in this work.

The combination of the length dependent calculations with disorder, which could be easily facilitated through the  $S$ -matrix multiplication, would be a perfect tool to study the localization length for different frequencies and, hence, would be a very interesting combination of the individual questions addressed in this chapter.

Of course, the present results are limited to one system and one specific type of disorder as well as one polarization and can therefore only be taken as an example for studies concerning other systems. Disorder in the position would probably have a greater impact on the resonances, since the periodicity would be disturbed. This would be a challenging problem because the disorder has to include two parameter and a reasonable database would require an appropriate choice of positions.

For simulating experimentally realizable structures, this approach could be varied to calculate the spectra using one fixed disorder configuration for all frequencies, instead of calculating them independently for all frequencies. By calculating several of these disordered structures and comparing the spectra, the impact on a single measurement could be estimated, allowing for a better comparison between theory and experiment. There are various other possible studies, e.g. the analysis of each diffraction order individually, which could be done using the approach presented above. All of them have in common that a large set of data has to be reduced to some significant quantities to describe the properties of the PC.



# 5 2D Distributed Feedback Lasing

The first 3D structure is discussed in this chapter. Although it is not a PBG material it can be considered as a PC since the dielectric material is periodically structured.

The main goal of this project is the determination of the coupling to the quasi-guided modes of a corrugated waveguide to identify possible laser modes of the distributed feedback laser created by this structure. The laser itself has been fabricated and studied by Karen Forberich at the Fraunhofer Institute for Solar Energy Systems (ISE) in Freiburg [108]. In this chapter, the experimental work (Sec. 5.1.1) as well as the underlying effective laser theory (Sec. 5.2) are briefly summarized as a motivation for the simulations and characterizations. The parameters for the hexagonal system are introduced in Sec. 5.3 together with a comment on the effective parameters needed in the laser theory. Finally the presented method is used to estimate two of these parameters using the resonances of the waveguide. The findings explain the lasing under an oblique angle.

More detailed information about the experimental aspects of the project can be found in the dissertation of Karen Forberich [108] or Chapter 13 in [6].

## 5.1 Photonic System

The distributed feedback laser consists of an active polymer on top of a corrugated (height-modulated) substrate, which can, in principle, have a 1D or 2D pattern. In this study, only a 2D hexagonal patterning will be considered although a square pattern has also been used previously [109]. In Fig. 5.1 the structure is illustrated schematically. The shown profile corresponds to the simulated structure and the analytical form of the height profile used in the simulation will be given later.

The polymer area, including the corrugated part, is forming a waveguide and confines the light in the vertical direction. The periodic structure leads to coherent Bragg-scattering of the waves, with the first Bragg-order being coupled out vertically and the second order giving the in-plane distributed feedback needed for the laser. In the simulation the structure is terminated in the substrate. This is possible since the interesting effects happen in the waveguiding region. To simulate transmittance through such a structure, the deep but finite substrate would have to be considered, leading to changes in the absolute value of the transmittance. The aim of the work presented here is to determine the coupling strength to the quasi-guided modes of the optical active waveguide system. Consequently, only the resonances due to the waveguide are of interest and these are well described by this setup. A corresponding experimental realization is shown in Fig. 5.2.

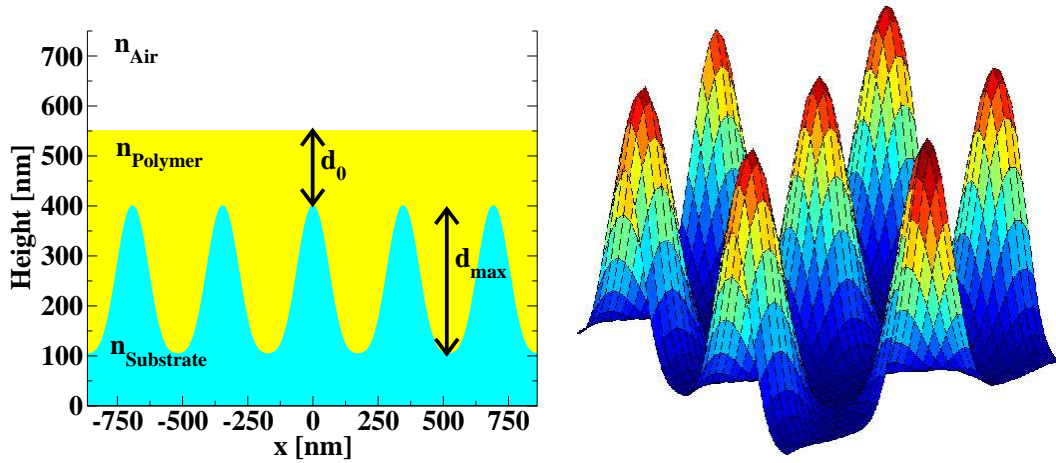


**Figure 5.1:** Left: Cut through the  $x$ - $z$ -plane of the structure as used in the simulation showing the substrate and the active polymer.  $d_0$  defines the thickness of the homogeneous top layer and  $d_{\text{max}}$  corresponds to the depth of the corrugated area. The structure is terminated in the substrate on the back side. Right: 3D surface plot of the structure showing the corrugation using values between 0.0 (blue) and 1.0 (red).

### 5.1.1 Fabrication

The laser is fabricated in several steps. Firstly, the periodic pattern is created in a photoresist using interference lithography (Fig. 5.3). For this, the beam of an Argon-ion laser ( $\lambda = 364\text{nm}$ ) is split into two coherent beams. These beams are then widened and directed onto the photoresist. The lattice constant  $a$  of the periodic pattern depends on the angle  $\vartheta$  between them

$$a = \frac{\lambda}{\sin \vartheta}. \quad (5.1)$$

A 1D periodic pattern can be created by a single exposure. For a 2D pattern at least two consecutive exposures steps are needed. Rotating the sample about  $90^\circ$  in

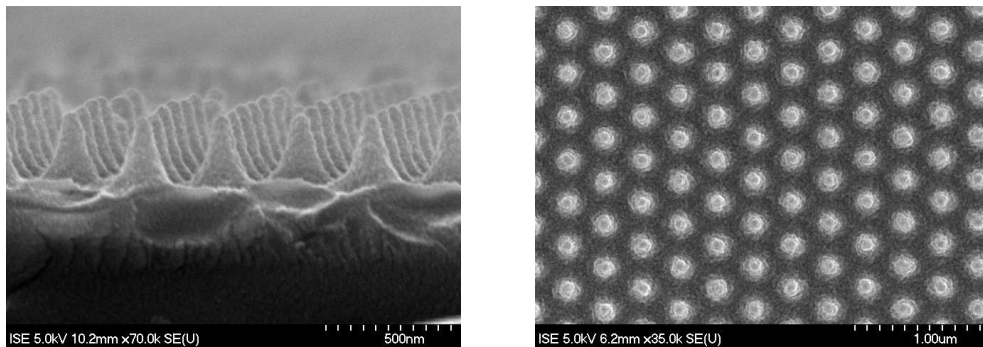


**Figure 5.2:** Side and top view of experimental realizations of the structure. Courtesy of Karen Forberich [108].

between the two exposures leads to a square lattice, whereas three exposure steps, each rotated by  $60^\circ$ , define a hexagonal lattice<sup>1</sup>. The photoresist is developed in areas, where the sum of the intensities of all exposure steps exceeds a threshold. The undeveloped part is then removed in a subsequent step. At the Fraunhofer ISE samples with up to  $1\text{m}^2$  with periodicities of a few hundred nm can be fabricated.

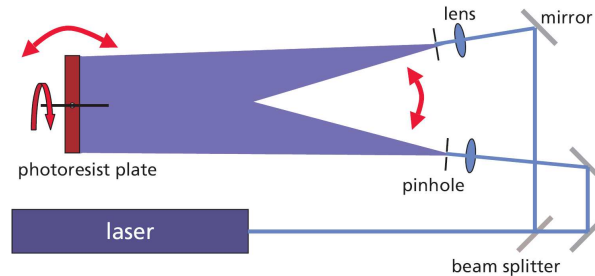


**Figure 5.3:** Schematic picture of the lithographic setup, showing the splitting of a coherent beam, the broadening and subsequent interference in the large photoresist plate. The periodicity depends on the angle between the two beams. For a 1D pattern, a single exposure with two beams is sufficient, for 2D pattern two or three exposure steps are needed. Copied from Chapter 13 in [6].

After the processing of the photoresist one ends up with a modulated 2D surface relief grating. Using this as a template, a nickel stamp can be produced to emboss the periodicity into a substrate (Fig. 5.4). Alternatively the substrate can be patterned directly using the photoresist structure, resulting in an inverse height profile. Patterning the substrate with the mask corresponds to a double inversion process, so the corrugation is the same as in the photoresist.

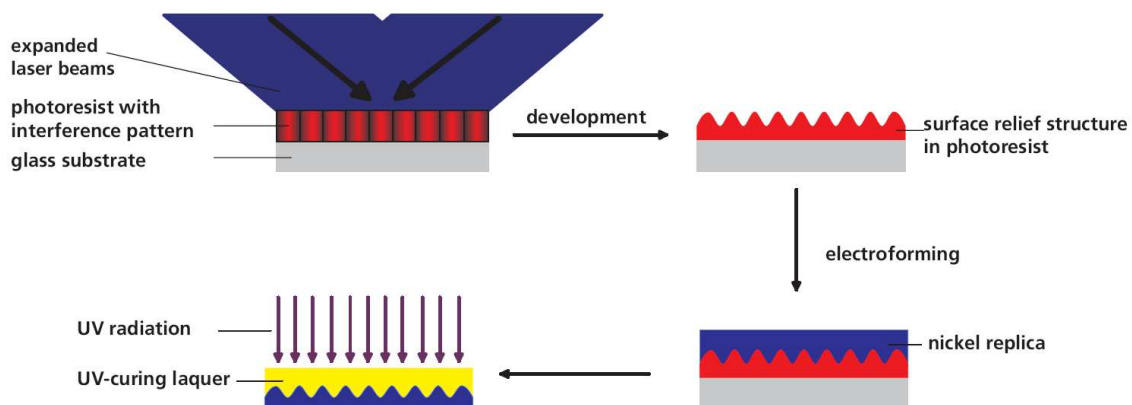


**Figure 5.4:** Illustration of the replication process for low-cost mass production using a nickel stamp. Copied from Chapter 13 in [6].

<sup>1</sup>The phase of the 3<sup>rd</sup> -exposure, which determines the position and shape of corrugation, cannot be controlled precisely in the experiment (Fig. 5.5).

The production of the grating is followed by spin-coating a laser active material, e. g. MeLPPP<sup>2</sup>(methyl-substituted ladder type poly(paraphenylene)) onto the substrate [110, 111]. The combined substrate-polymer system can now support quasi-guided waveguide modes in the polymer layer. For more details on the fabrication process and materials see [108].

This manufacturing process allows for the fabrication of large areas. The ability to use the nano-imprint technology with the nickel mask is another step toward a cheap, large scale mass production making this approach very interesting for applications.

### 5.1.2 Description of Corrugation

Although the corrugation is given by the interference pattern in first approximation, the analytical description is more complicated. Due to nonlinear processes during the exposure and the post-processing, the photoresist does not reproduce the intensity profiles exactly. In principle, numerical simulations allow for a computation of the resulting profile if all parameters of the resist are known [112]. However the results are not very accurate, since the determination of all parameters of the resist is not straightforward and the details of subsequent processing steps are difficult to model.

Therefore, the profile is described by functions determined from scanning electron microscopy pictures in the following. Depending on the phase of the 3<sup>rd</sup> exposure, two main patterns exist<sup>3</sup>, which are described by (Fig. 5.5)

$$f_{\text{tria},1} = d_{\text{max}} \frac{2}{9} \left( \sin\left(2\pi x + \frac{2\pi}{\sqrt{3}}y + \frac{\pi}{2}\right) + \sin\left(\frac{4\pi}{\sqrt{3}}y + \frac{\pi}{2}\right) + \sin\left(-2\pi x + \frac{2\pi}{\sqrt{3}}y + \frac{\pi}{2}\right) + \frac{3}{2} \right)^2, \quad (5.2)$$

or

$$f_{\text{tria},2} = d_{\text{max}} \frac{2}{9} \left( \sin\left(2\pi x + \frac{2\pi}{\sqrt{3}}y + \frac{3\pi}{2}\right) + \sin\left(\frac{4\pi}{\sqrt{3}}y + \frac{3\pi}{2}\right) + \sin\left(-2\pi x + \frac{2\pi}{\sqrt{3}}y + \frac{3\pi}{2}\right) + 3 \right)^2. \quad (5.3)$$

## 5.2 Basic Aspects of Lasing in Corrugated Structures

In this section, the basic ideas of lasing in periodic structures is summarized, showing how the results obtained with the developed code help to understand the lasing behavior. Due to the strong periodic patterning, the modes in the laser are Bloch-modes instead of plane waves. Therefore, standard coupled-wave theory [113], which requires that the index variation is weak, cannot be used.

In an alternative approach, it is possible to describe the lasing in PCs in a semi-classical way as lasing in a homogeneous material with effective parameters [114]

---

<sup>2</sup>This is a  $\pi$ -conjugated polymer with a high quantum yield often used in such systems.

<sup>3</sup>In the studies  $f_{\text{tria},1}$  was used.

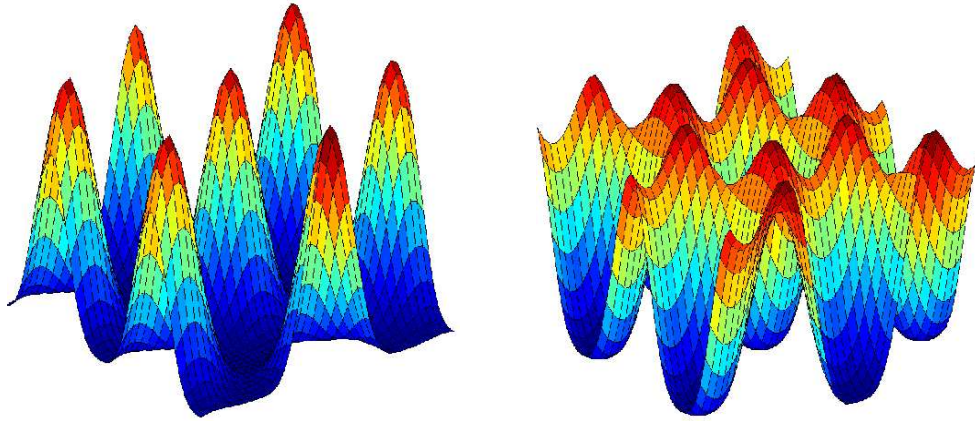


**Figure 5.5:** Surface relief structure defined by  $f_{\text{tria},1}$  (Left) and  $f_{\text{tria},2}$  (Right). Only the height of the corrugated part is plotted, ranging from 0.0 (blue) to 1.0 (red).

using Laser-rate equations in conjunction with information about the mode structure of the underlying PC. In this context the field is described as a classical field, based on the assumptions that many photons are present in one dominating mode of the 2D PC.

### Distributed Feedback

In regular lasers, the coherent feedback required for stimulated emission is created by mirrors defining a cavity. In distributed feedback lasers it is caused by the scattering of the wave at many distributed scatterers. Coherent scattering occurs if a fixed (constant) phase relation between the scatterers is given. The periodic patterning of the substrate-polymer interface provides the scattering elements in this case. Due to the periodicity, the wave vector can pick up a reciprocal lattice vector at each scattering event, leading to coherent backscattering. This feedback is facilitated by the second diffracted order, whereas first order is coupled out through the surface (surface-emitting laser). For lasing, a 1D structured substrate would be enough, but in the 2D case, the beam exiting the structure is confined to a smaller solid angle and, in addition, has a lower threshold [115].

### Semi-classical Theory of Lasing

The semi-classical theory of lasing has been developed previously by Busch et al. [114]. They introduce effective parameters to describe lasing in a periodically structured material in an approach formally equivalent to lasing in a homogeneous material.

For the combined atom field system the Laser-rate equations are used in the semi-classical approximation for a large number of photons. The basic equation for the

electric field in a nonlinear-medium is given by the scalar wave equation

$$\nabla^2 E(\vec{x}, t) - \frac{\varepsilon(\vec{x})}{c^2} \frac{\partial^2 E(\vec{x}, t)}{\partial t^2} - \frac{4\pi\tilde{\sigma}(\vec{x})}{c^2} \frac{\partial E(\vec{x}, t)}{\partial t} = \frac{4\pi}{c^2} \frac{\partial^2 \tilde{P}_{\text{nl}}^{\text{atoms}}(\vec{x}, t)}{\partial t^2}, \quad (5.4)$$

with the periodic dielectric function  $\varepsilon(\vec{x})$  incorporating the linear polarization effects. Losses caused by background absorption resulting from non-resonant atoms are introduced via the phenomenological conductivity<sup>4</sup>  $\tilde{\sigma}$ . The nonlinear macroscopic polarization due to the active material, modeled by resonant two-level atoms, is represented by  $P_{\text{nl}}^{\text{atoms}}$ . The polarization is created by the sum of single-atom polarizations, which can be described by

$$\frac{d^2 P_{\alpha}(t)}{dt^2} + 2\tilde{\gamma}_{\perp} \frac{dP_{\alpha}(t)}{dt} + \omega_{\alpha}^2 P_{\alpha}(t) = -2\omega_{\alpha} \tilde{\Omega}, |\vec{d}_{12}| \Delta N_{\alpha}(t) \quad (5.5)$$

with the change of the atomic population  $\Delta N_{\alpha}$  inversion given by:

$$\frac{d\Delta N_{\alpha}(t)}{dt} = \tilde{\gamma}_{\parallel} [\Delta N_{\text{eq},\alpha} - \Delta N_{\alpha}(t)] + 2 \frac{\tilde{\Omega}}{\omega_{\alpha}} \frac{1}{|\vec{d}_{12}|} \frac{dP_{\alpha}(t)}{dt}. \quad (5.6)$$

In these equations,  $\tilde{\gamma}_{\perp}$  corresponds to the dephasing rate of the atomic dipole having a resonance frequency of  $\omega_{\alpha}$  and a dipole matrix element  $\vec{d}_{12}$ .  $\tilde{\Omega} = \frac{|\vec{d}_{12}| E(\vec{x}, t)}{\hbar}$  defines the Rabi frequency, giving the interaction strength of the dipole and the driving field. Finally,  $\tilde{\gamma}_{\parallel}$  corresponds to the decay rate of the atomic upper level and  $\Delta N_{\text{eq},\alpha}$  is the steady state equilibrium inversion. This description requires the local density of states to vary slowly<sup>5</sup> on the scale of  $\gamma_{\parallel}^{-1}$ .

A slowly varying envelope formalism, which allows to discard the second derivatives [116], is used to solve these coupled equations for standard lasers. In structured lasers, such as the system under consideration, this is not possible. However the characteristic parameters for the laser such as polarization, decay rate and dephasing rates, i. e. all quantities depicted with a tilde  $\tilde{\phantom{x}}$  above, can be assumed to be small compared to the electric field and the optical frequency respectively. This allows for the introduction of a small parameter  $\mu$  and the expansion of all physical quantities, e. g. the electric field  $\vec{E}(\vec{x}, t)$ , the polarization  $\vec{P}(\vec{x}, t)$  and the population inversion  $\Delta N$ , as well as the derivatives in time and space in orders of this small parameter.

This expansion introduces several scales in space and time, each of which can be analyzed individually. The smallest of them are on the order of the wavelength and the frequency of the optical transition. This multi-scale analysis can be regarded as a generalized slowly varying envelope approximation.

---

<sup>4</sup>Losses due to the finite pumping area or due to coupling out of the structure can also be modeled by adjusting this parameter.

<sup>5</sup>This is not fulfilled near a 3D band edge. In this case the photon is emitted, interacts with the PC and is being reflected and re-absorbed. As a consequence, the photon is in a dressed state formed by the atom and the surrounding crystal. The state of the system then depends on previous moments in time and the Markovian approximation breaks down, rendering the description inaccurate.

The electric field and the polarization vary on all spatial and temporal scales, whereas the population inversion does not vary on the fastest time scale but on all spatial scales. The crystal properties, given by the dielectric function, conductivity and density of two-level atoms, on the other hand vary only on the smallest spatial scale. As a consequence the fastest scale only depends on the linear properties and the fields. For the linear part of the atomic polarization a slowly varying envelope approximation with a carrier wave holds. Nonlinear parts only contribute on longer timescales. In contrast to regular lasers, this carrier wave is not a plane wave but an eigenmode of the periodic system, i. e. a Blochmode of the PC. This Ansatz limits the possible transition frequencies to the eigenfrequencies of the used Blochmode. The underlying photonic system enters the description via the Blochmode. The surface relief grating discussed in this chapter constitutes a 2D periodic system and the 2D Blochmodes are required in the laser theory. The description of a corrugated 3D structure in an effective 2D model, taking into account the waveguide properties, is discussed in the next section.

The physically relevant envelope functions can be obtained by solving the equations on the next larger scale. In these equations, the above mentioned effective parameters play an important role. They connect the changes on the fast and small scale with the resulting changes for the envelope function. They are the result of an averaging process over the unit cell. The two most important ones describe gain enhancement and losses in these structures and are given by:

$$\alpha_m = \int_{\text{cell}} |\Phi_m(\vec{x}_0)|^2 n(\vec{x}_0) dx_0^2 \quad (5.7)$$

for the field enhancement factor which is a measure for the overlap of the strong fields of the Blochmode  $\Phi_m$  with the gain material and

$$\sigma_m = \int_{\text{cell}} |\Phi_m(\vec{x}_0)|^2 \sigma(\vec{x}_0) dx_0^2 \quad (5.8)$$

for the losses due to background absorption. The quantities not mentioned here involve the group velocity of the carrier wave, the effective population inversion and the nonlinear coupling enhancement factor responsible for the enhancement of the nonlinear saturation. The first is a property which can be derived from the band structure, and the latter two are integrals similar to the above ones. For plane waves as carrier waves, these expressions simplify to the regular laser expressions.

For an accurate description, the absorption term, until now only describing material losses, has to be modified to incorporate additional losses due to the finite sample or pumping spot ( $\kappa_m^{\parallel}$ ) or due to coupling out of the waveguide ( $\kappa_m^{\perp}$ ) so that the total loss is then given by:

$$\sigma_{m,\text{total}} = \sigma_m + \kappa_m^{\parallel} + \kappa_m^{\perp}. \quad (5.9)$$

$\kappa_m^{\parallel}$  describes the in-plane losses (cavity leakage) and is proportional to the group velocity. The relative magnitude of the out-of-plane losses  $\kappa_m^{\perp}$  can be estimated from the resonances in the transmittance spectra.

### Waveguide Properties

The knowledge of the band structure and Blochmodes of the PC is a necessity for the effective lasing theory. For the distributed feedback laser these cannot be calculated directly due to the height dependence of the 2D periodic pattern.

The height dependence can, however, be turned into an effective space dependent dielectric function ( $d(x, y) \rightarrow \varepsilon(x, y)$ ). For this purpose, the polymer layer is considered as a planar waveguide with a space-dependent thickness. For the quasi-guided modes of this waveguide, the dispersion can be calculated at each point  $(x, y)$ . In a next step the group velocity  $v_g(x, y) = \frac{\partial \omega}{\partial k}$  can be determined, which then allows the definition of an effective, space-dependent index of refraction  $n_{\text{eff}}(x, y) = \frac{c_0}{v_g(x, y)}$ . This effective index then defines a periodic 2D system, for which the band structure and Blochmodes can be determined.

In this Ansatz the TE-like and TM-like modes are then replaced by purely TE, respectively TM modes [108]. There are only deviations for the case of a very thin waveguide. An asymmetric, planar waveguide has a minimal thickness below which no mode exists. In a corrugated waveguide modes can exist although the minimal thickness in the thinnest polymer region is smaller than that of the cut-off thickness. However, in the effective index model no result could be obtained in these regions.

Another approach to determine the dispersion, respectively, band structure, of the 3D structure is examining the grating resonances. Sending in a wave under oblique incidence will give strong dips in the transmittance, each time the wave can couple to a quasi-guided waveguide mode. From this data, it is possible to determine the position and the width of the resonance. The position determines the frequency of the quasi-guided modes and the different widths can be used to compare the quality factor of individual modes. A narrow resonance corresponds to a high quality factor and, hence, the losses due to coupling out in the vertical direction are low. Plotting all the resulting resonances over the in-plane wave vector, respectively, angle yields the band structure.

## 5.3 Determination of Lasing Modes

The previously presented model is now used to identify relevant laser modes in a hexagonal structure. Comparing them with experimental observations in the far field (Fig. 5.6) helps to understand the lasing behavior of such a distributed feedback PC laser.

Beside the center spot, corresponding to a vertical emission with  $\vec{k}_{\parallel} = 0$ , several symmetric laser spots, radiating with an angle of a few degrees with respect to the surface-normal, can be identified in the hexagonal lattice. These are not present in the square lattice [108, 109]. In the work of Karen Forberich, the lasing from a hexagonal structure with the following parameters is studied:

- Lattice constant  $a = 346\text{nm}$

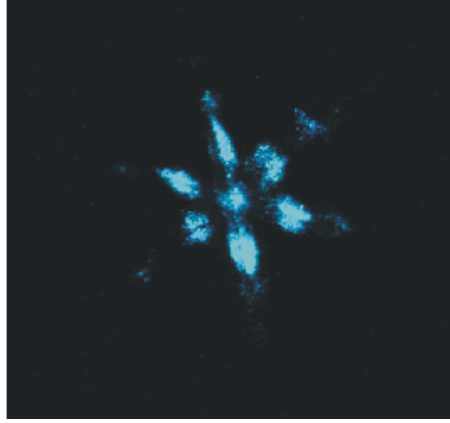


**Figure 5.6:** Experimental observation of the laser mode in the far field. Beside a bright spot in the middle (corresponding to  $\vec{k}_{||} = 0$ ) additional emission occurs with an angle of a few degrees to the surface normal. The oblique modes start lasing at a lower threshold than the center mode.

- Thickness of homogeneous polymer layer  $d_0 = 150\text{nm}$
- Thickness of corrugated area  $d_{\text{max}} = 300\text{nm}$
- Index of the substrate  $n_{\text{substrate}} = 1.5$
- Index of the active polymer layer  $n_{\text{polymer}} = 1.7$

The parameters identified in the effective laser theory are discussed in the following. For two of them ( $\kappa_{||}$  and  $\kappa_{\perp}$ ) regions which are suitable for lasing are identified in the simulation, complementing the work of Karen Forberich. Before discussing these two, results for the other parameters are repeated. The square lattice will not be discussed although similar studies have been conducted [109].

Based on the above approximations in the lasing theory and waveguide description it is obvious that no quantitative results can be expected. However a qualitative understanding of the processes determining the laser behavior can be achieved and an explanation for the oblique lasing mode can be found.

### Effective field enhancement/effective population inversion

The first parameter characterizes the overlap of the fields with the active material, which is needed for the field enhancement and the effective population inversion. For the evaluation of these overlap integrals, the Blochmodes of the band structure calculations have been used and weighted with the thickness at that position to give an estimate. A more sophisticated way could include the shape of the waveguide mode in the  $z$ -direction. Since the overall difference of the effective overlap found by Karen Forberich is less than 10% this parameter can be discarded as a significant factor for the selection of the lasing mode [108, 109, 117]. For the onset of lasing, another parameter, e. g. losses, must be more important as selection criterion.

## Losses

Many different loss terms contribute to the effective conductivity term eq. (5.9). Some of them, e. g. the material losses  $\sigma_m$ , vary very little for different modes similar to the effective overlap/gain discussed above. Therefore, the focus is on losses due to the finite pump region  $\kappa_{||}$  and out of plane losses  $\kappa_{\perp}$  in eq. (5.9), which strongly depend on the properties of the PC and exhibit a strong dispersion.

At this point, the method presented in this dissertation is very helpful. As discussed before, from the transmittance spectra the individual resonances from coupling to a quasi-guided waveguide mode can be determined and a band structure can be obtained from the resonance frequencies.

The slope of the band structure can then be used to determine modes with small in-plane losses (small slope  $\stackrel{!}{=} \text{small group velocity}$ ) and the width of the individual resonances represents a comparison for the quality factor of the modes and, therefore, out-of-plane losses (narrow resonance  $\stackrel{!}{=} \text{high quality}$   $\stackrel{!}{=} \text{low losses}$ ).

## 5.4 Estimates of Coupling Strength

The most promising lasing modes are determined qualitatively in this section, using the method presented in previous chapters. For this purpose, transmittance spectra in the wavelength region of interest (420nm - 500nm) have to be determined with a high frequency resolution to identify all resonance peaks (compare Fig. 5.8). These peaks then have to be analyzed one by one.

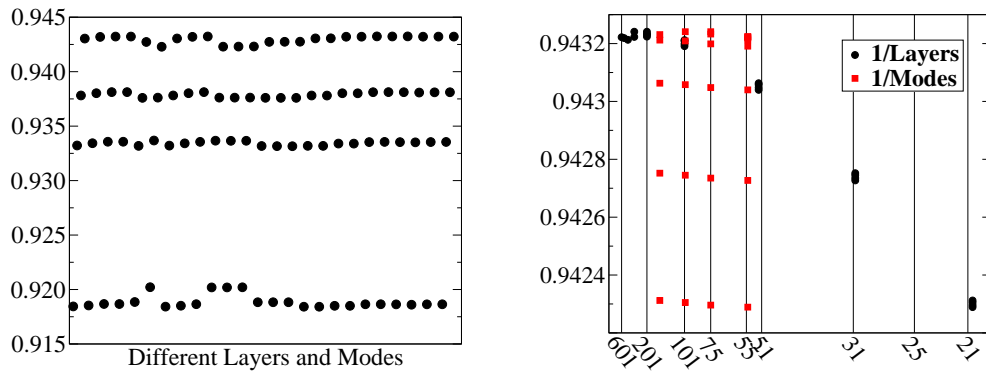


**Figure 5.7:** Convergence of the TM results for  $\lambda=400\text{nm}$ ,  $428.571\text{nm}$ ,  $461.538\text{nm}$  and  $500\text{nm}$  (bottom to top). Left: Transmittance for several configurations ( $\lambda = 500\text{nm}$ ). Each dot belongs to a layer (21,51,101,201,301,401,601) and mode (55, 75, 100, 150) combination. The strongly deviating points have been obtained using a very small number of layers. Right: Transmittance over  $\frac{1}{\text{Layers}}$  (black circles) and over  $\frac{1}{\text{Modes}}$  (red squares). For a fixed number of layers all different values for the mode are plotted and vice versa leading to several points. The importance of the number of layers is clearly visible.

Prior to starting the simulations, some test have to be done. The convergence for TM polarization is shown in Fig. 5.7 for 4 frequencies distributed over the complete range using several combinations of expansion orders and slicing layers. One can see that many layers are needed and that the number of modes plays a minor role in the convergence. For the following calculations, 61 modes and 501 layers have been used. Especially the large number of layers needed shows why the correct and efficient implementation of the recursion algorithm is important. Unfortunately, it is not possible to fully test the convergence in the peak area. Beside the total value of the transmittance, the peak position shifts a tiny bit with the number of modes. Since the peaks are very narrow, this results in larger changes of the transmittance for a fixed frequency. Testing the peak width rigorously would require to calculate the peak with a very high frequency resolution. This would then have to be done using different layer/mode configurations, followed by a detailed study of the shift. This approach is impractical. Looking at wider peaks with for several mode/layer combination shows only minor changes, so that the convergence can be assumed with a good enough confidence for these parameters. For TE polarization the same number can be used and the convergence plots exhibit the same behavior.

Others tests that were done in this structure include rotation about  $60^\circ$  as well as transmittance through a structure where  $\varepsilon_{\text{polymer}}$  and  $\varepsilon_{\text{substrate}}$  are set to the same value and comparing with regular Fresnel equations. The implementation of the structure was tested by reproducing the it from the Fourier expansion. These test only prove that the layers have been implemented correctly. With tests, such as comparison to band structures, the program itself had been tested before so that this is the only part which needs to be tested each time the structure changes.

### 5.4.1 Determination of Peaks

For a first calculation of the spectra the following parameters were used

- Wavelength:  $\lambda = 420\text{nm} - 500\text{nm}$  in 6000 steps ( $\Delta\lambda = 0.013\text{nm}$ )
- Angle to surface normal  $\theta$ :  $0.0^\circ - 1.0^\circ$  ( $0.1^\circ$  steps),  $1.2^\circ - 2.0^\circ$  ( $0.2^\circ$ ),  $2.5^\circ - 5.0^\circ$  ( $0.5^\circ$ )
- Polarization of incoming wave: TE/TM
- Orientation of electric field along  $y$ -axis (tilt in  $x$ - $z$  plane)<sup>6</sup>

In Fig. 5.8 all peaks as well as an example spectra (TM,  $0.6^\circ$ ) are shown to give an idea about the amount of data available. In the next step each peak had to be re-calculated again with a refined frequency resolution to find the minima and exact width. Some of the very narrow peaks could only be found by comparing spectra of several close angles and looking for the missing ones. The final dataset contains about 350.000 transmittance values.

---

<sup>6</sup>This corresponds to the detected emission in  $\Gamma K$  direction.

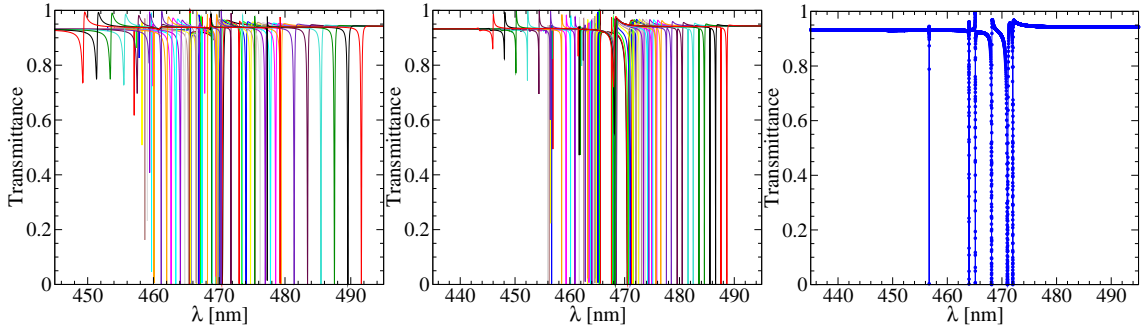


**Figure 5.8:** Left(Middle) all peaks for 17 different angles for TE(TM) polarization of the incoming wave. At the higher wavelength end the peaks shift to higher wavelength with increase of the angle. For TM there is also a more stable peak around 468nm. Right: Typical example of a spectra (TM,  $\theta = 0.6^\circ$ ). Around the peaks the frequency resolution has been increase in several steps to resolve the very small peaks. These intention of these plots is to give an idea about the amount of data. The total number of transmittance values in these plots is about 350.000.

From these data about 670 peaks can be identified and their center frequency and width can be determined. Since the refining of the transmittance in frequency space had to be done manually anyway, this can be done during this process.

In a next step, the main polarization of the fields inside the structure have to be determined to assign the resonance to a TE-like or TM-like mode of the band structure. For this the field is calculated for the center frequency of each peak inside one layer in the middle of the corrugated area. Since the calculation of the field inside one layer takes approximately as long as the calculation of one transmittance value, the calculation in all layers (501) would take too long and has been omitted. From the in-plane and out-of-plane components of the electric respectively magnetic field the characteristics of the mode can be determined in most cases<sup>7</sup>. In several cases, the answer is not straightforward. The reason for this might be, for example, that it was not exactly the center frequency of the resonance or that the layer chosen was having a node in one of the fields for that frequency. In these cases the characteristics is marked as unclear. However from the angle-dependent data the different band structures for TE-like and TM-like modes can be identified with great confidence. The peaks below 460nm are not identified since they are not overlapping with the frequency range of the active material. In Fig. 5.9 all peaks are shown with their corresponding properties.

### Losses from Band Structure and Width of Resonance

Knowing all peaks, the losses of individual modes can be compared. As discussed above, the two indicators are the group velocity, proportional to the slope of the

<sup>7</sup>Since there is no symmetry present in the structure which avoids polarization conversion, an incoming TE mode can be turned into a TM-like mode.

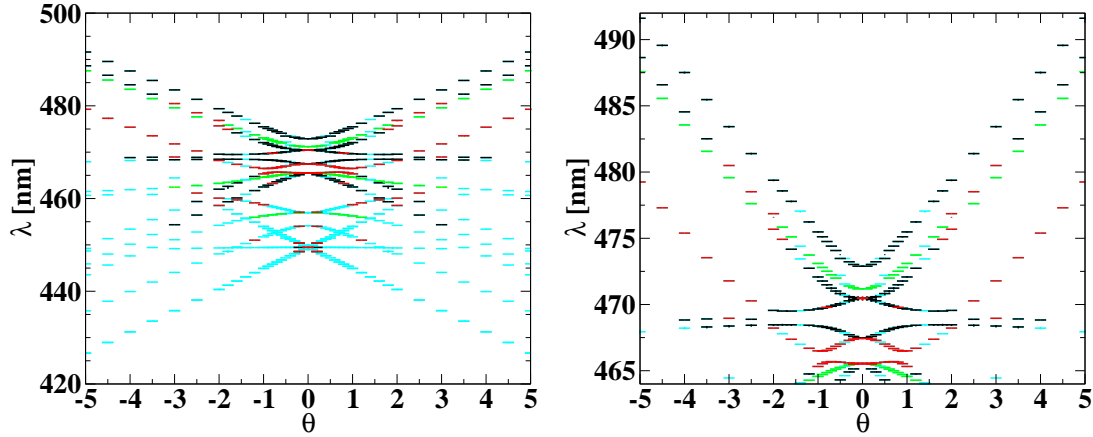


**Figure 5.9:** Band Structure obtained from the resonances and blow-up in the interesting frequency regime. Black: TE-like, Green: TM-like, Red: Ambiguous, Cyan: not analyzed.

band structure, and the in- and out-coupling losses, estimated by the width of the peaks.

Since thin polymer layers exhibit an anisotropy [118], which lead to a higher index for TE-like modes, it is expected that they are preferred for lasing over TM-like modes, due to the better confinement in the waveguide structure. In Fig. 5.10 only the TE-like modes are shown, with a bar indicating the width of the resonance.

It is noticeable that, beside the region close to perpendicular incidence, there are additional regions in the band structure with a vanishing or very low group velocity for oblique incidence. For the resonances around 469nm marked by the box, the peak width also becomes very small compared to the other peaks. With these properties these modes would be ideal candidates for lasing.

Comparing the results obtained from the resonance spectra with the experimental finding in Fig. 5.6 shows good qualitative agreement. The laser mode emitting perpendicular to the surface cannot be clearly identified in the band structure but it is assumed that it belongs to one of the higher modes with a narrow width e.g. the one around 471.2nm [117].

It should be mentioned that the wavelength cannot be directly compared with the measurement since the exact shape of the corrugation had to be estimated from the SEM measurements. The effective band structure and effective laser theory cannot determine the exact shape of the band structure due to the approximations in the 3D-to-2D mapping. Therefore, the explanation has to stay semi-quantitative.

## 5.5 Conclusion and Outlook

In this project significant contributions were provided to Karen Forberich which made it possible to identify the lasing modes of a hexagonal distributed feedback laser and to obtain a qualitative picture of the lasing mechanism. Using transmit-

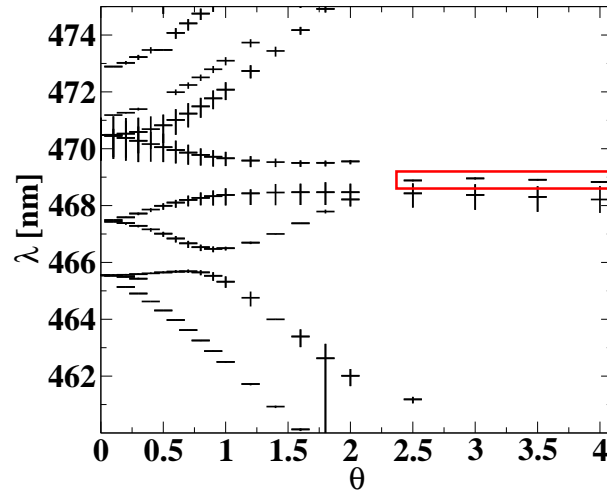


**Figure 5.10:** Modes with a TE-like characteristics with plotted width of the resonances. The horizontal bars indicate the center frequency. The vertical bars indicate the width of the resonance. They are terminated at the frequencies for which  $T=0.5$  (asymmetric). For illustration purpose the length is scaled by a factor of 5. The box marks a group of resonances corresponding to oblique incidence, which exhibit low group velocity and narrow peak width, making them ideal candidates for lasing modes.

tance calculations the resonances from coupling in and out of such a laser could be determined and characterized. From this data the band structure of the waveguide for TE- and TM-like modes as well as the quality factor could be determined. The knowledge of these properties allowed to compare the losses of different modes qualitatively and to identify the most promising candidates for lasing modes, which, again qualitatively, fit well to the experimental observation.

Additional work could improve the determination of the effective field enhancement by calculating the fields throughout the structure and determining the overlap integrals in more detail for more realistic structures than the approximated effective planar waveguide. It would also be possible to model the losses in greater detail by implementing dipoles into the structure and study their emission behavior.

Since this work shows that the losses are the determining factor for the selection of the laser modes it would also be possible to study different structures, e.g. honeycomb lattices, and compare the parameters. For larger studies, a more automated analysis of the peaks would have to be implemented to detect the promising candidates more efficiently.

# 6 Holography

In the two previous chapters, the structure of the system under study was assumed to be well known and the optical response of the systems was studied. In this chapter the desired structure is known but the realized structure is (strongly) deviating from the designed case. This is commonly true for holographically produced samples. In these structures, the developing process leads to deviations in the final structure from the isodose surfaces that define the nominal structure. The present work is a collaboration with Daniel Meisel at the Institute for Applied Physics (Universität Karlsruhe) who designed and fabricated the samples [119].

The theoretical simulations allow to study the changes in the angular dependent transmittance spectra<sup>1</sup> caused by deviations in different parameters. Once the most influential parameters are identified, the distortions can be compensated during fabrication to achieve the desired transmittance characteristic.

After presenting the photonic system and giving a description of the ideal structure, the possible changes in the parameters are introduced in Sec. 6.1. The following section (Sec. 6.2) describes aspects of the structure, e. g. symmetries, which have to be fulfilled and are used to test the implementation. Using a model system, the impact of the parameters is studied and some of the spectral features will be explained (Sec. 6.3). Finally, real experimental samples are characterized (Sec. 6.4).

## 6.1 Photonic System

The photonic system studied in this chapter consists of a 3D PC created in a photoresist by holographic lithography. The PC is located on top of a glass plate with a homogeneous polymer adhesion layer [120] in between (Fig. 6.1). The PC consists of a few unit cells in the vertical direction, corresponding to a height of several  $\mu\text{m}$ . The polymer substrate has a height of about  $10\text{--}20\mu\text{m}$  and the glass plate is about  $170\text{--}180\mu\text{m}$  thick. For the explanation of the spectra, these layers and their implementation are very important.

Using a chromium mask, the sample is divided into areas of about  $100\mu\text{m}$  by  $100\mu\text{m}$  surrounded by roughly  $60\mu\text{m}$  wide walls used as markers and for stabilization (Fig. 6.2). The PCs are then created inside the smaller areas and can be studied individually. Their lattice constant is on the order of  $600\text{nm}$  and the in-plane translational symmetries required for the numerical simulation is described by a hexagonal lattice. The exact shape of the unit cell is given later.

---

<sup>1</sup>Only the  $0^{\text{th}}$  order transmittance is used for characterization, however, all orders are calculated and some higher orders are required in the analysis.

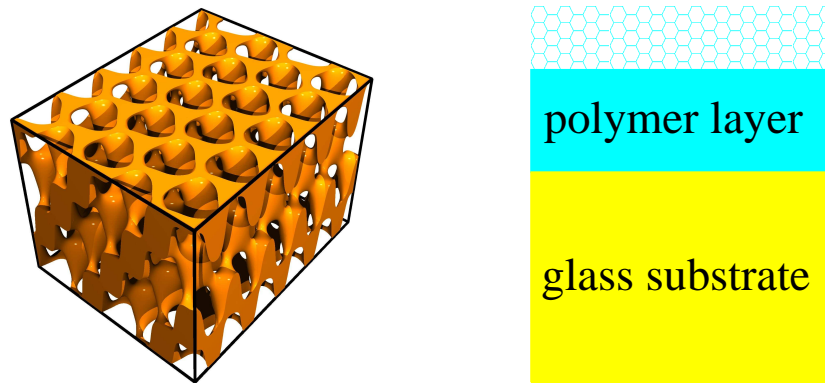


**Figure 6.1:** Left: A typical structure created using holographic lithography. Right: The entire system consists of the PC with a height of about  $1\mu\text{m}$  per unit cell, a polymer layer ( $10\text{--}20\mu\text{m}$ ) on top of a glass plate ( $170\text{--}180\mu\text{m}$ ). In the simulation the structure is periodic in the direction parallel to the surface. Left image courtesy of Daniel Meisel [119].

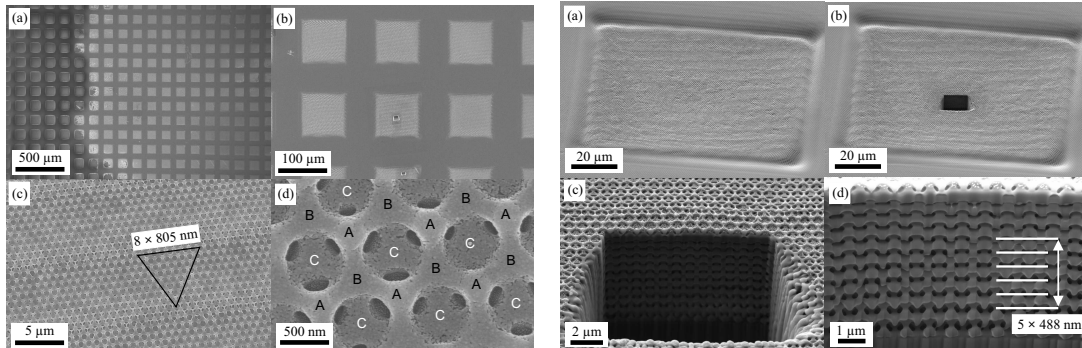


**Figure 6.2:** SEM pictures of sample #1 in Sec. 6.4 at different scales showing the patterned fields surrounded by  $60\mu\text{m}$  thick walls. The in-plane lattice constant and the vertical lattice constant can be measured by averaging over several periods. The upper images on the right indicate that the patterned region shrunk significantly in the  $z$ -direction compared to the surrounding walls. The rectangular shape of the patterned area is preserved. The vertical period can only be determined after destroying the sample using Focus Ion Beam (FIB). Courtesy of Daniel Meisel [119].

### 6.1.1 Fabrication

3Dholographic structures inside a photoresist can be created by either interfering 4 laser beams simultaneously or 3 times 2 beams in consecutive steps. In both cases this is followed by a chemical development process. During the processing, the photoresist exhibits a threshold behavior, which means that areas in which the exposure dose is below (above) a certain value are dissolved during the subsequent chemical processing in a negative (positive) photoresist [121, 122]. In principle, the structure is then defined by an isodose surface. However, there are many deviations which are discussed later. For a one step exposure, the deposited energy is proportional to the square of the electric field of the interference pattern, for several steps the individual doses (intensities) have to be added up. For the creation of a suitable interference pattern many details have to be taken into account, such as refraction at the air photoresist [123] but their discussion is beyond this work [119].

The translational symmetry is given by the orientation of the exposure beams, more precisely, the difference in the wave vectors define the reciprocal lattice vectors of the resulting crystal  $\vec{G}_{ij} = \vec{k}_i - \vec{k}_j$ . The distribution of the photoresist inside the unit cell, also called motif, depends on the details of the interference pattern of the beams, such as relative phase, amplitude and polarization. The final symmetry is determined by both, lattice and motif, and the design of a realizable structure with good optical properties is a tedious task [124, 125]. The samples considered in this chapter have all been produced by Daniel Meisel [119] with a 2 beam setup as depicted in Fig. 6.3.

### 6.1.2 Dose formula

The distribution of the dielectric material inside a unit cell is based on the deposited energy dose. To a good approximation, this can be described by the interference pattern of plane waves. In the case of a 4-beam setup the intensity formula contains only 4 parameters [126]:

- Prefactor  $P$ , describing the filling fraction (nonlinear)
- Offset  $O$ , describing the spatially homogeneous part of the dose
- Lattice constant of the 3D structure<sup>2</sup>  $a_{3D}$
- $\gamma$  corresponding to the opening angle of an umbrella configuration in a 4-beam setup

Since the 3-times-2-beams and the 4-beam setup lead to identical results for an appropriate choice of beam parameters [119], this description is valid for both ex-

---

<sup>2</sup>This is not the relevant lattice constant in the simulation. In the numerics, all quantities have to be expressed in terms of the in-plane lattice constant of the hexagonal lattice  $a_{\text{hex}}$ .

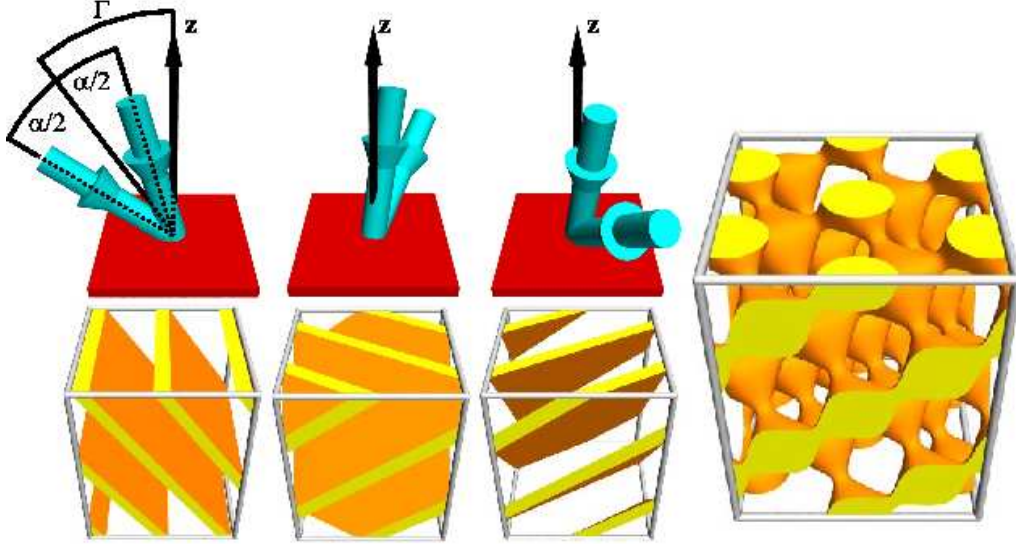


**Figure 6.3:** Left: Fabrication of the structure using a 2 beam interference setup. Each individual step would, if developed, create a set of parallel planes, which are rotated by  $120^\circ$  with respect to each other. Right: The resulting 3D PC if all three exposure steps are done before developing corresponds to the summation over the individually deposited doses. Courtesy of Daniel Meisel [119].

perimental setups. The dose formula is then given by

$$D(\vec{r}) = P \left[ O + \cos \left( \frac{2\pi}{a_{3D}} \left( -\frac{2}{3 \sin \gamma} y - \frac{1}{3 \cos \gamma} z \right) \right) + \cos \left( \frac{2\pi}{a_{3D}} \left( \frac{1}{\sqrt{3} \sin \gamma} x + \frac{1}{3 \sin \gamma} y - \frac{1}{3 \cos \gamma} z \right) \right) + \cos \left( \frac{2\pi}{a_{3D}} \left( -\frac{1}{\sqrt{3} \sin \gamma} x + \frac{1}{3 \sin \gamma} y - \frac{1}{3 \cos \gamma} z \right) \right) \right]. \quad (6.1)$$

Each cosine-term can be interpreted as one of the lamellas in Fig. 6.3. In the numerics, the hexagonal lattice constant and the vertical lattice constant are needed, which are related to the above quantities via

$$a_{\text{hex}} \equiv a_x = a_{3D} \sqrt{3} \sin \gamma, \quad a_y = a_{3D} 3 \sin \gamma, \quad a_z = a_{3D} 3 \cos \gamma. \quad (6.2)$$

The ratio of  $a_x$  to  $a_y$  corresponds to the ratios of the sides in the numerical unit cell of the hexagonal lattice in Fig. 4.1. For the comparison of data, it is also important to use the correct rescaled units, e. g. 3D band structures would be scaled in terms of the 3D lattice constant  $a_{3D}$ , the transmittance however in terms of in-plane lattice constant  $a_{\text{hex}}$ . The required conversion reads as

$$a_{z,\text{hex}} = \frac{a_z}{a_{\text{hex}}} = \frac{3 \cos \gamma}{\sqrt{3} \sin \gamma}, \quad \omega_{3D} = \frac{\omega_{\text{hex}}}{\sqrt{3} \sin \gamma}. \quad (6.3)$$

Parameter	sc	fcc	bcc
$\gamma$	$\arccos \frac{1}{\sqrt{3}} \approx 55^\circ$	$\arccos \frac{2}{\sqrt{6}} \approx 35^\circ$	$\arccos \frac{1}{3} \approx 71^\circ$
$\sin \gamma$	$\sqrt{\frac{2}{3}}$	$\frac{1}{\sqrt{3}}$	$\frac{8}{9}$
$\cos \gamma$	$\frac{1}{\sqrt{3}}$	$\sqrt{\frac{2}{3}}$	$\frac{1}{3}$
$a_{\text{hex}} = a_x$	$\sqrt{2}a_{\text{sc}}$	$a_{\text{fcc}}$	$\sqrt{\frac{8}{3}}a_{\text{bcc}}$
$a_y$	$\sqrt{6}a_{\text{sc}} = \sqrt{3}a_{\text{hex}}$	$\sqrt{3}a_{\text{fcc}} = \sqrt{3}a_{\text{hex}}$	$\sqrt{8}a_{\text{bcc}} = \sqrt{3}a_{\text{hex}}$
$a_z$	$\sqrt{3}a_{\text{sc}} = \frac{\sqrt{3}}{\sqrt{2}}a_{\text{hex}}$	$\sqrt{6}a_{\text{fcc}} = \sqrt{6}a_{\text{hex}}$	$a_{\text{bcc}} = \sqrt{\frac{3}{8}}a_{\text{hex}}$
$\omega_{\text{hex}}$	$\sqrt{2}\omega_{\text{sc}}$	$\omega_{\text{fcc}}$	$\sqrt{\frac{8}{3}}\omega_{\text{bcc}}$

**Table 6.1:** Parameters for different crystal structures. The relevant lattice constants in the experiment are  $a_{\text{sc}}$ ,  $a_{\text{fcc}}$  and  $a_{\text{bcc}}$ . In the simulation  $a_{\text{hex}}$  is used as reference. Rescaled frequencies are, therefore, not comparable  $\omega_{\text{hex}} = \frac{\omega a_{\text{hex}}}{2\pi c} \neq \omega_{3\text{D}} = \frac{\omega a_{3\text{D}}}{2\pi c}$  and the data has to be adjusted.  $a_x$  and  $a_y$  are not required and just given for completeness.

For the three main crystal lattices in the experiment, i. e. simple-cubic (SC), face-centered-cubic (FCC) and body-centered-cubic (BCC), the values for  $\gamma$  and the lattice constants are listed in Tab. 6.1.

Examples for individual layers of a simple-cubic crystal are plotted in Fig. 6.4 using an offset of  $O = 4.0$ , a prefactor  $P = 1.6$ , corresponding to a filling factor of 60%, and a threshold of  $D_{\text{thres}}=7.0$ . Above the threshold the polymer ( $\varepsilon_p=2.56$ , respectively  $n_p=1.6$ ) develops and stays, below it is washed out and an air pore ( $\varepsilon_{\text{air}}=n_{\text{air}}=1.0$ ) forms. The threshold and the permittivities are used throughout the rest of this chapter.

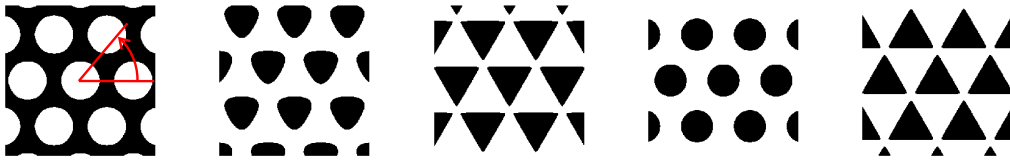


**Figure 6.4:** Examples of the dielectric distribution in individual layers (black: polymer, white: air pore). The hexagonal translational symmetry is clearly visible. The red lines on the left define the angle  $\phi$  for the orientation of the incoming wave with respect to the hexagonal lattice. The basis of the unit cell reduces the symmetry to  $C_{3v}$  in accordance with the 3 intersecting planes. The layers are chosen to illustrate different situations and are not equidistant. Throughout the crystal layers with interconnected air as well as resist regions exist. For parameters see text.

### Isodose and Motif

The distribution of dielectric material inside one of the unit cells, also called motif, is in general related to the isodose surface at the threshold of the photoresist calculated using eq. (6.1). However, for realistic simulations this model has to be improved.

The developing of the structure is a complicated process and does not exactly reproduce the isodose surface [93, 127]. The occurring deviations can be divided into two groups.

There will be “microscopic” aspects based on the local chemical process, e. g. diffusion or different concentration of the solvent, which lead to a transition region instead of a sharp threshold. Beside these effects, “macroscopic” effects change the properties of the entire crystal. This includes a change of the structure with depth due to absorption of the exposure beams in the upper regions of the photoresist. In addition, the whole crystal exhibits a shrinkage during the developing process<sup>3</sup>. Consequently, the fabrication of samples has to be adjusted to yield PCs, whose transmittance spectra correspond to the ones of the nominal structure. Or, looking at it from the other side, the isodose description has to be modified to achieve transmittance spectra which match the experiment. The determination of important factors for this process is the aim of the rest of this chapter.

## 6.2 Testing of the Simulation

Before moving on to the parameter studies, some of the tests done for the structure that show some interesting aspects, will be mentioned. In this chapter, simple test, e.g. Brewster angle, homogeneous structures and reproducing the sample by reconstructing the dielectric distribution from the Toeplitz-matrix, are excluded.

The convergence has been checked analogous to Fig. 5.7, however the required accuracy is less, since only structural changes in the transmittance are studied. In addition, the very long glass plate leads to very narrow Fabry-Perot resonances, which will always exhibit some shifts leading to changes in the transmittance. Since the experimental resolution is much smaller than the width of the Fabry-Perot resonances, averaging over a suitable window is done, and these shifts can be ignored. To allow for faster computation and more parameter studies, the transmittance values are only converged up to about 1%. Since, in addition the unit cell has larger feature sizes than the narrow tips at the top of the corrugated structure in the previous chapter, 85 layers and 45 modes are sufficient in these simulations.

### Lamellas

A correct implementation has to reproduce the symmetries of the structure. The individual lamellas can be used for a simple test. Each lamella is rotated by 120° with

---

<sup>3</sup>Because of their impact on the overall crystal structure, the last deviations are called macroscopic. Their reason, however, is still microscopic, e. g. cross-linking of individual molecules.

respect to each other<sup>4</sup>. For perpendicular incidence, the same transmittance should be obtained if the incoming wave is rotated by 180°. For the fields perpendicular or parallel to the lamellas, 2 angles correspond to the same physical situation, otherwise 4 orientations of the incoming beam are equivalent, since the field can be mirrored at a plane perpendicular to the lamellas. The following table summarizes the results. The first column shows the orientation of the electric field in TE polarization with respect to the lamellas and the others list the angles  $\phi$  for which the same results occur.

$\vec{E}$ orientation	lamella 1 —	lamella 2 \	lamella 3 /
$\perp$	0°, 180°	120°, 300°	60°, 240°
$\pm 60^\circ$	30°, 150°, 210°, 330°	90°, 150°, 270°, 330°	30°, 90°, 210°, 270°
$\pm 30^\circ$	60°, 120°, 240°, 300°	0°, 60°, 180°, 240°	0°, 120°, 180°, 300°
$\parallel$	90°, 270°	30°, 210°	150°, 330°

### Scaling of Vertical Lattice Constant

Rescaling the crystal in the  $z$ -direction by replacing  $z$  by  $z' = \frac{z}{s}$  and changing the lattice constant changes the lattice properties. A BCC lattice can be represented by a squeezed<sup>5</sup> SC lattice and a FCC crystal can be given by a stretched SC lattice. Fig. 6.5 shows the parameters for an example and the transmittance. Rescaling the lattice constant in  $z$ -directions has implications on several parameters, e. g. the  $z$ -values of the individual layers have to be chosen differently, since the ratio of  $a_z$  and  $a_{\text{hex}}$  changes and all values are given in units of  $a_{\text{hex}}$ . In addition, all quantities related to the termination of the crystal, e. g. surface, have to be adjusted since the length of the numerical unit cell changes. Therefore, these tests are important to make sure that no aspect is missed.

### Diamond lattice

Adding  $-\cos\left(\frac{2\pi}{a_{3D}}\left(\frac{1}{\cos\gamma}z\right)\right)$  to the dose formula eq. (6.1) and using the FCC parameters leads to a diamond lattice, which cannot be produced experimentally but has a stop band in the 111 direction which can be seen in the theoretical transmittance spectra.

## 6.3 Impact of Parameters on Transmittance Spectra

The simple dose formula describes the interference pattern of the laser beams during the exposure. This, however, does not correspond to the distribution of the polymer after processing due to many distortions. Before comparing actual samples, the

<sup>4</sup>From eq. (6.1) it follows that lamella 1 is parallel to (independent of)  $x$ , lamella 2 is then pointing along  $\phi = 120^\circ(300^\circ)$  and lamella 3 along  $\phi = 240^\circ(60^\circ)$ .

<sup>5</sup>Only along the  $z$ -direction. All other dimensions are still given by eq. (6.1) with the new lattice constant.

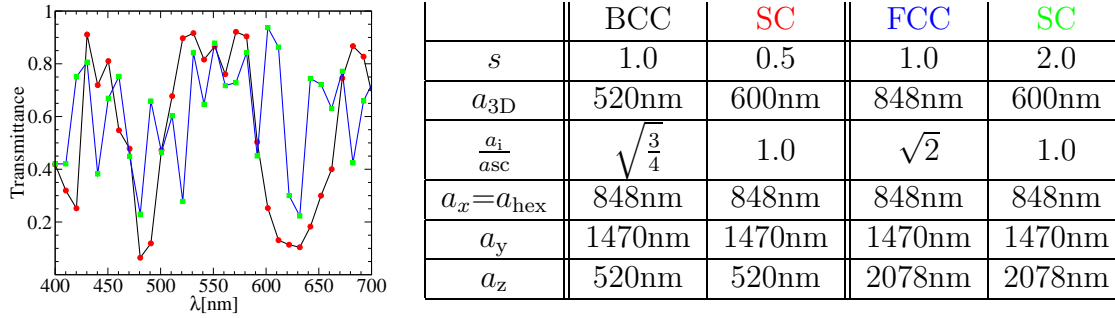


**Figure 6.5:** Test of the correct implementation of vertical shrinking. Plotted are the (identical) transmittance for BCC and scaled SC (red dots), respectively FCC and scaled SC (green squares). Parameters for the different structures can be found in the table on the right.  $s$  corresponds to the change of the lattice constant in  $z$ -direction compared to the regular SC structure. For the BCC and FCC structure the lattice constant of the 3D structure has to be adjusted as well.

impact of distortion in individual parameters on the transmittance spectra of the  $0^{th}$  order has to be studied. Based on the obtained results, the important parameters can be studied in more detail and compensated during fabrication to reach the nominal structure.

In the simulations, microscopic aspects can not be treated since they would require a number of different simulations as done by Rumpf et al. [93]. For the transmittance spectra, the macroscopic distortions which can be modeled by modifying the dose formula seem to be more important. Microscopic differences might be treated in a disorder framework, as discussed in Sec. 4.9 by smoothing the transition region with a random width. The presented results show that an accurate description of the experiment is possible and that the distortions can be compensated. Extrapolating the disorder results in Sec. 4.9, one can argue that small and unavoidable deviations lead to very wide transmittance distributions for wavelength on the order of or smaller than the lattice constant. In this case, a deterministic microscopic method might fail as well.

The presented studies are done for a model system corresponding to the nominal SC structure which should be fabricated in the end with a lattice constant of about  $a_{3D} = 600\text{nm}$  ( $a_{hex} = 848\text{nm}$ ). The parameters in the regular dose formula are given as offset  $O = 4.0$ , prefactor of  $P = 1.75$  and threshold  $D_{thres} = 7.0$ . The resulting filling factor is about 50%. The spectra ranges from 600nm to 1600nm.

For a complete PBG a refractive index of around 2.0 is needed [33, 34, 128]. The index  $n = 1.6$  of the polymer is not sufficient and no stop bands are visible for perpendicular incidence along the sample normal<sup>6</sup>.

<sup>6</sup>The polymer crystal will be used as template. Using chemical vapor deposition the structure can be (double) inverted and high index crystals with a complete PBG can be produced [129–131]. These template could still be enhanced by using two-photon direct laser writing to introduce defects in an otherwise perfect structure [132–134], once the template has a high quality.

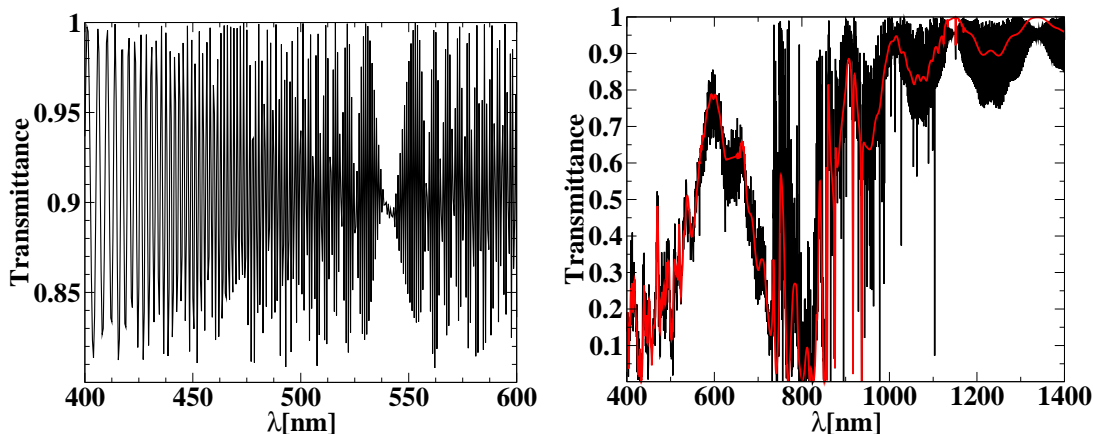


**Figure 6.6:** Left: Transmittance through the polymer and glass layer without crystal. Right: Transmittance through a 5 unit cell long crystal including polymer and glass layer. The very closely spaced resonances are clearly visible. The red curve corresponds to an infinite glass half-space.

Therefore, not only perpendicular incidence is considered but angle resolved transmittance spectroscopy is used with the angle  $\theta$  to the surface normal varying from  $-60^\circ$  to  $60^\circ$  in accordance with the experimental setup. This will introduce additional features based on diffraction. In all the color plots red(blue) corresponds to a high(low) transmittance of 1.0 (0.0) on a linear scale.

### 6.3.1 Frequency Resolution (Folding with Apparatus Function)

Before comparing spectra, the required frequency resolution has to be determined. Due to the large polymer and glass layers below the crystal, narrow Fabry-Perot resonances occur (compare to discussion of long crystals in Sec. 4.8) which can also be seen in the theoretical transmittance spectra (Fig. 6.6) and vanish if the structure is terminated in a glass half space instead.

The period of the Fabry-Perot resonances is significantly smaller than the resolution of the experimental setup. Due to the flat curve in the measurement of the line width of a HeNe-laser (Fig. 6.7), folding with the apparatus function can be done by simple averaging over about  $\pm 6$  nm. The entire width of 15 nm is not used since the plot is logarithmic to present the noise as well. In a separate experiment (not shown) the resolution of the spectrometer was changed and the Fabry-Perot resonances could be measured, confirming the thicknesses of the polymer layer and glass plate. The averaged result is very close to the result for termination in a glass half-space in the presented case. A more detailed discussion of glass and air termination effects can be found in Sec. 6.3.7.

The averaging process does not lead to significant changes in the transmittance spectra even if the averaging is done for about twice the laser line width (Fig. 6.8). In the following spectra, the system has been terminated in a glass half-space to be able to reduce the frequency resolution and avoid the averaging process for shorter

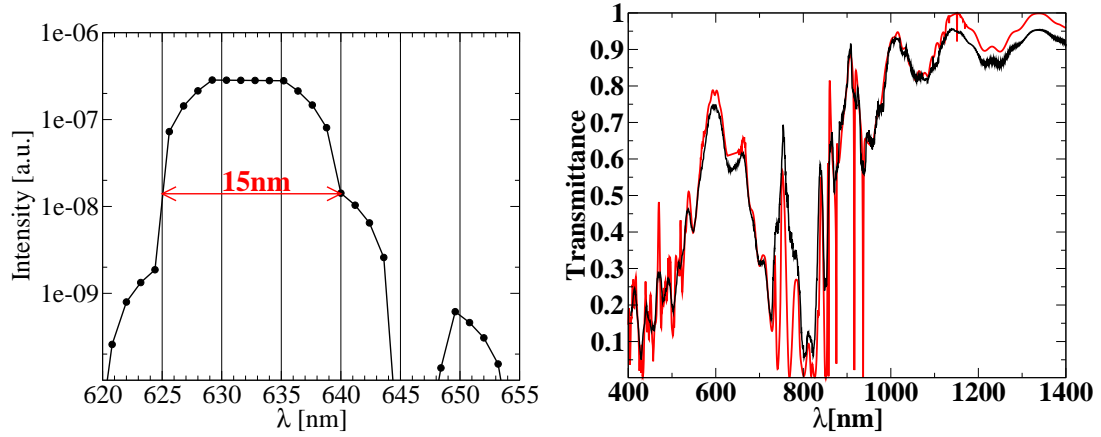


**Figure 6.7:** Left: Measurement of the HeNe laser line width using the resolution of the experimental setup. The peak on the right indicates the noise level. Right: Transmittance spectra averaged over  $\lambda_0 \pm 6\text{nm}$  (black) and transmittance through structure terminated in glass half-space (red). Termination effect are discussed in detail later.

computational time. For the experimental comparison averaging at the correct (finite-glass) setup has been used.

### 6.3.2 Rotation of the Sample

Another important aspect in the experiment is the orientation of the probe beam with respect to the sample. In the simulation, this can be studied by changing the angle  $\phi$  between the wave vector of the incoming wave and the  $x$ -axis (Fig. 6.4). For multiples of  $\phi = 60^\circ$ , the spectra is symmetric in the angle  $\theta$  to the surface normal. In this case, the electric fields are perpendicular (TE) or parallel (TM) (eq. (3.9)) to the lamellas forming the structure and inversion symmetry is present. In between, the spectra are asymmetric and the spectra for  $\phi \in (0^\circ, 60^\circ)$  can be obtained from the spectra  $\phi \in (60^\circ, 120^\circ)$  by inverting the angle  $\theta$  representing the  $C_{3v}$  symmetry of the structure<sup>7</sup> (Fig. 6.9). For the experiment  $\phi = 90^\circ$  is chosen, since alignment is easy for  $0^\circ$  respectively  $90^\circ$  and the asymmetry in the latter case spectra has more features for comparison due to the different dispersion for positive and negative  $\theta$ .

In order to test the stability of the analysis, the impact of small misalignments has been tested and found to be negligible.

### 6.3.3 Surface Termination

Surface termination is another aspect, which possibly has an important impact on the transmittance spectra, as already discussed for a 2D system in Chapter 4.

<sup>7</sup> $0^\circ$ ,  $60^\circ$  and  $120^\circ$  could be included in the intervals since the spectra are symmetric and the inversion of  $\theta$  is without consequences

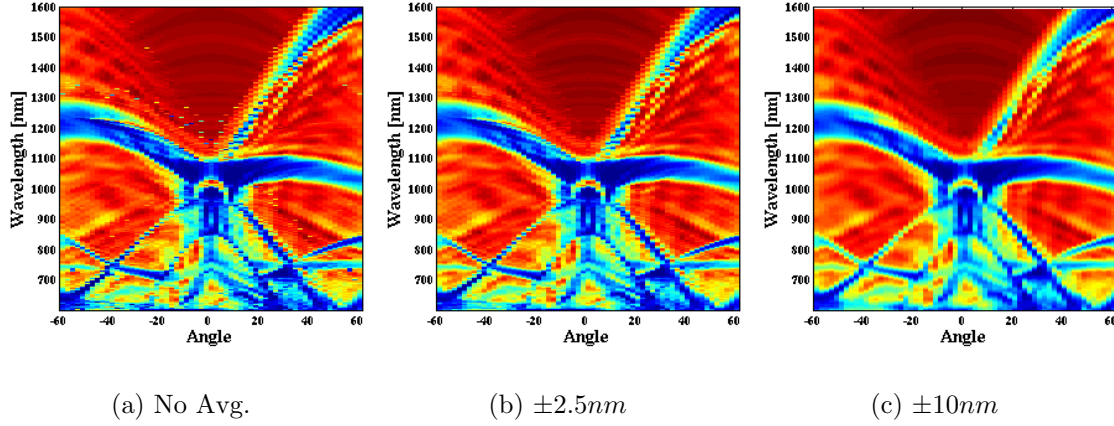


**Figure 6.8:** Transmittance spectra for different averaging lengths as indicated in the individual captions. All 3 structures are terminated in a glass half-space. In all color plots red(blue) corresponds to a high(low) transmittance of 1.0 (0.0) on a linear scale. The horizontal axis represents the angle  $\theta$  to the surface normal.

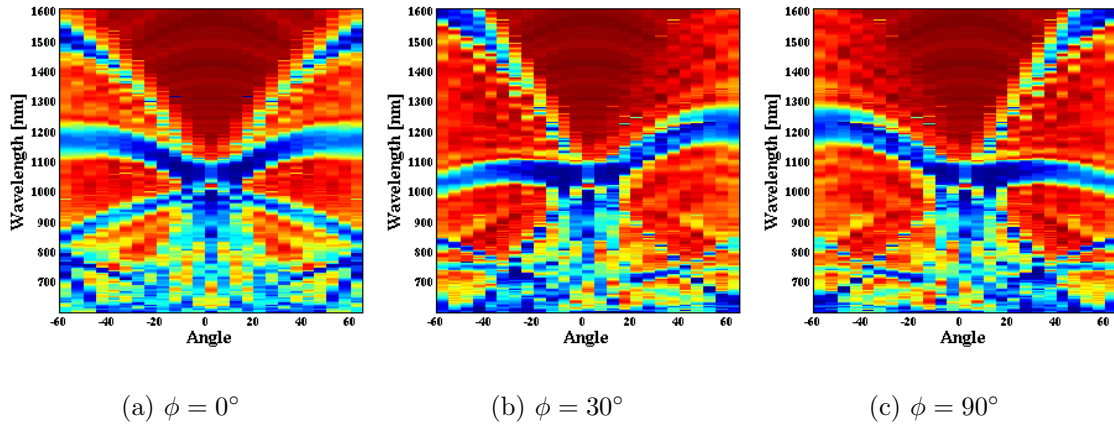


**Figure 6.9:** Spectra for different orientations of the incoming wave with respect to the lamellas. The horizontal axis corresponds to the angle  $\theta$  to the surface normal. For  $\phi = 0^\circ$  ( $60^\circ$ ,  $120^\circ$ ,  $180^\circ$ ,  $240^\circ$ ,  $300^\circ$ ) the electric field is perpendicular to one of the layers and symmetric spectra occur due to mirror symmetries. Due to the combination with the  $120^\circ$  symmetry the spectra for  $\phi \in (0^\circ, 60^\circ)$  correspond to the ones for  $\phi \in (60^\circ, 120^\circ)$  if the angle to the surface  $\theta$  is reversed. For the analysis  $\phi = 90^\circ$  was chosen to have two different dispersion for positive and negative  $\theta$ .

Different surface terminations are introduced into the isodose formula eq. (6.1) by replacing the  $z$ -coordinate by  $z' = z - \bar{z}$  and changing  $\bar{z}$  between 0.0 and  $a_z$ . This shift in the  $z$ -direction has to be implemented consistently with all the other parameters which also change  $a_z$ , e. g. shrinkage.

For the holographic structure, no significant changes in the spectra are observable in contrast to the 2D PC. This could be based on the low index contrast of the polymer which leads to smaller changes in the effective index if the filling factor in the surface layer changes. In addition, the filling factor only exhibits small differences for different layers/terminations (compare Fig. 6.4). In the 2D structure the termination can be a homogeneous substrate layer or a layer with 20% substrate and 80% ( $r = 0.4$ ) air pore.

### 6.3.4 Absorption of Exposure Beam

One of the parameters suggested by Rumpf et al. [93] with an impact on the structure of the unit cell is the absorption of the exposure beam in the photoresist. Consequently, more energy is deposited in the upper regions than in the lower part. This has to be modeled by adjusting the prefactor  $P$  with depth

$$P(z) = P(0) \cdot \exp^{-\alpha \frac{z}{a_z}} \quad (6.4)$$

The implementation of a depth dependent prefactor requires significant changes, since the periodicity in the vertical direction is broken. The  $S$ -matrix multiplication cannot be used any more and the entire structure has to be modeled. The experimental samples consist of 5 unit cells and hence this length is used in the simulation. Consequently, the number of discretization layers has to increase by the same factor and so does the computational time. The new numerical unit cell as a length of  $5a_z$  reflecting the number of vertical unit cells modeled individually. Again, all interdependent variables (surface, shrinking, ...) are also scaled accordingly.

The impact of the absorption is less than expected. For reasonable absorptions (in between Fig. 6.10(a) and Fig. 6.10(b)), the transmittance spectra is only changed at short wavelengths, where disorder very likely plays a more important role than structural deviations of this kind (Chapter 4.9). For high values the crystal loses the periodicity in the unit cell and strong oscillations are visible. The experiments did not show any signatures of this effect. This parameter has, therefore, been kept at a very low level throughout the simulations and not considered as a fitting parameter.

### 6.3.5 Prefactor/Filling Fraction

One of the most important parameters is the filling factor represented by the prefactor  $P$  in the dose formula (6.1). Fig. 6.11 illustrates this for 3 different values. The low transmittance regions at long wavelength shift significantly to longer wavelengths with increasing filling factor in accordance with the higher effective index of the structure. The relation of the prefactor and the filling factor is nonlinear [119] and in the following both values will always be listed.

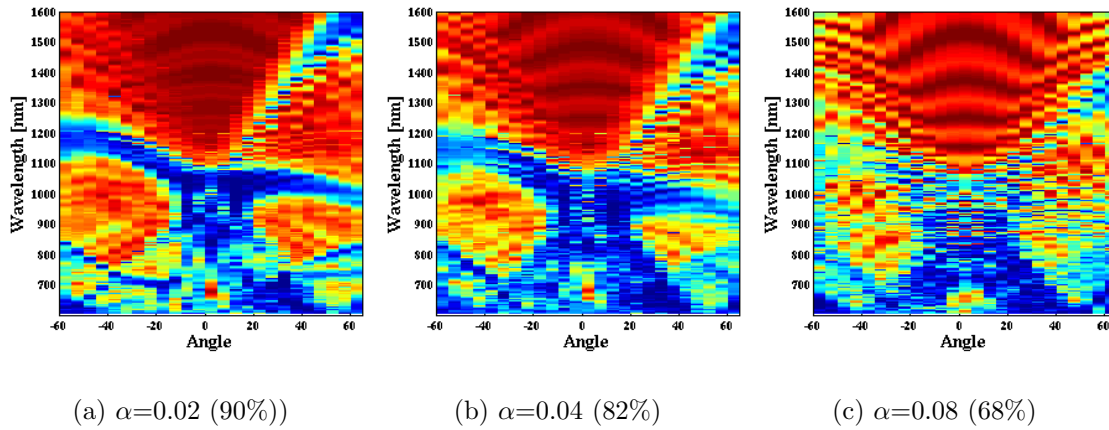


**Figure 6.10:** Effect of the absorption during exposure on the transmittance spectra. The listed values in the brackets give the intensity reduction at the end of 5 unit cells. Very high absorption rates have to occur before distortions are visible which are caused by losing the periodicity in the  $z$ -direction. For even higher absorption (not shown) the structure exhibits oscillations as in (c) for all regions of the spectra and all features are lost. The value estimated by Rumpf is in between (a) and (b).

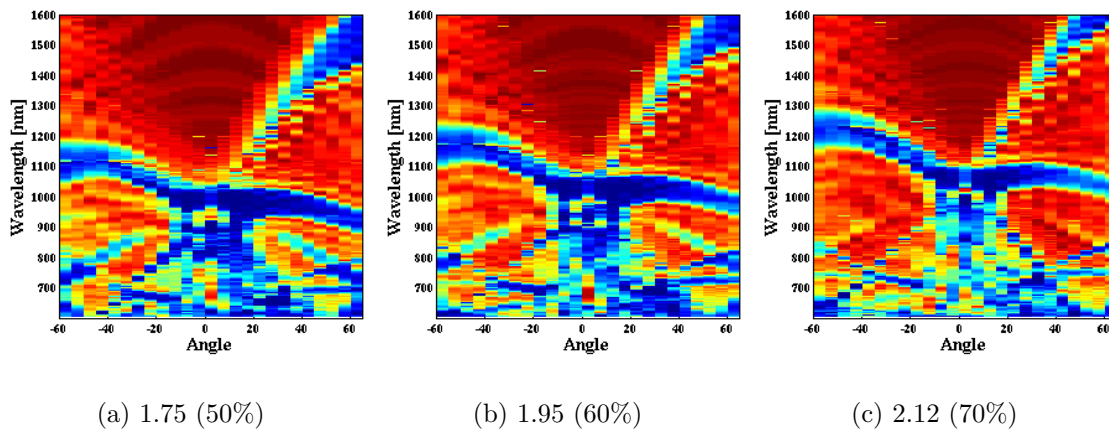


**Figure 6.11:** Impact of the prefactor  $P$  in the dose formula (eq. (6.1)) which defines the filling fraction in a non-linear way. For higher prefactors (filling fractions), the low transmittance bands at longer wavelengths red-shift as expected from an effective index model.

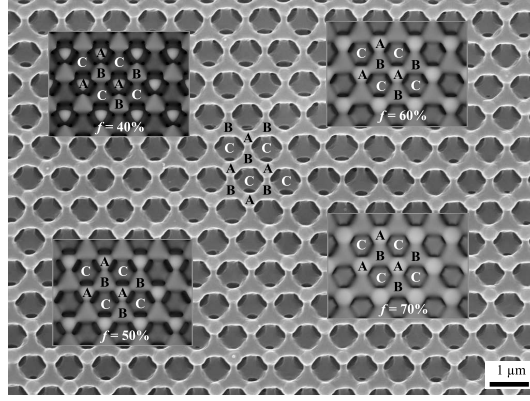


**Figure 6.12:** The darker insets show simulated surfaces with different values for the filling factor. From a comparison the filling factor can be estimated to be approximately 50% in this case. The upper row of pores cannot be used since the exact termination, e. g. at the maximum of pore radius or not, is unknown and the deviations are stronger there. Comparing the spectra with theoretical ones allows for an improvement of the estimate. Courtesy of Daniel Meisel [119].

The importance of theoretical simulations can be seen from Fig. 6.12. The insets in the SEM picture show theoretical surfaces for different filling factors by Daniel Meisel. From comparing them with the experimental data the filling factor cannot be determined very accurately. It has to be estimated using the second or third row of pores since for the first row it is unclear, whether the pores are cut at their maximum radius or not. The surface is also different from the inside, since the concentration of chemicals during the processing is higher and the structural stability is smaller due to missing neighboring structures.

### 6.3.6 Shrinkage in the Vertical Direction

Shrinkage of the structure because of cross-linking of the polymer during processing can be identified as the most important parameter for the deviations in the spectra. In principle, the shrinkage occurs in all directions but in the experimental setup the glass substrate and the side walls prohibit the in-plane shrinkage. This is also visible in Fig. 6.2 where the rectangular shape is preserved but the height changes in the patterned area. The vertical shrinkage is implemented by rescaling the  $z$ -coordinate

$$\frac{z - \bar{z}}{s}. \quad (6.5)$$

$\bar{z}$  is used to model the surface termination. Vertical shrinkage modifies the vertical lattice constant  $a_z$  and, hence, the  $z$  value of individual layers as well as the implementation of surface termination.

Comparing theoretical calculation with first measurements showed that shrinkage is indeed the most important parameter. Moreover it became clear that the structures shrunk as much as 60%, much more than listed in the literature, e. g. 5%

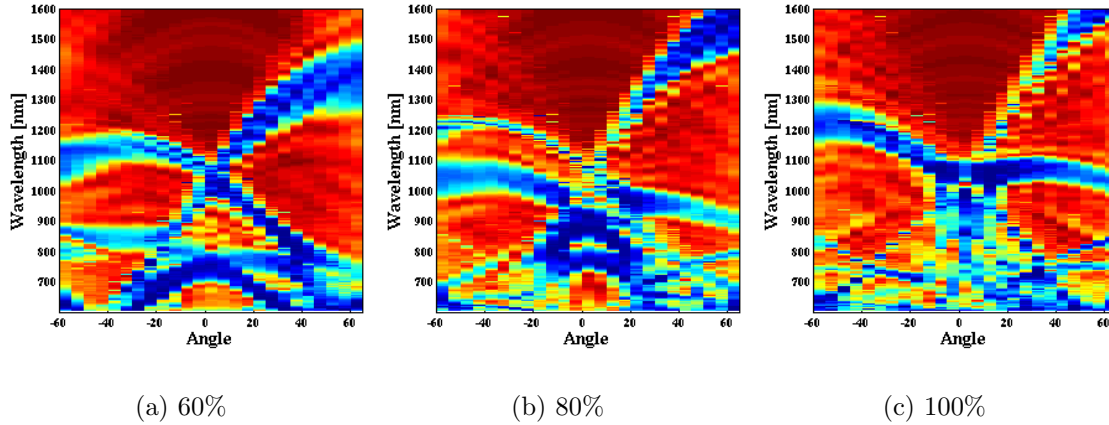


**Figure 6.13:** Transmittance spectra for different values of the shrinkage in  $z$ -direction given by the value below the plots. The shrinkage factor determines how much smaller the structure is in the vertical direction compared to the nominal one. For different shrinkage, low transmittance bands occur or disappear and the transmittance patterns changes drastically. Typical values for the shrinkage found in the experiment later on are 60%.

in [135] or 7.5% in [136], even if one takes into account that the shrinkage in the presented case is only vertical and in all directions in the literature. Using FIB it can be confirmed that the shrinkage is about 58% up to 66%.

### 6.3.7 Finite Glass and Substrate

Another important aspect of understanding the transmittance properties is the termination of the sample. In most simulations, a glass half-space is used, although the experimental situation with a glass plate of large but finite width is different (compare Sec. 6.3.1). Fig. 6.14 shows the spectra for terminating in air with a finite glass layer (a), the same with a small imaginary part in the dielectric constant of the glass and in an infinite glass half-space for a high resolution without averaging.

For the finite glass plate used in the experiment, the features at longer wavelength and larger angles disappear. To avoid that decaying crystal modes are enhanced again by resonances in the glass, the crystal size was increased to 30, respectively 50 unit cells without observing changes in the spectra. The line spectra for 60° in Fig. 6.15 shows that not all of the dips are associated with low transmittance ranges through the bulk crystal but that in all transmittance dips the absorption due to the glass is greatly enhanced compared to other parts of the spectra. Consequently, the low transmittance bands which vanish are due to crystal/glass interactions and correspond to modes which interact strongly with the glass, hence the high absorption.

Looking at the spectra in more detail by including additional diffraction orders,

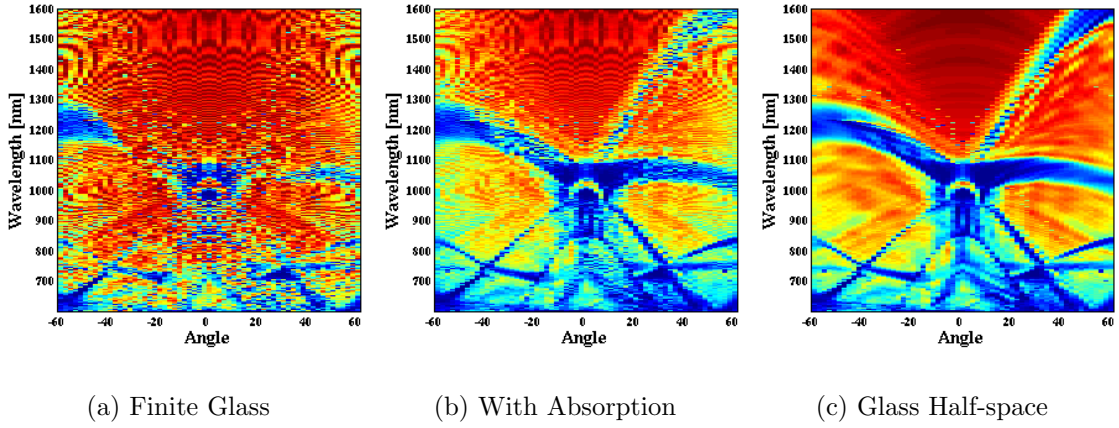


**Figure 6.14:** Effect of different terminations spectra without averaging. (a) Finite glass plate (thickness  $170\mu\text{m}$ ), termination in air. The features at higher wavelengths disappear. (b) Finite glass plate with a very small absorption ( $\text{Im } \varepsilon_{\text{Glass}} = 0.0005$ ). In both cases oscillations are visible, although they are damped in the second case. (c) Termination in a glass half-space with the same absorption as in (b). In all three cases the length of the crystal has been increased to 30 unit cell making sure that decaying modes in the crystal are completely damped and cannot be enhanced again due to resonances in the glass plate.

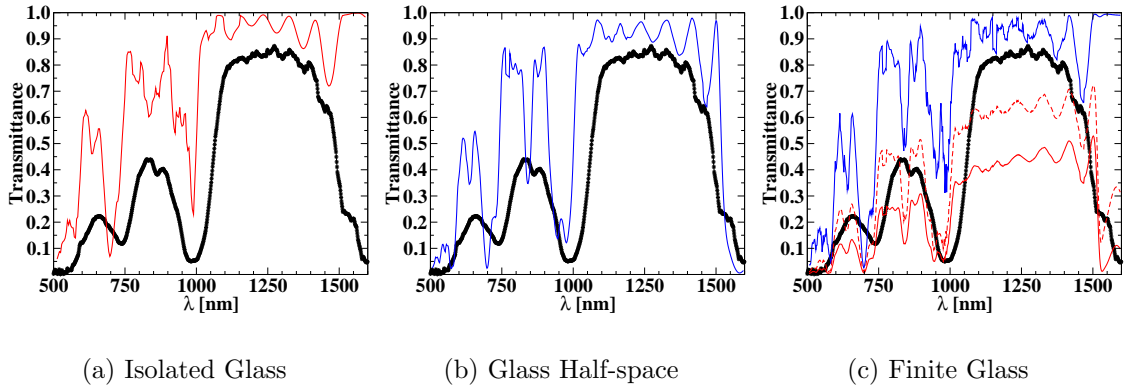


**Figure 6.15:** Comparing the frequency averaged ( $\pm 7\text{nm}$ ) line spectra for  $60^\circ$  for different cases. The black curve always corresponds to the experimental measurement. (a) Transmittance through the bulk crystal without glass/polymer layer (red). (b) Transmittance using infinite glass half-space (blue). (c) Transmittance using finite glass plate (blue) and finite glass plate with different absorption (red, solid  $\text{Im } \varepsilon = 0.001$  dashed  $\text{Im } \varepsilon = 0.0005$ ). For the plots with absorption, the averaged curve corresponds to the one without averaging. The impact of absorption is increased in the areas with low transmittance.

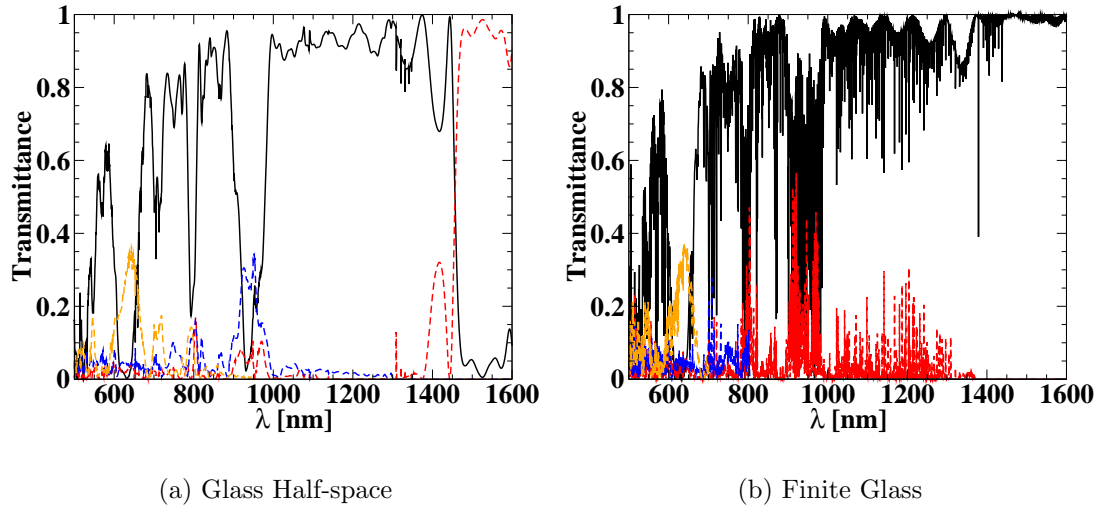


**Figure 6.16:** Transmittance  $0^{th}$  order (black) and  $1^{st}$  order modes. At 670nm and 495nm additional modes occur without significant changes in the transmittance of the others. Only one of the 6 first order modes is not excited over the spectra. None of the peaks are however related to the occurrence of an additional mode. All modes are present at higher and lower wavelengths around the peaks, only the energy distribution between the modes is changed.

one can see that all dips (which occur in the measured  $0^{th}$  order) are connected to peaks in other orders. In the total transmittance these peaks show up much weaker. An explanation can be given in Fig. 6.17 by comparing the situation in the simulation with the experiment.

The experimental situation can be understood from the picture, the theoretical however requires more explanations. Compared to the experimental situation, where energy can get lost to the sides of the sample or glass plate, in the periodic system used for the simulation this is not possible.

Since the  $S$ -matrix is energy conserving, the sum of all transmitted and reflected orders in the air region above and below the crystal is 1.0. If some of the energy is coupled to modes in the glass which undergo a total internal reflection, they are returning into the crystal since also the polymer layer and the crystal are periodic, thus, infinite in the in-plane direction. Since the polymer layer has a lower index than the glass, but higher than  $n_{\text{eff}}$  of the crystal, and all modes coming from the crystal have to pass through the polymer, the impact of the polymer can be ignored in first approximation since all modes exiting the crystal will propagate in the polymer and the glass. In addition, the polymer thickness is small compared to the glass. It can, therefore, be looked at as a kind of “index matching” material.

In the crystal these modes exchange their energy again with all the modes due to the coupling of the periodic system and parts of it leave the crystal through modes propagating in the detection (air) region. The other fraction of the energy couples

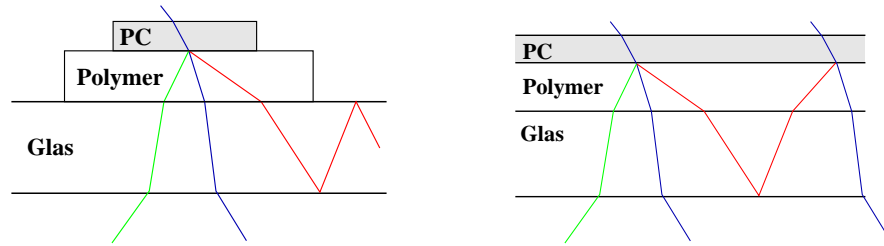


**Figure 6.17:** In the experiment (left), modes which can propagate in the glass but not in air propagate to the side and are lost since the crystal is finite and scattering at surface roughness occurs as well as the total internal reflection does not occur at the sides. In the simulation (right) with periodic boundary conditions for the crystal, polymer layer and glass substrate, the modes in the substrate cannot escape but return periodically on the left, and couple back into the crystal (shown here in the next unit cell to the right instead) where the energy is transferred completely to the propagating modes in the detection(air) region and the low transmittance bands vanish.

back to modes propagating in the glass and the cycle repeats. This explains why the absorption effect is drastically increased for these modes. They are restricted to this cycle of going back and forth between the glass and the crystal until they can exit via a propagating mode. In between energy is absorbed each time they pass through the glass.

These dips in the transmittance are often referred to as Wood anomalies [137, 138]. However, strictly speaking this is not the case. Wood anomalies are related to the onset of new propagating modes, or as often stated, the tangential diffraction of a mode. In the present case the mode is present at higher and lower wavelengths but the energy is redistributed at the dips. One could argue that the tangential diffraction takes place at the pore surface. In this case the effect would have to be surface dependent, since the pores shift with surface termination, which is not the case. In addition, the modes in the polymer and the glass never change during parameter changes of the crystal since these modes depend only on the homogeneous dielectric constant in these layers and the orientation of the incoming wave (see the solution for a homogeneous layer in Sec. 2.2). Especially the propagation angle and the profile of each individual plane wave eigenmode is the same for all crystal realization, as long as the angle and frequencies are the same. Only the coupling to these modes from the crystal changes. The low transmittance bands, however, change their position with prefactor and shrinking, so they depend on crystal properties and not on the number of propagating modes in the polymer or glass layer. Consequently the low transmittance bands are a good measure for the properties of the sample. This information can only be obtained by a detailed comparison of both cases as presented above.

## 6.4 Characterization of Samples

After studying the parameters individually, the results are used to help fabricating a sample with the desired properties [139] by iteratively adjusting the fabrication process to compensate for the distortions caused by the most important factor, the shrinkage [119].

In this section, a comparison of an experimental sample and a calculated transmittance spectra is given. This is in contrast to most of the papers of holographic structures where only structures are proposed [140, 141] or SEM pictures are shown [142, 143]. Although lately some papers showed transmittance measurements, they are not compared to calculated spectra [135, 144, 145].

In this work a total of 4 samples was characterized in great detail for two polarizations but their spectra are given in the appendix only (Sec. C), since for the aim of this chapter one example is sufficient. The final isodose formula contained all the parameters discussed in the previous section<sup>8</sup> and is given by

$$D(\vec{r}) = P(z) \left[ O + \cos \left( \frac{2\pi}{a_{3D}} \left( -\frac{2}{3 \sin \gamma} y - \frac{1}{3 \cos \gamma} \left( \frac{z - \bar{z}}{s} \right) \right) \right) \right. \\ + \cos \left( \frac{2\pi}{a_{3D}} \left( \frac{1}{\sqrt{3} \sin \gamma} x + \frac{1}{3 \sin \gamma} y - \frac{1}{3 \cos \gamma} \left( \frac{z - \bar{z}}{s} \right) \right) \right) \\ \left. + \cos \left( \frac{2\pi}{a_{3D}} \left( -\frac{1}{\sqrt{3} \sin \gamma} x + \frac{1}{3 \sin \gamma} y - \frac{1}{3 \cos \gamma} \left( \frac{z - \bar{z}}{s} \right) \right) \right) \right]. \quad (6.6)$$

The aim was to produce a simple-cubic sample which shows the nominal transmittance spectra. To obtain this, the exposure beams have been adjusted to create an elongated crystal, with the shrinkage compensating the elongation resulting in the desired structures. For this, 4 samples have been fabricated, which differ slightly in lattice constant and prefactor due to the adjustments of the setup. Tab. 6.4 summarizes the results.

---

<sup>8</sup>Polarization and orientation are introduced via the incoming wave though.

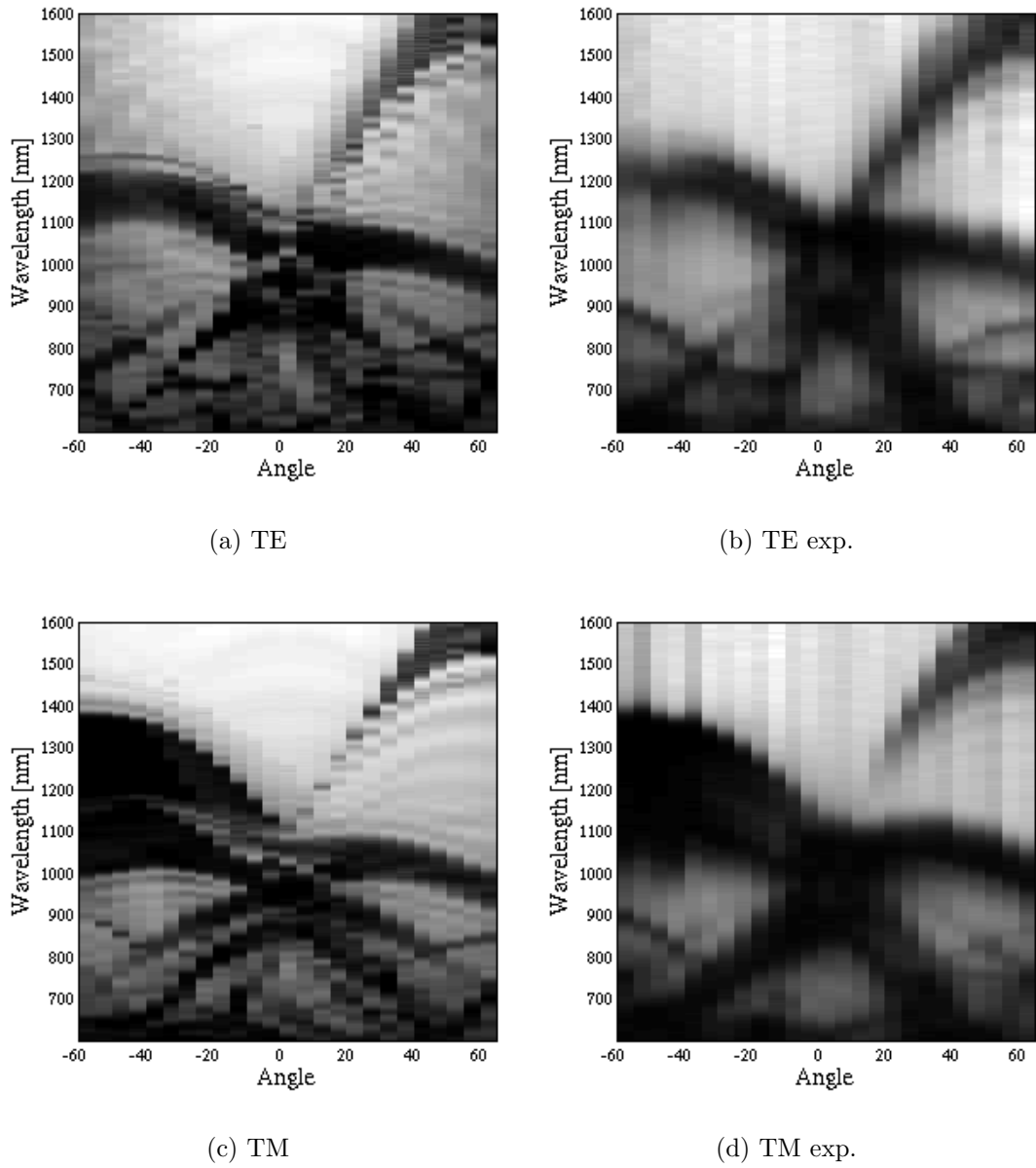


**Figure 6.18:** Spectra for sample #3. Black describes low transmittance (0.0) and white large transmittance (1.0). More spectra can be found in Chapter C of the appendix.

Probe Number	#1 D841	#2 D925	#3 D974	#4 D961
$a_{\text{hex}}$ (nm)	805	863	932	929
$a_z$ (nm)	603	817	1045	1270
elongation factor	1.00	1.33	1.60	1.70
ratio sample/nominal-SC	0.61	0.77	0.91	1.12
processing shrinkage	0.61	0.58	0.56	0.66
$a_{\text{sc}}$ (nm)	569	610	659	657
$f$ (%)	65	70	50	50

**Table 6.2:** Parameters for the 4 characterized samples.  $a_{\text{hex}}$ ,  $a_z$  and  $a_{\text{sc}}$  correspond to the hexagonal, vertical and simple-cubic (3D) lattice constant. The elongation factor describes how strongly the isodose has been stretched by adjusting the exposure beam. The ratio of the sample ( $a_z$ ) to the nominal  $a_{z,\text{sc}}$  shows how close the sample is to the desired simple-cubic structure and is the value used for shrinking in the simulation. It was guessed using simulations and confirmed with higher precision after FIB cutting. The processing shrinkage is the ratio of the elongation factor and the final sample shrinkage. This is the factor the sample shrunk during the processing. For all samples this value is roughly constant around 60%. The filling factor  $f$  has been determined by SEM pictures and refined by comparing with spectra.



# 7 Conclusions and Outlook

In the previous chapters, the basics and the implementation of a versatile, numerically stable and efficient method for the simulation of periodic dielectric photonic systems has been presented and the results for three completely different systems have been reported. In each project, different properties were studied, showing the flexibility and versatility of the method. The common property of all systems which can be modeled is their finite size in one direction ( $z$ ), also called propagation direction, and the periodicity in the other directions<sup>1</sup> ( $x,y$ ).

The primary aim of the simulation is to determine transmittance and reflectance for individual diffraction orders as well as the electromagnetic fields inside the structure. The implementation is based on the Rigorous Coupled Wave Analysis method in conjunction with a scattering matrix approach, leading to a Multilayer (Fourier) Modal Method.

The main concept is to facilitate the numerical mode propagation by slicing the photonic structure into thin layers which are assumed to be homogeneous in the propagation direction and then propagating the fields from layer to layer using boundary conditions. This staircase approximation of the real structure motivates the word “Multilayer”. In each of these layers the permittivity as well as the fields can be represented by Fourier expansions using reciprocal lattice vectors in the periodic lateral direction with a plane wave propagation in the homogeneous propagation direction. The different Fourier orders are coupled through the Maxwell equations, hence the term “Coupled Wave”. By using the Fourier expansion all spatial variables only occur in the exponential, which turns the differential equation into an algebraic equation for which the eigenmodes (lateral field distributions) and eigenvalues (propagation constants of the corresponding field distribution in the  $z$ -direction) can be calculated. This leads to an expansion of the fields in modes, which themselves are expanded in a Fourier series (“Fourier Modal Method”). In a homogeneous layer this expansion corresponds to the Rayleigh expansion of plane waves reflected or transmitted by a grating. The energy transport of individual, uncoupled plane-waves is easily calculated via the Poynting vector, allowing to determine the reflectance and transmittance for each individual diffraction-/Bragg order in the homogeneous (air) regions surrounding the structure. It should be mentioned that non-propagating modes have to be identified beforehand and have to be excluded from the transmittance calculation of the far field to obtain energy conservation.

The incoming/outgoing waves are related to the field expansion in the structure by matching the tangential fields at the layer boundaries. This is done by using a

---

<sup>1</sup>Periodicity in this case can also mean homogeneity.

scattering matrix formulation for better numerical stability although the implementation of a scattering matrix is more complicated than that of a transfer matrix.

Details on the implementation, e. g. how to choose unit cells and expansion orders or how to express the incoming wave correctly, were discussed in the implementation chapter (Chapter 3). Besides correct choices for convergence, optimization possibilities of the program for computational time and/or memory requirements were also discussed as well as possibilities to calculate long crystals with arbitrary surface termination efficiently. In addition technical details were discussed using the hexagonal lattice as an example. There the major issue was the relation of diffraction orders to the chosen in-plane expansion. Finally, the simulation was used to study several systems (Chapters 4–6).

The first system consisted of air pores in macroporous silicon and represents a two-dimensional system. In this chapter structures which can not be produced due to experimental restrictions, e. g. very long crystals, were studied showing how to extract attenuation lengths for crystals with absorption and how to reduce large amounts of data in length dependent spectra to fewer quantities in order to study different aspects of transmittance and reflectance. It was shown that the length dependence at the edge of a stop band cannot be described by a power law, exponential or Yukawa-like function and that an exponential decay for short crystals can only be found in the middle of the stop band. Studies of the surface termination revealed the same transmittance for cuts at different positions in the vertical position which corresponded to inverting the sample due to the choice of the unit cell. The final part of this chapter addressed radius fluctuations with emphasis on the full transmittance distributions for finite structures including the impact of Fabry-Perot resonances. The distributions could not be analyzed automatically, hence simulations were done for selected points (minima, maxima, . . .) in the frequency spectra and suitable indicators for the distribution properties were introduced. The main conclusion was that a description in terms of an average transmittance is only possible in the first band, excluding the maximum of the Fabry-Perot resonances, and at some frequency points in the second band. In all other regions the distributions become asymmetric and wide and cannot be described by a normal/log-normal distribution. These simulations were done by multiplying  $S$ -matrices corresponding to unit cells with different radii and checked by a finite size scaling approach using supercells.

A more applied study was done in the second project, during which a structure used for distributed feedback lasing (Chapter 5) consisting of an active polymer layer on top of a corrugated surface relief grating was simulated. For a semi-classical approach, a number of effective parameters taking into account the field distribution in a periodic system are required. Two of them, which turn out to be the important ones, namely in-plane and out-of-plane losses can be estimated by analyzing the resonance peaks that occur if an incoming wave couples to the quasi-guided modes of the waveguide. The in-plane losses depend on the group velocity and can be estimated from the band diagram, which is given by the position of the resonances. The out-of-plane losses depend on the coupling strength and can be compared using

---

the width of the resonances. In the simulation, modes with a low group-velocity and narrow peaks could be found in parameter regions where the lasing occurs in the experiment. This explained the non-perpendicular emission of the laser.

The last project is again closely related to an experiment, but this time the structure is not well defined and the aim was to study the impact of the parameters on the angle resolved transmittance spectra. The three-dimensional PC was created using lithographic holography in a photoresist. During the processing of the resist, strong deviations of the final structure from its nominal parameters, defined by the isodose surface during exposure, occur. The aim of the study was to characterize the impact of several parameters on the transmittance spectra and to identify the most important parameters causing the distortion. The results were then used to support the experimentalists in compensating the distortion. The study of a model system revealed that surface termination, absorption during the exposure and small misalignments can be ignored. The most important parameter was identified to be shrinkage of up to 60% in the vertical direction. During this study the reason for the spectral signatures at higher wavelength was also studied and found to be caused by the interplay of the substrate and the crystal. Therefore, the termination behind the crystal (air or glass half-space) plays an important role, which has been studied in detail. Finally, real samples were simulated and theory and experiment showed a very good agreement. The determination of the filling factor could be improved by comparing the spectra in comparison to the use of SEM pictures only.

In conclusion it was shown in these three selected projects, that the method is suitable for studying concepts and general aspects of light propagation in Photonic Crystals as well as for modeling realistic experiments either by simulating the response of a crystal and analyzing the spectra or by using a reference spectra and analyzing the structure by changing individual parameters determining their impact on the spectra. All three aspects are important in understanding light propagation in PCs and in improving fabrication processes to achieve better host structures in which later functional elements can be created.

All these systems are based on dielectric materials and unfortunately for metallic structure, e.g. described by a Drude formula, the current implementation fails to converge. The adaptation of the program to metallic structures is, therefore, a main task for future improvement to the code. Especially with respect to the growing sector of metamaterials, e.g. negative index materials in which a magnetic response is possible as well [30, 31, 146–148], this is a very interesting task. Experimental realizations of these structures have already been presented [149–151]. Metallic structures are also needed for large field enhancements in Surface Enhanced Raman Scattering (SERS) [152]. Some ideas and concepts for improving the code were previously mentioned at the end of Chapter 2. Since the bad convergence in the metallic case is based on the folding of Fourier functions in the eigenvalue problem, changing this part to the more complex and more memory consuming approach proposed by Li [49] could be a first step, allowing to reuse most of the ideas of the implementation and optimization chapter (Chapter 3). Alternatively, the replacement of the Fourier-expansion by a real-space method, e.g. Finite Differences (FD)

or Finite Elements(FE), keeping the concept of a Multilayer Modal Method could avoid the problem of Fourier Factorization completely. However, these methods are more time consuming and the very convenient expression in diffraction orders using the Rayleigh expansion in homogeneous layers would have to be abolished or introduced via a Fourier transformation of the fields. The efficiency of the combined (FE/FD with  $S$ -matrix-approach) methods would then have to be compared to three-dimensional implementation of the FE/FD solvers.

For the individual projects, future tasks were mentioned at the end of the individual sections. However, some interesting general questions relating to light propagation in photonic systems should be mentioned here. The results for the holographic structure showed that the investigation of the interplay of PCs and the substrate on which they are produced is a topic that is rarely addressed, since simulations tend to end in a glass half space. The correct modeling of these systems could be studied in more detail, especially if experimental measurements with a very high frequency/wavelength resolution could be obtained<sup>2</sup> as a comparison. Although already mentioned in the corresponding chapter (Chapter 4), the combination of length dependent calculations with disorder would add an interesting dimension to the simulations done so far, which could be compared to the work of Asatryan et al. [153], in which they identified different regimes (diffusive, anomalous diffusive and localized) of light propagation based on Greens tensor calculations for a finite numbers of cylinders.

Besides the more conceptual work mentioned above, the simulation of experimental structures can always be continued offering a large number of more applied projects.

---

<sup>2</sup>Technically this is no problem, however these measurements are time consuming and not very interesting from an experimental point of view and, therefore, they are hard to obtain for a theoretician.

# A Distributions for Selected Frequencies

The following graphs show the transmittance distribution for the frequencies corresponding to selected points in the spectra (minima, maxima, ...) for a structure with a length of 5 numerical unit cells (5 cylinders) as discussed in Sec. 4.9. The radius fluctuates by  $\pm 5\%$ , using a Gaussian distribution truncated at  $r_{\min} = 0.38$  and  $r_{\max} = 0.42$ , with these values corresponding to a  $3\sigma$  distance from  $r_0 = 0.4$ . The frequency points are shown in Fig. A.1.

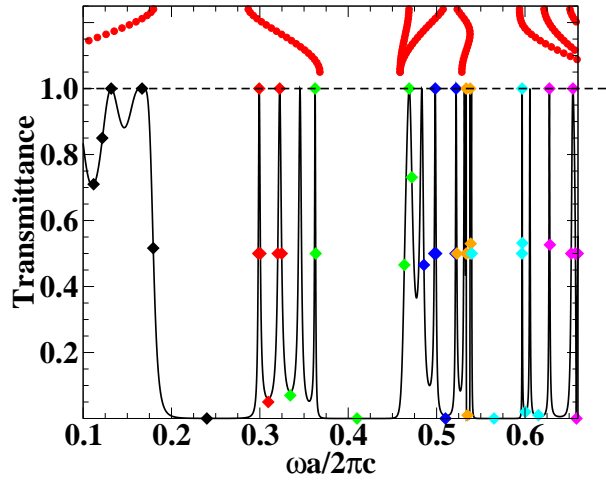


**Figure A.1:** Transmittance of a perfect structure with a length of 5 numerical unit cells (5 cylinders). The parameters are  $r_0 = 0.4$ ,  $\varepsilon_{\text{pore}} = 1.0$ ,  $\varepsilon_{\text{sub}} = 11.9$ , orientation in  $\Gamma X$  (Fig. 4.1). Each color depicts the frequencies plotted on one of the following pages. The red dots indicate the band structure.

The distributions for 1000 realizations are ordered with increasing frequency. On the left side, the normal distribution is shown followed to the right by the log-normal distribution, log-normal with a supercell containing 2 and 3 cylinders in the horizontal direction. For higher frequencies, no data for the larger supercell is available. The analysis can be found in Sec. 4.9 and the distributions are presented to give an overview about the agreement of the data (red) with the theoretical distributions using the average and standard variance determined from the data (black). In addition, the distributions can be compared to supercell calculations. In contrast to the next appendix, each plot is scaled to fit the distribution best, so that the  $x$ -axis giving the (width of the) transmittance can change in a row.

The supercell distributions generally become narrower, if the number of cylinders is increased, keeping the characteristic form of the distribution constant.

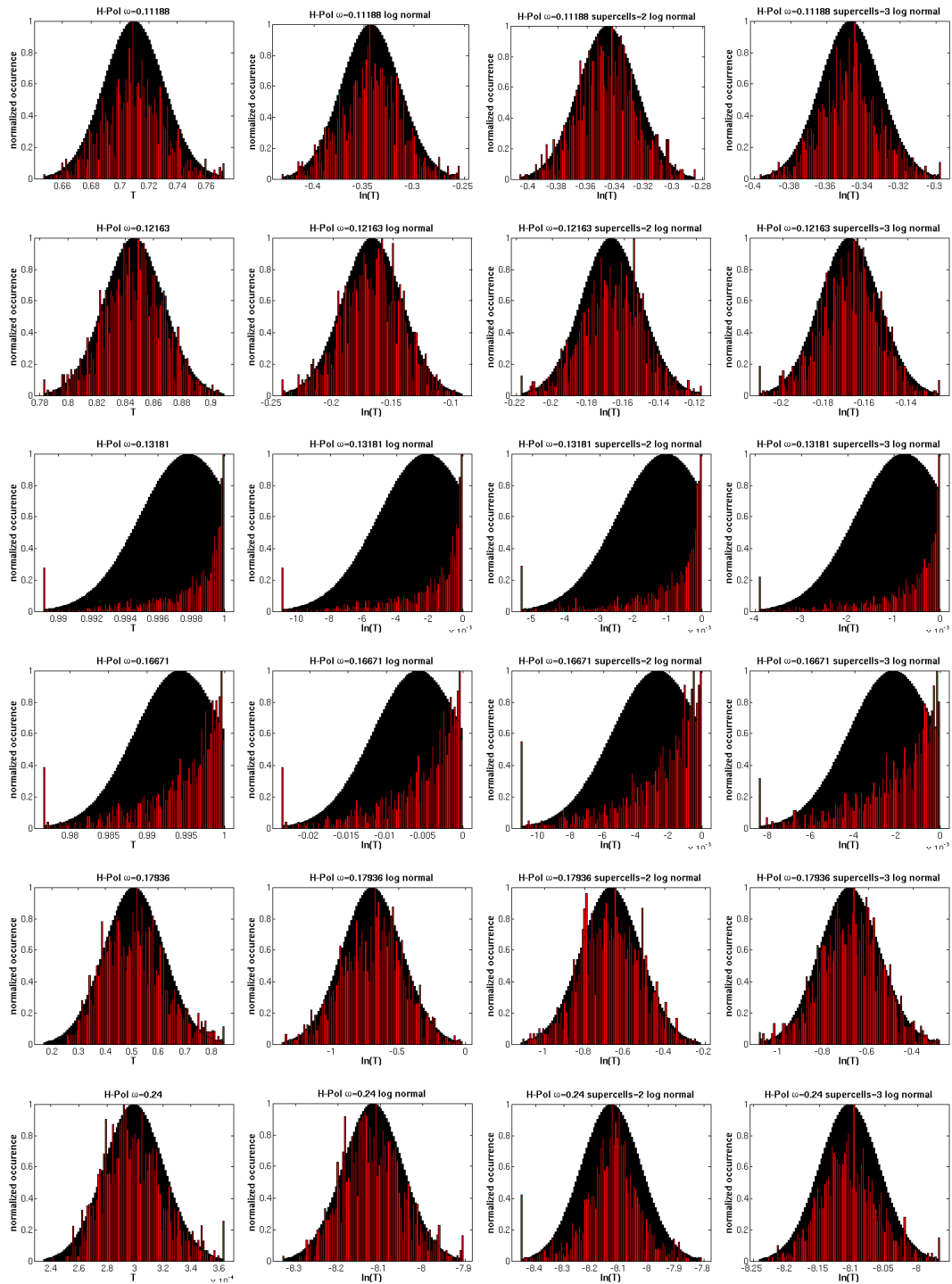


**Figure A.2:** Black diamonds in Fig. A.1: Normal, Log-normal, 2 and 3 Supercells

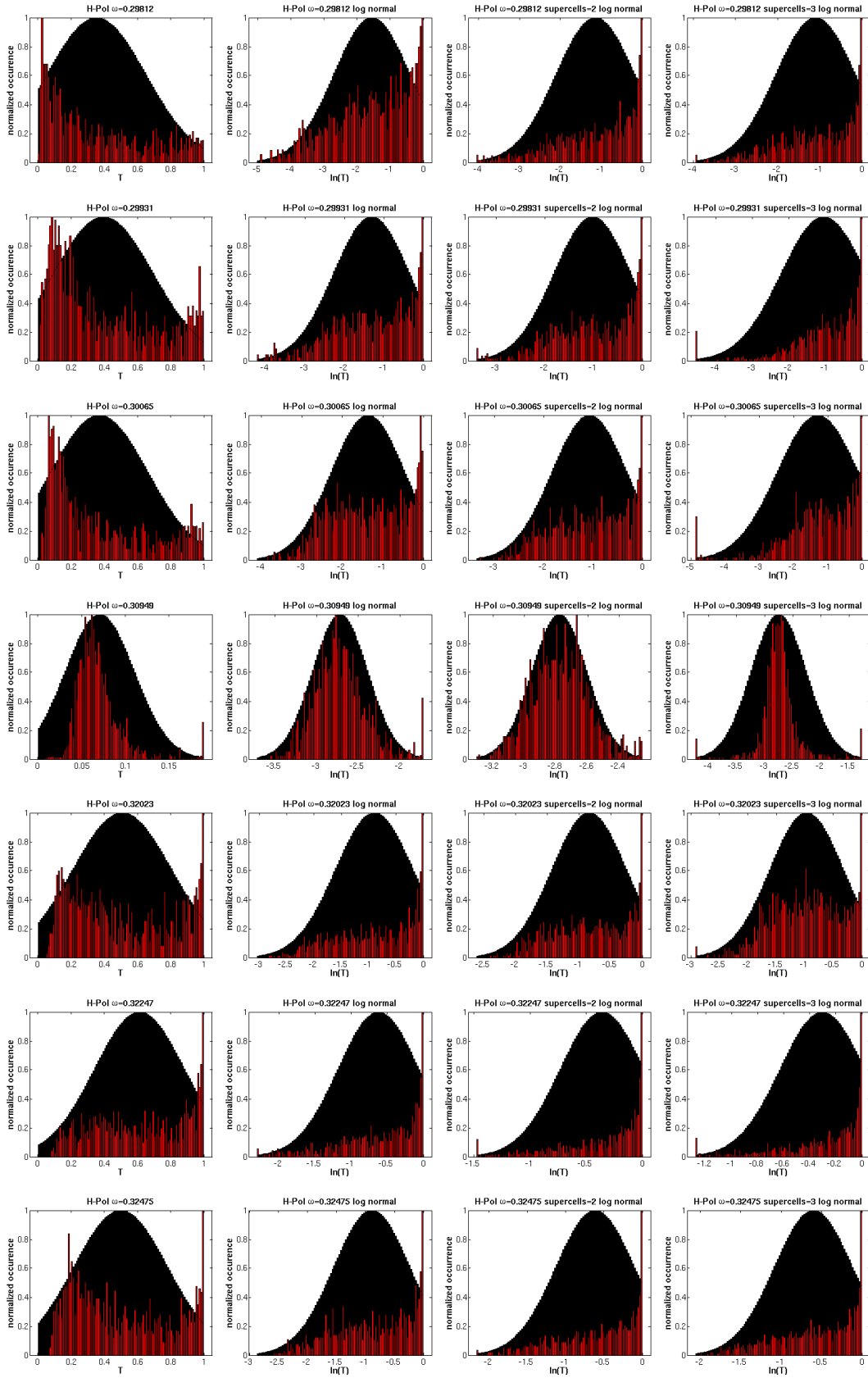


Figure A.3: Red diamonds in Fig. A.1: Normal, Log-normal, 2 and 3 Supercells

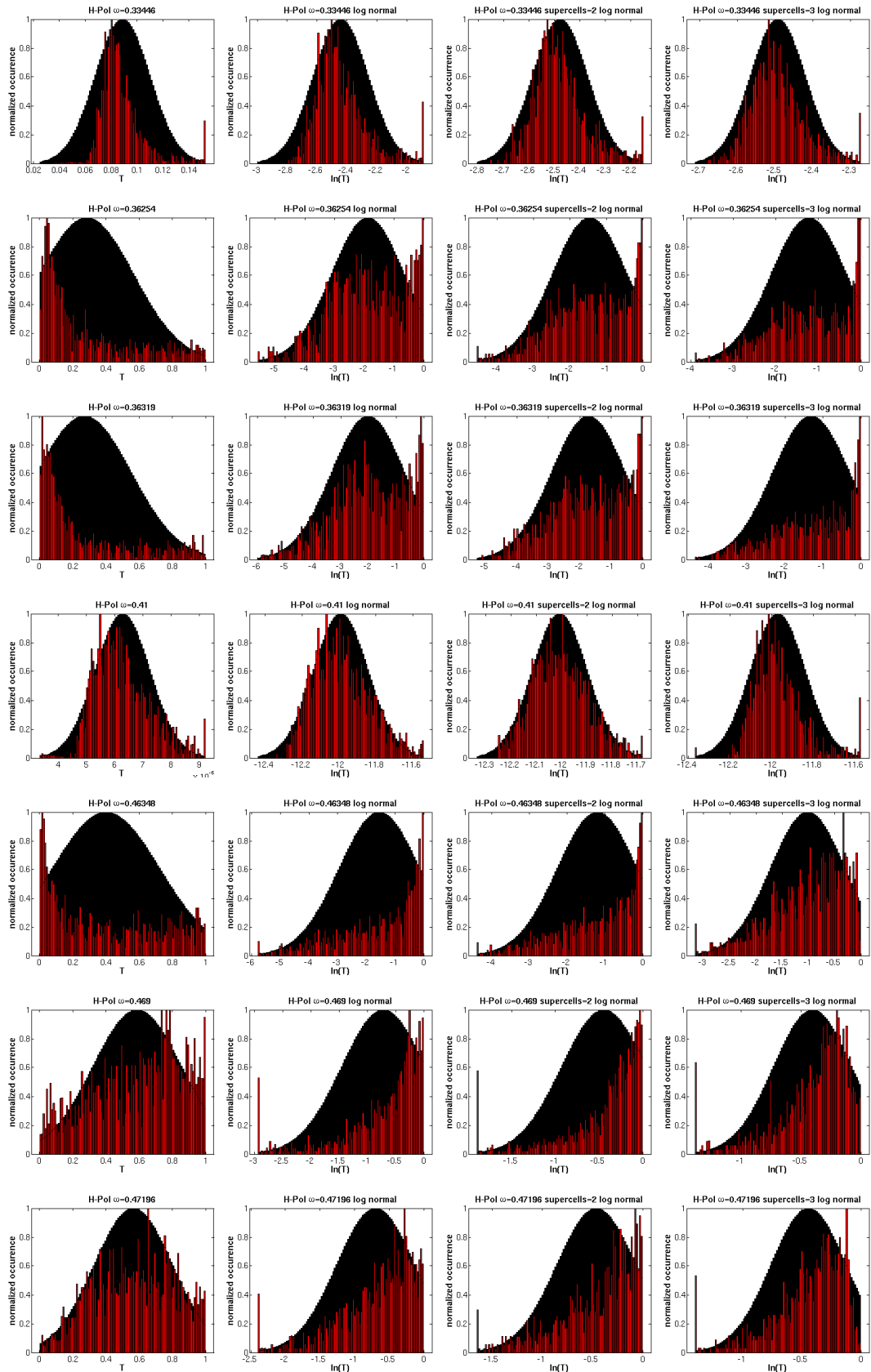


Figure A.4: Green diamonds in Fig. A.1: Normal, Log-normal, 2 and 3 Supercells

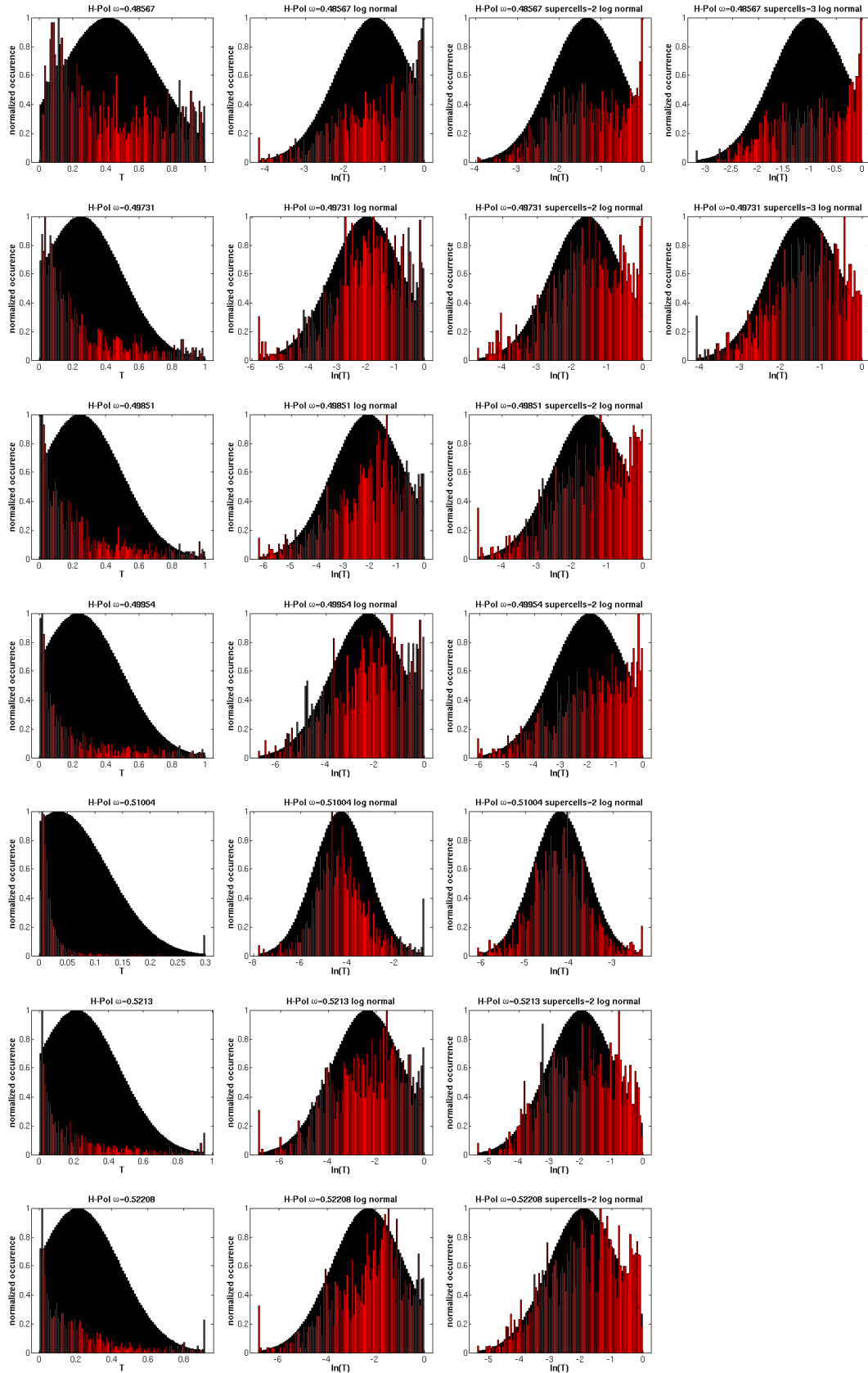


Figure A.5: Blue diamonds in Fig. A.1: Normal, Log-normal, 2 and 3 Supercells

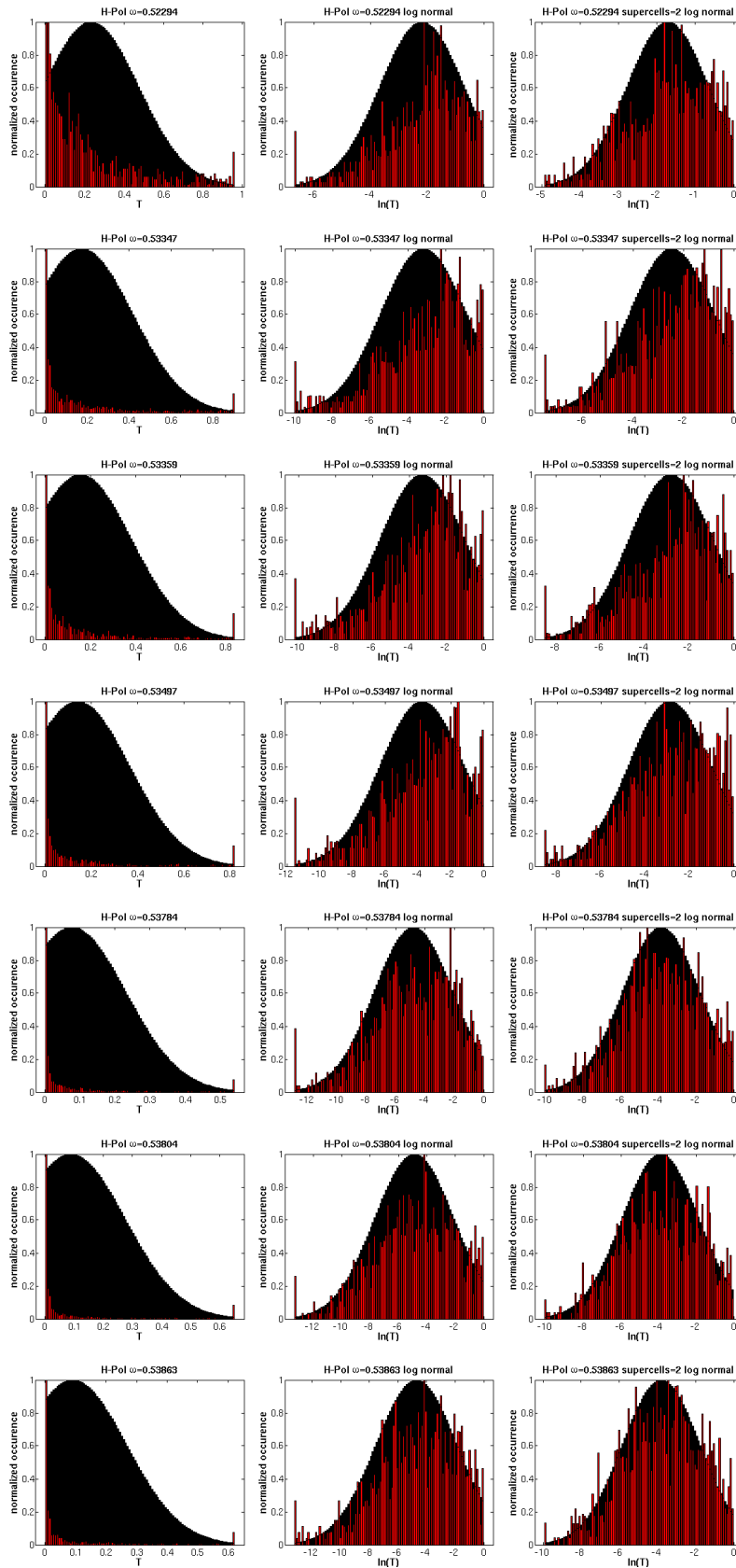


Figure A.6: Orange diamonds in Fig. A.1: Normal, Log-normal, 2 Supercells

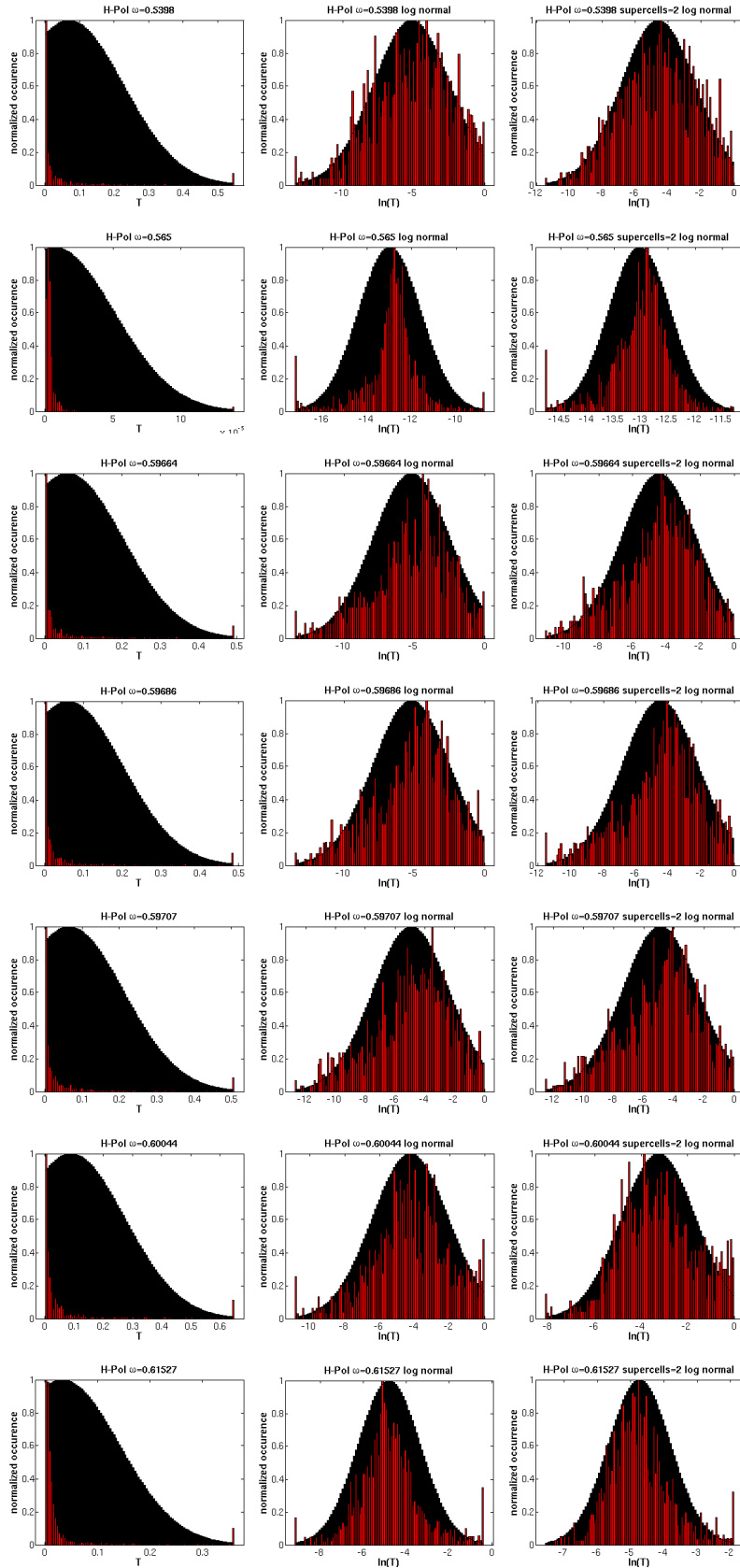


Figure A.7: Cyan diamonds in Fig. A.1: Normal, Log-normal, 2 Supercells

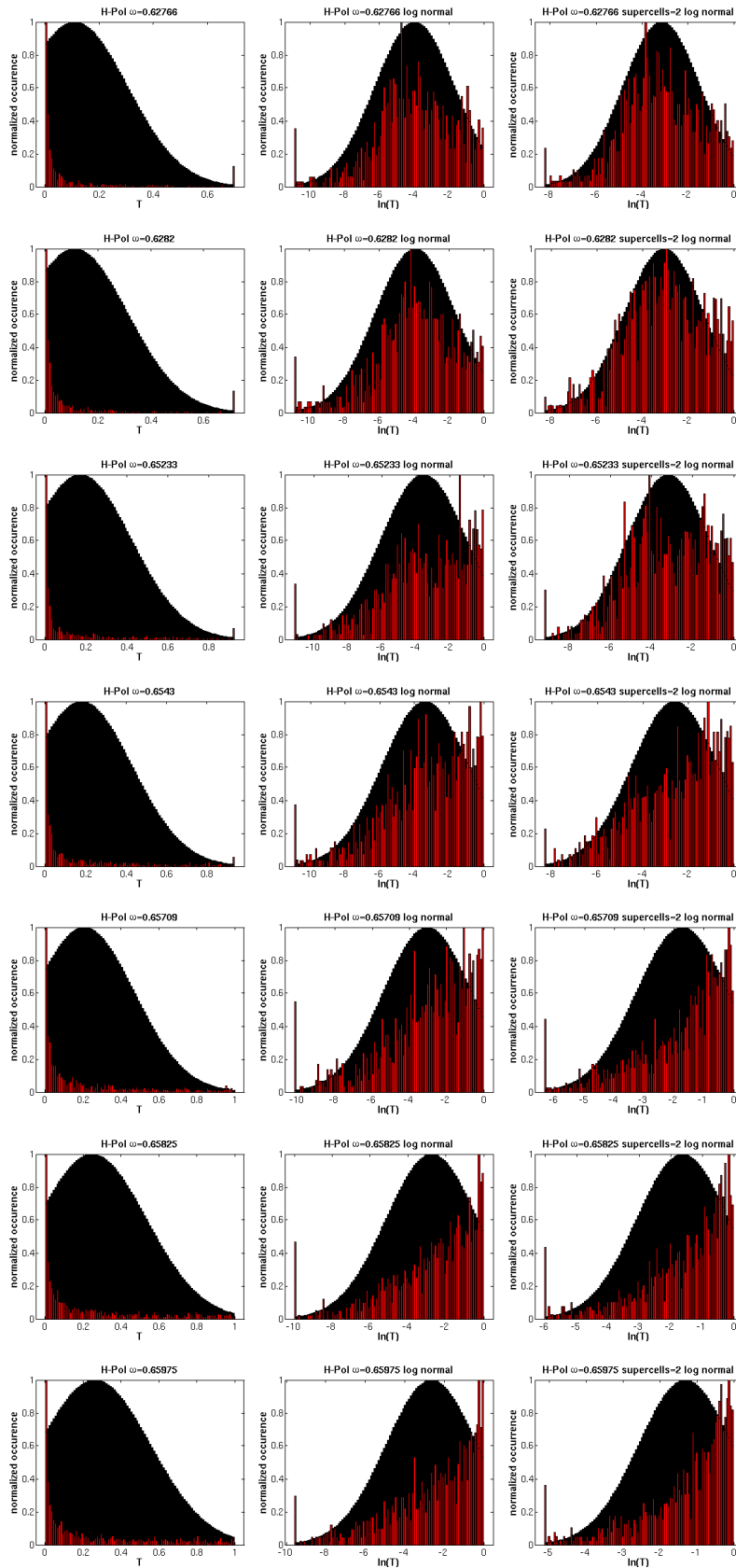
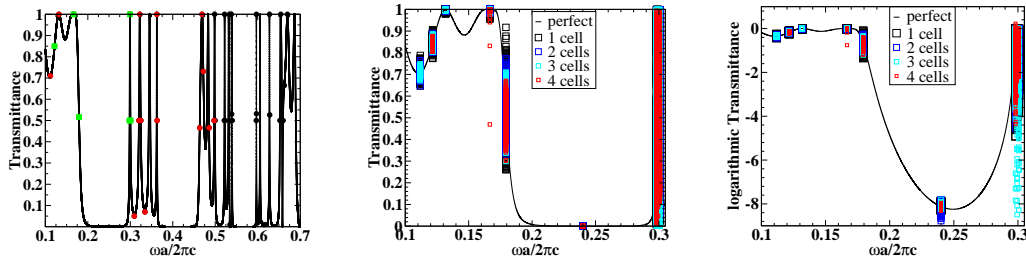


Figure A.8: Magenta diamonds in Fig. A.1: Normal, Log-normal, 2 Supercells

# B Transmittance Distributions for Supercells

The change of the distribution with the supercell size is illustrated using supercells containing 1 through 4 cylinders perpendicular to the propagation direction. Details are discussed in Sec. 4.9. The radius fluctuates by  $\pm 5\%$ , using a Gaussian distribution truncated at  $r_{\min} = 0.38$  and  $r_{\max} = 0.42$ , with these values corresponding to a  $3\sigma$  distance from  $r_0 = 0.4$ . The parameters of the crystal are given by  $r_0 = 0.4$ ,  $\varepsilon_{\text{pore}} = 1.0$ ,  $\varepsilon_{\text{sub}} = 11.9$ , orientation in  $\Gamma X$  and a length of 5 unit cells. For a definition see Fig. 4.1. The used frequency points are shown in Fig. B.1.



**Figure B.1:** Left: Selected Frequencies for supercell calculations. The color correspond to different maximal sizes of the supercell (Green=4, Red=3, Black=2). Middle: All transmittance values for 1-4 supercells at the green points (Normal). Right: Same in log-normal.

In the following figures the full distributions, each containing 1000 realizations, are plotted as a supplement to Sec. 4.9.7. The axis in each row are constant, so that the distributions can be compared directly.

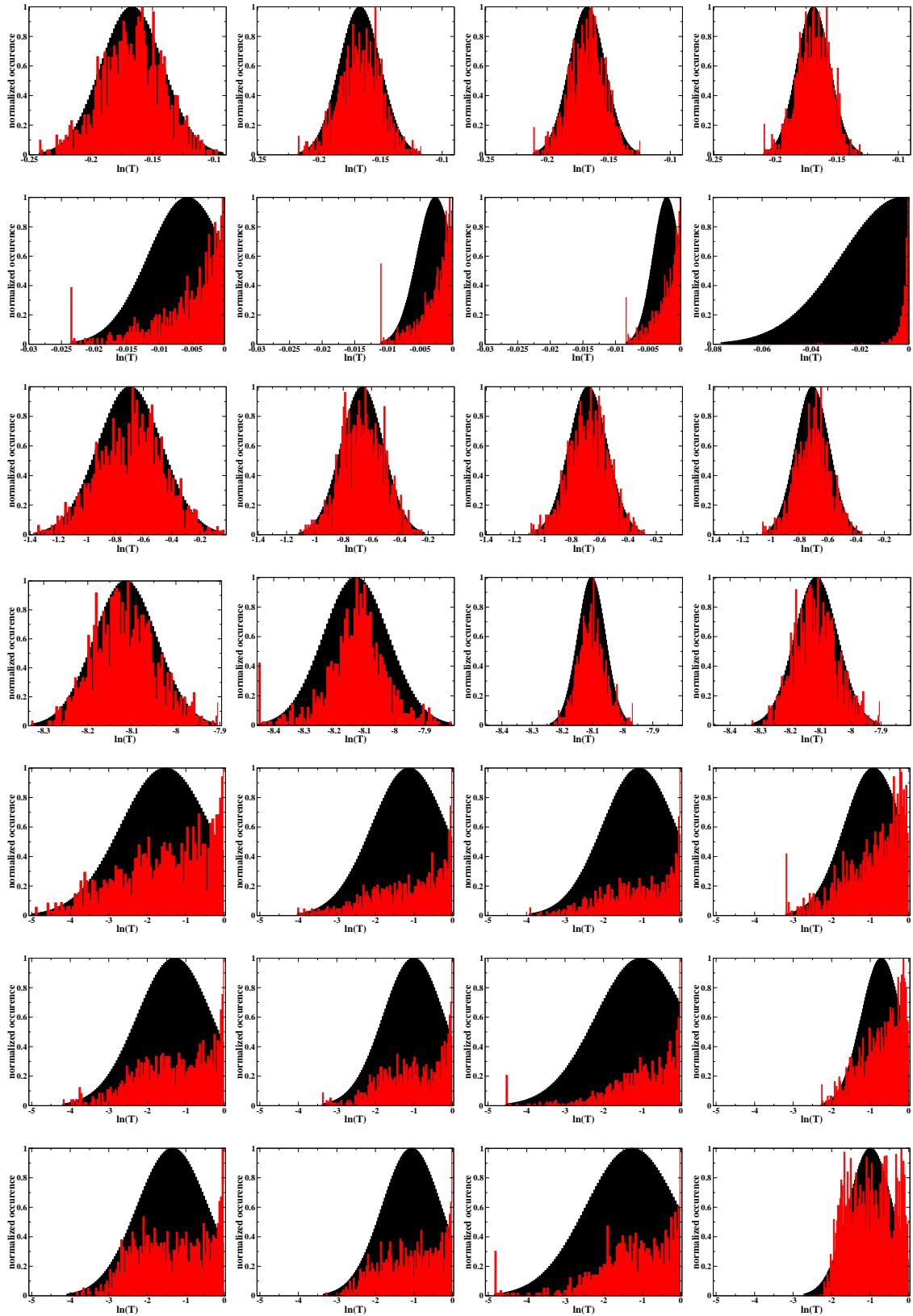


**Figure B.2:** 1-4 supercells shown on same scale for the frequencies depicted in Fig. B.1.

# C Comparison of Experiment and Theory for Holographic Structures

Using the approach described in Chapter 6, a series of samples was characterized [139]. This was done with the intention to compensate for the distortions of the structure during the fabrication to achieve the nominal simple-cubic crystal with the desired optical properties.

In contrast to the simple dose formula eq. (6.1) in Sec. 6.1.2 changes in all structural parameters are incorporated in a more complex dose formula (compare discussion in Sec. 6.3)

$$D(\vec{r}) = P(z) \left[ \begin{aligned} & \cos \left( \frac{2\pi}{a_{3D}} \left( -\frac{2}{3 \sin \gamma} y - \frac{1}{3 \cos \gamma} \left( \frac{z - \bar{z}}{s} \right) \right) \right) \\ & + \cos \left( \frac{2\pi}{a_{3D}} \left( \frac{1}{\sqrt{3} \sin \gamma} x + \frac{1}{3 \sin \gamma} y - \frac{1}{3 \cos \gamma} \left( \frac{z - \bar{z}}{s} \right) \right) \right) \\ & + \cos \left( \frac{2\pi}{a_{3D}} \left( -\frac{1}{\sqrt{3} \sin \gamma} x + \frac{1}{3 \sin \gamma} y - \frac{1}{3 \cos \gamma} \left( \frac{z - \bar{z}}{s} \right) \right) \right) \end{aligned} \right]. \quad (\text{C.1})$$

with the prefactor  $P$  defining the filling fraction of the structure, the lattice constant  $a_{3D}$  of the 3D lattice and the shift of the unit cell  $\bar{z}$  used to model different surface termination. The absorption of the exposure beam is incorporated into the prefactor as an exponential decrease. Including this parameter has the additional effect, that the entire crystal has to be modeled, since the periodicity in the  $z$ -direction is lost. Consequently the same number of vertical unit cells has to be used as in the experiment and the prefactor has to be changed through the complete structure. Since 5 unit cells had to be calculated this also required 5 times as many layers in the discretization and, therefore, 5 times as much memory if the dielectric Toeplitz-matrices were to be stored and roughly a 5 time longer computation time, requiring an efficient implementation of the method. The prefactor has been adjusted according to

$$P(z) = P(0) e^{-\alpha \frac{z}{a_z}}, \quad (\text{C.2})$$

and the different surface termination, as well as vertical shrinkage in the factor in the rescales  $z$ -coordinate

$$\frac{z - \bar{z}}{s}. \quad (\text{C.3})$$

For doses higher than a threshold  $D_{\text{thres}}$  the polymer is kept ( $\varepsilon_p = 2.56$ ), in all other cases the permittivity as assumed to be the one of air ( $\varepsilon_{\text{air}} = 1.0$ ).

Parameters which are not included in the dose formula are the orientation of the sample/probe beam, averaging of the transmittance over several frequencies and the lattice constant. Adjusting these parameters the theoretical and experimental spectra could be compared. The correct values of the individual parameters could be measured in SEM pictures ( $a_{\text{hex}}$ ), estimated from SEM pictures and fine-tuned by comparing with theoretical spectra ( $P$ ), respectively estimated from theoretical spectra and determined by destroying the sample using focused ion beam ( $a_z$ ). Other parameters could already be excluded during the simulation because of their minor impact (surface, misalignments, absorption of the exposure beam).

On the following pages the theoretical and experimental spectra are shown for four samples with the properties listed in Tab. C. The first page lists the theoretical spectra for the two polarizations<sup>1</sup>, the following the experimental. In both figures the samples are ordered vertically, starting with sample #1 at the top. The left column belongs to TE polarization and the right depicts TM polarization. This setup has been chosen because it allows the printing on transparencies and overlaying of the plots to compare the results.

---

<sup>1</sup>The caption use TE/TM describing the field which has no out-of-plane component. Experimentalist prefer the plane of incidence as reference. In this nomenclature the polarizations are given by s/p.

---

Probe Number	#1 D841	#2 D925	#3 D974	#4 D961
$a_{\text{hex}}$ (nm)	805	863	932	929
$a_z$ (nm)	603	817	1045	1270
elongation factor	1.00	1.33	1.60	1.70
ratio sample/nominal-SC $s$	0.61	0.77	0.91	1.12
processing shrinkage	0.61	0.58	0.56	0.66
$a_{\text{sc}}$ (nm)	569	610	659	657
$f$ (%)	65	70	50	50
prefactor $P(0)$	2.02	2.12	1.75	1.75
$\alpha$	0.0			
averaging	$\pm 6\text{nm}$			
absorption in glass	$\text{Im } \varepsilon_{\text{glass}} = 0.001$			
surface termination $\bar{z}$	0.0			

**Table C.1:** Parameters for the 4 characterized samples.  $a_{\text{hex}}$ ,  $a_z$  and  $a_{\text{sc}}$  correspond to the hexagonal, vertical and simple-cubic(3D) lattice constant. The elongation factor describes how strongly the isodose has been stretched by adjusting the exposure beam. The ratio of the sample ( $a_z$ ) to the nominal  $a_{c,\text{sc}}$  shows how close the sample is to the desired simple-cubic structure and is the value used for shrinking in the simulation and determined by measurements after focus ion beam cutting. The processing shrinkage is the ratio of the elongation factor and the final sample shrinkage. This is the factor the sample shrunk during the processing. For all samples this value is roughly constant. The filling factor  $f$  has been determined by SEM pictures and refined by comparing with spectra. The corresponding prefactor is used in eq. (C.1).

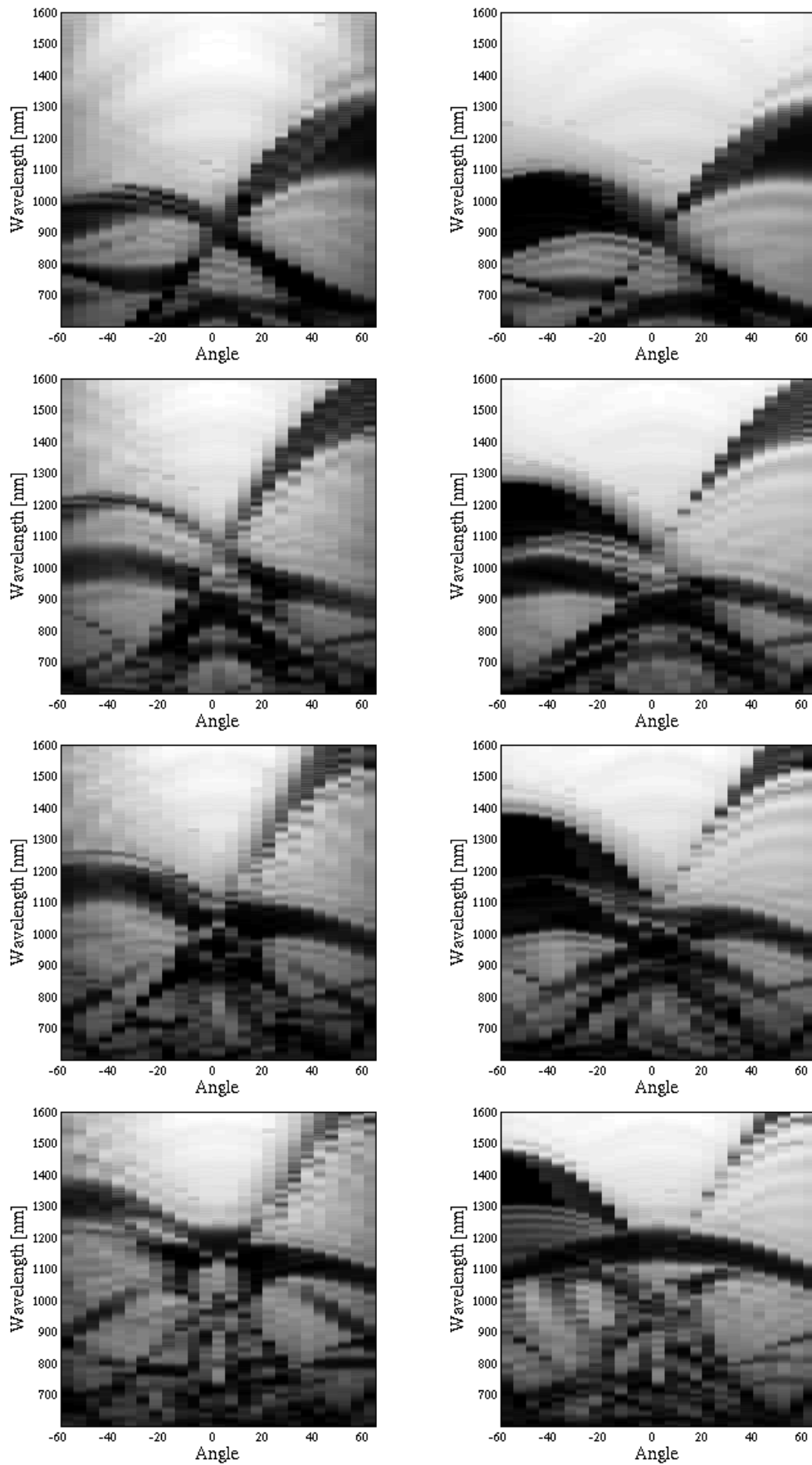


**Figure C.1:** Theoretical spectra: TE - sample #1 (top left), TM-sample #4 (bottom right)

---

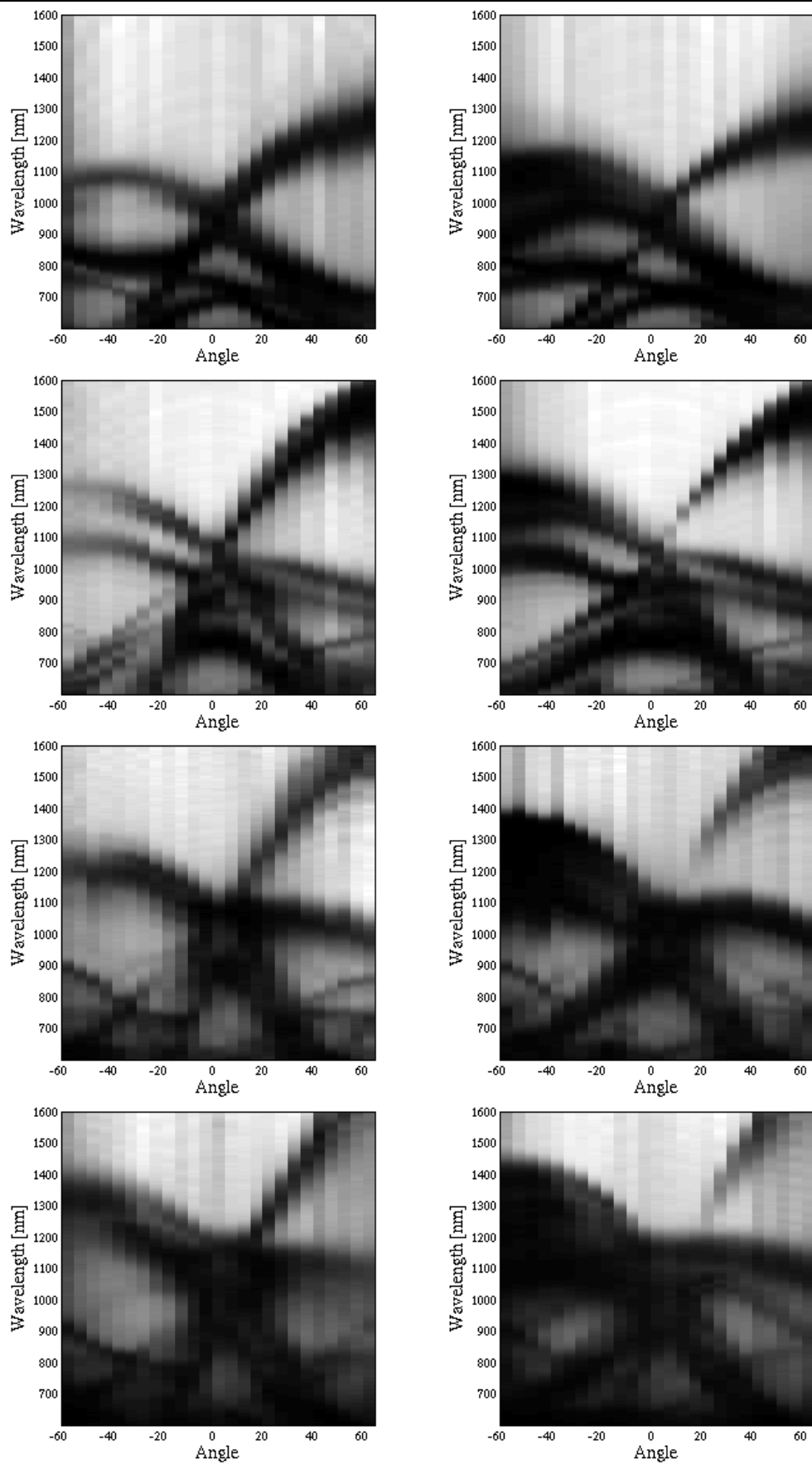


**Figure C.2:** Experimental spectra: TE - sample #1 (top left), TM-sample #4 (bottom right)



# Acronyms

<b>BZ</b>	Brillouin Zone
<b>FD</b>	Finite Differences
<b>FDTD</b>	Finite Difference Time Domain
<b>FE</b>	Finite Elements
<b>FIB</b>	Focused Ion Beam
<b>FMM</b>	Fourier Modal Method
<b>I-matrix</b>	Interface-matrix (T-matrix across the boundary of two layers)
<b>M-matrix</b>	Modal-matrix (containing the eigenmodes of the in-plane field components)
<b>MMM</b>	Multilayer Modal Method
<b>PBG</b>	Photonic Band Gap <sup>2</sup>
<b>PC</b>	Photonic Crystal
<b>1D</b>	one-dimensional
<b>2D</b>	two-dimensional
<b>3D</b>	three-dimensional
<b>RCWA</b>	Rigorous Coupled Wave Analysis
<b>S-matrix</b>	Scattering-matrix
<b>SEM</b>	Scanning Electron Microscope
<b>SERS</b>	Surface Enhanced Raman Scattering
<b>T-matrix</b>	Transfer-matrix
<b>WSC</b>	Wigner-Seitz Cell



# Bibliography

- [1] C. M. Soukoulis, editor, *Photonic Band Gaps and Localization*, vol. 308 of *NATO ASI Series B Physics*, Plenum Press (1993).
- [2] J. D. Joannopoulos, R. D. Meade, and J. N. Winn, *Photonic Crystals: Molding the flow of Light*, Princeton (1995).
- [3] C. M. Soukoulis, editor, *Photonic Band Gap Materials*, vol. 315 of *NATO ASI Series E Applied Sciences*, Kluwer Academic Publishers (1996).
- [4] K. Sakoda, *Optical Properties of Photonic Crystals*, vol. 80 of *Springer Series in optical sciences*, Springer (2001).
- [5] S. G. Johnson and J. D. Joannopoulos, *Photonic Crystals The Road from Theory to Practice*, Kluwer Academic Publishers (2002).
- [6] K. Busch, S. Loelkes, R. B. Wehrspohn, and H. Föll, editors, *Photonic Crystals: Advances in Design, Fabrication, and Characterization*, Wiley-VCH (2004).
- [7] K. Inoue and K. Ohtaka, *Photonic crystals : physics, fabrication, and applications*, Springer (2004).
- [8] E. Yablonovitch, “Inhibited Spontaneous Emission in Solid-State Physics and Electronics”, *Phys. Rev. Lett.* **58**, 2059 (1987).
- [9] S. John, “Strong localization of photons in certain disordered dielectric superlattices”, *Phys. Rev. Lett.* **58**, 2486 (1987).
- [10] J. Joannopoulos, “The Photonic Micropolis”, <http://ab-initio.mit.edu/photons/micropolis.html>.
- [11] S. Fan, P. R. Villeneuve, J. D. Joannopoulos, and H. A. Haus, “Channel Drop Tunneling through Localized States”, *Phys. Rev. Lett.* (1998).
- [12] S. Noda, A. Chutinan, and M. Imada, “Trapping and emission of photons by a single defect in a photonic bandgap structure”, *Nature* **407**, 608 (2000).
- [13] M. Y. Tekeste and J. M. Yarrison-Rice, “High efficiency photonic crystal based wavelength demultiplexer”, *Optics Express* **14**, 7931 (2006).

- [14] S. F. Mingaleev and K. Busch, “Scattering matrix approach to large-scale photonic crystal circuits”, *Opt. Lett.* **28**, 619 (2003).
- [15] K. Busch, S. F. Mingaleev, M. Schillinger, and D. Hermann, “The Wannier function approach to photonic crystal circuits”, *Journal of Physics: Condensed Matter* **15**, R1233 (2003).
- [16] E. Smirnova, A. Kesar, I. Mastovsky, M. Shapiro, and R. Temkin, “Demonstration of a 17-GHz, High-Gradient Accelerator with a Photonic-Band-Gap Structure”, *Phys. Rev. Lett.* **95**, 74801 (2005).
- [17] J. Bravo-Abad, M. Ibanescu, J. D. Joannopoulos, and M. Soljacic, “Photonic crystal optical waveguides for on-chip Bose-Einstein condensates”, *Phys. Rev. A* **74**, 053619 (2006).
- [18] J. D. Ania-Castanon, T. J. Ellingham, R. Ibbotson, X. Chen, L. Zhang, and S. K. Turitsyn, “Ultralong Raman Fiber Lasers as Virtually Lossless Optical Media”, *Phys. Rev. Lett.* **96** (2006).
- [19] P. Yeh, *Optical Waves in Layered Media*, Wiley (1988).
- [20] P. S. J. Russell, “Photonic crystal fibers”, *Science* **299**, 358 (2003).
- [21] Crystal Fibre A/S, “Photonic Crystal Fibre”, company website, <http://www.crystal-fibre.com/>.
- [22] Mesophotonics, “Photonic Crystal Application in SERS”, company website, <http://www.mesophotonics.com>.
- [23] Photonic Lattice, “Applications of Photonic Crystals”, company website, <http://www.photonic-lattice.com>.
- [24] A. R. Parker, “Natural photonic engineers”, *Materials Today* **5**, 26 (2002).
- [25] L. P. Biró, Z. Bálint, K. Kertész, Z. Vértesy, G. I. Márk, Z. E. Horváth, J. Balázs, D. Méhn, I. Kiricsi, V. Lousse, and J.-P. Vigneron, “Role of photonic-crystal-type structures in the thermal regulation of a Lycaenid butterfly sister species pair”, *Phys. Rev. B* **67** (2003).
- [26] O. Deparis, C. Vandenbem, M. Rassart, V. Welch, and J.-P. Vigneron, “Color-selecting reflectors inspired from biological periodic multilayer structures”, *Optics Express* **14**, 3547 (2006).
- [27] J. Huang, X. Wang, and Z. L. Wang, “Controlled Replication of Butterfly Wings for Achieving Tunable Photonic Properties”, *Nano Lett.* **6**, 2325 (2006).
- [28] E. Schonbrun, Q. Wu, W. Park, T. Yamashita, and C. J. Summers, “Polarization beam splitter based on a photonic crystal heterostructure”, *Opt. Lett.* **31**, 3104 (2006).

- 
- [29] A. Chutinan and S. John, “3 + 1 dimensional integrated optics with localized light in a photonic band gap”, *Optics Express* **14**, 1266 (2006).
- [30] D. R. Smith, J. B. Pendry, and M. C. K. Wiltshire, “Metamaterials and Negative Refractive Index”, *Science* **305**, 788 (2006).
- [31] J. Pendry, “Photonics: Metamaterials in the sunshine”, *Nature Mater.* **5**, 599 (2006).
- [32] A. Blanco, E. Chomski, S. Grabtchak, M. Ibisate, S. John, S.W.Leonard, C.Lopez, F.Meseguer, H. Miguez, J.P.Mondia, G.A.Ozin, O.Toader, and H. Driel, “Large-scale synthesis of a silicon photonic crystal with a complete three-dimensional bandgap near 1.5 micrometres”, *Nature* **405**, 437 (2000).
- [33] E. Özbay, A. Abeyta, G. Tuttle, M. Tringides, R. Biswas, C. T. Chan, C. M. Soukoulis, and K. M. Ho, “Measurement of a three-dimensional photonic band gap in a crystal structure made of dielectric rods”, *Phys. Rev. B* **50**, 1945 (1994).
- [34] K. M. Ho, C. T. Chan, and C. M. Soukoulis, “Existence of a photonic gap in periodic dielectric structures”, *Phys. Rev. Lett.* **65**, 3152 (1990).
- [35] D. Hermann, *Bandstrukturechnungen für Photonische Kristalle mittels Mehrgitter-Verfahren*, Diplomarbeit, Universität Karlsruhe, Institut für theoretische Festkörperphysik (2001).
- [36] M. Ashcroft and N. Mermin, *Solid State Physics*, Saunders (1975).
- [37] J. Jackson, *Classical electrodynamics*, Wiley, 2nd edn. (1975).
- [38] K. Busch and S. John, “Photonic band gap formation in certain self-organizing systems”, *Phys. Rev. E* **58**, 3896 (1998).
- [39] K. Busch, “Photonic band structure theory: assessment and perspectives”, *Compte Rendus Physique 3, 53-66* **3**, 53 (2002).
- [40] R. D. Meade, A. M. Rappe, K. D. Brommer, J. D. Joannopoulos, and O. L. Alerhand, “Accurate theoretical analysis of photonic band-gap materials”, *Phys. Rev. B* **48**, 8434 (1993).
- [41] K. Busch, A. Garcia-Martin, D. Hermann, L. Tkeshelashvili, M. Frank, and P. Wölflé, *Advance in Solid State Physics*, vol. 42 of *Advances in Solid State Physics*, chap. Photonic Crystals: Optical Materials for the 21st Century, pp. 41–53, Springer Verlag, Berlin Heidelberg (2002).
- [42] D. M. Whittaker and I. S. Culshaw, “Scattering-matrix treatment of patterned multilayer photonic structures”, *Phys. Rev. B* **60**, 2610 (1999).
-

- [43] L. Li, “Multilayer modal method for diffraction gratings of arbitrary profile, depth, and permittivity”, *J. Opt. Soc. Am. A* **10**, 2581 (1993).
- [44] G. G. Moharam and T. K. Gaylord, “Rigorous coupled-wave analysis of planar-grating diffraction”, *J. Opt. Soc. Am.* **71**, 811 (1981).
- [45] S. Peng, T. Tamir, and H. Bertoni, “Theory of periodic dielectric waveguides”, *IEEE Trans. Microwave Theory Tech* **23**, 123 (1975).
- [46] D. Y. K. Ko and J. R. Sambles, “Scattering matrix method for propagation of radiation in stratified media: attenuated total reflection studies of liquid crystals”, *J. Opt. Soc. Am. A* **5**, 1863 (1988).
- [47] N. P. K. Cotter, T. W. Preist, and J. Sambles, “Scattering-matrix approach to multilayer diffraction”, *J. Opt. Soc. Am. A* **12**, 12 (1995).
- [48] L. Li and C. W. Haggans, “Convergence of the coupled-wave method for metallic lamellar diffraction gratings”, *J. Opt. Soc. Am. A* **10**, 1184 (1993).
- [49] L. Li, “Formulation and comparison of two recursive matrix algorithms for modeling layered diffraction gratings”, *J. Opt. Soc. Am. A* **13**, 1024 (1996).
- [50] M. G. Moharam, D. A. Pommet, E. B. Grann, and T. K. Gaylord, “Stable implementation of the rigorous coupled-wave analysis for surface-relief gratings: enhanced transmittance matrix approach”, *J. Opt. Soc. Am. A* **12**, 1077 (1995).
- [51] L. Li, “Note on the S-matrix propagation algorithm”, *J. Opt. Soc. Am. A* **20**, 655 (2003).
- [52] D. Y. K. Ko and J. C. Inkson, “Matrix method for tunneling in heterostructures: Resonant tunneling in multilayer systems”, *Phys. Rev. B* **38**, 9945 (1988).
- [53] S. G. Tikhodeev, A. L. Yablonskii, E. A. Muljarov, N. A. Gippius, , and T. Ishihara, “Quasiguided modes and optical properties of photonic crystal slabs”, *Phys. Rev. B* **66**, 45102 (2002).
- [54] L. Li, “Use of Fourier series in the analysis of discontinuous periodic structures”, *J. Opt. Soc. Am. A* (1996).
- [55] L. Li, “Convergence of electromagnetic field components across discontinuous permittivity profiles: comment”, *J. Opt. Soc. Am. A* **19**, 1443 (2002).
- [56] L. Li, “New formulation of the Fourier modal method for crossed surface-relief gratings”, *J. Opt. Soc. Am. A* **14**, 2758 (1997).

- 
- [57] A. David, H. Benisty, and C. Weisbuch, “Fast factorization rule and plane-wave expansion method for two-dimensional photonic crystals with arbitrary hole-shape”, *Phys. Rev. B* **73**, 075107 (2006).
- [58] L. Li, J. Chandezon, G. Granet, and J.-P. Plumey, “Rigorous and Efficient Grating-Analysis Method Made Easy for Optical Engineers”, *Appl. Opt.* **38**, 304 (1999).
- [59] E. Silberstein, P. Lalanne, J. P. Hugonin, and Q. Cao, “Use of grating theories in integrated optics”, *J. Opt. Soc. Am. A* **18**, 2865 (2001).
- [60] J. Jin, *The finite element method in electromagnetics*, Wiley, 2nd edn. (2002).
- [61] A. Taflove and S. C. Hagness, *Computational electrodynamics: the finite-difference time-domain method*, Artech House, 3rd edn. (2005), ISBN 1-58053-076-1.
- [62] J. C. Ehrhardt, “Hexagonal Fast Fourier Transform with Rectangular Output”, *IEEE Transactions on Signal Processing* **41**, 1469 (1993).
- [63] M. Schneider and S. van Smaalena, “Discrete Fourier transform in arbitrary dimensions by a generalized Beavers-Lipson algorithm”, *Acta Cryst* **A56**, 248 (2000).
- [64] M. Frigo and S. G. Johnson, “The Design and Implementation of FFTW3”, *Proceedings of the IEEE* **93**, 216 (2005).
- [65] M. Frigo and S. G. Johnson, “Fastest Fourier Transform in the West (FFTW)”, <http://fftw.org/>.
- [66] S. Johnson and J. Joannopoulos, “Block-iterative frequency-domain methods for Maxwell’s equations in a planewave basis”, *Optics Express* **8**, 173 (2001).
- [67] W. H. Press, S. A. Teukolsky, W. T. Vetterling, and B. P. Flannery, *Numerical Recipes in C*, CAMBRIDGE UNIVERSITY PRESS, 2nd edn. (2002), <http://www.nrbook.com/>.
- [68] “LAPACK - Linear Algebra PACKage”, <http://www.netlib.org/lapack/>.
- [69] H. J. Monkhorst and J. D. Pack, “Special points for Brillouin-zone integrations”, *Phys. Rev. B* **5188**, 5188 (1976).
- [70] L. Ward, *The optical constants of bulk materials and films*, Hilger (1988), ISBN 0-85274-168-5.
- [71] B. R. Cooper, H. Ehrenreich, and H. R. Philipp, “Optical Properties of Noble Metals. II.”, *Phys. Rev.* **138**, A494 (1965).

- [72] P. B. Johnson and R. W. Christy, “Optical Constants of the Noble Metals”, *Phys. Rev. B* **6**, 4370 (1972).
- [73] “Landolt-Börnstein / Numerical data and functional relationships in science and technology”, in O. Madelung, editor, “Metalle: Elektronische Transportphänomene”, vol. 15, Springer.
- [74] J. C. Maxwell Garnett, “Colours in Metal Glasses and in Metallic Films”, *Philos. Trans. R. Soc. Ser. A* **203**, 385 (1904).
- [75] C. F. Bohren and D. R. Huffman, *Absorption and scattering of light by small particles*, Wiley (1983), ISBN 0-471-05772-X.
- [76] Andrew Greenwell, “Private Communications while at UCF”, (2005).
- [77] M. Diem, *Beschreibung der optischen Eigenschaften periodisch strukturierter dünner dielektrischer Filme mit Methoden der diffraktiven Optik*, Diplomarbeit, Universität Karlsruhe (2003).
- [78] G. von Freymann, W. Koch, D. C. Meisel, M. Wegener, M. Diem, A. Garcia-Martin, S. Pereira, K. Busch, J. Schilling, R. B. Wehrspohn, and U. Gösele, “Diffraction properties of two-dimensional photonic crystals”, *Appl. Phys. Lett.* **83**, 614 (2003).
- [79] C. W. M. Castleton, A. Hglund, and S. Mirbt, “Managing the supercell approximation for charged defects in semiconductors: Finite-size scaling, charge correction factors, the band-gap problem, and the ab initio dielectric constant”, *Phys. Rev. B* **73**, 035215 (2006).
- [80] I. Zambetaki, Q. Li, E. N. Economou, and C. M. Soukoulis, “Localization in Highly Anisotropic Systems”, *Phys. Rev. Lett.* **76**, 3614 (1996).
- [81] A. MacKinnon and B. Kramer, “One-Parameter Scaling of Localization Length and Conductance in Disordered Systems”, *Phys. Rev. Lett.* **47**, 1546 (1981).
- [82] A. W. Fang, H. Park, O. Cohen, R. Jones, M. J. Paniccia, and J. E. Bowers, “Electrically pumped hybrid AlGaInAs-silicon evanescent laser”, *Optics Express* **14**, 9203 (2006).
- [83] J. Schilling, R. B. Wehrspohn, A. Birner, F. Müller, R. Hillebrand, U. Gösele, S. W. Leonard, J. P. Mondia, F. Genereux, H. M. van Driel, P. Kramper, V. Sandoghdar, and K. Busch, “A model system for two-dimensional and three-dimensional photonic crystals: macroporous silicon”, *Journal of Optics A* **3**, 121 (2001).
- [84] A. Birner, R. B. Wehrspohn, U. Gösele, and K. Busch, “Silicon-based Photonic Crystals”, *Adv. Mater.* **13**, 377 (2001).

- 
- [85] V. Lehmann and H. Foll, “Formation Mechanism and Properties of Electrochemically Etched Trenches in n-Type Silicon”, *Journal of The Electrochemical Society* **137**, 653 (1990).
- [86] T. Geppert, S. Schweizer, U. Gösele, and R. Wehrspohn, “Deep trench etching in macroporous silicon”, *Appl. Phys. A* **84**, 237 (2006).
- [87] S. Matthias, F. Müller, C. Jamois, R. Wehrspohn, and U. Gösele, “Large-Area Three-Dimensional Structuring by Electrochemical Etching and Lithography”, *Adv. Mater.* **16**, 2166 (2004).
- [88] H. Benisty, D. Labilloy, C. Weisbuch, C. J. M. Smith, T. F. Krauss, D. Casagne, A. Beraud, and C. Jouanin, “Radiation losses of waveguide-based two-dimensional photonic crystals: Positive role of the substrate”, *Appl. Phys. Lett.* **76** (2000).
- [89] D. Hermann, M. Diem, S. Mingaleev, A. Garcia-Martin, P. Wölfle, and K. Busch, “Photonic Crystals with anomalous dispersion: Novel propagating modes in the gap”, .
- [90] M. Frank, *Verlustmechnismen in ungeordneten quasi 1D Photonischen Kristallen*, Dissertation, Universität Karlsruhe, Institut für theoretische Festkörperphysik (2007).
- [91] M. Schillinger, *Maximally localized photonic Wannier functions for the highly efficient description of integrated Photonic Crystal circuits*, Dissertation, Universität Karlsruhe, Institut für theoretische Festkörperphysik (2006).
- [92] A. A. Asatryan, P. A. Robinson, L. C. Botten, R. C. McPhedran, N. A. Nicorovici, and C. Martijn de Sterke, “Effects of disorder on wave propagation in two-dimensional photonic crystals”, *Phys. Rev. E* **60**, 6118 (1999).
- [93] R. Rumpf and E. Johnson, “Fully three-dimensional modeling of the fabrication and behavior of photonic crystals formed by holographic lithography”, *J. Opt. Soc. Am. A* **21**, 1703 (2004).
- [94] M. M. Sigalas, C. M. Soukoulis, C. T. Chan, R. Biswas, and K. M. Ho, “Effect of disorder on photonic band gaps”, *Phys. Rev. B* **59**, 12767 (1999).
- [95] A. A. Asatryan, P. A. Robinson, L. C. Botten, R. C. McPhedran, N. A. Nicorovici, and C. M. de Sterke, “Effects of geometric and refractive index disorder on wave propagation in two-dimensional photonic crystals”, *Phys. Rev. E* **62**, 5711 (2000).
- [96] M. Bayindir, E. Cubukcu, I. Bulu, T. Tut, E. Ozbay, and C. M. Soukoulis, “Photonic band gaps, defect characteristics, and waveguiding in two-dimensional disordered dielectric and metallic photonic crystals”, *Phys. Rev. B* **64**, 195113 (2001).

- [97] K. A. Muttalib and P. Wölfle, “One-Sided Log-Normal Distribution of Conductances for a Disordered Quantum Wire”, *Phys. Rev. Lett.* **83**, 3013 (1999).
- [98] P. Markos, K. A. Muttalib, P. Wölfle, and J. R. Klauder, “Conductance distribution in 3D Anderson insulators: Deviation from log-normal form”, *Europhys. Lett.* **68**, 867 (2004).
- [99] P. Markos and C. M. Soukoulis, “Intensity distribution of scalar waves propagating in random media”, *Phys. Rev. B* **71**, 054201 (2005).
- [100] M. A. Kaliteevski, D. M. Beggs, S. Brand, R. A. Abram, and V. V. Nikolaev, “Stability of the photonic band gap in the presence of disorder”, *Phys. Rev. B* **73**, 033106 (2006).
- [101] Z.-Y. Li, X. Zhang, and Z.-Q. Zhang, “Disordered photonic crystals understood by a perturbation formalism”, *Phys. Rev. B* **61**, 15738 (2000).
- [102] M. A. Kaliteevski, J. M. Martinez, D. Cassagne, and J. P. Albert, “Disorder-induced modification of the transmission of light in a two-dimensional photonic crystal”, *Phys. Rev. B* **66**, 113101 (2002).
- [103] B. C. Gupta, C.-H. Kuo, and Z. Ye, “Propagation inhibition and localization of electromagnetic waves in two-dimensional random dielectric systems”, *Phys. Rev. E* **69**, 066615 (2004).
- [104] V. N. Astratov, A. M. Adawi, S. Fricker, M. S. Skolnick, D. M. Whittaker, and P. N. Pusey, “Interplay of order and disorder in the optical properties of opal photonic crystals”, *Phys. Rev. B* **66**, 165215 (2002).
- [105] A. F. Koenderink and W. L. Vos, “Light Exiting from Real Photonic Band Gap Crystals is Diffuse and Strongly Directional”, *Phys. Rev. Lett.* **91**, 213902 (2003).
- [106] A. F. Koenderink, A. Lagendijk, and W. L. Vos, “Optical extinction due to intrinsic structural variations of photonic crystals”, *Phys. Rev. B* **72**, 153102 (2005).
- [107] R. B. D’Agostino and M. A. Stephens, editors, *Goodness-of-fit techniques*, Dekker (1986), ISBN 0-8247-7487-6, 0-8247-8705-6.
- [108] K. Forberich, *Organische Photonische-Kristall-Laser*, Dissertation, Albert-Ludwigs-Universität Freiburg i. B. (2005).
- [109] K. Forberich, A. Gombert, S. Pereira, J. Crewett, U. Lemmer, M. Diem, and K. Busch, “Lasing mechanisms in organic photonic crystal lasers with two-dimensional distributed feedback”, *J. Appl. Phys.* **100**, 023110 (2006).

- [110] A. Haugeneder, M. Neges, C. Kallinger, W. Spirkl, U. Lemmer, J. Feldmann, M.-C. Amann, and U. Scherf, “Nonlinear emission and recombination in conjugated polymer waveguides”, *J. Appl. Phys.* **85**, 1124 (1999).
- [111] U. Scherf, S. Riechel, U. Lemmer, and R. F. Mahrt, “Conjugated polymers: lasing and stimulated emission”, *Current Opinion in Solid State and Materials Science* **5**, 143 (2001).
- [112] C. Zanke, A. Gombert, A. Erdmann, and M. Weiss, “Fine-tuned profile simulation of holographically exposed photoresist gratings”, *Opt. Commun.* **154**, 109 (1998).
- [113] H. Kogelnik and C. V. Shank, “Stimulated emission in a periodic structure”, *Appl. Phys. Lett.* **18**, 152 (1971).
- [114] L. Florescu, K. Busch, and S. John, “Semiclassical theory of lasing in photonic crystals”, *J. Opt. Soc. Am. B* **19**, 2215 (2002).
- [115] S. Riechel, C. Kallinger, U. Lemmer, J. Feldmann, A. Gombert, V. Wittwer, and U. Scherf, “A nearly diffraction limited surface emitting conjugated polymer laser utilizing a two-dimensional photonic band structure”, *Appl. Phys. Lett.* **77**, 2310 (2000).
- [116] A. E. Siegman, *Lasers*, Univ. Science Books (1986), ISBN 0-935702-11-3.
- [117] K. Forberich, M. Diem, J. Crewett, U. Lemmer, A. Gombert, and K. Busch, “Lasing action in two-dimensional organic photonic crystal lasers with hexagonal symmetry”, *Appl. Phys. B* **82**, 539 (2006).
- [118] J. Sturm, S. Tasch, A. Niko, G. Leising, E. Toussaere, J. Zyss, T. C. Kowalczyk, K. D. Singer, U. Scherf, and J. Huber, “Optical anisotropy in thin films of a blue electroluminescent conjugated polymer”, *Thin Solid Films* **298**, 138 (1997).
- [119] D. C. Meisel, *Herstellung dreidimensionaler Photonischer Kristalle mittels holographischer Lithographie und deren Charakterisierung*, Dissertation, Universität Karlsruhe, Institut für Angewandte Physik (2006).
- [120] D. C. Meisel, *Herstellung und Charakterisierung dreidimensionaler Photonischer Kristalle auf der Basis von Vielstrahlinterferenzen*, Diplomarbeit, Universität Karlsruhe, Institut für Angewandte Physik (2002).
- [121] M. Campbell, D. Sharp, M. Harrison, R. Denning, and A. Turberfield, “Fabrication of photonic crystals for the visible spectrum by holographic lithography”, *Nature* **404**, 53 (2000).

- [122] S. Shoji and S. Kawata, “Photofabrication of three-dimensional photonic crystals by multibeam laser interference into a photopolymerizable resin”, *Appl. Phys. Lett.* **76**, 2668 (2000).
- [123] Y. Miklyaev, D. Meisel, A. Blanco, G. von Freymann, K. Busch, W. Koch, C. Enkrich, M. Deubel, and M. Wegener, “Three-dimensional face-centered-cubic photonic crystal templates by laser holography: fabrication, optical characterization, and band-structure calculations”, *Appl. Phys. Lett.* **82**, 1284 (2003).
- [124] D. C. Meisel, M. Wegener, and K. Busch, “Three-dimensional photonic crystals by holographic lithography using the umbrella configuration: Symmetries and complete photonic band gaps”, *Phys. Rev. B* **70**, 165104 (2004).
- [125] J. W. Rinne and P. Wiltzius, “Design of holographic structures using genetic algorithms”, *Optics Express* **14**, 9909 (2006).
- [126] D. Meisel, “private communications”, .
- [127] R. Rumpf and E. Johnson, “Comprehensive modeling of near-field nanopatterning”, *Optics Express* **13**, 7198 (2005).
- [128] E. Yablonovitch, “Photonic band-gap structures”, *J. Opt. Soc. Am. B* **10**, 283 (1993).
- [129] C. Lopéz, “Materials aspects of photonic crystals”, *Adv. Mater.* **15**, 1679 (2003).
- [130] N. Tétreault, H. Míguez, and G. A. Ozin, “Silicon inverse opal – a platform for photonic bandgap research”, *Adv. Mater.* **16**, 1471 (2004).
- [131] N. Tétreault, G. von Freymann, M. Deubel, M. Hermatschweiler, F. Pérez-Willard, S. John, M. Wegener, and G. A. Ozin, “New route to three-dimensional photonic bandgap materials: Silicon souble inversion of polymer templates”, *Adv. Mater.* **18**, 457 (2006).
- [132] M. Deubel, *Dreidimensionale Photonische Kristalle mittels direkten Laserschreibens: Herstellung und Charakterisierung*, Dissertation, Universität Karlsruhe (TH), Institut für Angewandte Physik (2006).
- [133] M. Deubel, G. von Freymann, M. Wegener, S. Pereira, K. Busch, and C. Soukoulis, “Direct laser writing of three-dimensional photonic crystal templates for telecommunications”, *Nature Mater.* **3**, 444 (2004).
- [134] M. Deubel, M. Wegener, A. Kaso, and S. John, “Direct laser writing and characterization of ”slanted pore” photonic crystals”, *Appl. Phys. Lett.* **85**, 1895 (2004).

- [135] S. Shoji, R. Zaccaria, H. B. Sun, and S. Kawata, “Multi-step multi-beam laser interference patterning of three-dimensional photonic lattices”, *Optics Express* **14**, 2309 (2006).
- [136] L. Guerin, M. Bossel, M. Demierre, S. Calmes, and P. Renaud, “Simple and low cost fabrication of embedded micro-channels by using a new thick-film photoplastic”, in “Solid State Sensors and Actuators (Transducers '97)”, vol. 2, p. 1419 (1997).
- [137] R. W. Wood, “On a remarkable case of uneven distribution of light in a diffraction grating system”, *Proc. Phys. Soc. (London)* **12**, 269 (1902).
- [138] R. W. Wood, “Anomalous Diffraction Gratings”, *Phys. Rev.* **48**, 928 (1935).
- [139] D. Meisel, M. Diem, M. Deubel, F. Prez-Willard, S. Linden, D. Gerthsen, K. Busch, and M. Wegener, “Shrinkage Precompensation of Holographic Three-Dimensional Photonic-Crystal Templates”, *Adv. Mater.* **18**, 2964 (2006).
- [140] Y. Lin, D. Rivera, and Z. Poole, “Five-beam interference pattern controlled through phases and wave vectors for diamondlike photonic crystals”, *Appl. Opt.* **45**, 7971 (2006).
- [141] J. H. Moon, S. Yang, and S.-M. Yang, “Photonic band-gap structures of core-shell simple cubic crystals from holographic lithography”, *Appl. Phys. Lett.* **88**, 121101 (2006).
- [142] H. Misawa, T. Kondo, S. Juodkazis, V. Mizeikis, and S. Matsuo, “Holographic lithography of periodic two- and three-dimensional microstructures in photore-sist SU-8”, *Optics Express* **14**, 7943 (2006).
- [143] Y. Liu, S. Liu, and X. Zhang, “Fabrication of three-dimensional photonic crystals with two-beam holographic lithography”, *Appl. Opt.* **45**, 480 (2006).
- [144] Y. K. Pang, J. C. Lee, C. T. Ho, and W. Y. Tam, “Realization of wood-pile structure using optical interference holography”, *Optics Express* **14**, 9013 (2006).
- [145] Y. C. Zhong, S. A. Zhu, H. M. Su, H. Z. Wang, J. M. Chen, Z. H. Zeng, and Y. L. Chen, “Photonic crystal with diamondlike structure fabricated by holographic lithography”, *Applied Physics Letters* **87**, 061103 (2005).
- [146] V. G. Veselago, “The electrodynamics of substances with simultaneously negative values of  $\epsilon$  and  $\mu$ ”, *Sov. Phys. USPEKHI* **10**, 509 (1968).
- [147] D. R. Smith, W. J. Padilla, D. C. Vier, S. C. Nemat-Nasser, and S. Schultz, “Composite Medium with Simultaneously Negative Permeability and Permittivity”, *Phys. Rev. Lett.* **84**, 4184 (2000).

- [148] D. R. Smith, S. Schultz, P. Markos, and C. M. Soukoulis, “Determination of effective permittivity and permeability of metamaterials from reflection and transmission coefficients”, *Phys. Rev. B* **65**, 195104 (2002).
- [149] G. Dolling, C. Enkrich, M. Wegener, C. M. Soukoulis, and S. Linden, “Low-loss negative-index metamaterial at telecommunication wavelengths”, *Opt. Lett.* **31**, 1800 (2006).
- [150] G. Dolling, C. Enkrich, M. Wegener, J. Zhou, C. Soukoulis, and S. Linden, “Cut-wire pairs and plate pairs as magnetic atoms for optical metamaterials”, *Opt. Lett.* **30**, 3198 (2005).
- [151] C. Enkrich, M. Wegener, S. Linden, S. Burger, L. Zschiedrich, F. Schmidt, J. F. Zhou, T. Koschny, and C. M. Soukoulis, “Magnetic Metamaterials at Telecommunication and Visible Frequencies”, *Phys. Rev. Lett.* **95**, 203901 (2005).
- [152] K. Kneipp, editor, *Surface-enhanced Raman scattering*, Springer (2006), ISBN 3-540-33566-8,978-3-540-33566-5.
- [153] A. A. Asatryan, P. A. Robinson, R. C. McPhedran, L. C. Botten, C. M. de Sterke, T. L. Langtry, and N. A. Nicorovici, “Diffusion and anomalous diffusion of light in two-dimensional photonic crystals”, *Phys. Rev. E* **67**, 036605 (2003).

Ich erkläre hiermit, dass ich die vorliegende Arbeit selbständig verfasst und keine anderen als die angegebenen Quellen und Hilfsmittel verwendet habe.

Karlsruhe, 22. Dezember 2006

---

Marcus Diem



# Danksagung

Die letzte Seite ist den Personen gewidmet, die mich bei der Erstellung dieser Arbeit unterstützt haben. Besonders bedanken möchte ich mich bei:

Prof. Dr. Kurt Busch für die Betreuung meiner Promotion sowie die Unterstützung und die Ermöglichung meines Auslandsaufenthaltes. Das sehr gute Arbeitsklima in der Photonics Group ist seinem Einsatz zu verdanken. Sein Interesse und Vertrauen führte zu vielen anregenden Diskussionen und Ideen, gab mir aber gleichzeitig Freiraum bei der Umsetzung der Fragestellungen. Seine guten Kontakte zu experimentellen Gruppen waren in dieser Arbeit von großer Bedeutung.

Prof. Dr. Peter Wölfle, für die Übernahme des Korreferates, die Möglichkeit meine Promotion am Institut für Theorie der Kondensierten Materie zu beginnen sowie die Unterstützung meines Auslandsaufenthaltes.

Meinen langjährigen Kollegen Meikel Frank, Frank Hagmann, Daniel Hermann und Matthias Schillinger für die vielen schönen Stunden nicht nur im Büro, den zahlreichen Diskussionen, Anregungen und Hilfestellungen sowie gelegentlich notwendigen Ablenkungen. Lasha Tkeshelashvili for numerous, very interesting discussions.

Den weiteren Mitgliedern der Photonics Group (Julia Budde, Maria Dienerowitz, Sabine Essig, Antonio Garcia-Martin, Johannes Hagmann, Michael König, Patrick Mack, Sergei Mingaleev, Martin Pototschnig, Jens Niegemann, Suresh Pereira, Mauro Schelb und Christian Wolff) für das gute Arbeitsklima und die interessanten Diskussionen. Thank you for your support and many interesting discussions over the last years.

Meinen experimentellen Kooperationspartnern Karen Forberich und Daniel Meisel für die vielen interessanten Diskussionen. Die Erarbeitung einer gemeinsamen „Sprache“ war einer der sehr interessanten Aspekte dieser Arbeit.

Den Personen im Hintergrund (Frau Herzog, Frau Schwartz, Frau Schrempp, Gaston), die mir in vielen alltäglichen Dingen behilflich waren.

Prof. Mucciolo, Sergio Tafur, Tom Fleniken at the University of Central Florida for the administration of and help with the cluster.

Abschließend möchte ich meinen Eltern für die jahrelange Unterstützung danken, ohne die dies alles nicht möglich gewesen wäre.